

Mechanical
Engineering Theory
and Applications

Eugenio Brusa
Editor

Mechatronics

Principles, Technologies and Applications

NOVA

MECHATRONICS

PRINCIPLES, TECHNOLOGIES AND APPLICATIONS

No part of this digital document may be reproduced, stored in a retrieval system or transmitted in any form or by any means. The publisher has taken reasonable care in the preparation of this digital document, but makes no expressed or implied warranty of any kind and assumes no responsibility for any errors or omissions. No liability is assumed for incidental or consequential damages in connection with or arising out of information contained herein. This digital document is sold with the clear understanding that the publisher is not engaged in rendering legal, medical or any other professional services.

MECHANICAL ENGINEERING THEORY AND APPLICATIONS

Additional books in this series can be found on Nova's website
under the Series tab.

Additional e-books in this series can be found on Nova's website
under the e-book tab.

MECHANICAL ENGINEERING THEORY AND APPLICATIONS

**MECHATRONICS
PRINCIPLES, TECHNOLOGIES
AND APPLICATIONS**

**EUGENIO BRUSA
EDITOR**



Copyright © 2015 by Nova Science Publishers, Inc.

All rights reserved. No part of this book may be reproduced, stored in a retrieval system or transmitted in any form or by any means: electronic, electrostatic, magnetic, tape, mechanical photocopying, recording or otherwise without the written permission of the Publisher.

We have partnered with Copyright Clearance Center to make it easy for you to obtain permissions to reuse content from this publication. Simply navigate to this publication's page on Nova's website and locate the "Get Permission" button below the title description. This button is linked directly to the title's permission page on copyright.com. Alternatively, you can visit copyright.com and search by title, ISBN, or ISSN.

For further questions about using the service on copyright.com, please contact:

Copyright Clearance Center

Phone: +1-(978) 750-8400 Fax: +1-(978) 750-4470 E-mail: info@copyright.com.

NOTICE TO THE READER

The Publisher has taken reasonable care in the preparation of this book, but makes no expressed or implied warranty of any kind and assumes no responsibility for any errors or omissions. No liability is assumed for incidental or consequential damages in connection with or arising out of information contained in this book. The Publisher shall not be liable for any special, consequential, or exemplary damages resulting, in whole or in part, from the readers' use of, or reliance upon, this material. Any parts of this book based on government reports are so indicated and copyright is claimed for those parts to the extent applicable to compilations of such works.

Independent verification should be sought for any data, advice or recommendations contained in this book. In addition, no responsibility is assumed by the publisher for any injury and/or damage to persons or property arising from any methods, products, instructions, ideas or otherwise contained in this publication.

This publication is designed to provide accurate and authoritative information with regard to the subject matter covered herein. It is sold with the clear understanding that the Publisher is not engaged in rendering legal or any other professional services. If legal or any other expert assistance is required, the services of a competent person should be sought. FROM A DECLARATION OF PARTICIPANTS JOINTLY ADOPTED BY A COMMITTEE OF THE AMERICAN BAR ASSOCIATION AND A COMMITTEE OF PUBLISHERS.

Additional color graphics may be available in the e-book version of this book.

Library of Congress Cataloging-in-Publication Data

Mechatronics (2015)

Mechatronics : principles, technologies and applications / editors, Eugenio Brusa, Dip. Ingegneria Meccanica e Aerospaziale, Politecnico Di Torino, Corso Duca Degli Abruzzi, Torino, Italy.

 pages cm. -- (Mechanical engineering theory and applications)

 Includes index.

ISBN: ; 9: /3/856: 4/: 76/5 (eBook)

1. Mechatronics. I. Brusa, Eugenio. II. Title.

TJ163.12.M42245 2015

621--dc23

2015015687

Published by Nova Science Publishers, Inc. † New York

CONTENTS

Preface	vii	
Chapter 1	Mechatronics of Hard Disk Drives: Rise Feedback Track Following Control of a R/W Head	1
	<i>M. Taktak-Meziou, A. Chemori, J. Ghommam and N. Derbel</i>	
Chapter 2	Sagittal Biped Chaos Control Modeling	23
	<i>Riaan Stopforth and Glen Bright</i>	
Chapter 3	Hardware and Fluid in the Loop Testing: The Application to the Testing of Fluid Systems, Some Examples and Applications	53
	<i>Emanuele Galardi, Daniele Nocciolini and Luca Pugi</i>	
Chapter 4	The Low Cost Design of a 3D Printed Multi-Fingered Myoelectric Prosthetic Hand	85
	<i>Drew van der Riet, Riaan Stopforth, Glen Bright and Olaf Diegel</i>	
Chapter 5	Mechatronic Integration for Search and Rescue Applications: UAV Vision System for Mining and Manufacturing Environments	119
	<i>Sibonelo Motepe and Riaan Stopforth</i>	
Chapter 6	A Low Cost, Extendable Prosthetic Leg for Trans-Femoral Amputees	139
	<i>Drew van der Riet and Riaan Stopforth</i>	
Chapter 7	Integration of Sensors and Actuators to Suppress Vibrations on Carbon Fiber Structures	167
	<i>Gabriele Cazzulani, Simone Cinquemani and Francesco Braghin</i>	
Chapter 8	Emerging Role of the Mechatronic Design of Industrial Systems for the Material Processing Technology	185
	<i>Eugenio Brusa</i>	
Chapter 9	Prediction and Control of Vibrations and Chatter in Machining	207
	<i>Marco Sortino and Giovanni Totis</i>	
Index		241

PREFACE

A recent experience within the frame of the EMEA (Europe – Middle East and Africa) District of the ASME (American Society of Mechanical Engineers) encouraged me to actively participate to this editorial project whose aim is giving an impression of some current topics in *mechatronics*, being subject of several research activities and of industrial efforts focused on a continuous innovation of product, process and professional expertise. As the Reader could realize the Authors replied to a call from the Mediterranean area and Africa, obviously without any inhibition to collaborate with other institutions outside the EMEA region. They propose herein an overview of *applications*, *methodologies* and *technologies* which are nowadays characterizing the ongoing activity within the field of *mechatronics*. Those issues are a little bit melt inside each chapter, since in everyone some item related to a specific application, technology and method used in designing, controlling and manufacturing the system is described. Actually those details assure the originality of each contribution herein enclosed, as the Authors wrote.

To present the result of this effort a common understanding about the meaning of *mechatronics* is required, because it is well known that a number of definitions was worldwide proposed. After more than thirty years, the interpretation of *mechatronics* written by Bradley and Dawson (1991) as “the synergistic combination of precision mechanical engineering, electronic control and systems thinking in the design of products and processes” still brightly and shortly describes some essential properties of systems designed and manufactured by following the so-called *mechatronic approach*. As that sentence states typical nature of *mechatronics* is to be inter-disciplinary, since all the technical competences of engineering, computer and material sciences cooperate to design a unique product which includes and exploits some artificial intelligence or simply *smartness*. This one is usually associated to the system capability of perceiving any abrupt variation of the operating conditions and to its skill of self-adapting, through a suitable control action which modifies its own configuration.

Examples of *control* target and technology are proposed through the chapters. A very traditional mechatronic application of hard disc drive is proposed in Chapter one to show how the position tracking of the read/write head can be suitably controlled, by resorting to the technology of neural networks. Distinction between linear and nonlinear dynamics control is a matter of discussion in Chapter two, which describes the arising of chaos and a control technique applied to the human locomotion eventually assisted by prostheses. Dynamic behavior is evenly the goal of Chapter three, although in this case the Authors deal with the

control of fluids for industrial automation purpose. It is worth noticing how they resort to the solution of hardware-in-the-loop to implement the control by facing even the problem of a rapid prototyping of the mechatronic system, being a critical issue of the design activity. A nice application of control is that of multi-fingered prosthetic hand, described in Chapter four. Human–system interface is here a key issue of design, since myoelectricity is used to operate the biotronic hand by converting the electric stimulation into the mechanical grip.

Electromechanical coupling is exploited in all those cases, while a completely different technology is applied to detect the human presence through a vision system, as in Chapter five. It is focused on the use of unmanned air vehicles for search and rescue purpose, applied to mining and manufacturing environments. Vibration control and monitoring of flexible structures instead of mechanisms and rigid bodies are object of Chapters seven, eight and nine. A first contribution, in Chapter seven, is concerning the structural health monitoring and control of flexible composite structures, equipped with piezoelectric patches and fiber optics. In this case a modal control approach is applied to detect any failure of composite material and to suppress vibration. Problem of predicting and controlling simultaneously the motion of rigid bodies and vibration of flexible elements is analyzed in Chapter eight. Dynamic behavior of heavy structural equipments undergoing thermo–electro–mechanical coupling effects induced by heat transfer and magnetic field is there modeled through an integrated numerical approach. In particular the ‘multi–body dynamics’ and ‘finite element’ methods are applied, by resorting to a ‘multi–physic’ numerical solution. Control of self–excited vibration and chatter of elements of tooling machines is the goal of Chapter nine. In this case dynamic stability is achieved through an active control.

All the above mentioned examples provide an overview of applications where *synergy* among different competences clearly appears, as they are exploited in several technical domains, as computer science, bioengineering, industrial automation, manufacturing and machining systems and aeronautics. In some cases *system thinking* is strictly applied to *product* development, as for the hard disc drive, prostheses and UAV, while *process* is expressively considered in embedding of fiber optics into the smart composite structures, in control of steel material processing or of turning operation. Product life management is a well recognized goal of mechatronic design too, as in Chapter six. Extendable prosthetic leg imposes a bright analysis of all the product life cycle, as is foreseen by the so–called *Systems Engineering*. A detailed design of the product architecture is therefore performed to fulfill requirements of compatibility with the actuator used to extend the artificial leg, of cost, maintenance and ergonomics. A good inter–operability between the numerical tool used to investigate the material behavior and the modeler of the system geometry or the simulator of the actuator device has to be assured. Moreover, a rapid prototyping of the mechanical system may help in validating both the modeling and control techniques. This task can be accomplished by some new technology like 3D printing, as it is described in Chapter four or through an integration of hardware and software as is detailed in Chapter three.

All the Authors wish the Reader to get a nice impression of *mechatronics* as it currently looks in daily practice more than in theory, as this book was aimed to preliminarily show.

It might be realized that nowadays, a mechatronic system, being either a product or a process, takes advantage not only from its *smartness*, but even more from the benefit of *contamination* among different domains, methodologies and technologies, that could be applied in the early stage of design and *system thinking*.

Eugenio Brusa

Dept. Mechanical and Aerospace Engineering,
Politecnico di Torino, Turin, Italy
Email: eugenio.brusa@polito.it

Chapter 1

MECHATRONICS OF HARD DISK DRIVES: RISE FEEDBACK TRACK FOLLOWING CONTROL OF A R/W HEAD

M. Taktak-Meziou^{1*}, A. Chemori^{2†}, J. Ghommam^{1‡} and N. Derbel^{1§}

¹CEM Lab, Department of Electrical Engineering, University of Sfax, Tunisia

²LIRMM, University Montpellier, France

Abstract

This chapter addresses design challenges associated with a servo system of a Hard Disc Drive (HDD). A P-RISE-NN control approach is proposed. The main objective of this novel controller is to enhance the track following in a Hard Disc Drive. Indeed, P-RISE-NN approach involves an optimal gain selection, in a RISE-NN controller. Taking advantage of the prediction feature, the controller is able to anticipate the future behavior of the system. Consequently, it can easily handle various constraints that may be imposed on its variables. Furthermore, the boundedness of the closed-loop signals as well as the convergence of the tracking error to zero are ensured. Comprehensive comparison between the classical RISE-NN and P-RISE-NN are provided through numerical simulations in different operating conditions. It is shown that P-RISE-NN can maintain a good control performance in nominal case and in the presence of external disturbances. Besides, the controller is also robust towards uncertainties on the system parameters.

Keywords: Hard-Disc-Drives servo-systems, predictive control, RISE feedback, neural networks, nonlinear systems, control design and asymptotic stability

*E-mail address: manel.taktak@yahoo.com, National School of Engineers of Sfax (ENIS), BP, W 3038 Sfax Tunisia

†E-mail address: Ahmed.Chemori@lirmm.fr, CNRS, UMR5506, CC477, 161 rue Ada, 34095 Montpellier Cedex 5, France

‡E-mail address:jawhar.ghommam@gmail.com, National School of Engineers of Sfax (ENIS), BP, W 3038 Sfax Tunisia

§E-mail address:n.derbel@enis.rnu.tn, National School of Engineers of Sfax (ENIS), BP, W 3038 Sfax Tunisia

1. Introduction

One of the most important parts of a computer is the hard drive (HDD). All of the information displayed on the screen of a computer are stored on the hard drive. For this reason, higher capacities HDD are always required and new generations of computers are expected to contain larger storage capacities with a rapid access to the stored data.

Consequently, the HDD industry has undergone a tremendous growth. This big change is noticeable both in the physical size and the performance characteristics. The first generation of this devise, known as RAMAC 305, has been introduced in 1956 by IBM. It was a huge material with fifty 24" disks able to store about 5 Megabytes of digital data at a bit density of $2K \text{ bits/in}^2$. The data throughput was about $8.8K \text{ bits/s}$. Today's used HDD are very advanced with a storage capacity close to 5 Terabytes of data on one disk surface whose the factor form ranges from 2.5" to 3.5" drive.

Along with this trend toward smaller HDD, the task of the head positioning servo-system is the most objective to be accomplished with the highest possible performances. In a HDD, the Read/Write (R/W) head is moved from its actual position to the desired destination track to record or to retrieve data onto the disc. For a reliable data treatment, the position error defined as the distance between the head tip and the target track center, has to be as minimal as possible. Besides, the transition from one position to another is required to be achieved in minimum time using a bounded control effort.

Unfortunately, the HDD servo-positioning system is often subject to several errors' sources leading to the degradation of the overall closed-loop system performances. These sources may include: (i) mechanical resonance modes caused by the flexibility of the materiel and vibrations induced by the high-speed air flowing around the suspension arm and head assembly, (ii) nonlinearities in the dynamics and uncertainties on the parameters of the whole system, (iii) presence of measurement noise, (iv) run-outs due to the spindle motor bearings and (v) track miss-registration caused by the nonlinear hysteresis behavior of the pivot bearing.

All these factors have been neglected in the earliest drive versions. However, in small drives, they require a rigorous analysis and become one of the challenges in the head positioning servo systems control design. Therefore, several efforts have been put into the HDD research. Their main objective is to find an effective control solution able to treat these factors and compensate as much as possible their degrading; Subsequently, this enables the system to meet the increasing demands for a high track density, accurate and rapid functionality of the HDD servo-positioning system.

A survey of the different control approaches developed to design servo controllers for HDDs allows to classify them into different categories. These latter range from classical approaches such as PID controllers (Isayed & Hawwa, 2007), lead-lag compensator (Ishikawa & Tomizuka, 1998) and different filters (Atsumi, et al., 2007), to more advanced control solutions including adaptive control (Horowitz & Li, 1995)(Kobayashi, et al., 2004), sliding mode control (Yamaguchi, et al., 1997)(Yamaguchi & Hirai, 1998)(Venkataramanan, et al., 2002), robust control (Nie, et al., 2011)(Graham & De Callafon, 2006)(Hirata, et al., 2003), Robust and Perfect Tracking (RPT) (Goh, et al., 2001), Composite Non-linear Feedback (CNF) control (Chen, et al., 2003) and more recently predictive control (Taktak, et al., 2013)(Taktak, et al., 2012) and prediction based state feedback control (Lee

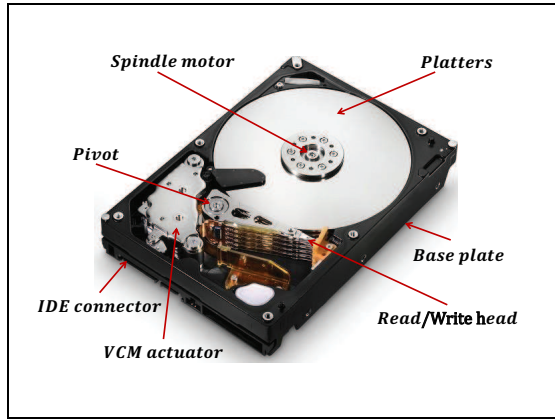


Figure 1. Schematic diagram of a typical HDD.

& Suh, 2011). Despite the diversity of the control techniques, more researches need to be conducted to carry out the functioning of the HDD and achieve higher performances.

This chapter focuses on the positioning control problem of a HDD servo system's track following. The main contribution of this paper consists of combining MPC with a classical RISE based Neural Network control method (Patre, et al., 2008b)(Makkar, et al., 2007). The key benefit of the proposed method is its ability to control the sensitivity of the gain feedback term of RISE to variation which impact the overall closed-loop system under the imposed restrictions. The fundamental idea is inspired from the Nonlinear Model Predictive Control (NMPC) (Camacho & Bordons, 2004). Indeed, instead of calculating an optimal control sequence, the proposed method determines the optimal value of the feedback gain based on the predicted behavior of the system. The controller, called P-RISE-NN, is able to predict the evolution of the system in the future over a prediction horizon. Besides, it can deal with any external disturbances affecting the controlled system and any change in the dynamic parameters.

The proposed P-RISE-NN scheme will be studied for its effectiveness not only to the mitigate inappropriate responses, but also to ameliorate the tracking performances in terms of speed, robustness and accuracy in various HDD operating conditions.

2. Hard Disc Drive: Mechatronic System

2.1. Components of a HDD

According to the general definition of the Mechatronic Forum (Mahalik, 2003), *Mechatronics is the synergistic integration of mechanical engineering with electronics and control in the design and manufacturing of product process*. Therefore, the HDD is obviously an amazing mechatronic device. Its components can be classified into four essential categories including: Electronic part, mechanical components, automatic and real-time computing. The main components of a typical HDD are illustrated in Figure 1.

2.1.1. Electronic part

The electronic part of an HDD includes the necessary components to perform the following various functions: reading/ writing data, spinning the discs, positioning the R/W head onto the platter surface, controlling the various operation of the disc (reading/ writing/ transfer data), interface with the host system, RAM-ROM, etc. A brief description of these components is elaborated in the following.

Disk platters: In a HDD, digital data are recorded on magnetic continuously rotating disk in the form of circular patterns called tracks. A disk has two surfaces called platters which are coated with thin layers of magnetic material (cf. Figure 2). These platters are placed around a rotating axis driven by an electric motor (spindle motor). The speed varies according to both the mark and the model of hard drive. It is usually between 5400 rpm and 15000 rpm. The manufacture of the platters surfaces requires an accurate treatment that remove any impurity and guarantee a smooth-lightweight material for the best data storage performances.



Figure 2. Multiple platters of a HDD.

Spindle-motor assembly: It is the primarily responsible of spinning the disk platters of the HDD with constant, stable and reliable speed for thousands of hours (cf. Figure 3). The spindle motor assembly is mainly composed of a servo-controlled brushless DC motor directly connected to the HDD platters. The fluid dynamic or aerodynamic bearing spindles are normally used in high performance HDDs in which the spindle speed exceeds 10000 rpm. However, several HDD models devoted for desktop use and mobile environment are still using a lower spindle speed varying between 5400 rpm and 6000 rpm. Recently, designed HDDs are using higher spinning rates of up to 15000 rpm for superior operating performance.

Setting spindle motor bearings at the extremity of each spindle shaft in one of the most critical component in HDD's spindle motor. Indeed, with the increasingly demand for higher areal density and faster spindle speed, the fluid dynamic bearing (FDB) spindle motor are more adopted in HDDs. It turned out that in ball bearing motors, the mechanical contact between the ball and race of the bearings contributes to the degradation of the system working performances. Moreover, it is worth noting that the variation of spindle speed is a key source of disturbance generation in the tracking task of the HDD; hence the need for an accurate control of the motors' speed.

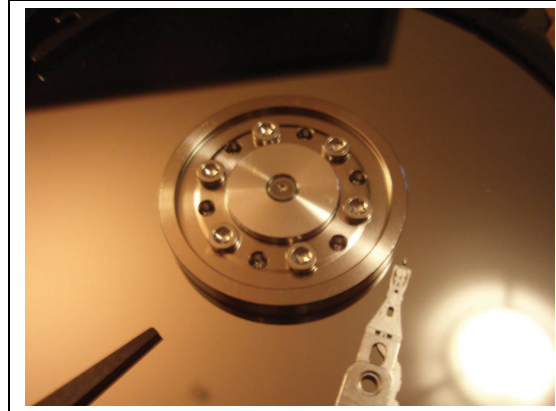


Figure 3. Spindle motor assembly of the HDD.

Actuator assembly: In a HDD, the actuator assembly is dedicated to ensure the displacement and the positioning of the R/W head over the disk surface. It consists of a Voice Coil Motor (VCM), a pivot bearing, data flex cable or printed circuit cable carrying signal to/from the R/W heads and VCM, and actuator arms.

The actuator is located at the end attached to the actuator arm. This latter is somewhat long and triangular-shaped with the base being attached to the actuator itself. Earlier actuators tended to be solid metal pieces but increasingly today they are largely hollow, more like a triangular frame. The actuator is connected to a Voice Coil Motor (VCM) (cf. Figure 4). Through the operation of the VCM, it moves the actuator arm back and forth over the disk surface in an arc. This allows the actuator arm to be moved into position above every data track and sector on the disk. The actuator/VCM assembly lifts the actuator arm up and moves it over the track where the data sought is located. The actuator assembly is able to displace the actuator arm and its head at a feverish pace with a high rotating speed of the disks.

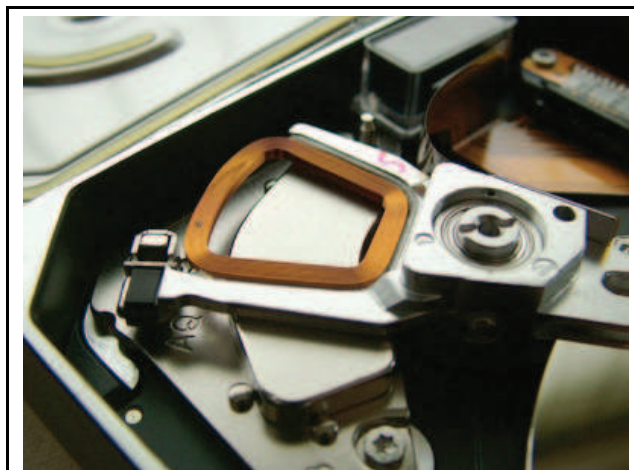


Figure 4. VCM actuator of a HDD.

Head positioning actuator assembly: The R/W heads are used to treat date on the disk. They are small mobile components able to move in both directions over the disc. Older HDDs used the electromagnetic induction principle with ferrite, metal-in-gap and thin-film single head. However, modern HDD use separate heads for reading (giant-magneto-resistive heads) and other for writing (thin-film inductive heads).

Each disk surface is accessed by a typical head slider mounted at the suspension arm. The movement of the slider between any two tracks of the disc is driven by the VCM actuator. It is worth knowing that the heads are positioned only micro-inches above the recording medium on an air-bearing surface. A gimbal attaches the slider to a stainless steel suspension to allow for pitch and roll, and the suspension is attached to the arm of the actuator by a ball swaging (cf. Figure 5).

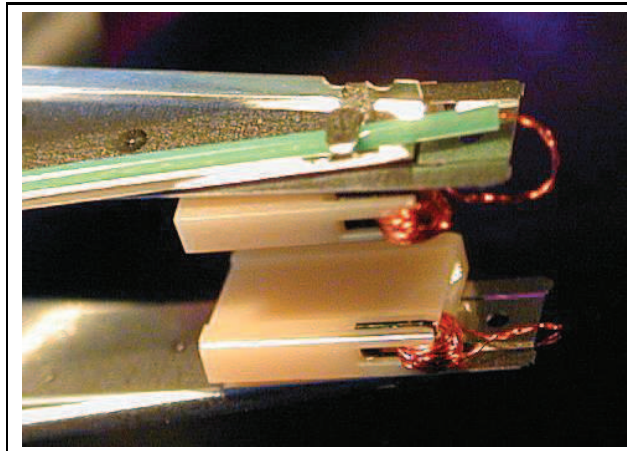


Figure 5. Head positioning actuator assembly.

Electronic card: This component is responsible for making the relationship between the host personal computer and the hard disk. There are different types of electronic cards. They include: (i) the Parallel Advanced Technology Attachment (PATA) used for a long time and can link up to two hard drives or CD / DVD on a ribbon cable. An element must be configured as master and the other slave using jumpers, (ii) the Serial Advanced Technology Attachment (SATA) available since 2003; this technology uses different connectors and requires no special configuration. It is even possible to connect / disconnect a turned on SATA element and (iii) the Small Computer Systems Interface (SCSI) which is highly efficient; they are also very expensive and require an additional controller card. SCSI technology is reserved for the professional field.

All these integrated circuits have a power driver for the spindle motor, VCM, R/W electronics, servo demodulator, controller chip for timing control and control of interface, micro-controller/digital signal processor (DSP) for servo control, and ROM and RAM for microcode and data transfer.

2.1.2. Mechanical components

The most important component of the HDD is the device enclosure. It is responsible of the reliability of the prototype. It is sealed to protect the inner components from any danger

that may damage it. It is essential that the enclosure is capable of isolating the drive of the dust, humidity, temperature and dirt that can enter inside the enclosure. This will keep components safe and reduce the risk of damaging them. Therefore, because the head is so close to the disc's surface, any particles could damage the disc resulting in data loss. So, the idea is to place a recirculating filter in the airflow. It removes small particles scraped off the platter. Thus, the mechanical hard drive is treated as a clean room to ensure the perfection of the surfaces and the smooth operating of the drive.

2.1.3. Automatic

Control engineering is an important part of the design process of the HDD. The HDD, as a physical system, has a nonlinear behavior due to many factors, essentially due to disturbances and external shocks. The challenge is therefore to drastically improve the HDD performances despite the ever presence of these factors.

In order to safeguard the digital information in the disks, it is important to robustly controlling the HDD. An effective control have to regulate the head position throughout their working such as the position error is minimized. In fact, the imposed constraints on the controlled system , external disturbances and uncertainties in the system's model have to be compensated properly.

2.1.4. Real-time computing

Real-time control system is required when the HDD is involved in operations such as closed-loop tracking control problems for R/W head, state estimation and external disturbance compensation. At this point, it is oblivious to verify the quality of the HDD model, to discover unexpected effects and consider ways to improve the control design. This can be achieved by implementing the controller using an embedded software/hardware which run periodically on the basis of a clock that can be derived from an I/O signal or a precise CPU timer.

2.2. Operating Principle of HDD Servo Systems

A home computer is a powerful tool which must store data reliably for a more efficient functioning. To better manage its operation, it is essential to understand how its HDD works.

Principally, a HDD is devoted to store data in binary form, 1's and 0's. The actuator arm supports a head. It is an electromagnet that scans over the disc and either writes data by changing the magnetization of specific sections on the platter or it just reads the data by measuring the magnetic polarization. The key focus lies in being sure that the head can precisely, error free, read and write to the disc. The first order of business is to move it with great control.

To position the arm, engineers use a voice coil actuator (cf. Figure 4). The base of the arm sits between two powerful magnets. They're so strong, they're actually kind of hard to pull apart. The arm moves because of a Lorentz force. Passing a current through a wire that's in a magnetic field and then the wire experiences a force. Reverse the current and the force also reverses. As current flows in one direction in the coil, the force created by the

permanent magnet makes the arm move in one direction. Reverse the current and it moves back. The force from the arm is directly proportional to current through the coil, which allows the arms position to be finely tuned. Unlike a mechanical system of linkages, there is minimal wear and it is not sensitive to temperature.

At the end of the arm lies the head. As it passes over the magnetized sections of the platter, it measures changes in the direction of the magnetic poles, the so-called Faraday's law, a change in magnetization produces a voltage in a nearby coil. So, as the head passes a section where the polarity has changed, it records a voltage spike. The spikes, both negative and positive represent a 1 and when there is no voltage spike, corresponds to a 0.

The head gets astonishingly close to the disc surface about 100 nanometers in older drives. However, today, under 10 nanometers in the newest ones. As the head gets closer to the disc, it's magnetic field covers less area, allowing for more sectors of information to be packed onto the discs surface.

To keep that critical height, the head floats over the disc: as the disc spins it forms a boundary layer of air that gets dragged past the stationary head at 80 mph at the outer edge. The head rides on a slider aerodynamically designed to float above the platter and the genius of this air-bearing technology, is it's self-induced adjustment. If any disturbance causes the slider to rise too high, it floats back to where it should be.

For a comprehensive reading on the HDD magnetic operating principle in specific, interested readers may refer to (Mee & Daniel, 1996).

3. System Modeling

3.1. High Frequencies Dynamics

At high frequencies, the flexibility of the pivot bearing, flex cable, arm, etc, are at the origin of several resonance modes in the Hard drive. It is imperative to take these factors into consideration while modeling the VCM actuator, then treat them carefully. Otherwise, they may degrade the system stability and generate steady state in tracking performances.

Based on the work of (chen, et al., 2006), a realistic model of a VCM actuator can be expressed by the following linear model:

$$G(s) = \frac{k_v k_y}{s^2} \prod_{i=1}^N G_{r,i}(s) \quad (1)$$

where k_y is the position measurement gain, $k_v = \frac{k_t}{m}$, with k_t is the current-force conversion coefficient and m is the mass of the VCM actuator. u is the control input (in volts), y and v are respectively the position (in μm) and the velocity of the R/W head (in $\mu m/s$). N is the number of resonance modes and $G_{r,i}(s)$ for $i = 1, \dots, N$ are their transfer functions.

In order to ensure superior performances, the high-frequency resonance mode effects are often minimized by the use of a notch filter as a pre-compensator. Such a filter is able to suppress lightly damped poles and replace them by a pair of well-damped poles (Weaver & Ehrlich, 1995).

3.2. Low Frequencies Dynamics

At low frequencies, the actuator rotary pivot bearing and data flex cable behaviors have to been rigorously analyzed. Indeed, while the R/W head moves from one track to another, the data flex cable is subjected to expansions and contractions. These factors causes frictional forces and nonlinearities in HDD VCM actuators, especially those with reduced form. Such factors cause not only the generation of significant residual errors, but also make difficult to maintain the head as close as possible to the desire track center. Hence, a good comprehensive of all the aforementioned factors' behavior is essential to include a comprehensive modeling and compensation schemes of the degrading effect of nonlinearities and friction.

The resulting nonlinear VCM actuator dynamics is expressed as follows (San, et al., 2009):

$$\begin{aligned} M(q)\ddot{q} + F(q, \dot{q}) &= u \\ y = q + w_{out} \end{aligned} \quad (2)$$

where $M(q)$ denotes the system inertia verifying $M(q) > 0$. q , \dot{q} and \ddot{q} denote the position, velocity and acceleration of the VCM-actuator head tip respectively. u is the control input, y is the actual position of the VCM-actuator in presence of the output disturbance w_{out} . Such a disturbance is mainly caused by spindle rotation run-outs. $F(q, \dot{q})$ represents the nonlinear hysteresis friction induced by the pivot bearing. The behavior of $F(q, \dot{q})$ in HDD applications has been investigated in (De Wit, et al., 1995). It has been shown that the LuGre friction model is able to capture all the static and dynamic characteristics of the hysteresis friction such that:

$$F(q, \dot{q}) = \sigma_0 z + \sigma_1 \dot{z} + \sigma_2 \ddot{q} \quad (3)$$

$$\dot{z} = \dot{q} - \alpha(\dot{q}) \mid \dot{q} \mid z \quad (4)$$

$$\alpha(\dot{q}) = \frac{\sigma_0}{f_c + (f_s - f_c)e^{-(\frac{\dot{q}}{q_s})^2}} \quad (5)$$

where z is an internal state of the friction model assumed to be unmeasurable. σ_0 , σ_1 and σ_2 are the model parameters reflecting the small displacements which are the stiffness, the micro damping and viscous coefficient respectively. f_s corresponds to the stiction force, f_c is the Coulomb friction force and the parameter q_s is the Stribeck velocity (Astrom & De Wit, 2008).

4. Control Problem Formulation

The displacement of the R/W head tip on the surface of the disc is one of the most important issues in a HDD servo-control system. The principle goal of such a system is to carry out two main functions: The first function is to ensure a quick transition of the head tip from one target track to another using bounded control effort (track seeking). This function is required to be achieved with the smallest possible the seek time, which is defined as the needed time duration to move the R/W head tip from its actual position to another. The second function is to maintain the head as close as possible to the desired track center while

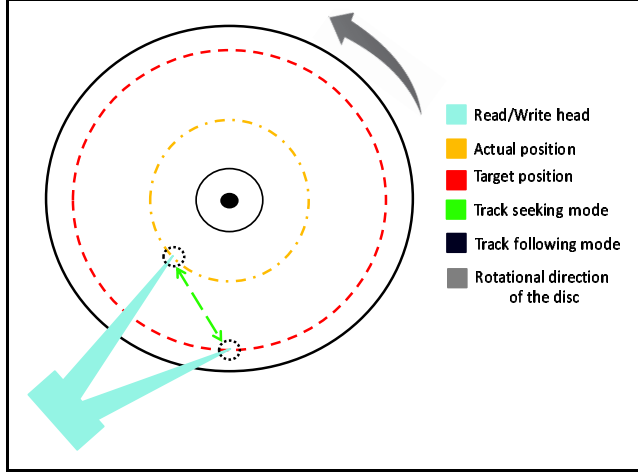


Figure 6. Main operating functions in a HDD servo-system.

digital information is being read/written from/on the disc (track following). These two control problems can be represented graphically as shown in Figure 6.

Let q_d be the target track position. The tracking error can be expressed as follows:

$$e_1 = q_d - q \quad (6)$$

The control objective is then to ensure the convergence of the R/W head to the desired destination. Then, the head must be maintained super near this target track center such that following objective is obtained:

$$\lim_{t \rightarrow \infty} |e_1(t)| = \lim_{t \rightarrow \infty} |q_d(t) - q(t)| = 0 \quad (7)$$

Unfortunately, as the track density increases and the track pitch decreases, several error sources are becoming more challenges due to the continuing decrease in the allowable Track Miss-registration (TMR) limits. The most relevant error sources include external vibration and shocks, nonlinearities and parametric uncertainties. These are caused by the head movement effect, non-repeatable and repeatable run-outs due to the spindle bearing and thermal effect respectively.

A good HDD servo-system controller is required not only to achieve the desired track seeking and following tasks, but also to ensure a reliable data treatment and superior tracking performances in terms of speed and accuracy.

In this work, our main objective is to design an effective robust controller based on the low-frequencies nonlinear VCM actuator model (2-5). The effectiveness of the proposed controller will be tested in various operating conditions ranging from nominal case without disturbances to cases with external disturbances and parametric uncertainties in the system dynamics.

To reach this aim, filtered tracking errors, denoted by $e_2(t), r(t)$ are introduced to facilitate the ulterior key analysis. They are defined as:

$$e_2 = \dot{e}_1 + \alpha_1 e_1 \quad (8)$$

$$r = \dot{e}_2 + \alpha_2 e_2 \quad (9)$$

where $\alpha_1, \alpha_2 \in \mathcal{R}$ are positive tuning gains. $r(t)$ is an immeasurable quantity since its expression (9) depends on $\ddot{q}(t)$.

5. Rise Feedback Based Neural Network Control

In this section, the classical RISE feedback based Neural Network controller (RISE-NN) is introduced. As its name indicates, this technique combines the universal approximation property of Neural Network control to approximate unknown uncertainties in the system dynamics, with the recently developed RISE feedback method originating in (Xian, et al., 2004) and nominated as RISE feedback in (Patre, et al., 2008a). This combination is advantageous in terms of asymptotic stability of the controlled system. It's a technique that can be used to develop a tracking controller for nonlinear systems even in the presence of additive disturbances and uncertainties on the dynamic system parameters. This is feasible under the assumption that the considered disturbances are \mathbb{C}^2 with bounded time derivatives. First, we propose to introduce the NN feedforward controller. Then, the RISE feedback principle is detailed.

5.1. Feedforward NN Estimation

Consider a three-layer NN as in (Lewis, 1999). Then, consider a compact set \mathbb{S} and a smooth continuous function $f(x)$ expressed by:

$$f(x) = W^\top \sigma(V^\top x) + \varepsilon(x) \quad (10)$$

were $x(t) \in \mathbb{R}^{a+1}$ is the inputs vector. $V \in \mathbb{R}^{(a+1) \times L}$ and $W \in \mathbb{R}^{(L+1) \times 1}$ are bounded constant weights for the first-to-second and the second-to-third layers of the network, respectively. a denotes the number of neurons in the input layer and L is the number of neurons in the hidden layer. Only one neuron describes the third layer. In (10), the activation function is denoted by $\sigma(\cdot) : \mathbb{R}^{a+1} \rightarrow \mathbb{R}^{L+1}$. However, the functional error approximation is denoted by $\varepsilon(x) : \mathbb{R}^{a+1} \rightarrow \mathbb{R}$. The basic Neural Network principal is as shown in Figure 7.

Different activation functions could be exploited for the control development. They include for example sigmoid, hyperbolic tangent or radial basis functions. In this paper, we propose the use of radial basis functions expressed as follows:

$$\sigma(x_i) = \exp\left(-\frac{\|x_i - c_i\|^2}{\sigma_i^2}\right) \quad \forall i \in \mathbb{R} \quad (11)$$

where c_i and σ_i are respectively center and the width of the basis functions. These parameters are *a prior* chosen and kept fixed in simulations. Taking advantage of the universal NNs estimation property, the function $f(x)$ given in (10) can be approximated (Lewis, 1999):

$$\hat{f}(x) = \hat{W}^\top \sigma(V^\top x) \quad (12)$$

were $\hat{W} \in \mathbb{R}^{(L+1) \times 1}$ is the approximated ideal weights of the network.

Assumption 2 There exist bounds on the ideal weights and the activation function such that $\|W\| \leq W_m$, $\|\sigma\| \leq \sigma_m$, where W_m and σ_m are known positive constants.

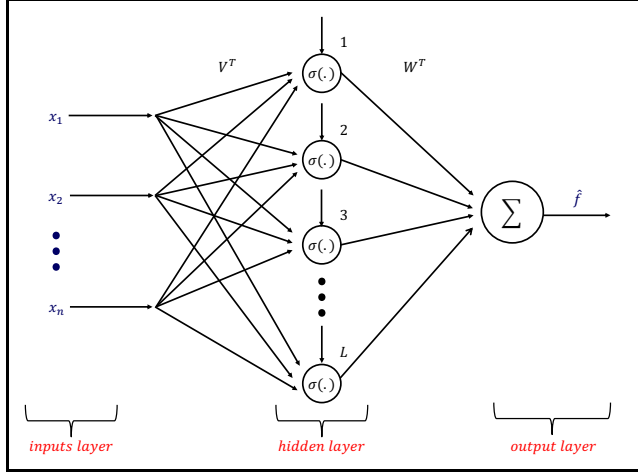


Figure 7. Illustration of a three-layer Neural network.

5.2. Background on RISE Feedback Control

In the sequel, the control input $u(t)$ is developed based on RISE feedback approach. First, the filtered error (9) is pre-multiplied by $M(q)$ and the system dynamic model (2)-(5) is used such that we get:

$$M(q)r = F_d + S - u \quad (13)$$

where F_d and S are auxiliary functions defined by:

$$F_d = M(q)\ddot{q}_d + F(q_d, \dot{q}_d) \quad (14)$$

$$S = M(q)(\alpha_1\dot{e}_1 + \alpha_2\dot{e}_2) + F(q, \dot{q}) - F(q_d, \dot{q}_d) \quad (15)$$

The expression of F_d in (14) can be approximated using a three-layer NN as given by equation (12), that is:

$$F_d = W^\top \sigma(V^\top x_d) + \varepsilon(x_d) \quad (16)$$

In (16), the input vector $x_d(t) \in \mathbb{R}^{(3a+1)}$ is defined as $x_d = [1 \quad q_d \quad \dot{q}_d \quad \ddot{q}_d]^\top$. Since the desired trajectory is bounded as stated in assumption 1, $\varepsilon(x_d)$ satisfies the following inequalities:

$$\|\varepsilon(x_d)\| \leq \varepsilon_N, \quad \|\dot{\varepsilon}(x_d)\| \leq \varepsilon'_N \quad (17)$$

where ε_N and ε'_N are known positive constants.

The control input $u(t)$ of the system (2)-(5) is composed of the three-layer NN feedforward control term $\hat{F}_d(t)$ plus the RISE feedback control term $\mu(t)$ such that:

$$u = \hat{F}_d + \mu \quad (18)$$

The RISE feedback term $\mu(t) \in \mathbb{R}^{(a)}$ is defined as (Xian et al., 2004):

$$\begin{aligned} \mu(t) &= (k_s + 1)e_2(t) - (k_s + 1)e_2(0) \\ &+ \int_0^t [(k_s + 1)\alpha_2 e_2(s) + \beta_1 \text{sgn}(e_2(s))] ds \end{aligned} \quad (19)$$

where $k_s, \beta_1 \in \mathbb{R}^+$ are positive constant feedback gains. In this paper, the optimal tuning of the feedback gain k_s is the main objective. To the author's best knowledge, this technique is a new contribution in the field of nonlinear system's control. We propose to generate an optimal variable tuned parameter k_s^{opt} capable of ensuring an effective path tracking of the HDD servo system with much better performance than a fixed gain. A detailed description of the proposed approach will be developed in the next section.

The feedforward NN component \hat{F} in (18) is defined by equation (12). The estimates of the NN weights \hat{W}^\top are generated online and take the following forms:

$$\dot{\hat{W}} = K[\sigma(V^\top x_d)e_2^\top - \kappa\hat{W}] \quad (20)$$

where κ is a positive design constant parameter. K is a symmetric constant positive definite control gain matrix $K = K^\top > 0$. The boundedness of \hat{W} is easy to prove based on assumption 2. Time derivative of (19) is given as:

$$\dot{u}(t) = (k_s + 1)r(t) + \beta_1 sgn(e_2(t)) \quad (21)$$

Using (12) and (21), the time derivative of the overall control input of the system can be expressed as:

$$\dot{u} = \hat{W}^\top \sigma(V^\top x_d) + (k_s + 1)r(t) + \beta_1 sgn(e_2(t)) \quad (22)$$

In order to formulate the closed-loop system dynamics, equations (22) and (16) are combined such that we get:

$$\begin{aligned} M(q)\dot{r} &= -\dot{M}(q)r + \dot{F}_d + \dot{S} - \dot{u} \\ &= -\frac{1}{2}\dot{M}(q)r + \tilde{W}^\top \sigma(V^\top x_d) + \epsilon(x_d) - (k_s + 1)r(t) \\ &\quad + (-\frac{1}{2}\dot{M}(q)r + \dot{S} + e_2) - \beta_1 sgn(e_2(t)) - e_2 \end{aligned} \quad (23)$$

where $\tilde{W}^\top = W^\top - \hat{W}^\top$ is the weight estimation error.

Equation (23) can be further formulated as follows:

$$\begin{aligned} M(q)\dot{r} &= -\frac{1}{2}\dot{M}(q)r + \tilde{N} + N_{B_1} + N_{B_2} - e_2 \\ &\quad - (k_s + 1)r(t) - \beta_1 sgn(e_2(t)) \end{aligned} \quad (24)$$

where

$$\tilde{N} = -\frac{1}{2}\dot{M}(q)r + \dot{S} + e_2 \quad (25)$$

$$N_{B_1} = \epsilon(x_d), \quad (26)$$

$$N_{B_2} = \tilde{W}^\top \sigma(V^\top x_d) \quad (27)$$

Based on the Mean Value Theorem and following the same procedure detailed in (Xian et al., 2004), one concludes that \tilde{N} is upper bounded as follow:

$$\|\tilde{N}\| = \left\| -\frac{1}{2}\dot{M}(q)r + \dot{S} + e_2 \right\| \leq \rho(\|z\|) \|z\| \quad (28)$$

where $z(t) = [e_1^\top \ e_2^\top \ r^\top]^\top \in \mathbb{R}^3$ and $\rho(\|z\|)$ is a positive non decreasing bounding function.

6. Extended Version of Rise Control: P-Rise-NN

In this section, a new enhanced version of the classical RISE-NN controller will be presented. The proposed controller is capable of achieving better track following of the R/W head position in the servo system. Based on the control parameter setting in the RISE-NN technique, it turned out that a little variation of the parameter k_s can affect the working of the HDD and degrade or improve the tracking performance. In order to deal with this issue, we propose to add a prediction based optimization to the classical RISE-NN which allows the determination, at each sampling time, of the optimal value of k_s . Such a solution will be able to improve the overall system behavior in terms of speed of convergence and robustness against unexpected external disturbances and dynamic changes on the system parameters.

The proposed prediction based optimal gain tuning solution, called P-RISE-NN, is inspired from the Model Predictive Control (MPC) approach (Camacho & Bordons, 2004). Several works have been developed in the literature to show the effectiveness of the predictive approaches and illustrate their importance in trajectory tracking system control. The principle is mainly based on an online optimization dedicated to predict the future outputs of the plant and calculate an optimal control parameter $k_s^{opt|k}$ instead of an optimal control sequence as in the classical MPC method. $k_s^{opt|k}$ is derived from the minimization of a cost function J often subject to different constraints. The basic idea of the P-RISE-NN control algorithm is illustrated in Figure 8.

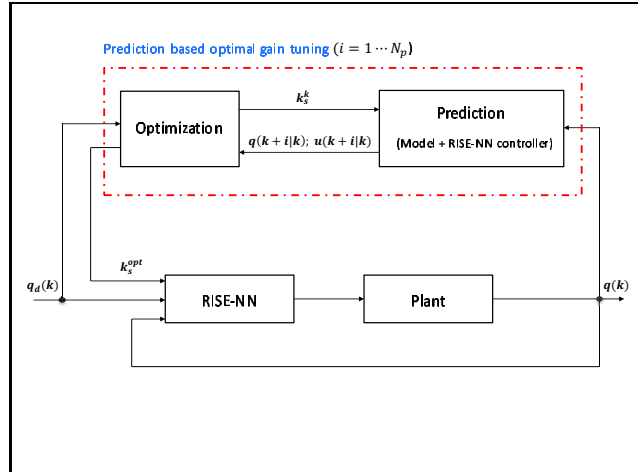


Figure 8. Block Diagram of the proposed P-RISE-NN controller.

At each time instant kT_e , where k is a positive constant integer and T_e is the sampling time, the prediction of the future behavior of the controlled system is performed. Vectors of future outputs and control inputs denoted respectively by $\hat{q}(k+i|k)$ and $\hat{u}(k+i|k)$, for $i = 1, \dots, N_p$, are generated over a predefined prediction horizon N_p . Their calculation shall use the nonlinear model of the system described by (2)-(5) according to the basic principle of RISE-NN procedure detailed in section 5.. Through the minimization of a performance index, the optimal control gain $k_s^{opt|k}$ is determined at each time instant k . The objective

function denoted J can be stated as a quadratic function including the future control inputs and tracking errors as follows:

$$e(k+i|k) = q_d(k+i|k) - \hat{q}(k+i|k) \quad (29)$$

where $q_d(k+i|k)$ is the desired track trajectory to follow assumed to be known *a priori* and $\hat{q}_d(k+i|k)$ is the future predicted outputs. The objective function J can be expressed as follows:

$$J = \sum_{i=1}^{N_p} \|e(k+i|k)\|_Q^2 + \|u(k+i|k)\|_R^2 \quad (30)$$

where $\|\mathbf{x}\|_M^2 = \mathbf{x}^T M \mathbf{x}$. Q and R are the symmetric positive definite weighting matrices, $Q \geq 0$ and $R > 0$. In addition to the calculation of the optimal control gain parameter $k_s^{opt|k}$, the proposed prediction based optimal control aims to maintain the output as close as possible to the reference trajectory.

$$k_s^{opt|k} \equiv \arg \min_{k_s} J \quad (31)$$

Since the HDD has a nonlinear dynamic model, the optimization is in general a non-convex problem. Therefore, an online nonlinear programming algorithm should be used to find the optimal solution $k_s^{opt|k}$. Once $k_s^{opt|k}$ is obtained, it will be applied to the controlled system over the next sample period $[k, k+1]$. Then, the prediction horizon is shifted, the state of the system is measured and all the above procedure is repeated at the next sampling time. The time history of the proposed extended version P-RISE-NN parameters is illustrated in Figure 9.

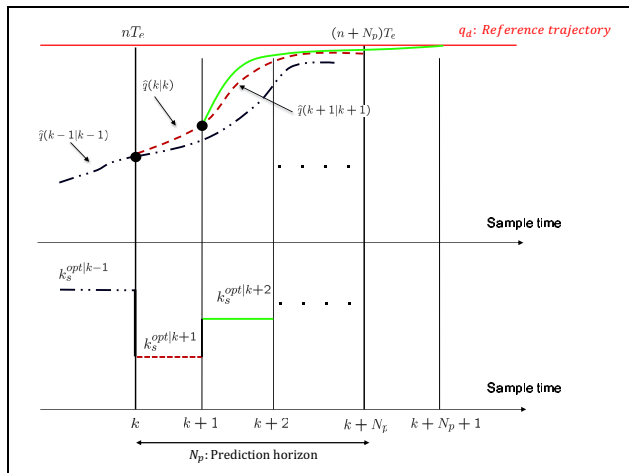


Figure 9. Prediction-based optimal tuning.

7. Simulation Results: A Comparative Study

In this section, we present different simulation results obtained with the proposed P-RISE controller and their comparison with those of the classical RISE-NN controller. The simulation studies have been performed using Matlab 7.9 software of MATHWORKS. The NN

parameters are manually tuned to obtain the best possible performances of the controllers. Since the predictive algorithm is based on a nonlinear optimization problem, this makes it extremely difficult to find an analytical solution of the optimal gain $k_s^{opt|k}$. Consequently, the optimization problem in the P-RISE-NN approach has to be solved online using the MATLAB routine *fmincon* including the control constraints. The parameters of the applied controllers are summarized in Table 1.

Table 1. Parameters of the RISE-NN and P-RISE-NN controllers

Reference trajectory	q_d	$1\mu m$
Minimum control effort	u_{min}	-3v
Maximum control effort	u_{max}	3v
Prediction horizon	N_p	25
Weighting matrix	Q, R	$100I, 100I$
Sampling time	T_e	0.05ms
Simulation duration	N_{sim}	400
Control gain parameters	$\alpha_1, \alpha_2, \beta_1$	1500, 1500, 1
Inertia matrix	m	1

All the initial conditions are chosen to be at the origin. Three different tests are considered. In the first scenario, the track following task is performed in nominal case without any external disturbance. The second scenario includes external disturbances, which are challenging for controllers and must be compensated as much as possible. Finally, the third scenario deals with uncertainties on the system parameters. For this, uncertainties of 20%, 40% and 80% of the nominal value of the system inertia are considered to check the robustness of the controllers against these changes. To facilitate the comparative study, an energy function E is introduced, it is defined as follows:

$$E = \sum_{i=1}^{N_{sim}} |u_i|$$

where N_{sim} is the simulation duration, u_i is the control input value at time instant i .

7.1. Scenario 1: Track Following in Nominal Case

The objective behind this scenario is to control the position of the R/W head tip of the HDD servo system without any external disturbances. The nominal value of the control gain parameter is chosen $k_s = 1850$ for RISE-NN controller. Figure 10 displays the evolution of the measured output, the tracking error and the control input. As shown in the figure, both RISE-NN and P-RISE-NN are able to steer the R/W head to the desired target track and to maintain it on this target location. However, the convergence with P-RISE-NN controller is much faster and has very little overshoots. Moreover, with P-RISE-NN, less control energy is consumed. The resulting 5% settling time and energy function E (defined above) are summarized in Table 2.

Table 2. Track following performance of both controllers in nominal case without disturbances: scenario 1

	RISE-NN	P-RISE-NN
Settling time (ms)	4.13	1.55
Energy (v)	62.783	25.60

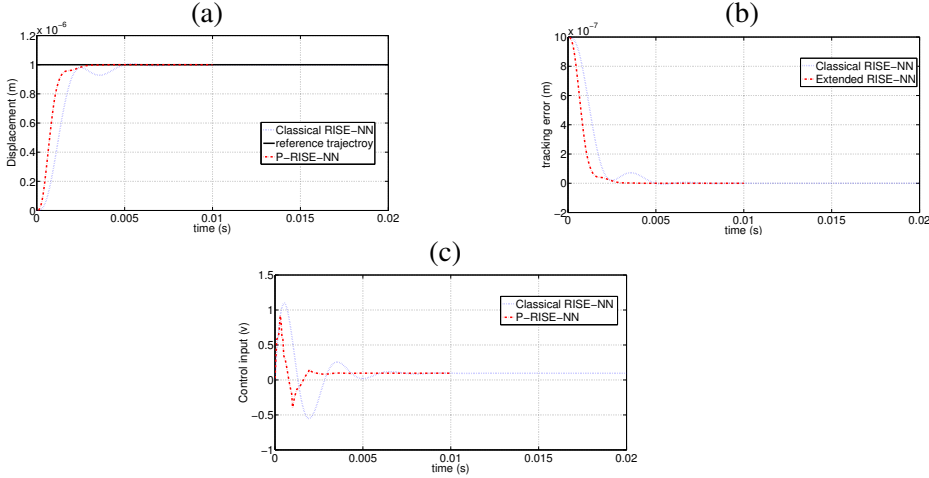


Figure 10. Simulation results without external disturbances (Plots with RISE-NN and P-RISE-NN controllers): (a) Evolution of the measured outputs, (b) Evolution of the tracking error and (c) Evolution of the control input.

7.2. Scenario 2: Track Following with External Disturbances

This second scenario was performed while considering external disturbances w_{out} (on output) and w_{in} (on input). Therefore, the main objective is to check the robustness of both controllers towards perturbations and their ability to compensate them. The unexpected impulse output disturbance $w_{out} = 0.3 \mu\text{m}$ is assumed to affect the controlled closed-loop system at the time instant $t = 10 \text{ ms}$. However, the input disturbance w_{in} is often an unknown perturbation satisfying $|w_{in}| \leq 3 \text{ mV}$ (chen et al., 2006). Consider the case of a persistent perturbation $w_{in} = -3 \text{ mV}$ representing an offset of the control input in this scenario. The obtained simulation results are depicted in Figure 11. For comparison purpose, the recovery time t_{rec} performance index is introduced. It is defined as the time needed by the system to reach the 2% of the desired final value after the application of the output disturbance. Figure 11-(a) shows the evolution of output. With the RISE-NN controller, the positioning of the R/W head tip is much more affected by the disturbance and has a longer recovery time compared with that with P-RISE-NN controller. Furthermore, in Figure 11-(c), it can be clearly seen that a higher control energy is consumed and several overshoots are generated with RISE-NN. However, P-RISE-NN control provides a better performance in the case of disturbance rejection. This can be explained by the prediction aspect of the latter approach which uses the system's model in the optimization procedure. This allows it to predict the

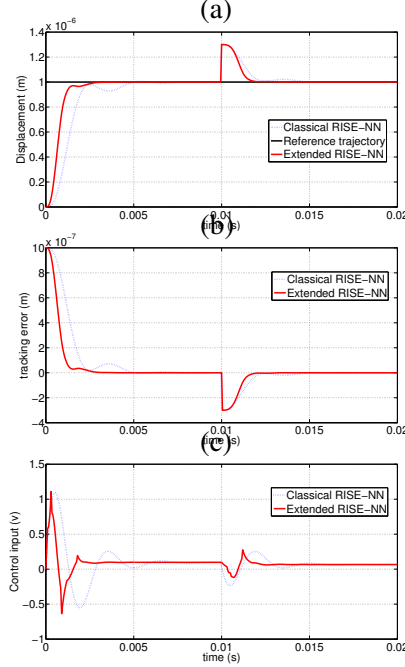


Figure 11. Simulation results with external disturbances (Plots with RISE-NN and P-RISE-NN controllers): (a) Evolution of the measured outputs, (b) Evolution of the tracking error and (c) Evolution of the control input

behavior of the closed-loop system over the prediction horizon N_p and to choose the best feedback gain k_s . Table 3 summarizes the performances of the two applied controllers.

Table 3. Performances of the track following controller in case with disturbances: scenario 2

	RISE-NN	P-RISE-NN
Recovery time (ms)	13.8	11.5
Energy (v)	61.63	42.84

7.3. Scenario 3: Track Following with Parameter Uncertainties

In this scenario, the model of the controlled system is considered to be affected by parametric uncertainty on the mass inertia of the system m . Such dynamic parameter is expected to undergo some changes during the movement of the R/W head from one track to another. The objective is to see whether the proposed controllers are robust enough to deal with this uncertainty and ensure a good performance of the overall closed-loop system in terms of precision and speed. Errors of 20% and 80% on the mass inertia are considered. The obtained simulation results for this scenario are as depicted in Figures 12 and 13.

The system's response with RISE-NN is hardly effected by the considered uncertainties, whereas with P-RISE-NN, the behavior of the system is much better. In fact, up to 80%

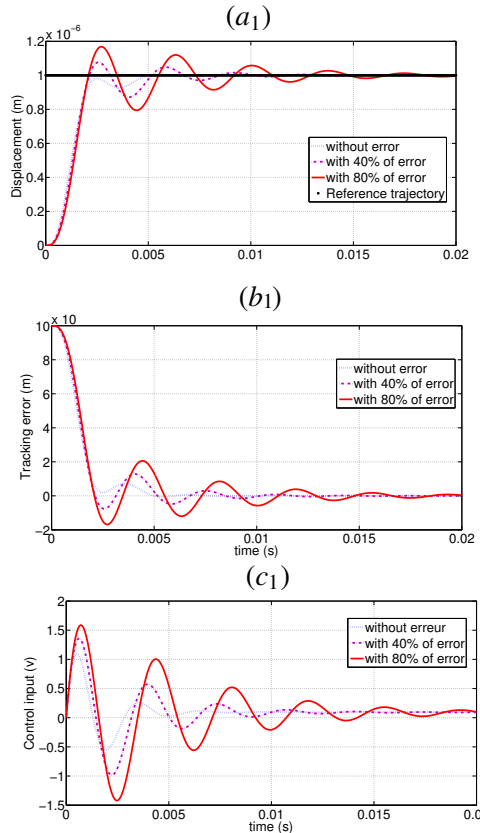


Figure 12. Robustness towards parameter's uncertainties (Plots with RISE-NN controller): (a₁) Evolution of the measured outputs, (b₁) Evolution of the tracking error and (c₁) Evolution of the control input

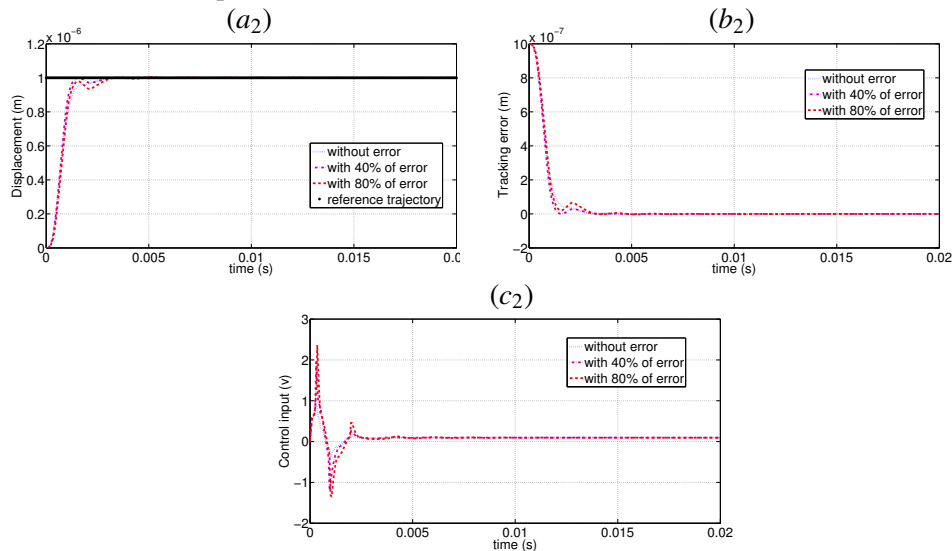


Figure 13. Robustness towards parameters' uncertainties (Plots with P-RISE-NN controller): (a₂) Evolution of the measured outputs, (b₂) Evolution of the tracking error and (c₂) Evolution of the control input

of uncertainty, P-RISE-NN is able to converge faster to the desired position with small tracking errors and negligible oscillations. These results clearly show the effectiveness of the P-RISE-NN over the classical RISE-NN controller. Thereby, the importance of its predictive aspect is illustrated through the robustness against even strong model parameter uncertainties.

Conclusion

In this chapter, the mechatronics of a Hard Disc Drive has been presented. Then, a P-RISE-NN control scheme have been proposed for a path tracking problem. Compared with a classical RISE-NN approach. The P-RISE-NN shows much better performance in terms of accuracy and speed compared with a classical RISE-NN approach. Moreover, the P-RISE-NN controller has a significant robustness towards unexpected disturbances and parameters' uncertainties. Small overshoots were noticed and the controller was able to converge faster. Thanks to the predictive aspect, P-RISE-NN is able to anticipate the future behavior of the controlled system. Such a feature would have a great consideration when controlling the HDD and especially in meeting the increased demands on the servo performance. The real-time implementation of this proposed control solution on a HDD will be the subject of our future work.

References

- K. J. Astrom & C. De Wit (2008). ‘Revisiting the LuGre Model Stick-slip motion and rate dependence’. *IEEE Control Systems* 28(6):101–114.
- T. Atsumi, et al. (2007). ‘Track-following control using resonant filter in Hard Disk Drives’. *IEEE/ASME Transactions on Mechatronics* 12(4):472–479.
- E. Camacho & C. Bordons (2004). *Model Predictive Control*. Springer.
- B. chen, et al. (2006). *Hard Disk Drive Servo-Systems*. Springer, Germany.
- B. Chen, et al. (2003). ‘Composite nonlinear Feedback control for linear systems with input saturation: Theory and an application’. *IEEE Transaction on Automatic Control* 48(3):427–439.
- C. De Wit, et al. (1995). ‘A new model for control of systems with friction’. *IEEE Transactions on Automatic Control* 40(3):419–425.
- Z. Goh, T.B.and Li, et al. (2001). ‘Design and implementation of a Hard Disk Drive servo system using robust and perfect tracking approach’. *IEEE Transaction on Control Systems Technology* 9(2):221–233.
- M. Graham & R. De Callafon (2006). ‘Modeling and robust control for Hard Disk Drives’. In *ASME/JSM Conference on Micromechatronics for information and Precision Equipement (MIPE)*, Santa Carla, CA, USA,.

- M. Hirata, et al. (2003). ‘Track-following control of Hard Disk Drives using multi-rate sampled-data H_∞ control’. In *Proc. 42nd Conference on Decision and Control*, vol. 4, pp. 3414–3419, Maui, Hawaii, USA.
- R. Horowitz & B. Li (1995). ‘Adaptive control for disk file actuators’. In *Proc. 34th Conference on Decision and Control*, vol. 1, pp. 655–660, New Orleans, LA.
- B. Isayed & M. Hawwa (2007). ‘A nonlinear PID control scheme for Hard Disk Drive servosystems’. In *MED 07. Mediterranean Conference on Control and Automation*, pp. 1–6.
- J. Ishikawa & M. Tomizuka (1998). ‘A novel add-on compensator for cancellation of pivot nonlinearities in Hard Disk Drives’. *IEEE Transactions on magnetics* 34(4):1895–1897.
- M. Kobayashi, et al. (2004). ‘Adaptive control of dual-stage-actuator for Hard Disk Drives’. In *Proc. American Control Conference*, vol. 1, pp. 523–528, Boston, MA, USA.
- C. Lee & S. Suh (2011). ‘Model prediction based dual-stage actuator control in discrete-time domain’. *IEEE Transaction on magnetics* 47(7):1830–1836.
- F. Lewis (1999). ‘Nonlinear Network Structures for Feedback Control’. *Asian Journal of Control* 1(4):205–228.
- N. Mahalik (2003). *Mechatronics - Principles, Concepts and Applications*. Tata McGraw Hill, Germany.
- C. Makkar, et al. (2007). ‘Lyapunov-based tracking control in the presence of uncertain non-linear parameterizable friction’. *IEEE Transaction on Automatic Control* 52(10):1988–1994.
- C. Mee & E. Daniel (1996). *Magnetic recording technology*. McGraw-HILL, New York.
- J. Nie, et al. (2011). ‘Optimal H_∞ control for Hard Disk Drives with an irregular sampling rate’. In *American Control Conference*, CA, USA.
- P. Patre, et al. (2008a). ‘Asymptotic Tracking for Systems with Structured and Unstructured Uncertainties’. *IEEE Transactions on Control Systems Technology* 16(2):373–379.
- P. M. Patre, et al. (2008b). ‘Asymptotic tracking for uncertain dynamic systems via a multilayer neural network Feedforward and RISE Feedback control structure’. *IEEE Transaction on Automatic Control* 53(9):2180–2185.
- P. San, et al. (2009). ‘Adaptive neural network control of Hard Disk Drives with hysteresis friction nonlinearity’. *IEEE Transactions on Control Systems Technology* 19(2):351–358.
- M. Taktak, et al. (2012). ‘Track following problem of a VCM actuator servo system for Hard Disk Drives using predictive control’. In *9th International Multi-Conference on Systems, Signals and Devices*, pp. 1–7, Chemnitz, Germany.

- M. Taktak, et al. (2013). ‘Model predictive Tracking Control for a Head-Positioning in a Hard Disk Drive’. In *Proc. 21st Mediterranean Conference on Control and Automation*, Platanias, Chania, Crete, Greece.
- V. Venkataraman, et al. (2002). ‘A new approach to the design of mode switching control in Hard Disk Drive servo systems’. *Control Engineering Practice* 10(9):925–939.
- P. Weaver & R. Ehrlich (1995). ‘The use of multirate notch filters in embedded servo disk drives’. In *American Control Conference*, vol. 6, pp. 4156–4160.
- B. Xian, et al. (2004). ‘A Continuous Asymptotic Tracking Control Strategy for Uncertain Nonlinear Systems’. *IEEE Transaction on Automatic and Control* 49(7):1206–1211.
- T. Yamaguchi & H. Hirai (1998). ‘Control of transient response on a servosystem using mode-switching control, and its application to magnetic disk drives’. *Control Engineering Practice* 6(9):1117–1123.
- T. Yamaguchi, et al. (1997). ‘A mode-switching controller with initial value compensation for Hard Disk Drive servo control’. *Control Engineering Practice* 5(11):1525–1532.

Chapter 2

SAGITTAL BIPED CHAOS CONTROL MODELING

Riaan Stopforth¹ and Glen Bright²

¹Mechatronics and Robotics Research Group (MR2G)

Bio-Engineering Unit, University of KwaZulu-Natal, Durban, South Africa

²Mechatronics and Robotics Research Group (MR2G),
University of KwaZulu-Natal, Durban, South Africa

ABSTRACT

This chapter investigates the method of chaos control namely the Ott-Grebogi-Yorke method. In non-chaotic systems, large system parameter changes are required for performance changes. A sagittal plane biped model which is capable of exhibiting periodic and chaotic locomotion was researched and investigated. The locomotion was either periodic or chaotic depending on the design parameters. Nonlinear dynamic tools such as the Bifurcation Diagram, Lyapunov Exponent and Poincaré Map were used to differentiate parameters which generated periodic motion apart from chaotic ones. Numerical analytical tools such as the Closed Return and Linearization of the Poincaré Map were used to detect unstable periodic orbit in chaotic attractors. Chaos control of the model was achieved in simulations. The system dynamic is of the non-smooth continuous type. Differing from other investigated chaotic systems, the biped model has varying phase space dimensions which can range from 3 to 6 dimensions depending on the phase of walking.

1. INTRODUCTION

Chaos is found in different fields of study. One example of the presence of chaos in nature, is the weather and simple nonlinear equations, such as the Logistic Map (Sprott, 2003). Other well-known examples of chaos are Chua's Circuit in electrical circuits (Chua et al., 1992) and the Lorenz model: a model for convecting fluids (Hilborn, 1994).

Many researchers have utilised chaos controlling theory to stabilise chaotic behaviours (Ditto et al., 1990), since the publication of *Controlling Chaos* by Ott, Grebogi and Yorke

(Ott et al., 1990). Ott et al., have shown that it is possible to stabilise trajectories within a chaotic system through small parameter perturbations.

All chaotic systems consist of orbits of different periods. A system with diverse dynamic characteristics can be achieved through the control of the orbits. High order chaos control has been achieved of up to 90 orders (Shinbrot et al., 1993). Only small perturbations are required with the extended functionality of the system, to be flexible and dynamic control of chaotic systems. Large system parameter changes are required for performance changes, unlike non-chaotic systems.

The simplest walking model (or the compass model), was probably the first used to analyse chaotic locomotion (Schwab & Wisse, 2001). The compass model consists of two links with hip and feet point masses for the model walking down a gentle slope. The walking cycle starts with a single support phase after the heel-strike, followed by a swing phase, and concludes with a heel strike in the double support phase. All motions occur in the sagittal plane as it is assumed that no frontal motions take place. The compass model has 2 degrees of freedom (DOF) and the motion involves leg swings and heel strikes.

Garcia et al., has investigated the effects of variant slope angles on the walking cycle of the simplest walking model (Garcia et al., 1998). The research indicated that period doubling occurs as the slope angle is increased. Due to this characteristic, two or more consecutive steps of different periods are required before the model returns to its starting configuration. Period doubling increases until chaotic gait occurs. No two walking steps reflect the same condition for a chaotic gait. The simplest walking model has a deterministic, nonlinear dynamics or a chaotic system.

Goswami et al., investigated the stability and progression of the gait behaviours of the simplest walking model (Goswami et al., 1998), where nonlinear dynamic assessing tools Phase diagram and Poincaré Map are used (Garcia et al., 1998). The research focuses on the relationship of altering the system parameters to affect the passive gait of the biped. The gait of the biped model varied from symmetrical to asymmetrical and became chaotic as the system parameters were varied.

The stability of the periodic cycles of the simplest walking model, have been investigated by Schwab and Wisse and quantified the stability of the periodic cycles, by finding the basin of attraction size and the eigenvalues of Poincaré Function's Jacobian (Schwab & Wisse, 2001). The basin of attraction quantifier is more suitable for measuring stability. Wisse et al., have determined the bifurcation diagram of the simplest walking model with an upper body (Wisse et al., 2004).

Kurz et al., have illustrated experimentally that a robot can exhibit chaos behaviour due to its underlying mechanical system. The robot used the simplest walking model in the experimentation. Chaos behaviour is possible in a passive walking robot, which was confirmed by calculating the largest Lyapunov exponent and using a surrogate analysis method (Kurz et al., 2008). Kurz and Stergiou presented control of the simplest walking model using hip actuation. Their simulations indicated that periodic gait is achievable in a chaotic dynamic system through hip actuation (Kurz & Judkins, 2007). Garcia et al., have investigated the chaotic locomotion of a kneeled biped and illustrated simulations of slope angle versus walking periods through a bifurcation diagram. The diagram showed the gait is periodic or chaotic as a function of slope angle, but a kneeled model was used for this case study (Garcia et al., 1998).

1.1. Anthropometric Proportionality

Improved walking abilities have been shown with bipeds designed with anthropometric mass (Sardain et al., 1997). Figure 1 (redrawn from the information researched by Drillis and Contini (Drillis & Contini, 1966)) shows the proportionality of body segment lengths and masses of humans which are incorporated into the biped design. The percentage mass of the body segments is (Winter, 1990): lower body = 46.6%; pelvis = 14.2%; mass per leg = 16.1%; thigh = 10%; shank = 4.65%; foot = 1.45%. A model designed with anthropometric parameters will also result to the locomotion being more anthropomorphic.

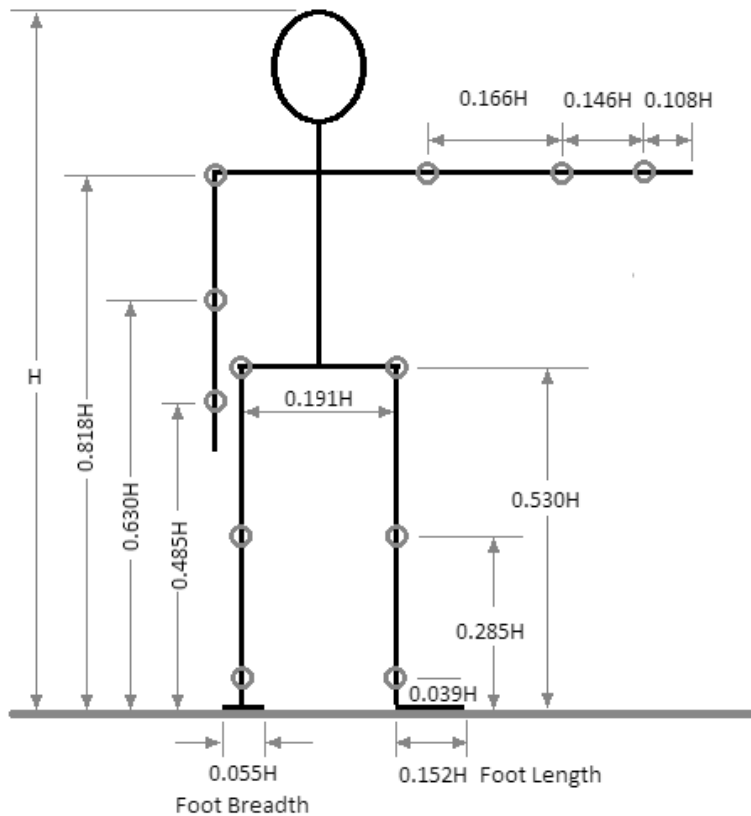


Figure 1. Proportionality of body segments lengths. The symbol H represents the total height of the body.

1.2 Roll-Over Feet

Human feet are shaped such that during a forward step, the centre of pressure shifts forward along the foot during a forward step. Hansen et al., have researched and developed feet that imitate the function of the human foot, which has different roll-over shapes (Hansen et al., 2000). Curved feet are used to replicate this shift in centre of pressure behaviour, as the feet cannot be designed to bend like a human's. Roll-over feet in biped designs are more robust to disturbances and therefore provide greater stability (Garcia et al., 1998). Wisse and

van Frankenhuizen have researched that increasing the foot radius, improves a biped's robustness against disturbances (Wisse & Frankenhuizen, 2003). A large radius foot may be very robust but has a higher chance of experiencing foot scuffing (Garcia et al., 1998). There is a relationship and finite range of foot length for which robustness and foot clearance is optimal (McGeer, 1990).

This chapter presents the methodology of chaos control and its application for a mechatronic biped model which has been built (Stopforth et al., 2013) and is shown in Figure 2. The background understanding of chaos is outlined. The preparation procedures required for chaos control of the biped model are presented. Simulation control of a chaotic orbit into a limit cycle has been achieved with the aid of different chaos analysing tools presented. The chapter's conclusion evaluates the application of chaos control in a biped model in terms of advantages and disadvantages. An unexpected outcome regarding the underlying chaotic system of the biped model was realized.



Figure 2. Biped assembly Isometric view.

2. UNDERSTANDING CHAOS

Chaos is used to describe systems that are not only deterministic but also very sensitive to the set initial conditions. Initial conditions with a small difference can, due to the nature of the system, diverge over time (commonly known as the butterfly effect) (Shinbrot et al., 1992). The divergence behaviour is not due to external influences or randomness, as the outputs of chaotic systems are predictable. No two instantaneous conditions of any trajectory are the same in the chaotic phase space, therefore the trajectories of chaotic systems do not cross over time (Ott, 2002). Chaotic basin of attraction is formed by chaotic trajectories that are bounded within closed regions. The phase space of a chaotic system must have at least three dimensions (Hilborn, 1994), since all chaotic flows are bounded to a closed region and do not cross themselves.

Ergodicity is one of the most important properties of chaos. In an ergodic system, any trajectory will eventually visit all parts of the phase space after a sufficiently long time (Eckmann & Ruelle, 1985). This characteristic is due to that any unstable periodic orbits, in the chaotic system, are attainable.

2.1. Unstable Periodic Orbits (UPO)

An UPO is defined as a periodic orbit that is unstable. The slightest change or disturbance can offset the UPO. UPOs are characterised by stable and unstable manifolds which attract and repel nearby trajectories respectively. The places where the manifolds cross, is a saddle point, which is the fixed point of UPO. This statement means that trajectories near the saddle point are either attracted or repelled, except when on the fixed point. Orbit dynamics remain constant if the orbit travel remains on a path of saddle points and only if there were no disturbances acting on it, but this characteristic is unlikely. Stable and unstable manifolds cross each other many times in chaotic systems (Hilborn, 1994). Large numbers of UPOs being embedded in the chaotic system's basin of attraction, are resulted by these crossings (Ott et al., 1990). Orbit behaviour seem to be random due to the attraction and repulsion of orbits around UPOs.

2.2. Poincaré Map Function

Poincaré Map function or simply the Poincaré Map, is the tool commonly used for analysing nonlinear dynamic flow (González-Miranda, 2004). A Poincaré Map is a function that describes the dynamics between intersection points of a chosen plane section and the orbits of a continuous system results a continuous orbit system into a recurrence map, or a discrete dynamical system (Boccaletti et al., 2000). This tool has the advantage that it reduces the phase space observed by one dimension while still preserving the properties of the original system (Ott, 2002). The reduced dimension advantage is only valid if the plane section is modelled as autonomous equation(s) (explicitly time-independent equations). This characteristic allows the information presented to be easier visualised through the reduced dimensionality.

The Poincaré Section intersects a system flow. The Poincaré Section (a plane) is called a Poincaré Plane for a 3D system. Two types of intersection directions can occur between the system trajectory and the Poincaré Section. The first type is the crossing of trajectory from the one side of the section to the other (example positive z-axis direction). The second type is vice versa (example negative z-axis direction). With the calculations of eigenvalues, the dynamic behaviours of intersection points can be determined. The intersection points of periodic orbits have eigenvalues of attractors. The consecutive intersection points will be drawn toward the fixed point(s) of the attractor for an intersection point that is within the Basin of Attraction (BOA). Only one Poincaré crossing is at steady state for period 1 orbits, which also are called limit cycles. Similarly, a period n orbit will have n Poincaré intersections at steady state. Time of travel for periodic orbits remains constant at steady state.

3. CHAOS CONTROL PROCEDURES

A number of procedural steps were carried out for the chaos control of the biped model. The first step is to determine the biped's stability. The biped is categorized as stable, if it is capable of walking a hundred consecutive steps. A large number of steps is needed as the typical waiting time for a system flow to get close to the target point, is long. Control conditions are met only if the biped walks large number of steps. The calculation of the Lyapunov Exponent determines whether the system is chaotic or not, since chaos control can only occur in chaotic systems. The Ott-Grebogi-Yorke (OGY) method involves the control of state points near UPO fixed points. The selection of a Poincaré Section is used to focus on one fixed UPO point since all the trajectory points of an UPO are fixed points. The convergence of the entire orbit is due to the converging of one UPO fixed point. The closed return method was used for the detection of UPOs on Poincaré's Section and the approximation of UPO fixed point coordinates.

By means of the linearization of the Poincaré Map method, the precise fixed point coordinates were determined, resulted from the closed return method as a starting point. The linearization of the Poincaré Map method was also used for the calculation of the linearized Poincaré Map. Chaos control is applicable only if all the control method conditions and linearization limitations are met. The steps in the above procedure are summarised in the following list:

- Step 1: Continuous walking of at least 100 steps is required to check for stability.
- Step 2: Through the calculation of the Lyapunov Exponent, the system is determined chaotic or non-chaotic.
- Step 3: Selection of a suitable Poincaré Section.
- Step 4: The closed return method is used to detect and approximate period p UPO fixed point(s), if the system is chaotic.
- Step 5: Linearization of the Poincaré Map method is used to calculate the linearized Poincaré Map equation and to determine the precise fixed point coordinate.
- Step 6: The control parameter value is determined using the linearized Poincaré Map Equation.
- Step 7: If the control conditions and linearization limitations are met, then Perturbation control is applicable.

3.1. Poincaré Section

A Poincaré Section needs to be selected before the Poincaré Map is determined. A Poincaré Section is chosen based on the time or occurrence of events. The dynamics are analysed at different times, separated by equal periods for time-based sections. Time-based sections are mostly applied to smooth continuous flows. It is more appropriate to select an event-based Poincaré Section for the sagittal model. Sections with the same time interval spacing will lead to a Poincaré Map that shows the comparison between the different walking stages of a step, since the periods of the walking steps are not constant. The Poincaré Section is best chosen at events, such as the knee or heel strike transitions, for same-phase

comparisons. As phase space dimensions differ between choosing the moment before or after strike transitions, there is a noticeable difference. Immediate moments after transition was selected as these have the least dimensions. As Poincaré Sections cannot be modelled using autonomous equations, the dimension reducing advantage of using a Poincaré Map does not apply (i.e. the modelled flows have its usual phase dimensions). Two Poincaré Sections were used in one walking step for reasons that will be discussed in section 3.3.

3.2. Approximation of the Linearisation Poincaré Function

The linearised form of the Poincaré Map about a fixed point is approximated as shown in equation 1. Matrix A of equation 1 is approximated as equation 2 (Shinbrot et al., 1993):

$$Z_{n+1} - Z_f(p_n) = A(Z_n - Z_f(p_n) - B(p_{n+1} - p_n)) + B(p_{n+1} - p_n) \quad (1)$$

$$A \sim C \quad (2)$$

where the matrix C is determined from equation 3 [55].

$$[C \ D] = EF^T(FF^T)^{-1} \quad (3)$$

where C is the Jacobian matrix of the linearization and D the constant vector. E = $[Z_{n+1}^1 \dots Z_{n+1}^m]$ and $F = \begin{bmatrix} Z_n^1 & \dots & Z_n^m \\ 1 & \dots & 1 \end{bmatrix}$. The derivation of equation 3 is described in detail below.

Two sets of data pairs is used to determine Matrix B of equation 1. Both sets of data have the same parameters except for the control parameter. The control parameter changes from $p_n \rightarrow p_n + \Delta p$ where Δp is small. Matrix B is approximated as equation 4 (Shinbrot et al., 1993):

$$B \sim (Z_f(p_n + \Delta p) - Z_f(p_n)) / \Delta p \quad (4)$$

The selection of perturbation difference Δp in equation 4 is dependent on the magnitude of control parameter p_n . Control algorithm is only effective for $p_n > \Delta p$ due to approximations. As the system dynamics is greatly altered by Δp , a large Δp is selected, resulting that the approximation will also be inaccurate. Δp must be larger and in similar magnitude with p_n for effective approximation and control.

The linearized Poincaré Map of period 1 UPO was determined using UPO detection equations. State points and their second recurrence points are used for period 2 Poincaré Map. The terms Z_{n+1} and p_{n+1} of equation 1 was also replaced by Z_{n+2} and p_{n+2} respectively. The UPO Detection equations are used for the determining of the linearised Poincaré Map for a period p UPO ($p \in$ counting numbers), with replacement equations as:

$$D_n = \|Z_{n+p} - Z_n\| \quad (5)$$

Equation 5 replaces equation 4 and equation 6 to equation 9 replaces the UPO detection equations respectively.

$$Z_{n+p} = CZ_n + D \quad (6)$$

$$Z_{n+p}^1 = CZ_n^1 + D$$

$$Z_{n+p}^2 = CZ_n^2 + D$$

$$Z_{n+p}^m = CZ_n^m + D \quad (7)$$

$$[Z_{n+p}^1 \dots Z_{n+p}^m] = [C \ D] \begin{bmatrix} Z_n^1 & \dots & Z_n^m \\ 1 & \dots & 1 \end{bmatrix} \quad (8)$$

$$[C \ D] = EF^T(FF^T)^{-1} \quad (9)$$

Equation 1 is then replaced by the equation:

$$Z_{n+p} - Z_f(p_n) = A(Z_n - Z_f(p_n) - B(p_{n+p} - p_n)) + B(p_{n+p} - p_n) \quad (10)$$

The linearised Poincaré Map equation above, approximates mapping of points within the region of radius ε_r . The mapping becomes more accurate, the closer the state point is to the fixed point and vice versa.

3.3. Implementing chaos control in the sagittal biped model dynamics

Chaos control was applied after strike transitions in a walking step. A number of unstable manifolds resulted from phase space dimension changes according to different stages of walking. System flow is not smooth due to strike transitions. The Poincaré Mapping method does not model the dynamic effects between recurrence points as it only predicts outcome states based on the inputs. The non-smooth dynamics of strike transitions that occur between mappings are not accounted for. Strike transition could affect the outcome states at times, beyond the approximation of the Poincaré Map. Applying perturbation control only once in a walking step is insufficient due to the effects of strike transitions and the unstable manifold number variation.

There are four distinct events (four possible Poincaré sections) that control can be applied, which are the immediate moments before and after knee and heel strike transitions. Events before the transitions cannot be used due to unsolvable matrices. All dependant variable vectors, at moments just before strike transitions, have linearly dependent generalised coordinates resulting in the matrix (EF^T) of equation 9, which have linearly dependent columns. Matrices with linear dependent columns do not have inverses which results that equation 9 has no solutions. The dependant variable vectors, at immediate moments after strike transitions, have phase space independency, (i.e. the matrices are solvable and solutions exist). Chaos control was applied twice within a step (after knee and

heel strikes) resulting that the controlled parameter may change twice in magnitude during a step. It must be noted that the control parameter remains constant for the duration of the locked or unlocked knee swing phase.

Due to the presence of transition events in the sagittal model, chaos control can be applied twice in one step, instead of only once per cycle. This additional perturbation control helps to stabilise the system as the delay time between disturbance and the reaction is reduced. The procedure used to control the sagittal biped model, which is conducted using closed return and linearization of the Poincaré Map method, is indicated by the detection of a period p UPO. The selection of period p UPO was based on the heel strike Poincaré Map. The UPO at heel strike is easier to determine as it has a smaller phase dimension than UPO at knee strike. The respective linearized Poincaré Map functions were determined from the knee and heel strike UPO. The approximated map functions (from equation 10) are:

Linearised Poincaré Map at instant after knee strike:

$$Z_{n+p}^k + Z_f^k(p_n^k) = A^k \left(Z_n^k - Z_f^k(p_n^k) - B^k(p_{n+p}^k - p_n^k) \right) + B^k(p_{n+p}^k - p_n^k) \quad (11)$$

Linearised Poincaré Map at instant after heel strike:

$$Z_{n+p}^h + Z_f^h(p_n^h) = A^h \left(Z_n^h - Z_f^h(p_n^h) - B^h(p_{n+p}^h - p_n^h) \right) + B^h(p_{n+p}^h - p_n^h) \quad (12)$$

where the superscript k and h denotes knee and heel strike respectively.

The variable u_1 , u_2 and u_3 described below and further in this chapter, refer to stance foot joint torque, hip joint torque and swing knee joint torque respectively. The generalised coordinates in the following state condition vectors are: $Z^h = [q_1, q_1, q_2]^T$ and $Z^k = [q_1, q_2, q_1, q_2]^T$, where q_1 is the angle between normal of the ground and stance leg, while q_2 is the angle between normal of the ground and swing thigh. The perturbation or control parameter (p_n) of the biped model is the hip joint torque u_2 . The objective was to control u_2 such that the system orbit crosses both the knee (Z_f^k) and heel (Z_f^h) fixed points. Perturbation control was only considered when system flow was close to the fixed points. The matrices of equation 11 and equation 12, were used to calculate the perturbation difference of equation 13 and equation 17 respectively. Control was implemented at immediate moments after strike transitions.

3.4. Locked Knee Swing Phase Control

For locked knee swing phase control, control was applied according to the conditions:

$$p_{n+1}^k = \begin{cases} p_n^k + \Delta p_{n+1}^k, & r_n^k < \varepsilon_{rf}^k \varepsilon_r^k \\ p_n^k, & r_n^k > \varepsilon_{rf}^k \varepsilon_r^k \end{cases} \quad (13)$$

where the symbol $\varepsilon_{rf}^k \in (0, 1]$ is a constant fraction.

Successful control only occurs when r_n^k is a fraction of ε_r^k , even though the linearized Poincaré Map region covers a radius of ε_r^k . The accuracy of control is dependent on the magnitude of the perturbation force. The linearization approximation becomes inaccurate if the perturbation is too large. The following perturbation magnitude condition also applies:

If $\Delta p_{n+1}^k > \Delta p_{max}^k$,

$$\Delta p_{n+1}^k = 0 \quad (14)$$

where the symbol Δp_{max}^k denotes the maximum perturbation difference for locked knee swing phase control.

The control parameter u_2 for locked knee swing phase is as follows:

$$u_2 = \Delta p_{n+1}^k + p_n^k \quad (15)$$

Equation 15 with $u_1=0$ is used to compute the locked knee swing phase dynamics as shown in equation 16.

$$\boldsymbol{\tau} = \begin{bmatrix} \tau_1 \\ \tau_2 \end{bmatrix} = \begin{bmatrix} -(\Delta p_{n+1}^k + p_n^k) \\ \Delta p_{n+1}^k + p_n^k \end{bmatrix} \quad (16)$$

3.5. Unlocked Knee Swing Phase Control

For unlocked knee swing phase control, control is implemented according to the conditions:

$$p_{n+1}^h = \begin{cases} p_n^h + \Delta p_{n+1}^h, r_n^h < \varepsilon_{rf}^h \varepsilon_r^h \\ p_n^h, r_n^h > \varepsilon_{rf}^h \varepsilon_r^h \end{cases} \quad (17)$$

where the symbol $\varepsilon_{rf}^h \in (0, 1]$ is a constant fraction.

Constant ε_{rf}^h serves the same purpose as ε_{rf}^k . Condition 14 applies in this case too.

The control parameter u_2 for unlocked knee swing phase is:

$$u_2 = \Delta p_{n+1}^h + p_n^h \quad (18)$$

Equation 18 with $u_1 = 0$ and $u_3 = 0$ is to compute the unlocked knee swing phase dynamics, resulting in equation 19:

$$\boldsymbol{\tau} = \begin{bmatrix} \tau_1 \\ \tau_2 \\ \tau_3 \end{bmatrix} = \begin{bmatrix} -(\Delta p_{n+1}^h + p_n^h) \\ \Delta p_{n+1}^h + p_n^h \\ 0 \end{bmatrix} \quad (19)$$

4. CHAOS AND PERIODIC ORBITS SIMULATIONS

Simulations were conducted on the passive walking of the biped model while on a constant angled slope. It was determined that each slope angle has underlying periodic or chaotic dynamics, provided no actuations were involved. A bifurcation diagram and the calculation of the Lyapunov exponent were used to categorising periodic or chaotic dynamic process. Period 1 and 2 orbit system characteristics were analysed. Identifying the trend patterns of the periodic orbit, assisted with the understanding of chaotic orbits that are periodically controlled. Chaos control of a period 1 UPO was conducted.

4.1. Differentiating Chaotic and Periodic Regions

A bifurcation diagram of the modelled system was generated first. The bifurcation diagram simulation, as initial conditions, were used for plotting of the Lyapunov exponents which uses the converged states. The Lyapunov exponent is determined by averaging the Lyapunov exponents of different initial conditions to improve the accuracy. Only one initial condition is used per slope angle. The sign of the values are the same for both methods but the magnitude of the determined Lyapunov exponents may not be as accurate. System behaviour (chaotic or periodic) can be identified from the sign of the Lyapunov exponent, using table 1.

Table 1. Categories of the Lyapunov exponent

Lyapunov Exponent	System Behaviour
$\lambda > 0$	Chaotic diverging
$\lambda = 0$	Periodic, neither converging or diverging
$\lambda < 0$	Stable periodic converging

The bifurcation diagram, shown in Figure 3 and the Lyapunov exponent graph, shown in Figure 4, share the same categorisation of system behaviour, as a function of the slope angle γ . Both Figures show that the orbits are periodic for $\gamma \in [0.0189, 0.095]$ rad and mostly chaotic for $\gamma \in (0.095, 0.1]$ rad. For slope angles within the abovementioned range, stable walking does not occur passively. Period-doubling occurred first at $\gamma=0.08$ rad, in terms of increasing slope angle. It bifurcates into period 2 orbits for $\gamma \in [0.08, 0.09]$ rad. It continues to bifurcate into higher order periods (period 4, 8, 16 etc.) for $\gamma \in [0.09, 0.095]$ rad. The Lyapunov exponent graph confirms the abovementioned categorisation as shown in Figure 4. The Lyapunov exponent graph indicates better results when it comes to the exact slope angles at which bifurcation occurs, as illustrated at high period bifurcations. Figures 4 (a) and (b) show that all bifurcation points occur at zero crossings of the graph. Figure 4 (b) shows that there are regions of periodic orbits within the chaotic region ($\gamma \in (0.095, 0.1]$ rad). This is illustrated by the negative Lyapunov exponents on the graph (Figure 4 (b)). These periodic regions immersed within the chaotic regions are called periodic windows. One example occurs at $\gamma = 0.0974$ rad. In Figure 6 (b), it can be seen that there appears to be a gap located at

$\gamma = 0.0974$ rad. This periodic window is confirmed by the $\gamma = 0.0974$ rad negative Lyapunov exponent spike of Figure 4 (b).

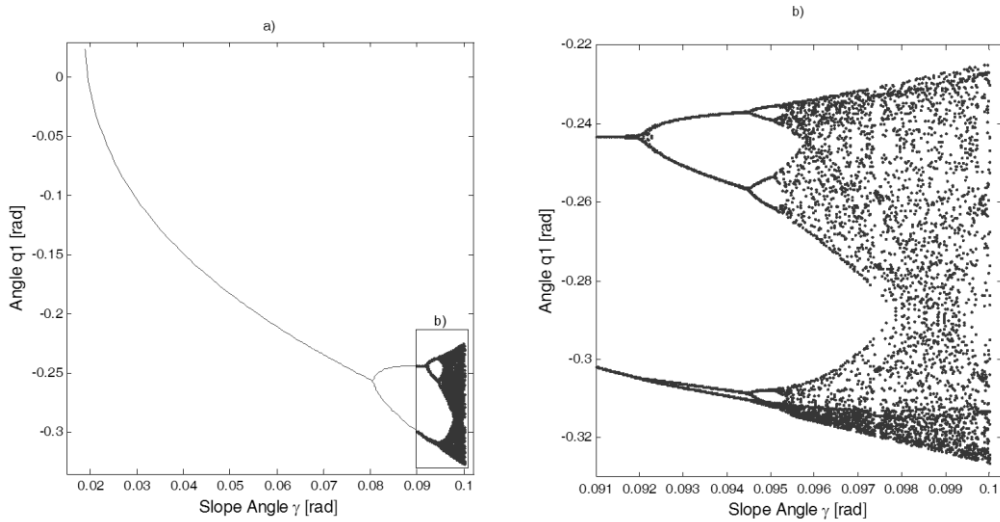


Figure 3. Bifurcation diagrams of the simulated biped model – a) Entire slope angle range of stable walking, b) Magnified view of chaotic regions.

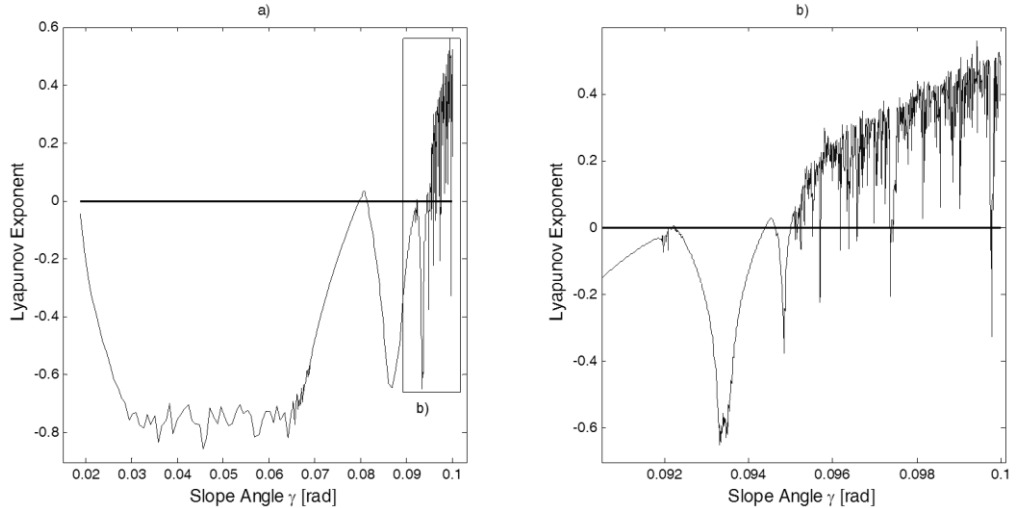


Figure 4. Lyapunov exponent graph of the simulated biped model - a) Entire slope angle range of stable walking b) Magnified view of chaotic regions.

System dynamics at three slope angles were investigated. Period 1 and 2 orbits were analysed, located at $\gamma = 0.06$ rad and $\gamma = 0.09$ rad respectively. Analysis and control of chaos at $\gamma = 0.0985$ rad were conducted. The three slope angles selected above do not lie close to period-doubling points or periodic windows. This feature ensures that the observed behaviour is not effected by orbits of different characteristics due to rough slope angle interval and resolution.

4.2. Limit Cycle

The limit cycle (period 1 orbit) of $\gamma = 0.06$ rad were studied. Figure 5 indicates the BOA on the heel strike Poincaré section of the limit cycle (shaded area). It is a section plane of the 3D initial condition phase space. The generalised coordinates q_1 and \dot{q}_1 were varied with $\dot{q}_2 = 0.6\dot{q}_1$. The full BOA includes the independent variation of \dot{q}_2 . For simplicity of presentation, the BOA region was reduced to a single plane. The entire section range of BOA is shown in Figure 5 (a), where most initial condition combinations are unrealistic as they correspond to irregular configurations of the biped (e.g. legs wide apart). The typical stable operation ranges are shown in Figure 5 (b). The area of BOA in Figure 5 (b) illustrates that stable walking is more likely to occur in typical operation ranges instead of the range of Figure 5 (a). Figure 5 (b) also show that for stable walking, the initial step length increases and the initial stance leg velocity (\dot{q}_1) also increases. The magnitude of q_1 at the starting position is proportional to the initial step length. As stride length increases, a larger stance leg momentum is required as pitch motions are dependent on such momentum.

All trajectories with initial conditions within the BOA of the system will converge to a single fixed point. The fixed points on the knee and heel Poincaré sections are indicated in vector 20 and vector 21:

$$\begin{aligned} Z_f^k &= [q_1, q_2, \dot{q}_1, \dot{q}_2]^T \\ &= [0.1303 \quad -0.3630 \quad 0.8991 \quad -0.8045]^T \end{aligned} \quad (20)$$

$$\begin{aligned} Z_f^h &= [q_1, \dot{q}_1, \dot{q}_2]^T \\ &= [-0.2105, \quad 1.4589 \quad 0.4023]^T \end{aligned} \quad (21)$$

where the units are rad and rad/s for q and \dot{q} respectively, and is applicable to the entire chapter unless otherwise specified.

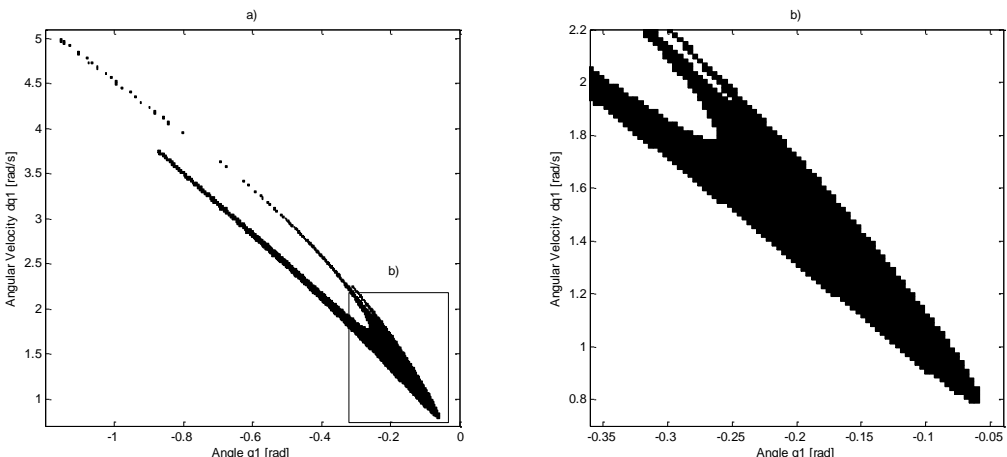


Figure 5. Limit cycle's basin of attraction - a) Entire BOA, b) Typical operational BOA.

The above coordinates are rounded off to four decimal places. The most robust initial condition (on heel Poincaré Map) is located at $q_1 = -0.22$ rad and $\dot{q}_1 = 1.5$ rad/s

(approximate centre of the BOA area), as indicated in Figure 5 (b). These parameters are located closely to the fixed point coordinates stated above. The eigenvalues at the fixed points are:

$$Z_f^k \text{ Eigenvalues: } \lambda_1=0.6160; \lambda_2=0; \lambda_3=0; \lambda_4=0$$

$$Z_f^h \text{ Eigenvalues: } \lambda_1=0.7001; \lambda_2=0; \lambda_3=0$$

All eigenvalues of fixed points are real and less than one. This implies, according to table 1, that the fixed points are stable nodes. All state points within the BOA of the fixed point, converge radially toward the fixed point. Figure 6 shows the plot of ($\ln d_n$) versus the iteration number which was used for the calculation of the Lyapunov exponent. The graph shows that the saturation of D_n occurs from iteration number 15 onwards. The Lyapunov exponent is the gradient of the straight line approximation of the first 15 iterated points (the gradient of the line in Figure 6). The Lyapunov exponent of the limit cycle, using one initial condition, is $\lambda=-1.0982$ and corresponds to stable periodic orbit which validates the determined eigenvalues.

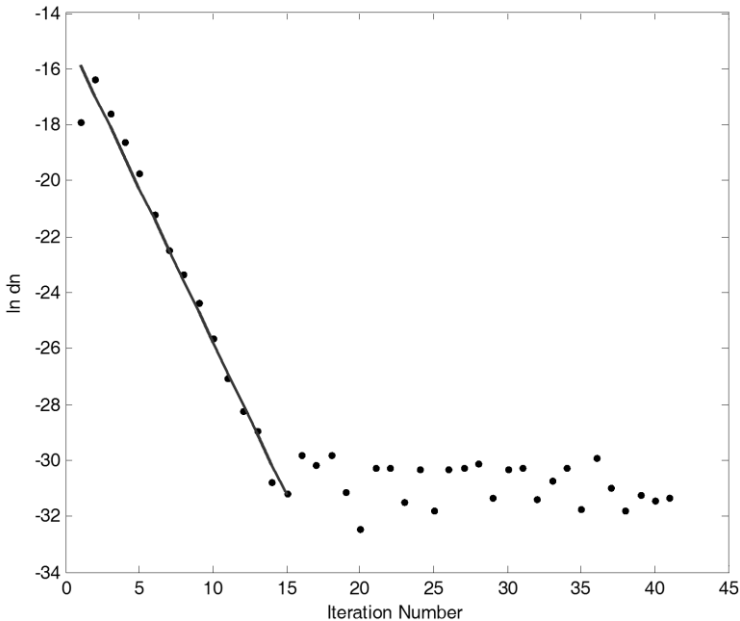


Figure 6. Plot of $\ln D_n$ versus iteration number.

Closed return plots using the knee and heel Poincaré Section are as shown in Figure 7. The initial conditions of the plot are $[q_1, \dot{q}_1, q_2] = [-0.23 \text{ rad}, 1.7 \text{ rad/s}, 1.02 \text{ rad/s}]$ (immediate moment after heel strike). The r_n distance between the initial and fixed point condition is 0.6634. The closed return plots show that the distance between the consecutive recurrence points (D_n) converges after 7 iterations. The limit cycle closed return diagrams shows that D_n approaching zero when the system flow converges. Since the eigenvalues of knee and heel fixed points are similar, their rate of convergence is similar according to the figure.

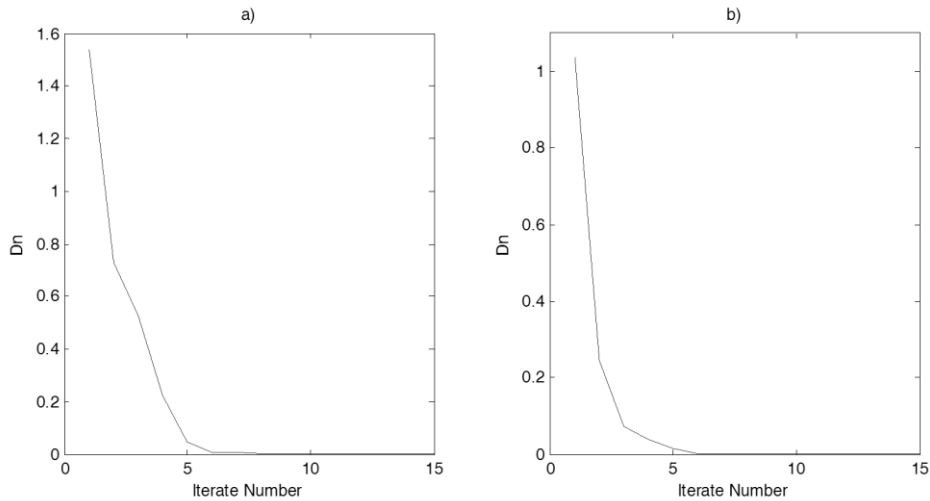


Figure 7. Period 1 Closed Return Plot - a) Knee plot, b) Heel plot

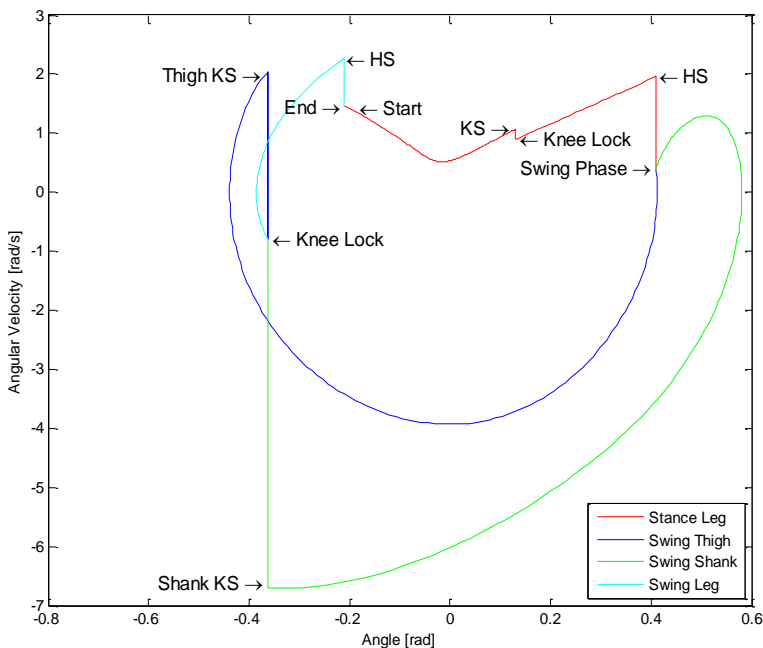


Figure 8. Period 1 phase portrait.

The phase portrait of Figure 8 shows the progression of periodic generalised coordinates for one of the biped's legs. For limit cycles, both left and right leg phase portraits are the same as the steps are symmetrical. The phase portrait is the projection of a dynamical system's state trajectory onto a phase plane (a 2D plane) for easier visualization. The projection may be either curves or points, from which the system's flow trend can be observed. The plotted phase portrait illustrates an initial stance leg walking cycle (two walking steps). Walking starts at coordinates $[q_1, \dot{q}_1] = [-0.2105 \text{ rad}, 1.4589 \text{ rad/s}]$ along the stance leg phase curve. At

the beginning of the second step, the leg becomes a swinging leg and its trajectory is described in the swing thigh and shank phase curves. The swinging leg then joins at knee lock and the cycle repeats after the swing leg's heel strike. It must be noted that for limit cycles, the starting and ending coordinates are the same point. The limit cycle has a walking step length and time of 0.369 m and 0.634 s respectively, which corresponds to a walking speed of 0.582 m/s.

To transform a periodic system to a chaotic one, is possible through actuation. Figure 9 shows the evolution of the long-term state of walking with the varying of the hip joint torque u_2 . For constant values of u_2 at $\gamma=0.06$ rad, the figure shows the evolution of periodic to chaotic orbits as u_2 decreases. The variation of u_2 is capable of changing the system dynamics as shown in Figure 9 but when compared to the control of chaotic systems, actuation torque is relatively high.

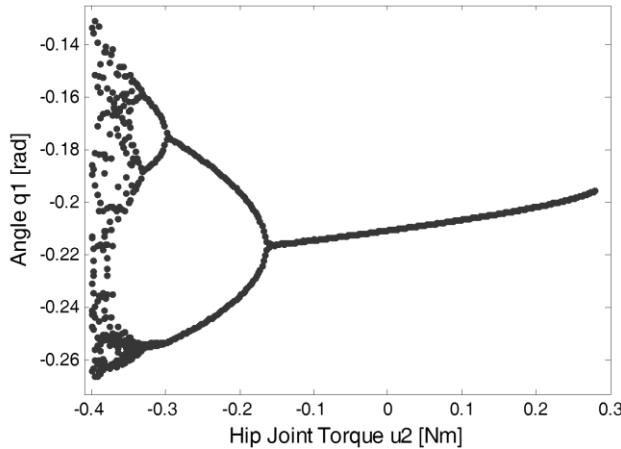


Figure 9. Bifurcation diagram of hip joint torque u_2 variation at $\gamma = 0.06$ rad.

4.3. Period 2 Orbit

A period 2 orbit of $\gamma = 0.09$ rad were studied. Its BOA is shown in Figure 10 which uses the same simulation conditions as defined in the previous section. Figure 10 (a) shows the range of initial conditions, for which walking is stable. The initial conditions during operations are shown in Figure 10 (b). The initial stance leg velocity q_1 range between steeper and gentle slopes. They are similar (stable q_1 of Figure 10 (b) and Figure 5 (b)) as stable orbits of higher slope angles, which have larger initial inner leg angles (see Figure 10 (b)) and larger step lengths.

All trajectories starting within the BOA of period 2 orbit, converges to two fixed point pairs. The fixed point pairs and their eigenvalues are:

Fixed point pair 1:

$$\begin{aligned} Z_f^k &= [q_1, q_2, \dot{q}_1, \dot{q}_2]^T \\ &= [0.0446 \quad -0.5384 \quad 0.8570 \quad -1.3879]^T \end{aligned} \tag{22}$$

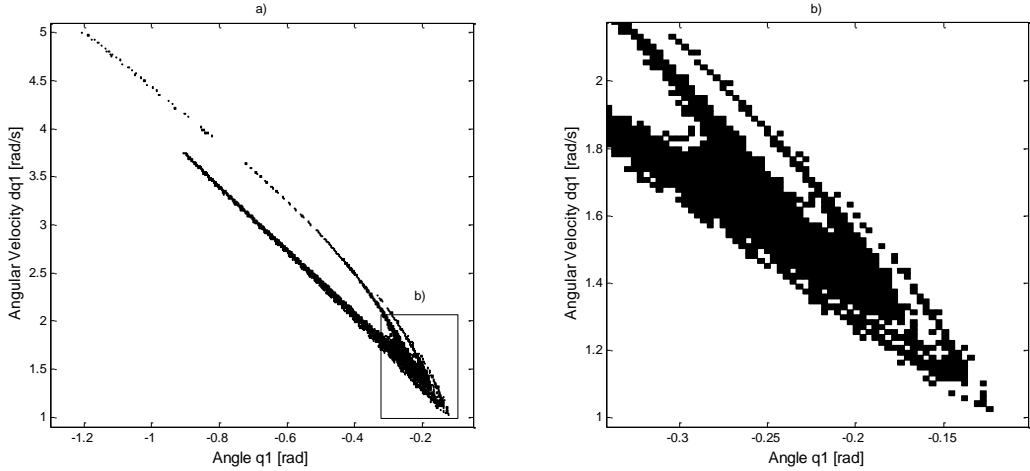


Figure 10. Period 2 orbit's basin of attraction - a) Entire BOA b) Typical operational BOA.

$$\begin{aligned} Z_f^h &= [q_1, \dot{q}_1, q_2]^T \\ &= [-0.2432 \quad 1.5830 \quad 0.1128]^T \end{aligned} \quad (23)$$

with:

$$Z_f^k \text{ Eigenvalues: } \lambda_1 = 0.7470; \lambda_2 = 0; \lambda_3 = 0; \lambda_4 = 0$$

$$Z_f^h \text{ Eigenvalues: } \lambda_1 = 0.7205; \lambda_2 = 0; \lambda_3 = 0$$

Fixed point pair 2:

$$\begin{aligned} Z_f^k &= [q_1, q_2, \dot{q}_1, \dot{q}_2]^T \\ &= [0.1733 \quad -0.4088 \quad 1.2679 \quad -0.8341]^T \end{aligned} \quad (24)$$

$$\begin{aligned} Z_f^h &= [q_1, \dot{q}_1, q_2]^T \\ &= [-0.2989 \quad 1.6447 \quad -0.1291]^T \end{aligned} \quad (25)$$

with:

$$Z_f^k \text{ Eigenvalues: } \lambda_1 = 0.7143; \lambda_2 = 0; \lambda_3 = 0; \lambda_4 = 0$$

$$Z_f^h \text{ Eigenvalues: } \lambda_1 = 0.7376; \lambda_2 = 0; \lambda_3 = 0$$

All eigenvalues of fixed points are real and have a value less than one. Trajectories will converge to the first and second fixed point on the respective Poincaré recurrence. The Lyapunov exponent for the period 2 orbit is determined from Figure 11. The Lyapunov exponent calculated from the first 50 iterations is $\lambda = -0.2402$, indicating that the orbit is periodically stable.

The knee and heel closed return plots are illustrated in Figure 12. The initial conditions of the plot are $[q_1, \dot{q}_1, q_2] = [-0.24 \text{ rad}, 1.6 \text{ rad/s}, 0.96 \text{ rad/s}]$ which are the immediate moment after heel strike. The r_n distance between initial and the first fixed point condition is 0.8474. The plot in Figure 12 indicates convergence after 15 iterations with the knee and heel converged, results the D_n values of 0.7132 and 0.3609 respectively. Period 2 closed return

diagrams have the D_n equal to a constant non-zero value at convergence. The value of D_n is the distance between the two fixed points on the Poincaré Map. For period 3 and greater periodic orbits, the magnitude of D_n varies according to the iteration number at flow convergence. For a period p orbit, D_n varies between p constant values at convergence.

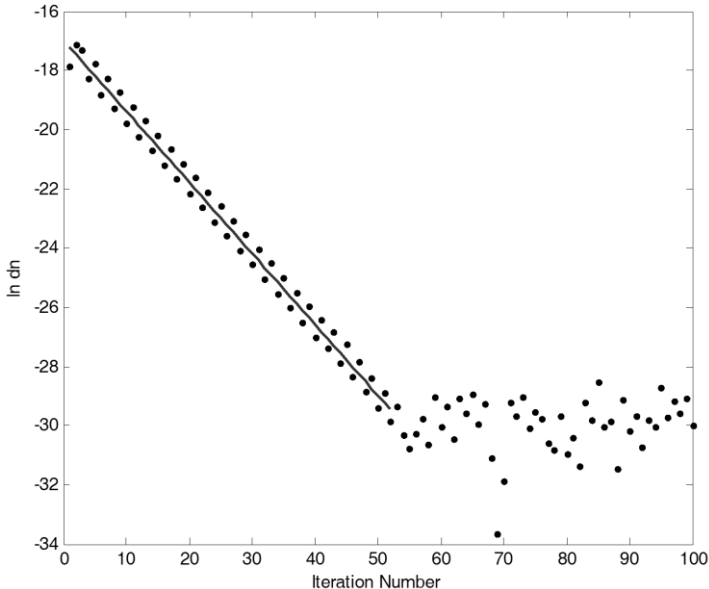


Figure 11. Plot of $\ln D_n$ versus iteration number.

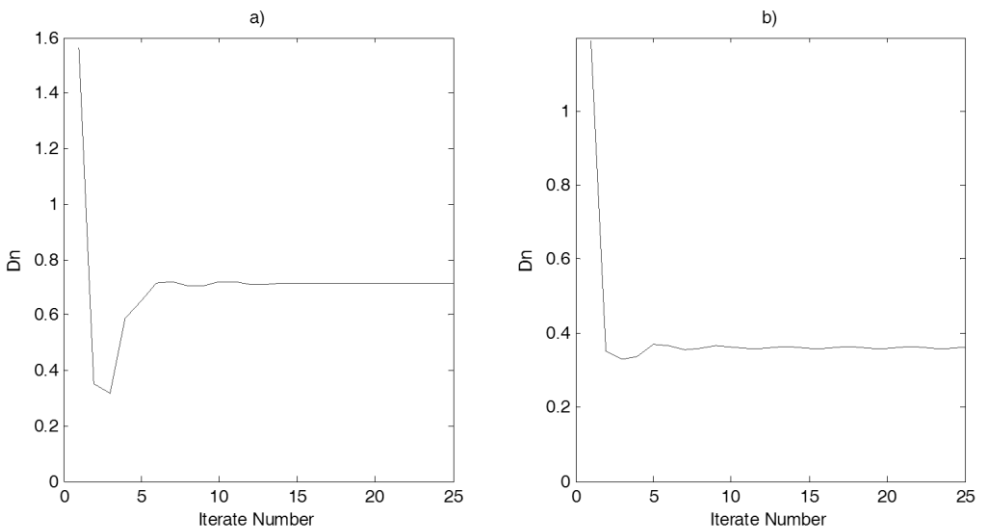


Figure 12. Period 2 Closed Return Plot - a) Knee plot, b) Heel plot.

Figure 13 shows the plot of generalised coordinate as a function of time. The generalised coordinates plotted are states after convergence. The plots start with the heel condition of the first fixed point. Figure 13 portrays the trajectories of a two-step walking cycle where each

leg takes a turn in being the stance or swing leg. The step length and time of the first step are 0.464 m and 0.598 s respectively (step speed of 0.776 m/s). The second step has a length and time of 0.412 m and 0.679 s respectively (step speed of 0.607 m/s). The above corresponds to a limping gait as one leg always takes smaller steps as the other.

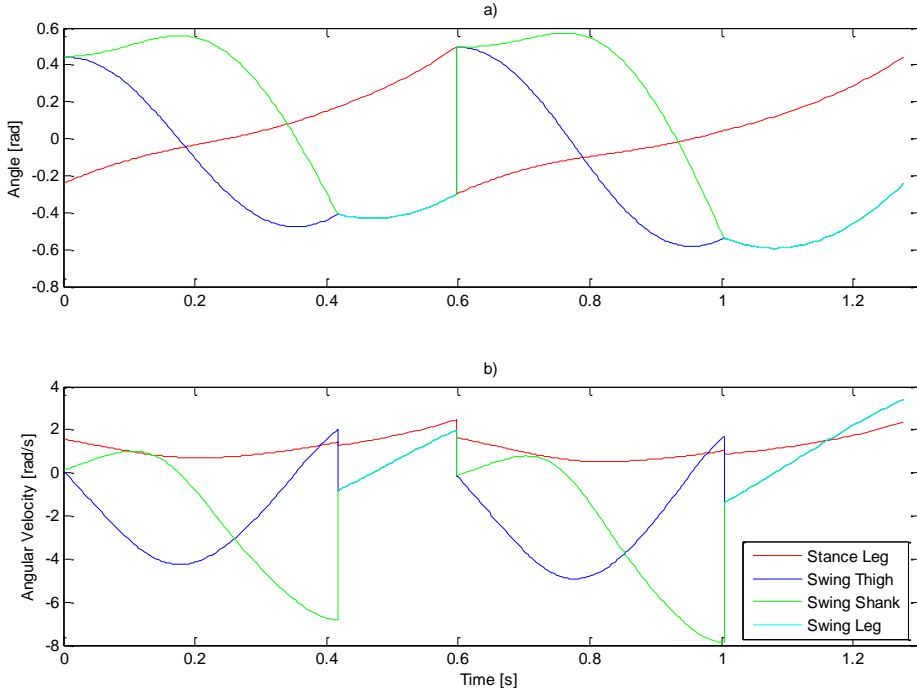


Figure 13. Plot of generalised coordinates versus time - a) Angular generalised coordinates, b) Angular velocity generalised coordinates.

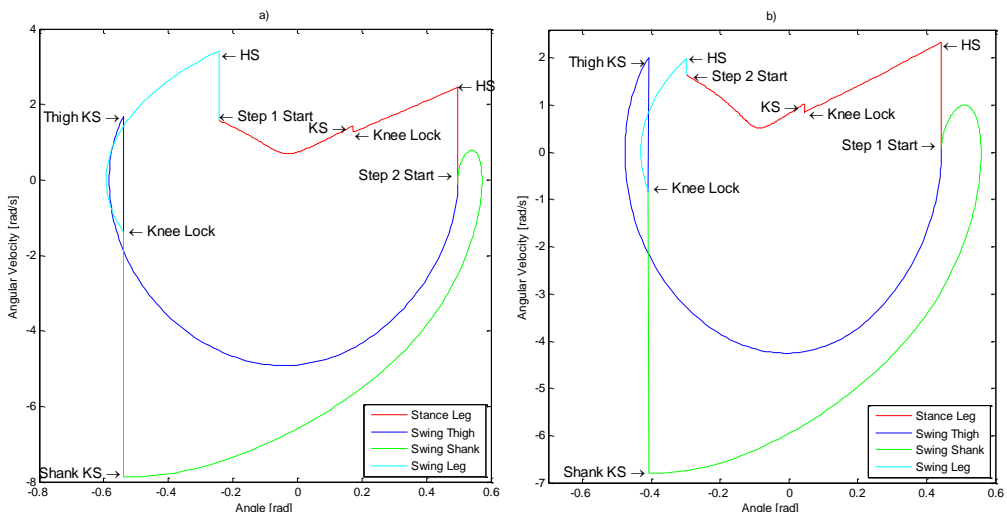


Figure 14. Period 2 phase portraits - a) Right leg (initial stance), b) Left leg (initial swing).

Figure 13 shows the phase portrait of the left and right leg of the biped model. The generalised coordinate of each leg in a cycle is plotted in Figure 14. The right leg is the initial stance leg while the left leg is the corresponding swing leg.

Similar to the limit cycle system, chaotic orbits are achievable in the period 2 system through actuation. Depending on the value of the controlled parameter, different system behaviours are possible. Figure 15 shows that as the chaotic region moves closer to the passive condition ($u_2=0$), the slope angle is decreased (compared with Figure 9). Periodic orbits are dominant for $u_2>0$. Smaller actuation torque is required to generate chaotic walks ($u_2<-0.54$ Nm).

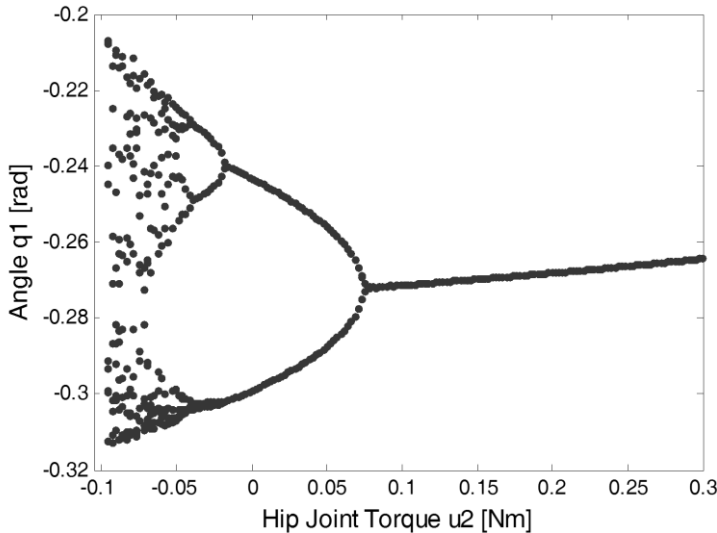


Figure 15. Bifurcation diagram of hip joint torque u_2 variation at $\gamma = 0.09$ rad.

4.4. Period 1 UPO Control

This section involves the control of a period 1 UPO at $\gamma = 0.0985$ rad. The planned BOA for this slope angle is illustrated in Figure 16 (with $\dot{q}_2=0.6\dot{q}_1$). Similar to the BOA figures in previous sections, the operational initial condition range is the shaded area in Figure 16 (b). As the slope angle increases, the area of BOA of typical operational ranges scatters, which result that initial conditions becoming sensitive to disturbances or deviations. The size of the BOA area also dictates whether the operating conditions are robust enough for experimental walks. The chance of stable experimental walks decreases if the area is too small (limited q_1 and \dot{q}_1 range), because the initial condition of the walks cannot be accurately controlled. The Lyapunov exponent determined from Figure 17 is $\lambda = 0.3870$. It was determined by using the gradient of the first 25 unsaturated points. The gradient is positive which confirms that the system is chaotic.

Closed return distances for 200 consecutive walking steps were plotted as shown in Figure 18. All initial conditions with $D_n < 0.1$ were inspected. The lowest D_n pair (consecutive knee and heel D_n) was selected as the initial fixed points for linearization of the Poincaré Map. Figure 18 show that the lowest D_n pair is at the 135th iteration / step. All points in

Figure 18 with $D_n < 0.1$ are closed returns from a single fixed point. In any chaotic system of certain conditions and parameters, there is typically more than one period p UPO (Hilborn, 1994).

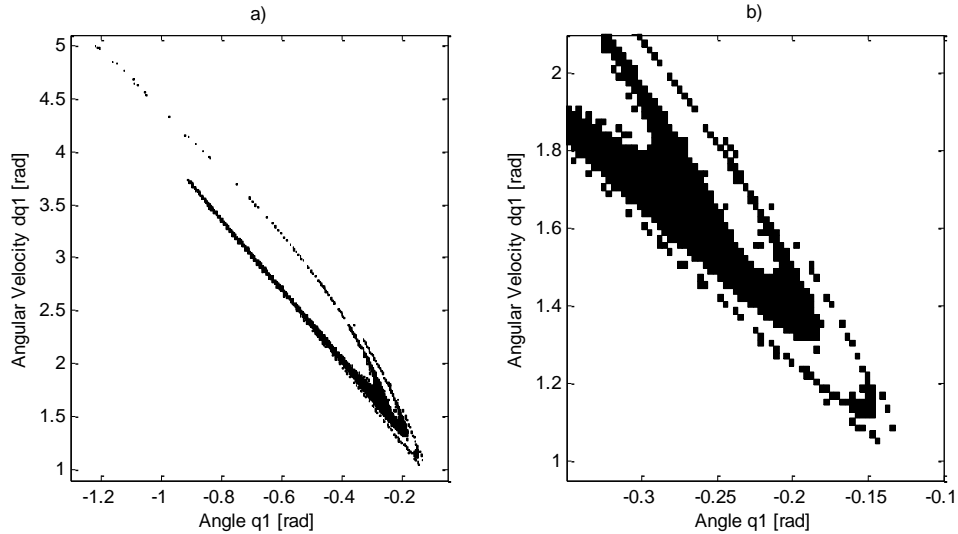


Figure 16. Period 1 UPO's basin of attraction - a) Entire BOA, b) Typical operational BOA.

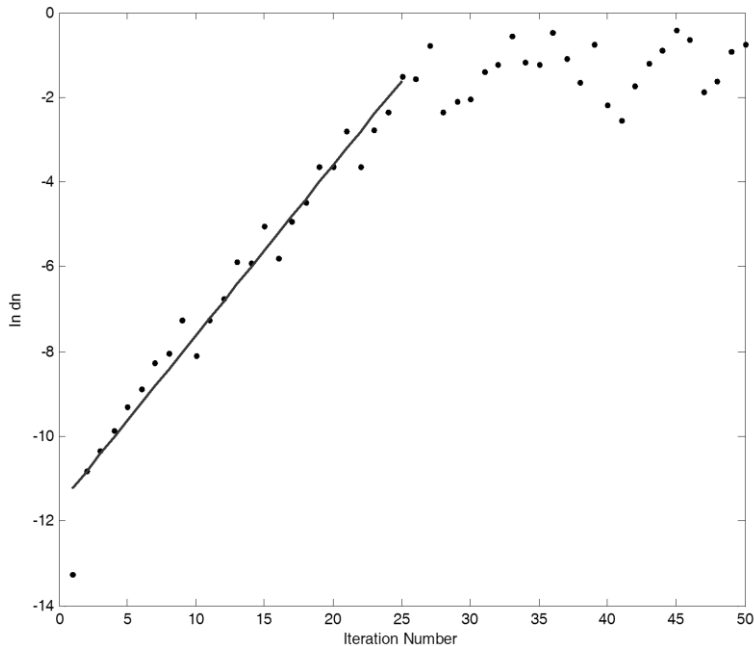


Figure 17. Plot of $\ln D_n$ versus iteration number.

It is not the case here as only a single period 1 UPO could be found for $\gamma = 0.0985$ rad. The fixed points found, using linearization of the Poincaré Map method are:

$$\mathbf{Z}_f^k = [0.0807 \quad -0.5199 \quad 1.0230 \quad -1.2620]^T \quad (26)$$

$$\mathbf{Z}_f^h = [-0.2891 \quad 1.6320 \quad -0.1708]^T \quad (27)$$

with corresponding control parameter:

$$\mathbf{p}_n^k = \mathbf{p}_n^h = 0 \quad (28)$$

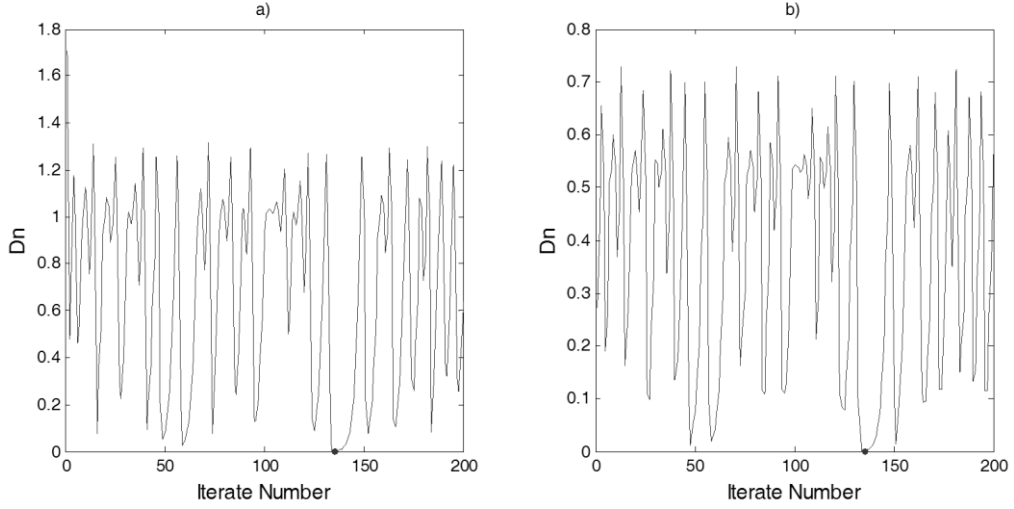


Figure 18. UPO detection Closed Return Plot - a) Knee plot, b) Heel plot.

The period 1 UPO has a walking step length and time of 0.459 m and 0.653 s respectively (walking speed of 0.703 m/s). For the calculation of the linearized Poincaré Map, data for 300 consecutive walking steps were used. The tolerance values used are as follows:

The tolerance value of knee and heel r_n : $\varepsilon_r^k = 0.2$; $\varepsilon_r^h = 0.1$

The tolerance value of knee and heel D_n : $\varepsilon_d^{knee} = 0.2$; $\varepsilon_d^{heel} = 0.1$

Figure 19 illustrates the plots of heel and knee r_n as a function of the iteration number. All points below the ε_r line (dashed line) are considered within the ε_r limit. All points that satisfy both ε_r and ε_d limits, are used to determine the linearized Poincaré Map matrices. The use of smaller ε_r or ε_d limits results in more accurate but smaller linearised space mapping. Smaller tolerance limits also result in a smaller acceptable data set. If the iteration number is limited (as with the number of walking steps in the experiments) then the mapping accuracy will also be limited due to insufficient data sets.

The selection of control parameter change Δp (equation 4) for the linearization of the Poincaré Map process is dependent on the underlying dynamics of the system. Figure 20 shows the bifurcation diagram of the u_2 variation on the long-term dynamic of the system. For $\gamma = 0.0985$ rad, if u_2 is in the range of [0.025, 0.3] Nm, the orbits are considered periodic. If

orbits are periodic, no recurrence point near the linearized fixed point can be found which results in no shift of vector B (equation 29).

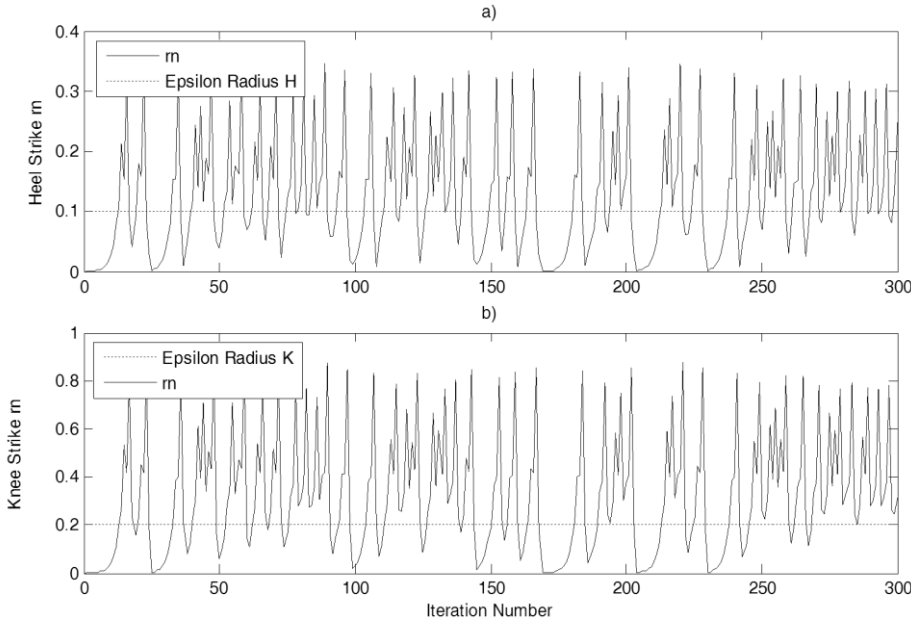


Figure 19. Plot of r_n as a function of iteration number. a) Heel r_n plot b) Knee r_n plot.

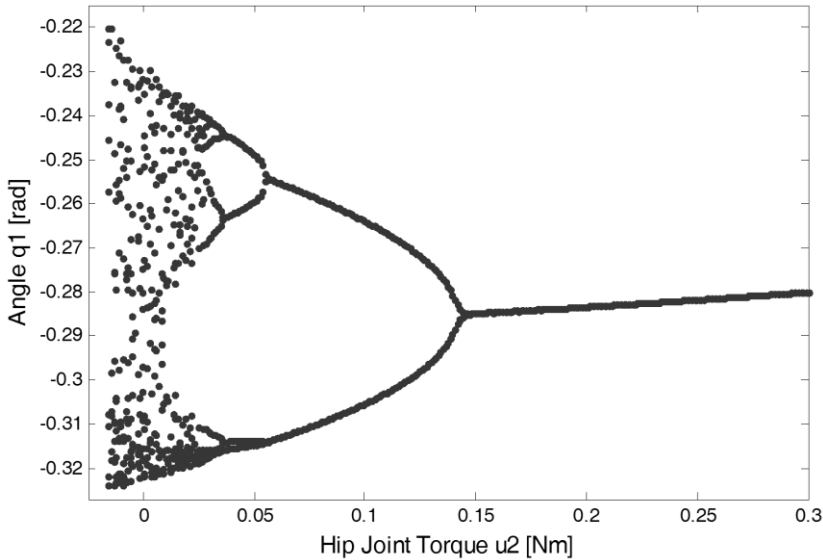


Figure 20. Bifurcation diagram of hip joint torque u_2 variation at $\gamma = 0.985$ rad.

If $u_2 < -0.0157$ Nm, then walking becomes unstable, therefore the selected control parameter change Δp must be in the range of $[-0.0157, 0.25]$ Nm for the period 1 UPO control.

$$B = \frac{\partial}{\partial p} Z_f(p) \Big|_{p=p_n} \quad (29)$$

For the period 1 UPO, the matrices of the knee and heel linearized Poincaré Maps of equation 11 and equation 12 respectively are:

Knee linearized Poincaré Map matrices:

$$A^k = \begin{bmatrix} -31.4881 & 8.4255 & 5.2538 & 1.0807 \\ -26.5639 & 7.1739 & 4.3177 & 0.9403 \\ -109.9170 & 29.3161 & 18.5407 & 3.7247 \\ -180.5760 & 48.1321 & 31.3741 & 5.8548 \end{bmatrix} \quad (30)$$

$$B^k = [0.1070 \quad 0.3720 \quad 0.2439 \quad 0.1750]^T \quad (31)$$

Heel linearized Poincaré Map matrices:

$$A^h = \begin{bmatrix} -2.1509 & -0.6530 & 0.0311 \\ 0.9707 & 0.2548 & -0.0074 \\ -13.484 & -4.4472 & 0.2985 \end{bmatrix} \quad (32)$$

$$B^h = [0.0323 \quad 0.0842 \quad 0.5073]^T \quad (33)$$

The computation of the perturbation difference Δp_{n+1} depends on the number of unstable manifolds at the fixed point. The eigenvalues of the fixed points are:

Z_f^k Eigenvalues: $\lambda_1 = 1.6760$; $\lambda_2 = -1.6386$; $\lambda_3 = 0.0767$; $\lambda_4 = -0.0328$

Z_f^h Eigenvalues: $\lambda_1 = -1.6528$; $\lambda_2 = 0.0830$; $\lambda_3 = -0.0278$

There are two unstable manifolds at Z_f^k and one unstable manifold at Z_f^h . The perturbation difference equations of the fixed points are:

$$\Delta p_{n+1}^k = \frac{\lambda_1^k f_1^k (Z_n^k - Z_f^k)}{(\lambda_1^k - \lambda_2^k)(\lambda_1^k - 1)f_1^k B^k} - \frac{\lambda_2^k f_2^k (Z_n^k - Z_f^k)}{(\lambda_1^k - \lambda_2^k)(\lambda_2^k - 1)f_2^k B^k} \quad (34)$$

where

$$\lambda_1^k = 1.6760$$

$$\lambda_2^k = -1.6386$$

$$f_1^k = [-80.8295 \quad 21.3354 \quad 15.5580 \quad 2.2361]$$

$$f_2^k = [-48.4328 \quad 13.0523 \quad 6.6158 \quad 2.0589]$$

and

$$\Delta p_{n+1}^h = \frac{\lambda_1^h f_1^h (z_n^h - z_f^h)}{(\lambda_1^h - 1) f_1^h B^h} \quad (35)$$

where:

$$\lambda_1^h = -1.6528$$

$$f_1^h = [7.7268 \quad 2.3789 \quad -0.1142]$$

f_x^k are adjoint vectors of the eigenvector of A^k and A^h .

The perturbation difference (equations 34) were applied in conjunction with equation 13 to equation 19 in the control of period 1 UPO. The constants in equation 13 and equation 17 are $\varepsilon_{rf}^k = 0.5$ and $\varepsilon_{rf}^h = 0.5$ respectively. The limits of perturbation difference in equation 14 are $\Delta p_{max}^k = \Delta p_{max}^h = 0.04 \text{ Nm}$. Limitations due to the effects of u_2 variation on system dynamics, as illustrated in Figure 20, are not a concern in the chaos control process. Since the perturbation torque changes between iterations (except after convergence), long-term dynamic effects, which require constant u_2 , will not influence the intended chaotic behaviour.

Control of the period 1 UPO began with the unlocked knee swing phase initial condition:

$$[q_1, \dot{q}_1, \ddot{q}_1] = [-0.28 \text{ rad}, 1.6 \text{ rad/s}, -0.17 \text{ rad/s}] \quad (36)$$

Chaos control was activated for the first 20 steps, deactivated the next 30 steps, and activated for the last 30 steps. Figure 21 is a plot of the distance (r_n) between the state point and the fixed point, for knee and heel Poincaré sections.

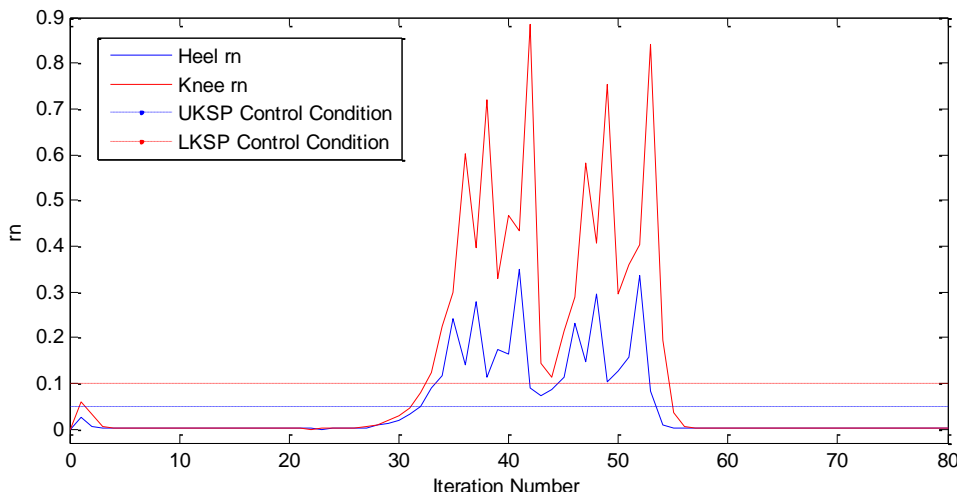


Figure 21. Plot of r_n distance versus iteration number with control. The Knee r_n is the top graph, while the Heel r_n is the lower graph. The LKSP control condition is the top dash line, while the UKSP control condition is the bottom dash line.

The red and blue dash lines on Figure 21 are the control conditions for condition 13 and condition 17 respectively. Chaos control algorithm was initiated if one of the knee or heel r_n values was below its control condition line. From Figure 21, it can be seen that with iteration one (or step one), both control conditions are satisfied which results in unlocked or locked knee swing phase perturbation control (depends on which one comes first).

Figure 22 shows the plot of the perturbation torque u_2 as a function of the iteration number. The control parameter remains constant for the duration of a walking phase. Since chaos control can be applied twice in a single step, the control parameter may change its value between walking phases. Figure 22 shows that after the control condition was met in the first step, perturbation was applied in step two. After step two, the perturbation torque decreases significantly because the state point is now on the stable manifold. The state converges toward the fixed point along the stable manifold in the next couple of steps.

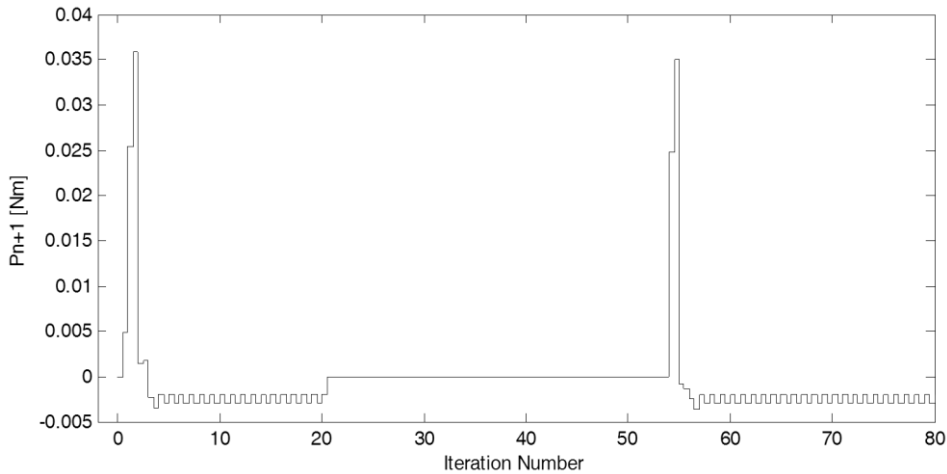


Figure 22. Plot of perturbation torque as a function of iteration number.

The converged state points are:

$$\begin{aligned} Z_{\text{converged point}}^k &= [q_1, q_2, \dot{q}_1, \dot{q}_2]^T \\ &= [0.0802, -0.5208, 1.0217, -1.2633]^T \end{aligned} \quad (37)$$

$$\begin{aligned} Z_{\text{converged point}}^h &= [q_1, \dot{q}_1, \ddot{q}_1]^T \\ &= [-0.2892, 1.6318, -0.1722]^T \end{aligned} \quad (38)$$

The distance between the fixed points and the converged points are: $r_n^k = 0.00208$ and $r_n^h = 0.00144$. After 4 iterations at convergence, the control parameter oscillates around 0.0025 Nm. Since UPOs are unstable by nature, it will require control to maintain periodicity. The value of the actual point and the calculated fixed point may differ due to linearization and approximation. Due to this difference, the control parameter at convergence is close but not exactly equal to its nominal value of $p_n^k = p_n^h = 0$.

The state moves away from the fixed point and wanders chaotically as shown in Figure 21, when the control was deactivated at the 20th iteration. Control activated after the 50th

iteration. At iteration number 54, the control condition was met again. The chaotic orbit converges onto the previous UPO fixed point once again. If no control is applied to the system, the chaotic orbit will wander around the UPO fixed point as indicated in Figure 23. It can be seen that the frequency of a chaotic orbit approaching close to a period 1 UPO, when the fixed point is low. This depends on the radius of the ‘neighbourhood’ of the fixed point.

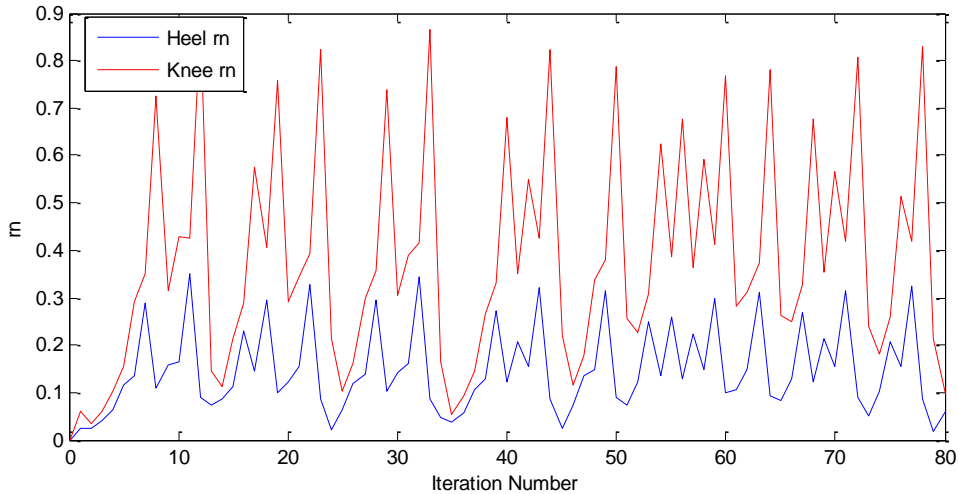


Figure 23. Plot of r_n distance versus iteration number without control. The Knee r_n is the top graph, while the Heel r_n is the bottom graph.

CONCLUSION

The OGY method for chaos control does not require prior knowledge of the system and modelling equations. The control of a chaotic system using control parameters, derived from a previous trajectory data set, has been experimentally conducted by Ditto et al., (Ditto et al., 1990) and Shinbrot et al., (Shinbrot et al., 1992). None of the chaos control algorithms presented in this chapter is based on the governing equations of the biped model. For both theoretical and experimental chaos control of the biped model, the required inputs are the captured results of walking trajectories. The requirements of the chaos control procedure are large numbers of data points from heel and knee strike conditions. From the gathered data, UPO point(s) are detected and the one of interest is selected. Using the captured data set, a linearized Poincaré Map and a perturbation equation about the UPO fixed point are calculated. Chaos control is applied to the system if the control conditions are met.

This chapter has demonstrated the control of a period 1 UPO using a stated biped model. The convergence results of the period 1 UPO at the specified slope angle was presented. A period 2 UPO was located but the control was not achieved due to reasons previously discussed. Asymmetric gaits are not desirable as their system dynamics vary from step to step. High dimensional orbit control may be possible but it is not desirable for the biped model due to performance inconsistency.

The statement regarding the use of small perturbation in controlling chaotic systems has been authenticated. Figure 20 shows the change of long-term states due to hip torque variations: large torque variation is required in order to shift a chaotic orbit at $u_2=0$ Nm to a period 1 cycle ($|u_2|>0.15$ Nm). Figure 21 shows the control torque required to converge a period 1 UPO with the same conditions as indicated above. Both the maximum perturbation torque ($|u_2|>0.035$ Nm) and converged torque ($|u_2|>0.0025$ Nm) of chaos control are smaller than the torque used to shift chaotic orbit into periodic regions. This characteristic proves that the energy efficiency of chaos control over conventional parameter variations of periodic systems.

The goal was to locate many period 1 UPOs for a certain operating condition. The system performance can be altered through the control of chaotic orbits onto the different UPOs. Chaotic systems have shown to have large numbers of UPOs in their chaotic attractors (Ott et al., 1990). There are also more than one period p UPOs for any given condition (Hilborn, 1994) which was not the case for the simulated model. From simulations it has been determined that there is only a single period 1 UPO for each slope angle. It is uncertain whether only a single period 1 UPO exists with different model parameters. The system remains chaotic due to the dynamics of different orders of UPOs co-existing. Even though there is only a single period 1 UPO fixed point per Poincaré section, there are other UPO fixed points of a different order. The initial goal of directing a chaotic orbit to different period 1 UPO was proven not possible. Obtaining performance change through the control of orbits onto higher dimensional orbits is undesirable for the reasons previously stated.

ABOUT THE AUTHORS



Riaan Stopforth graduated with a B.Sc. Eng (Electronics), M.Sc. (Computer Science) and Ph.D. Eng (Mechanical) from the University of KwaZulu-Natal, who has specialized in the field of Mechatronics Engineering. His research interest is in the area of search and rescue robotics and bio-engineering systems. He is currently appointed as an Associated Professor at the University of KwaZulu-Natal.



Glen Bright graduated with a B.Sc. Eng (Mechanical), M.Sc. Eng (Mechanical), Ph.D. Eng (Mechanical) and MBA from the University of KwaZulu-Natal, who has specialized in the field of Mechatronics Engineering. His research interest is in the area of advanced manufacturing systems. He is currently appointed as a Professor at the University of KwaZulu-Natal.

REFERENCES

- Boccaletti, S., Grebogi, C., Lai, Y.-C., Mancini, H. and Maza, D., "The control of chaos: theory and applications", *Physics Reports*, Vol. 329, Issue 3, pp. 103-197, 2000.
- Chua, L. O., Kocarev, L. J., Eckert, K. and Itoh, M., "Experimental chaos synchronization in Chua's circuit", *International Journal of Bifurcation and Chaos*, Vol. 2, No. 3, pp. 705-708, 1992.
- Ditto, W. L., Rauseo, S. N. and Spano, M. L., "Experimental control of chaos", *Physical Review Letters*, Vol. 65, pp. 3211-3214, 1990.
- Drillis, R. and Contini, R., "Body Segment Parameters", New York: Office of Vocational Rehabilitation, Report No. 1166-03, New York, 1966.
- Eckmann, J.-P. and Ruelle, D., "Ergodic theory of chaos and strange attractors", *Reviews of Modern Physics*, Vol. 57, No. 3, 617-656, 1985.
- Garcia, M., Chatterjee, A., Ruina, A. and Coleman, M., "The simplest walking model: Stability, Complexity, and Scaling", *ASME Journal of Biomechanical Engineering*, Vol. 120, Issue 2, pp. 281-288, 1998.
- Garcia, M., Chatterjee, A. and Ruina, A., "Speed, efficiency, and stability of small-slope 2d passive-dynamic bipedal walking", Proceedings of IEEE International Conference on Robotics and Automation, Piscataway, NJ, pp. 2351-2356, 1998.
- González-Miranda, J. M., "Synchronization and Control of Chaos", Imperial College Press, 2004.
- Goswami, A., Thuiilot, B. and Espiau, B., "A study of the passive gait of a compass-like biped robot: Symmetry and chaos", *International Journal of Robotics Research*, Vol. 17, No. 12, pp. 1282-301, 1998.
- Hansen, A. H., Childress, D. S. and Knox, E. H., "Prosthetic foot roll-over shapes with implications for alignment of trans-tibial prostheses", *Prosthetics and Orthotics International*, Vol. 24, pp. 205-215, 2000.

- Hilborn, R. C., “*Chaos and Nonlinear Dynamics*”, Oxford University Press Inc., 1994.
- Kurz, M. J. and Stergiou, N., “Hip actuators can be used to control bifurcations and chaos in a passive dynamic walking model”, *ASME Journal of Biomechanical Engineering*, Vol. 129, No. 2, pp. 216-222, 2007.
- Kurz, M. J., Judkins, T. N., Arellano, C. and Scott-Pandorf, M., “A passive dynamic walking robot that has a deterministic nonlinear gait”, *Journal of Biomechanics*, Vol. 41, No. 6, pp. 1310-1316, 2008.
- McGeer T., “Passive walking with knees”, Proceedings of IEEE International Conference on Robotics and Automation, Los Alamitos, CA, pp. 1640–1645, 1990.
- Ott, E., “Chaos in Dynamical Systems”, Cambridge University Press, 2002.
- Ott, E., Grebogi, C. and Yorke, J. A., “Controlling chaos”, *Physical Review Letters* 64, pp. 1196-1199, 1990.
- Sardain P., Rostami, M., Thomas, E. and Bessonnet, G., “Biped Robots: Correlations between technological design and dynamic behaviour”, *5th IFAC Symposium on Robot Control*, pp. 417-424, Nantes, France, 1997.
- Schwab, A. L. and Wisse, M., “Basin of attraction of the simplest walking model”, Proceedings of ASME Design Engineering Technical Conference, DETC2001/VIB-21363, Pittsburgh, PA, 2001.
- Shinbrot, T., Ditto, W., Grebogi, C., Ott, E., Spano, M. and Yorke, J. A., “Using the sensitive dependence of chaos (the "butterfly effect") to direct trajectories in an experimental chaotic system”, *Physical Review Letter*, Vol. 68, No. 19 , pp. 2863-2866, 1992.
- Shinbrot, T., Grebogi, C., Ott, E. And Yorke, J. A., “Using small perturbations to control chaos”, *Nature*, Vol. 363, pp. 411-417, 1993.
- Sprott, J. C., “Chaos and Time-Series Analysis”, Oxford University Press Inc., 2003.
- Stopforth, R., Bright, G., Feng, C., “*A Hip Actuated Passive Dynamic Walking Biped*”, IEEE EuroCon 2013, Zagreb, Croatia, 2013.
- Winter, D. A., “Biomechanics and Motor Control of Human Movement”, 2nd Edition, Wiley, New York, 1990.
- Wisse, M. and van Frankenhuyzen, J., “Design and construction of mike; a 2d autonomous biped based on passive dynamic walking”, *Proceeding of Conference on Adaptive Motion of Animals and Machines*, Paper number WeP-I-1, Kyoto, Japan, 2003.
- Wisse, M., Schwab, A. L. and van der Helm, F. C. T., “Passive dynamic walking model with upper body”, *Robotica*, Vol. 22, pp. 681–688, 2004.

Chapter 3

HARDWARE AND FLUID IN THE LOOP TESTING: THE APPLICATION TO THE TESTING OF FLUID SYSTEMS, SOME EXAMPLES AND APPLICATIONS

***Emanuele Galardi, Daniele Nocciolini
and Luca Pugi****

Department of Industrial Engineering,
University of Florence, Florence, Italy

ABSTRACT

Continuous development of technologies for the fast prototyping of Real Time (RT) code has really contributed to speed up the diffusion of complex Hardware In the Loop (HIL) testing techniques. Fluid systems technology covers different range of applications: pneumatic brake systems in the railway sector; also, in the industrial field, hydraulic and pneumatic distributed systems (e.g., lube oil units); moreover, in the automation area, control strategies for fluid components and plants are tested with an HIL approach.

In complex plants, the accurate modelling of these systems results in a high computation times that is not acceptable for RT simulations.

This chapter introduces some general concepts for the creation of fast and efficient lumped models, optimized for RT simulation and consequently Hardware in the loop testing of both hydraulic and pneumatic components. In particular, bond-graph modelling techniques are adopted, for a mono dimensional flow, in order to approximate the distributed models in high efficiency lumped ones. More attention is paid on troubles deriving from fixed step implementation of Real Time systems that is constrained by the need of a limited execution time in order to respect assigned scheduling and timing of tasks.

Some modelling application examples are also introduced: the hydraulic and pneumatic components that are employed in industrial and mechatronics units (for instance valves, pumps, accumulators).

* E-mail address: luca.pugi@unifi.it; phone +39 3482106954; fax +39 0554796342. Via S. Marta 3, 50139, Florence, Italy.

In particular the authors focus on the use of well diffused commercial simulation packages (MATLAB-Simulink®, LMS AMESim®) and on some examples of targets used for Real Time implementation.

Keywords: real time code, lumped fluid systems, hardware in the loop, numerical efficiency

ADOPTED SYMBOLOGY

Symbol	Quantity	Unit (SI)
A	Section	m^2
C	Sonic conductance	$\text{m}^3/(\text{s}\cdot\text{Pa})$
C_m	Flow parameter	$\text{s}\cdot\sqrt{\text{K}/\text{m}}$
c_p	Specific heat at constant pressure	$\text{J}/(\text{kg}\cdot\text{K})$
C_q	Constant orifice	-
c_q	Flow coefficient	-
c_{turb}	Critical discharge coefficient	-
c_v	Specific heat at constant volume	$\text{J}/(\text{kg}\cdot\text{K})$
D	Diameter	mm
D_h	Hydraulic diameter	mm
f	Friction factor	-
f_x	Axial tangential effort	$\text{kg}/(\text{m}^2\cdot\text{s}^2)$
g	Acceleration of gravity	m/s^2
h	Specific enthalpy	J/m^3
J_m	Mechanical inertia	$\text{kg}\cdot\text{m}^2$
k	Absolute roughness	-
L	External work	J
l	Length	m
m	Mass	kg
n	Rotation speed	rpm
P	Perimeter	m
p	Pressure	Pa
p_{atm}	Atmospheric pressure	Pa
P_w	Power coefficient	-
Q	Heat exchanged	J
Q_h	Enthalpy flow rate	J/s
Q_m	Mass flow rate	kg/s
Q_v	Volumetric flow rate	m^3/s
R	Constant for a specific gas	$\text{kJ}/(\text{kmol}\cdot\text{K})$
Re	Reynolds number	-
rr	Relative roughness	-
R_t	Critical Reynolds number	-
R_u	Universal gas constant	$\text{kJ}/(\text{kmol}\cdot\text{K})$

Symbol	Quantity	Unit (SI)
T	Temperature	K
t	Time	s
$T_e(n)$	Speed-torque response	N·m
T_m	Required torque	N·m
u	Flow velocity	m/s
V	Volume	m^3
\dot{V}	Volume variation	m^3/s
W_h	Hydraulic power	W
W_m	Mechanic power	W
α	Thermal expansion coefficient	1/K
β	Bulk modulus	Pa
ζ	Total friction factor	-
η	Efficiency	-
λ	Thermal conductivity	W/(m·K)
μ	Absolute viscosity	Pa·s
v_s	Specific volume	m^3/kg
z	Liquid height	m
$\xi(Re)$	Viscous friction factor	-
ϕ	Load coefficient	-
ρ	Density	kg/m ³
τ	Shear stress tensor	N/mm ²
ψ	Flow coefficient	-

1. INTRODUCTION

In this chapter, the fluid systems are analyzed; in particular, the authors, from University of Florence, have gained experience and know how in the development and the implementation of real time models of fluid systems. In complex plants, the accurate modelling of fluid systems results in an high computation times, that is not acceptable for RT simulations and Hardware In the Loop testing.

Consequently, the aim of this chapter is the introduction of some general concepts for the creation of fast and efficient lumped models, optimized for RT simulation and consequently Hardware in the loop testing of the components commonly used in many industrial fields.

In the following section, the lumped parameters models are introduced. The approach followed by authors are the discretization criteria of dynamic systems that are proposed by well known works (Karnopp et al., 1975 and Kulakowski et al., 2007), and the bond-graph modelling techniques (Yu et al., 2012 and Bouamama 2003), for a mono dimensional flow, adopted to approximate the distributed models in high efficiency lumped ones. In particular, the information exchange and the blocks coupling strategies are pointed out. Resistive and capacitive elements are treated in detail, focusing on the distributed and lumped losses modelling.

In section 3, the authors describe the implementation, in the proposed architecture, of the main thermal-hydraulic and thermal-pneumatic components, starting from the main physical equations that describe the behaviour of the component. In particular, the properties are described by second order polynomial functions that are dependent from pressure and temperature. Hence, numerical operations (exact derivations) in the main equations are more efficient.

Section 4 is relative to the main problems and criteria for the Real Time implementation of the developed models.

Examples are introduced considering the implementation in a standard Matlab-Simulink™ environment that is widely diffused and adopted in the research community. However, the discussed matter should be used also for a better use and comprehension of other commercial softwares widely used for the simulation of fluid systems, such as LMS Amesim™ or Flowmaster™.

In particular, two examples of Real Time applications developed for commercially available Real Time Targets are introduced: the DSP TMS320F28335 by Texas Instruments® and the MicroAutoBox II board by dSPACE®. Some modelling application examples are finally introduced in section 5 - the hydraulic components (orifice, centrifugal pumps and accumulators) and the pneumatic components (three different implementations of the pneumatic orifices). Each of these elements is defined according to the input/output variables and the implemented equations.

2. LUMPED PARAMETER MODELS

For the dynamical simulation of a distributed fluid plant systems several references are available in literature. In particular, the approach followed by the authors discredits the criteria of dynamic systems that is proposed by well-known works (Karnopp et al., 1975 and Kulakowski et al., 2007). The same strategy was also followed in the more recent works of some of the authors (Conti et al., 2014). In particular, application (Conti et al., 2014) is referred to the development of a Simulink library for the thermal-hydraulic simulation of auxiliary lubrication circuits employed in rotating machinery and in previous works where similar concepts were used.

Consequently, the approach used to model the continuous fluid and the elements (valves, filters, pumps, etc.) is to discretize the fluid through capacitive and resistive elements. In this way, it is possible to decouple the equations that describe both the hydraulic and the pneumatic models:

- Resistive Element: equation of conservation of momentum.
- Capacitive element: continuity equation and energy equation.

The decoupling of these equations implies that the circuit architecture must be discretized through a network of resistive elements connected with capacitive ones. Therefore, the resulting architecture allows bidirectional exchange of variables, as shown in Figure 1.



Figure 1. Bidirectional network of lumped elements.

2.1. Capacitive Element

In the capacitive elements “C” (in Figure 2), the enthalpy and mass balances are performed in order to calculate the local value of pressure, enthalpy and temperature. Mass and enthalpy flows are supposed to be known inputs provided by adjacent resistive blocks. Typical Capacitive Blocks are pipes, tanks and large capacities in which energy exchanges occurs such as heaters and coolers. In addition, compressibility effects on long pipes should be modeled.

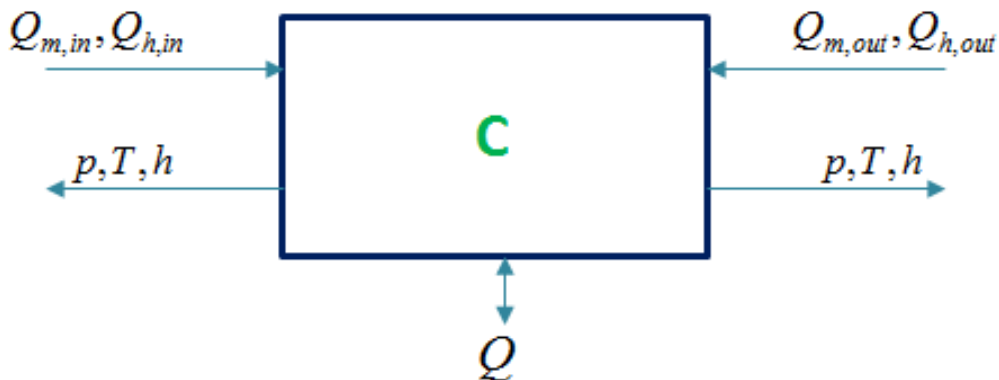


Figure 2. Input and output variables of a lumped capacitive element.

This element is modeled through the continuity equation and energy conservation equation; hence, temperature and pressure are obtained. The continuity Equation (1) is defined respect to the derivative of the density.

$$\frac{d\rho}{dt} = \frac{\frac{dm}{dt} - \rho \frac{dV}{dt}}{V(t)} \quad (1)$$

$$\rho(t) = \rho(0) + \int_0^t \frac{Q_{m,in} - Q_{m,out} - \rho \dot{V}}{V(t)} dt$$

The density expression can be reversed, in order to get the specific volume equation (2).

$$v_s(t) = \frac{1}{\rho(t)} \Rightarrow \dot{v}_s = -\frac{\dot{\rho}}{\rho^2} \Rightarrow \dot{v}_s = -\rho v_s^2 = -v_s^2 \left(\frac{Q_{m,in} - Q_{m,out} - \rho \dot{V}}{V(t)} \right) \quad (2)$$

The temperature is calculated according to the energy conservation equation (4), neglecting kinetics and potential effects inside the control volume. Substituting the density with specific volume into the expression of the enthalpy derivative the Eq. (3) is achieved.

$$\frac{dh}{dt} = \left(c_p \frac{dT}{dt} - T \left(\frac{\partial v_s}{\partial T} \right)_p \frac{dp}{dt} + v_s \frac{dp}{dt} \right) \quad (3)$$

$$\begin{aligned} Q_{h,in} - Q_{h,out} - \rho V h + Q &= \rho V \left(c_p \frac{dT}{dt} - T \left(\frac{\partial v_s}{\partial T} \right)_p \frac{dp}{dt} + v_s \frac{dp}{dt} \right) \\ \frac{dT}{dt} &= \frac{Q_{h,in} - Q_{h,out} - \rho V h + Q}{V c_p} v_s + \frac{1}{c_p} T \left(\frac{\partial v_s}{\partial T} \right)_p \frac{dp}{dt} \\ T(t) &= T(0) + \int_0^t \left(\frac{Q_{h,in} - Q_{h,out} - \rho V h + Q}{V c_p} v_s + \frac{1}{c_p} T \left(\frac{\partial v_s}{\partial T} \right)_p \frac{dp}{dt} \right) dt \end{aligned} \quad (4)$$

The use of fluid properties described in Eq. (27), the specific volume derivative is written in Eq. (5).

$$\left(\frac{\partial v_s}{\partial T} \right)_p = v_{s0} \left(f_{t1} + 2f_{t2}(T - T_{ref}) + f_{pt}(p - p_{ref}) \right) \quad (5)$$

Since density is a thermodynamic property of the liquid, is pressure and temperature dependent. Hence, deriving respect to pressure and temperature, the continuity equation is written in term of pressure derivatives. In addition substituting the Bulk modulus and the volumetric expansion coefficient (both shown in Eq. (7)), Eq. (6) is obtained.

$$\frac{dp}{dt} = \beta \left[\frac{1}{\rho} \frac{d\rho}{dt} + \alpha \frac{dT}{dt} \right] = \beta \left[-\frac{1}{v_s} \frac{dv_s}{dt} + \alpha \frac{dT}{dt} \right] \quad (6)$$

$$\begin{aligned} p(t) &= \int \beta \left[-\frac{1}{v_s} \frac{dv_s}{dt} + \alpha \frac{dT}{dt} \right] dt \\ \beta &= \frac{\rho}{\left(\frac{\partial \rho}{\partial p} \right)_T} = \frac{1}{v_s \left(\frac{\partial \rho}{\partial p} \right)_T} = \frac{-v_s}{\left(\frac{\partial v_s}{\partial p} \right)_T} = -\frac{v_s}{v_{s0}} \frac{1}{\left(f_{p1} + 2f_{p2}(p - p_{ref}) + f_{pt}(T - T_{ref}) \right)} \\ \alpha &= -\frac{1}{\rho} \left(\frac{\partial \rho}{\partial T} \right)_p = \frac{1}{v_s} \left(\frac{\partial v_s}{\partial T} \right)_p = \frac{v_{s0}}{v_s} \left(f_{t1} + 2f_{t2}(T - T_{ref}) + f_{pt}(p - p_{ref}) \right) \end{aligned} \quad (7)$$

2.2. Resistive Element

In the resistive elements “R” (in Figure 3), the momentum balance is performed in order to calculate mass and enthalpy flows. Inlet pressure, temperature and enthalpy values are calculated by adjacent sources or capacitive elements. Typical resistive elements are orifices or valves that can be modelled as lumped pressure losses in the circuit. For fast transients it is

also possible to take count in the momentum balance of inertial terms usually implemented in terms of mean lumped speed of the lumped pipe element. In this case, the element is often called “RI”, acronyms of resistive-inertial. Also for this application case authors have same previous experiences both with self made Matlab-Simulink® codes and with commercial software, concerning the modeling of railway pneumatic brake circuits which are usually discretized as mono-dimensional arrays of “C” and “RI” elements where the compressed air is treated as an ideal gas.



Figure 3. Input and output variables of a lumped resistive element.

This element is modeled through the motion equation (momentum conservation) generalized in the three dimensional case in which also the inclination contribution is considered (8).

$$\rho \left(\frac{\partial v_x}{\partial t} + v_x \frac{\partial v_x}{\partial x} + v_x \frac{\partial v_x}{\partial y} + v_x \frac{\partial v_x}{\partial z} \right) = - \frac{\partial p}{\partial x} - \left(\frac{\partial \tau_{xx}}{\partial x} + \frac{\partial \tau_{yx}}{\partial y} + \frac{\partial \tau_{zx}}{\partial z} \right) + \rho g_x \quad (8)$$

The Eq. (8) can be modified for the mono dimensional case with constant properties as shown in Eq. (9).

$$\begin{aligned} \rho l \dot{Q}_v &= (p_{in} - p_{out}) A - \xi(Re) \frac{\rho Q_v^2}{2A} + \rho g \sin(\alpha) V \\ \dot{Q}_v &= \frac{(p_{in} - p_{out})}{\rho l} A - \xi(Re) \frac{Q_v^2}{2Al} + g \sin(\alpha) A \\ Q_v(t) &= Q_v(0) + \int_0^t \left(\frac{(p_{in} - p_{out})}{\rho l} A - \xi(Re) \frac{Q_v^2}{2Al} + g \sin(\alpha) A \right) dt \end{aligned} \quad (9)$$

The Eq. (9) represents the resistive-inertial element since the derivative of the volumetric flow rate is present. For a pure resistive element, the Eq. (10) is used.

$$Q_v = \sqrt{\frac{2A^2(p_{in} - p_{out})}{\xi(Re)\rho} + \frac{2Ag \sin(\alpha)V}{\xi(Re)}} \quad (10)$$

In Eq. (11) the mass flow rate and enthalpy flow rate relations are obtained from Eq. (10).

$$\begin{aligned} Q_m(t) &= \rho Q_v(t) \\ Q_h(t) &= \rho Q_v(t) h \end{aligned} \quad (11)$$

Enthalpy h is calculated respect to the inlet section.

2.2.1. Lumped Losses Modelling

These sub-models do not have a friction factor expressed as a function of the total length. These components evaluate the local pressure drop, considering their local geometry. Such local geometries induce a sudden change in the speed and direction of flow.

The flow coefficient C_q is deducted from the total friction factor ζ (Eq. (12)).

$$c_q = \frac{1}{\sqrt{\zeta}} \quad (12)$$

The total friction factor is obtained from specific tables and graphs available in literature (Hughes et al., 1982), (White, 1999), (Munson et al., 1998).

2.2.2. Distributed losses modelling

These sub-models are used to model the flow resistances in straight pipes.

The pressure losses along a straight tube having a constant section of passage are represented by the total friction factor ζ in Eq. (13)

$$\zeta = \frac{(f \cdot l)}{D_h} \quad (13)$$

where:

- f = friction factor of a pipe sketch having relative length unit $l/d = 1$;
- D_h = hydraulic diameter or equivalent;
- l = length of the pipe.

The hydraulic diameter is the diameter of the circular cross section conduit and, more generally, consists in the ratio between four times the section area and the perimeter P (Eq. (14)).

$$D_h = \frac{(4A)}{P} \quad (14)$$

The flow coefficient C_q is still deducted from Eq. (12).

In straight pipes, the resistance to motion of a liquid or a gas in laminar motion conditions is due to internal friction forces. This is possible when a layer of liquid or gas has a relative motion comparable with another. These viscous forces are proportional to the flow velocity. Hence, the friction factor depends from the Reynolds Number.

When the Reynolds number increases, the inertial forces (which are proportional to the square of the speed) tend to dominate. The flow becomes turbulent since there is a significant increase of the resistance to movement. Part of this increase is due to the roughness of the wall surface, in fact the duct surfaces are never perfectly smooth, since they present protrusions and recesses with respect to the ideal surface.

In addition, the average value of the protrusions Δ is added to the variables that determine the geometric similarity; hence, the friction factor is function of two dimensionless numbers: the Reynolds number and the relative roughness. The relative roughness is calculated as the average of all the protrusions (i.e., the absolute roughness k) in the inner diameter of the tube, as seen in the Figure 4.

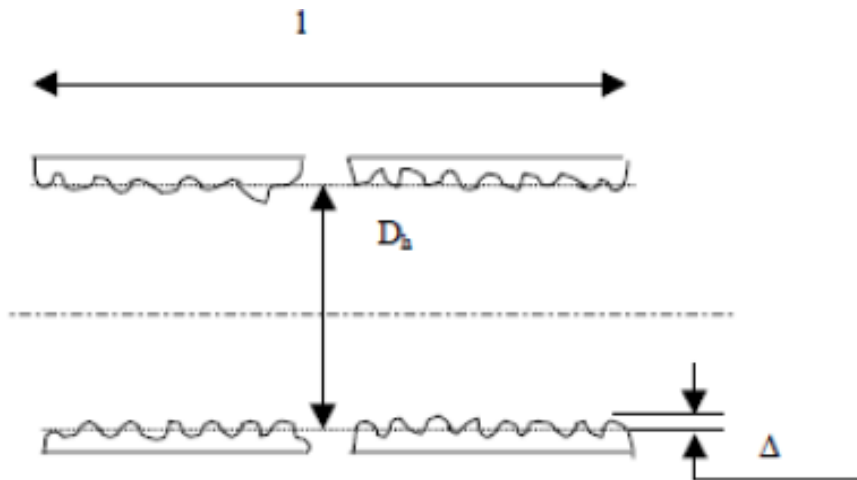


Figure 4. Roughness of the wall surface in straight pipes.

Hence, the relative roughness is expressed in Eq. (15).

$$rr = \frac{k}{D_h} \quad (15)$$

Some values of pipe absolute roughness k , according to the material type, are reported in Table 1.

Regarding the calculating method of the friction factor f , it uses the dependence to f from Reynolds number and the relative roughness, through the Colebrook iterative formula (16).

$$\frac{1}{\sqrt{f}} = -2 \cdot \log \left(\frac{rr}{3.7} + \frac{2.51}{Re \cdot \sqrt{f}} \right) \quad (16)$$

Since the Eq. (16) is iterative (respect to f), will be used one of its approximations, the Haaland equation (17), so to obtain immediately the value of the friction factor:

$$\frac{1}{\sqrt{f}} = -1.8 \cdot \log \left[\left(\frac{rr}{3.7} \right)^{1.11} + \frac{6.9}{Re} \right] \quad (17)$$

Table 1. Absolute roughness for some common materials

Surface	Absolute Roughness Coefficient - k -	
	(m) 10^{-3}	(feet)
Copper, Lead, Brass, Aluminum (new)	0.001 - 0.002	$3.33 - 6.7 \cdot 10^{-6}$
PVC and Plastic Pipes	0.0015 - 0.007	$0.5 - 2.33 \cdot 10^{-5}$
Stainless steel	0.015	$5 \cdot 10^{-5}$
Steel commercial pipe	0.045 - 0.09	$1.5 - 3 \cdot 10^{-4}$
Stretched steel	0.015	$5 \cdot 10^{-5}$
Weld steel	0.045	$1.5 \cdot 10^{-4}$
Galvanized steel	0.15	$5 \cdot 10^{-4}$
Rusted steel (corrosion)	0.15 - 4	$5 - 133 \cdot 10^{-4}$
New cast iron	0.25 - 0.8	$8 - 27 \cdot 10^{-4}$
Worn cast iron	0.8 - 1.5	$2.7 - 5 \cdot 10^{-3}$
Rusty cast iron	1.5 - 2.5	$5 - 8.3 \cdot 10^{-3}$
Sheet or asphalted cast iron	0.01 - 0.015	$3.33 - 5 \cdot 10^{-5}$
Smoothed cement	0.3	$1 \cdot 10^{-3}$
Ordinary concrete	0.3 - 1	$1 - 3.33 \cdot 10^{-3}$
Coarse concrete	0.3 - 5	$1 - 16.7 \cdot 10^{-3}$
Well planed wood	0.18 - 0.9	$6 - 30 \cdot 10^{-4}$
Ordinary wood	5	$16.7 \cdot 10^{-3}$

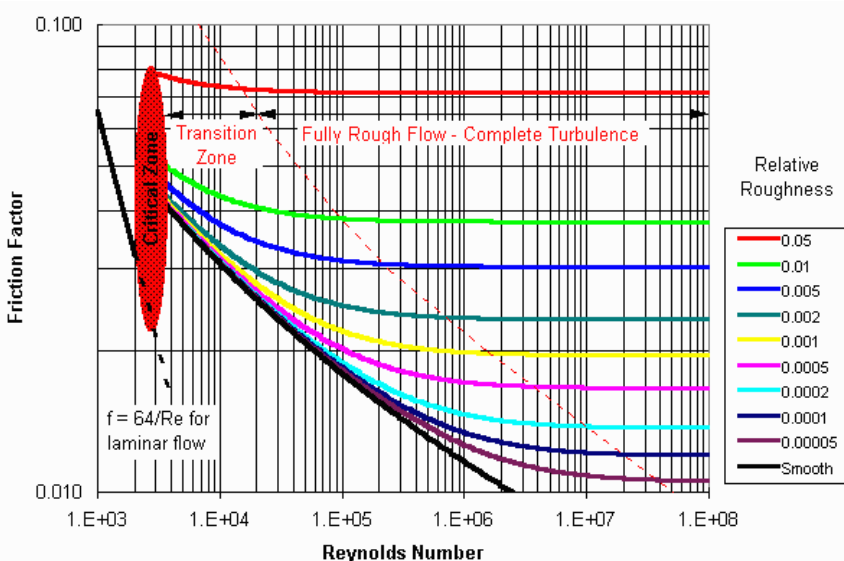


Figure 5. Moody Diagram.

Finally, Figure 5 highlights the evolution to f in function of the dimensionless coefficients. As can be observed, for the laminar flow the value of f is simply given by $f = 64/Re$, regardless of the relative roughness.

Then, follows a measurement uncertainty zone, corresponding to the transition between laminar and turbulent flow.

Finally, for the turbulent flow, the relationship between f and the Reynolds number also depends on the relative roughness with laws more complex not obtainable through theoretical treatises, where f declines with increasing to Re up to a limit value, above which the friction factor is constant.

3. FLUID PROPERTIES

Thermal-hydraulic and thermal-pneumatic model require analytical functions in order to compute the fluid properties according to the state variables (pressure and temperature); however, in Matlab-Simulink[®], specific functions or blocks are absent.

The main properties describing a fluid are the density, absolute viscosity, specific heat and thermal conductibility. In the models described in this chapter, the properties are described by second order polynomial functions that are dependent from pressure and temperature. Hence, numerical operations (exact derivations) in the main equations are more efficient.

Moreover, in literature (Wagner et al., 2000) are present several databases and tables in which the variables, for instance enthalpy or entropy, are calculated according to pressure and temperature. For this reason, tabulated data can be imported in Matlab and optimized through interpolating functions, for Real Time (RT) implementation. In particular, vectors and matrices dimension must be reduced as possible, especially in low gradients zones.

3.1. Thermal-Pneumatic Models Properties

Steam and other gases employed in pneumatics are modelled according to the law of perfect gases (18).

$$p = \rho * R * T \quad (18)$$

T [K] defines the temperature and R is a constant for a specific gas given by the ratio between the universal gas constant R_u ($R_u = 8.314472 \text{ kJ/(kmol K)}$) and the gas molar mass MM . The constant for a specific gas can be deduced, with good approximation, from Eq. (18) and density as shown in Eq. (19).

$$R = p_0 (\rho_0 * T_0) \quad (19)$$

The absolute viscosity [$\text{kg/m} * \text{s}$] is calculated thanks to the second order polynomial function (20).

$$\mu = \mu_0 * 10^\psi \quad (20)$$

where ψ is explicated in Eq. (21).

$$\psi = a_{c0} + a_{t1} * \Delta T + a_{t2} * \Delta T^2 \quad (21)$$

μ_0 is the reference absolute viscosity, a_{c0} is the constant coefficient of absolute viscosity, a_{t1} is the temperature coefficient of absolute viscosity, a_{t2} is the square temperature coefficient of absolute viscosity, ΔT is the difference between actual and reference temperatures.

Specific heat at constant pressure [$J/(kg * K)$] is computed thanks to the second order polynomial function of temperature in Eq. (22).

$$c_p = c_{p0} * \left[b_{c0} + b_{t1} * \Delta T + b_{t2} * (\Delta T)^2 \right] \quad (22)$$

Where c_{p0} is the reference specific heat at constant pressure, b_{c0} is the constant coefficient of the specific heat at constant pressure, b_{t1} is the temperature coefficient of the specific heat at constant pressure, b_{t2} the square temperature coefficient of the specific heat at constant pressure.

The thermal conductivity [$W/(m * K)$] is defined in Eq. (23).

$$\lambda = \lambda_0 * \left[l_{c0} + l_{t1} * \Delta T + l_{t2} * (\Delta T)^2 \right] \quad (23)$$

λ_0 represents the reference thermal conductivity, l_{c0} is the constant coefficient of thermal conductivity, l_{t1} is the temperature coefficient of thermal conductivity, l_{t2} is the square temperature coefficient of thermal conductivity.

In Eq. (24) the link between the specific heat at constant volume (c_v) and constant pressure (c_p) is shown.

$$\begin{aligned} c_v &= c_p - R \\ \gamma &= \frac{c_p}{c_v} \end{aligned} \quad (24)$$

3.2. Thermal-Hydraulic Models Properties

Liquids are modelled according to the same polynomial approximation employed for thermal-pneumatic systems.

Absolute (dynamic) viscosity ($kg/m * s$) is explicated in Eq. (25).

$$\begin{aligned} \mu &= \mu_0 * 10^\psi \\ \psi &= e_{p1}(p - p_0) + e_{t1}(T - T_0) + e_{t2}(T - T_0)^2 \end{aligned} \quad (25)$$

Thermal conductivity is defined in Eq. (26).

$$\lambda_p = \lambda_{p0} * \left[1 + d_t(T - T_0) + d_{t2}(T - T_0)^2 \right] \quad (26)$$

Specific volume [m^3/kg] is shown in Eq. (27).

$$v_s = \frac{1}{\rho} = v_{s0} * [1 + f_{p1}(p - p_0) + f_{p2}(p - p_0)^2 + f_{t1}(T - T_0) + f_{t2}(T - T_0)^2 + f_{pt}(p - p_0)(T - T_0)] \quad (27)$$

Finally, the specific heat at constant pressure ($J/kg\text{ }^\circ\text{C}$) is expressed in Eq. (28).

$$c_p = c_{p0} * \left[1 + g_{t1}(T - T_0) + g_{t2}(T - T_0)^2 + g_{p1}(p - p_0) + g_{pt}(p - p_0)(T - T_0) \right] \quad (28)$$

4. REAL TIME IMPLEMENTATION

One of the most important aspects treated in this chapter is the implementation of complex models on a low cost commercial electronic control, in order to execute HIL tests. For the RT Implementation, in this work, are cited some commercial DSP (Digital Signal Processing) such as the board by Texas Instruments, shown in Figure 6 which has also successfully used by authors both for research and didactical activities.

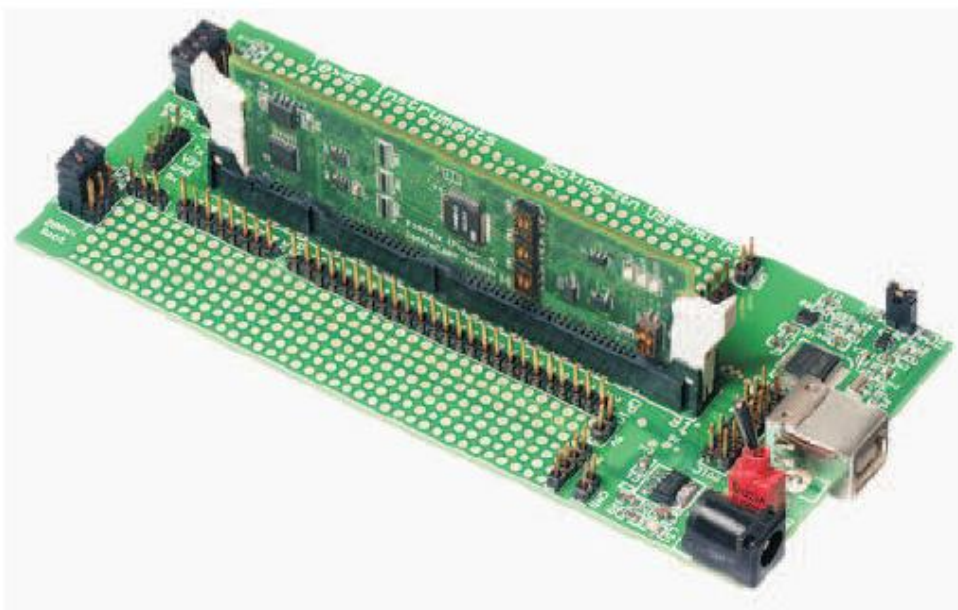


Figure 6. Digital Signal Processing board by Texas Instruments®.

Table 2. Main features the Texas Instrument Delfino DSP board

Data	Value	Units of Measure
Model	TMS320F28335	-
Processor	150	MHz
I/O Design Voltage	3.3	V
DMA Controller	SIX Channels	-
On-Chip Memory	256K x 16 Flash	B
PWM outputs	18	-
CAN modules	2	-
SCI modules	3	-
ACD 12 bit channels	16	-
GPIO pins	88	-
Estimate of the cost	20(mass prod.)-70 (single piece)	euro

The board, whose main feature are described in Table 2, was chosen considering the following criteria:

- The chosen DSP board is supported by Matlab Real Time Workshop® so Simulink code can be easily compiled and download for RT execution on the board.
- The cost of the proposed board is very low respect to a possible industrial application.
- The chosen board provides a wide range of analog and digital I/O in order to be integrated in a more complex system including sensor, actuators and communication bus (CAN and Serial communication modules) in order to be easily integrated on more complex mechatronic systems.

RT implementation of the Simulink® models should depend from the features of the chosen hardware and the corresponding Target® for which Mathworks Real Time Workshop® compiles the model, producing a program that is clearly optimized for a specific environment. In particular, the authors adopted the following approach:

- Integration: according to the Target specifications, the integration of continuous states in differential equations using Matlab-Simulink® integrators should be supported or not. In order to avoid potential portability and stability troubles related to specific features of the target, authors implemented all the differential equations in terms of discrete states (Bi-Linear ‘Tustin’ conversion method is adopted) with assigned integration steps corresponding to execution frequencies of tasks. A non-secondary advantage of this approach was a higher numerical efficiency of the generated code granted by a multi-tasking implementation. Heavy calculations corresponding to systems with a quite slow dynamic behavior (e.g., a boiler) where implemented considering an integration step of few Hertz, reserving higher integration frequencies (10^2 - 10^3 Hz) to the simulation of fast transients and dynamics as the ones associated to safety and communication tasks of the system (or the closed loop controllers of valves). Numerical stability of the fixed step, multi-tasking integration is verified by comparing obtained results with the corresponding solution

obtained with a robust variable step solver running on an offline simulation (Matlab solver ode23tb (Shampine, 1994)).

- Data Types: the use of data types is accurately optimized in order to reduce Data Type conversions.
- Specific Target Blocks: some of the implemented blocks or instructions cannot be independent from the chosen Target®, in particular when affecting or interacting with low level hardware functions such as I/O conversions or communications. These tasks are clearly separated respect to the other ones and can be easily customized without altering significantly the core model of the plant.
- Modularity: the structure of the Simulink model is organized in different subsystems, whose topology resembles the structure of the simulated plant. The proposed approach also makes easier modifications of the simulated plant layout.

RT simulation are performed with an external PC connected to the board, in order to provide to download the code and to provide indispensable interface functionalities.

For more demanding applications such as real time test rig, and simulators, or the development of complex mechatronics systems, it should be highly advisable the use of a dedicated hardware which are produced by several different commercial brands (dSpace, National Instruments, etc.).

In particular some tests have been also performed considering the dSPACE® MicroAutobox II board in Figure 7, whose main features have been highlighted in Table 3.

MicroAutoBox II is a RT system for performing fast function prototyping in fullpass and bypass scenarios. It operates without user intervention, just like an ECU (Electronic Control Unit), which can be used for many different rapid control prototyping (RCP) applications.

This board has been employed for the RT simulation of thermal hydraulic plants, composed by many elements that can be embedded into dSPACE MicroAutoBox II Control Unit. For larger simulations, it should be considered the use of modular-multiprocessor units such as in the example (Pugi et al., 2006) where Hardware Simulation of a railway vehicle with its brake plant have to be performed.



Figure 7. MicroAutoBox II board by dSPACE ®.

Table 3. Main features the dSPACE® MicroAutobox II board

Data	Value
Model	MicroAutoBox II 1401/1511
Processor	900 MHz
I/O Design Voltage	5/4.5 V
Memory	16Mbit (main) +16Mbit (flash)
CAN modules	4
Host interface	Ethernet connection
Real Time I/O interface	(100/1000 Mbit/s)
ADC I/O channels	16/4
GPIO pins	40/40
PWM inputs/outputs	40/40
Estimate of the cost	15000-20000 euro

5. APPLICATIONS EXAMPLES: COMPONENT DESIGN

This section introduces several commonly used models being employed in industrial and mechatronics units:

- Pneumatic orifice;
- hydraulic orifice;
- hydraulic pump;
- hydraulic accumulator.

5.1. Pneumatic Orifice

The first instance presented in this chapter is the pneumatic orifice depicted in Figure 8. The pneumatic orifice is a resistive component; consequently, the inputs of the model are represented by the inlet/outlet pressure, temperature and enthalpy, while the computed outputs are the mass flow rate and enthalpy flow rate exchanged with the adjacent capacitive components.

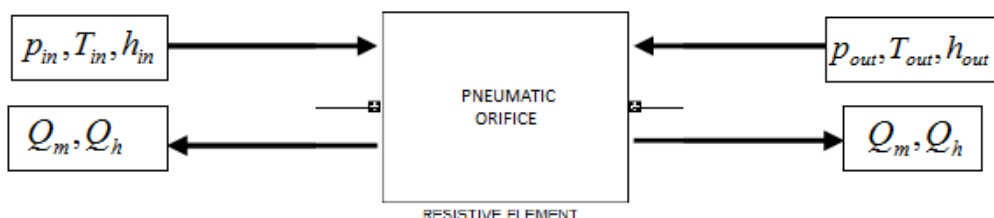


Figure 8. Inputs and outputs of a pneumatic orifice.

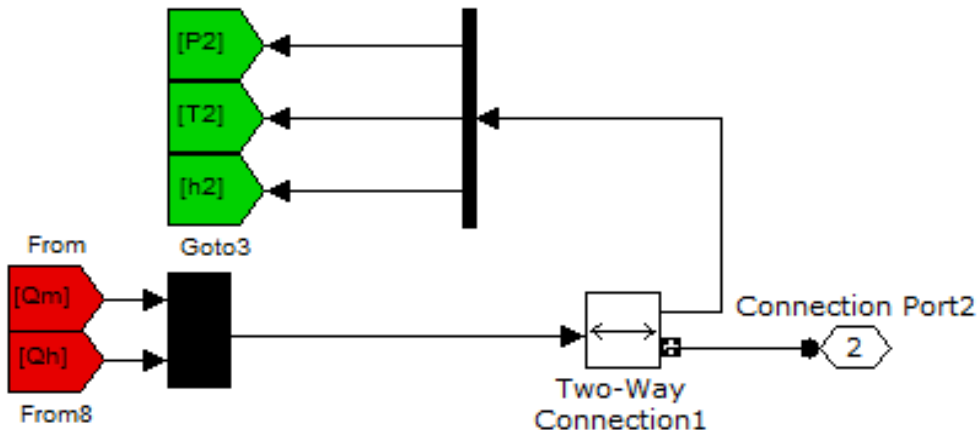


Figure 9. Simulink implementation of the bidirectional exchange of information.

As previously said, and according to Figure 8, this component must guarantee a bidirectional exchange of information through the network topology; therefore, a particular architecture was implemented, whose approach was already used in Simscape libraries of Matlab-Simulink and in other softwares, as LMS Amesim. In Figure 9, the employed simulink blocks are shown; in particular, the block featuring the bidirectional exchange of information is the two way-connection.

Authors realized three different models of pneumatic orifice, explained in the following subsections.

5.1.1. Constant C_q orifice

The constant C_q orifice is defined by a constant area and therefore a constant flow coefficient, whose value can be adjusted accordingly to user's specifics. In Tables 4, 5 and 6 the external variables, internal variables, and user's setting parameters are respectively shown.

Table 4. External variables of a constant C_q orifice

Name	Symbol	S.I. unit
Mass flow rate	Q_m	kg/s
Enthalpy flow rate	Q_h	J/s
Inlet/outlet temperature	T_{in} / T_{out}	K
Inlet/outlet pressure	p_{in} / p_{out}	Pa

Table 5. Internal variables of a constant C_q orifice

Name	Symbol	S.I. unit
Reynolds number	Re	-
Flow parameter	C_m	$s\sqrt{K/m}$
Gas velocity	u	m/s
Friction factor	F	-

Table 6. User's setting parameters of a constant Cq orifice

Name	Symbol	S.I. unit
Pipe diameter	d	m
Pipe length	l	m
Relative roughness	rr	-

The mass flow rate is computed according to equation (29).

$$Q_m = A C_q C_m \frac{P_{in}}{\sqrt{T_{in}}} \quad (29)$$

Where A is the orifice section, C_m is the flow parameter, p_{in} and T_{in} are the inlet pressure and temperature.

The coefficient C_q is in fact used to include the losses due to friction and to the local kinetic energy losses. The C_q can be used, for example, to describe the friction losses in tubes, or in the local resistances due to the geometric changes of the ducts or directional flow.

The critical pressure p_{cr} , associated to the subsonic to sonic flow transition, can be calculated using the following equation (30).

$$p_{cr} = \left(\frac{2}{\gamma + 1} \right)^{\frac{\gamma}{\gamma - 1}} \quad (30)$$

If $p_{out}/p_{in} > p_{cr}$ the flow is subsonic. When $p_{out}/p_{in} \geq p_{cr}$ the flow becomes supersonic.

When the flow is subsonic, the flow parameter C_m is calculated as a function of the pressure ratio p_{out}/p_{in} and depends on the gas properties, γ and R.

When the fluid is sonic, C_m is constant and depends only on the properties of the gas, γ and r.

- If $p_{out}/p_{in} > p_{cr}$, C_m is calculated according to Eq. (31).

$$C_m = \frac{\sqrt{2 * \gamma}}{\sqrt{R * (\gamma - 1)}} \cdot \sqrt{\left(\frac{p_{out}}{p_{in}} \right)^{2/\gamma} - \left(\frac{p_{out}}{p_{in}} \right)^{(\gamma+1)/\gamma}} \quad (31)$$

If $p_{out}/p_{in} \leq p_{cr}$, C_m is calculated according to Eq. (32).

$$C_m = \frac{\sqrt{2\gamma}}{\sqrt{R(\gamma+1)}} \cdot \left(\frac{2}{\gamma+1} \right)^{\frac{1}{\gamma-1}} \quad (32)$$

The enthalpy flow rate is obtained from the product (33).

$$Q_h = Q_m \cdot h \quad (33)$$

5.1.2. Perry Orifice

Since the flow parameters are variable according to the pressures ratio, the flow parameter C_q can be expressed by a polynomial function in P_{out}/P_{in} .

The Perry flow coefficient (in Eq. (34)) can be employed to describe many components; for instance, sharp edge orifices are modelled using Eq. (34), in addition to the others equations presented in subsection 5.1.1.

$$C_q = 0.8414 - 0.1002 \cdot \left(\frac{P_{out}}{P_{in}} \right) + 0.8415 \cdot \left(\frac{P_{out}}{P_{in}} \right)^2 - 3.9 \cdot \left(\frac{P_{out}}{P_{in}} \right)^3 + 4.6001 \cdot \left(\frac{P_{out}}{P_{in}} \right)^4 - 1.6827 \cdot \left(\frac{P_{out}}{P_{in}} \right)^5 \quad (34)$$

5.1.3. ISO 6358 Orifice

When experimental data are available, the static features of a pneumatic orifice, according to ISO-6358 normative, are defined by two parameters: The critical pressure p_{cr} (in Eq. (30)) and the sonic conductance $C[m^3/(s·Pa)]$.

Hence, ISO-6358 normative defines the equations for evaluating the mass flow rate Q_m .

- If $p_{out}/p_{in} > p_{cr}$, Q_m is calculated according to Eq. (35).

$$Q_m = C p_{in} \rho_0 \cdot \sqrt{\frac{T_0}{T_{in}}} \cdot \sqrt{1 - \left(\frac{\left(\frac{P_{out}}{P_{in}} \right) - p_{cr}}{1 - p_{cr}} \right)^2} \quad (35)$$

- If $p_{out}/p_{in} \leq p_{cr}$, Q_m is calculated according to Eq. (36).

$$Q_m = C p_{in} \rho_0 \cdot \sqrt{\frac{T_0}{T_{in}}} \quad (36)$$

ρ_0 is the gas density at reference conditions:

- $T_0 = 293.15$ K;
- $P_0 = 10^5$ PaA;
- 65% of relative humidity.

The velocity of the gas contracted vein cannot be estimated since its density is unknown (many informations are absent, as the evolution of the transition between upstream and contracted vein, the flux equivalent area and the flow coefficient).

5.2. Hydraulic Orifice

The hydraulic orifice is depicted in Figure 10. The hydraulic orifice is a resistive component; consequently, the model inputs are represented by the inlet/outlet pressure,

temperature and enthalpy, while the computed outputs are the mass flow rate and enthalpy flow rate exchanged with the adjacent capacitive components.

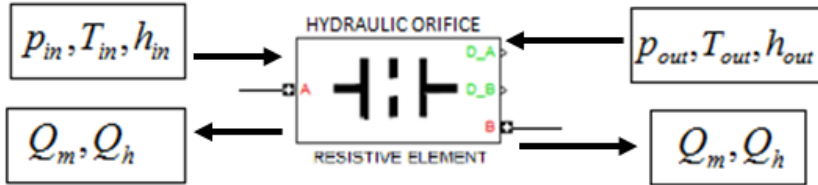


Figure 10. Inputs and outputs of an hydraulic orifice.

Authors implemented the hydraulic orifice model (Borutzky et al., 2002) according to Eq. (37).

$$Q_v = \left(C_{turb} A \sqrt{\frac{2}{\rho} |\Delta p| + \left(\frac{\mu R_t}{2 \rho C_{turb} D_h} \right)^2} - A \frac{\mu R_t}{2 \rho D_h} \right) \quad (37)$$

Where R_t is the critical Reynolds Number, at which the transition from laminar flow to turbulent flow occurs; C_{turb} is the critical discharge coefficient, obtained for large values of the Reynolds Number, since it is known (Merrit, 1967 and Manning, 2005) that the discharge coefficient C_d is a non-linear function of \sqrt{Re} , represented in Figure 11.

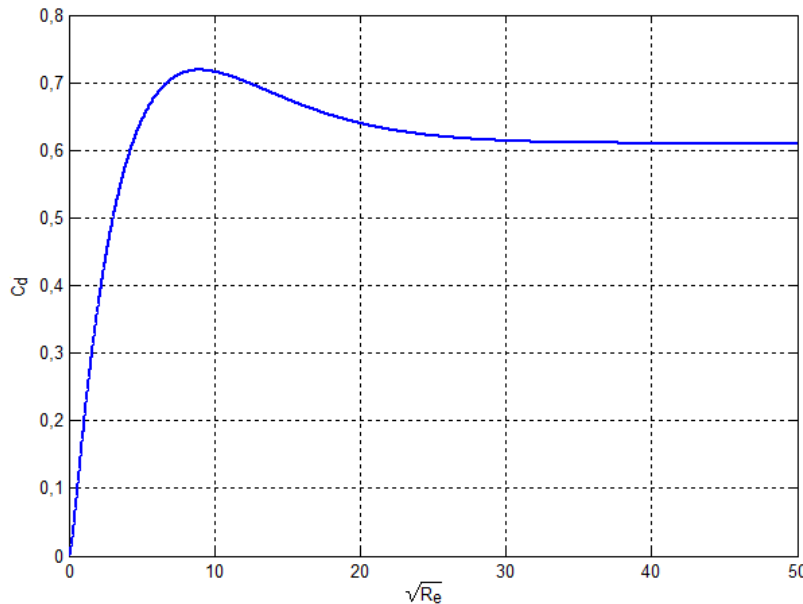


Figure 11. Discharge coefficient versus the square root of the Reynolds number.

The formula (37) has been implemented since improves the overall stability of the simulated component: in facts, many small losses are often neglected, while it may be preferable to over-estimate losses, when using numerical integration.

5.3. Hydraulic Centrifugal Pump

The inputs and outputs of a hydraulic centrifugal pump are depicted in Figure 12. The hydraulic pump is a peculiar resistive component. The model inputs are represented by the inlet/outlet pressure, temperature and enthalpy, while the computed outputs are the mass flow rate and enthalpy flow rate exchanged with the adjacent capacitive components. In addition, since it is driven by an electric motor, the pump model receives the angular speed (rpm) and provides the volumetric flow rate and the resistant torque.

Generally, the hydraulic pump is characterized by two fundamental curves:

- 1) The flow rate-prevalence curve.
- 2) The power-flow rate curve.

The first characteristic curve is employed to compute the volumetric flow rate Q_v . The pump flow rate-prevalence curve is plotted experimentally for points, at constant speed, by plotting in the x-axis the prevalence $\Delta p / (\rho g)$ and in the y-axis the flow rate Q_v in a system of orthogonal Cartesian axes. The prevalence decreases with increasing flow rate (and vice versa). Consequently, when the flow rate is zero, the prevalence reaches the maximum value.

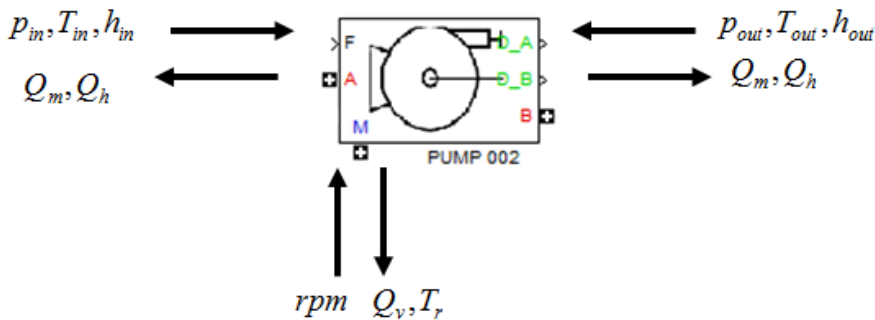


Figure 12. Inputs and outputs of a hydraulic pump.

The second characteristic curve is utilized to calculate the developed power. The power W_h is the product of the flow rate Q_v , by the prevalence and the density of the fluid (Eq. (38)).

$$W_h = Q_v \frac{\Delta p}{\rho g} \cdot \rho = \frac{Q_v \cdot \Delta p}{g} \quad (38)$$

The pump power-flow rate curve is plotted experimentally for points, at constant speed, by plotting in the x-axis the flow rate Q_v and in the y-axis the power W in a system of orthogonal Cartesian axes. Therefore, the power increases as the volumetric flow rate grows.

Authors, in order to eliminate the rotational speed dependence in the proposed model, both curves were rendered dimensionless. Hence, the prevalence dimensionless coefficient ψ is given by the ratio of the prevalence itself and the square of the rotational speed; the flow rate dimensionless coefficient ϕ is given by the ratio of the flow rate and the rotational speed; finally, the power coefficient P_W is calculated through the ratio of the power and the cube of the rotational speed. The dimensionless characteristics are plotted in Figure 13.

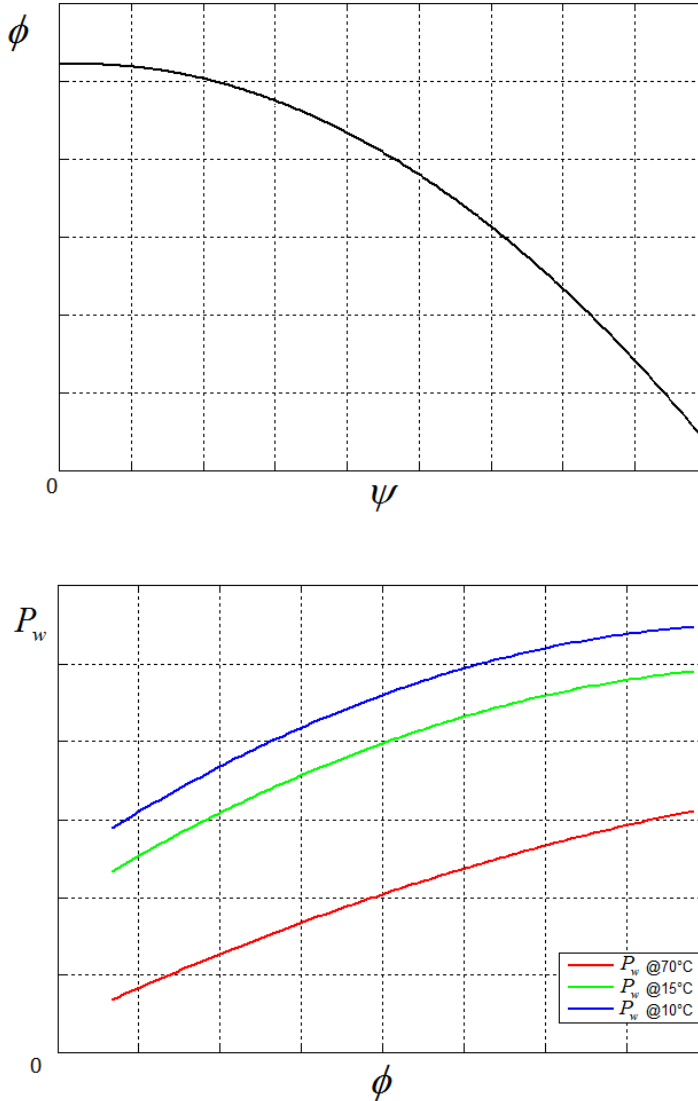


Figure 13. Dimensionless characteristics flow rate-prevalence (ϕ - ψ) and power-flow rate (P_w - ϕ).

The dimensionless characteristic power-flow rate, as shown in Figure 13, also depends from temperature T. Consequently, the inputs of the second curve are both the dimensionless flow rate ϕ and the temperature T.

Even if, in the developed architecture, the resistive components have an isenthalpic behaviour, due to the pump efficiency losses, the outlet enthalpy flow rate must be calculated as visible in Eq. (39).

$$Q_{h,out} = Q_{m,out} \cdot [h_{in} + V(p_{out} - p_{atm})] \quad (39)$$

5.4. Hydraulic Accumulator

This element represents a customizable thermal-hydraulic tank used for oil accumulation and release in generic industrial systems. The inputs and outputs of a hydraulic accumulator are depicted in Figure 14. The hydraulic accumulator is a capacitive component, whose inputs are represented by the mass flow rate and enthalpy flow rate from an adjacent resistive component (inlet/outlet valve), while the computed outputs are the pressure, temperature and enthalpy calculated by the block.

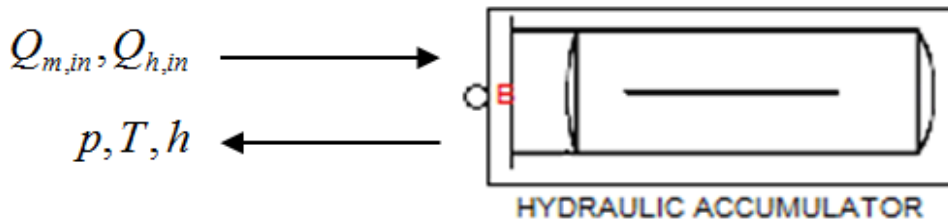


Figure 14. Inputs and outputs of an hydraulic accumulator.

The pressure inside the hydraulic accumulator is computed as the sum of the atmospheric pressure and the pressure due to the oil height inside the accumulator:

$$p = \rho g z + p_{atm} \quad (40)$$

The temperature within the reservoir is obtained by the integral equation (41), in which are considered the contributions of the inlet oil temperature, and a possible heat contribution exchanged with the external environment:

$$T = \int \left[\frac{Q_h + Q - \rho h dV}{\rho V c_p} + \frac{T \left(\frac{\partial v_s}{\partial T} \right)_p \dot{p}}{c_p} \right] dt \quad (41)$$

where $\left(\frac{\partial v_s}{\partial T} \right)_p$ is the derivative of specific volume with respect to the temperature, at constant pressure. Finally, the specific enthalpy is calculated according to the following equation:

$$h = c_p \cdot [T - T_{ref}] \quad (42)$$

6. APPLICATION EXAMPLE: A SIMPLE PLANT

In Figure 15 an example of hydraulic industrial plant is depicted, which represents simplified lube oil consoles typically employed in industrial applications. The system (whose main features are described in Table 7) is characterized by a single centrifugal pump operated by an asynchronous motor. The plant branches out, through a T-junction, in an orifice and in

a vertical accumulator. The accumulator is a customizable thermal-hydraulic tank used for oil accumulation and release in the hydraulic system, whose input stage is represented by a valve that allows the transit of inlet or outlet oil flow. Both the pump and the vertical tank affect the oil flow in the load orifice (e.g., a bearing in lubrication plants).

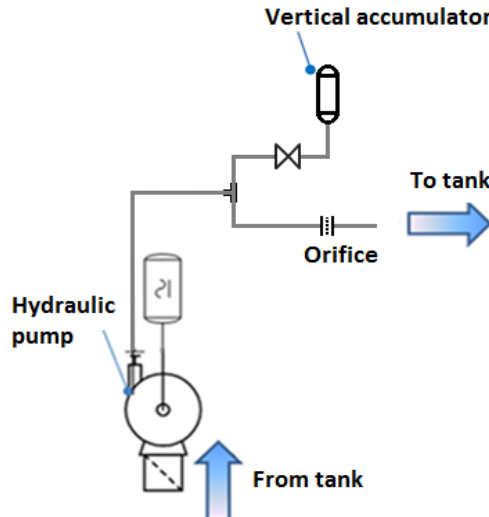


Figure 15. Simple scheme of an hydraulic plant.

Table 7. Components data of the hydraulic plant

Data	Value
Nominal speed [rpm]	3000
Pump inertia [$\text{kg}\cdot\text{m}^2$]	0.129
Motor inertia [$\text{kg}\cdot\text{m}^2$]	1.41
Pump volume [m^3]	0.002262
Initial pressure [bar]	1
Initial temperature [$^\circ\text{C}$]	65
Pipe diameter [m]	0.1
Accumulator maximum height [m]	8.5
Accumulator area [m^2]	1
Orifice diameter [mm]	55.6
Plant fluid	ISO VG 32

In Figure 16 the corresponding simulink scheme is represented, showing the resistive-capacitive behaviour of every single component.

The dynamic simulations of the proposed model have been carried out compiling and uploading the simulink code into the dSPACE board, considering a fixed step solver (*ode14x*) and an integration frequency of 1 kHz. The states present in the simulink model are 9: pressures and temperatures in the three pipes, height and temperature of the vertical accumulator, and the angular speed of the asynchronous motor. In particular, a simulation of 20 seconds is performed, in which the hydraulic pump is switched off at $t=10$ s, as visible in the pressure and rotation speed represented respectively in Figure 17 and Figure 18.

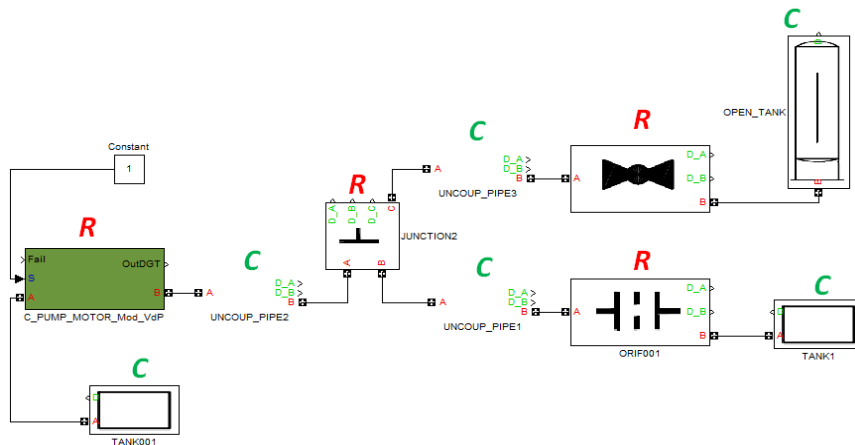


Figure 16. Simulink scheme of the hydraulic plant.

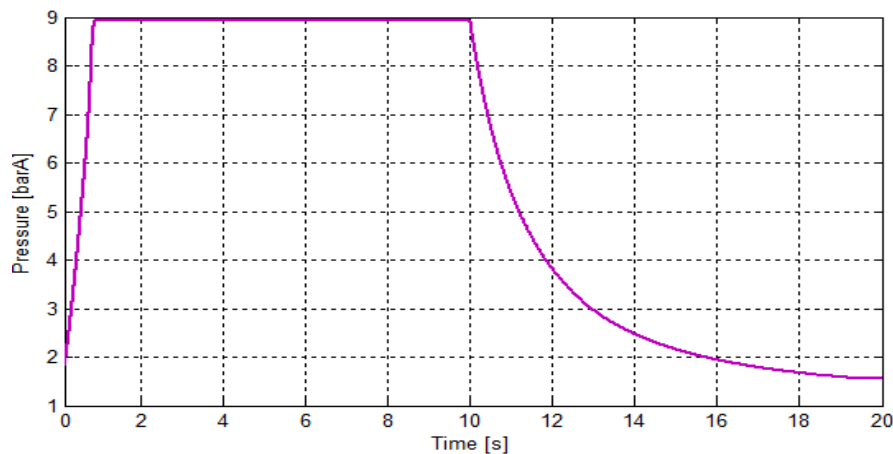


Figure 17. Hydraulic pump pressure.

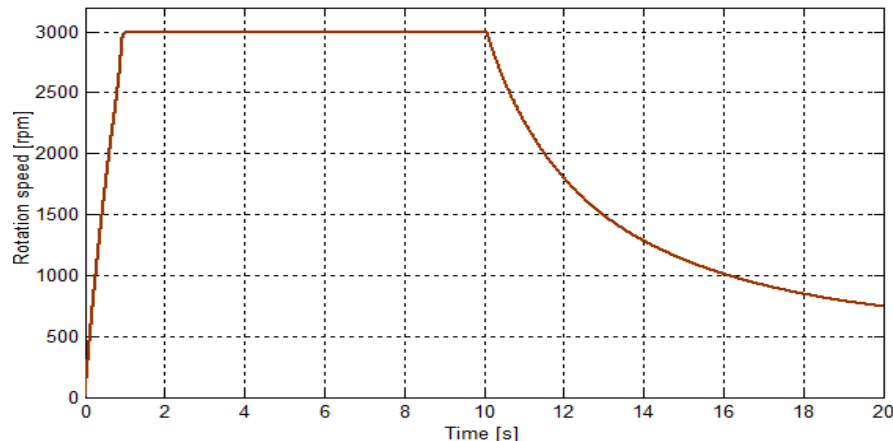


Figure 18. Rotation speed of the hydraulic pump.

The accumulator dynamics is explained in Figure 20 and Figure 21: when the pump is running, a (positive) inlet flow behaviour can be noticed (Figure 20), while the oil height increases (Figure 21). Few seconds after the pump switch off, the pressure of the capacitive element adjacent to the valve drops below the tank pressure; hence, the mass flow rate becomes negative (outlet flow rate) and the oil height in the accumulator decreases. In addition, this plant behavior can be confirmed by the mass flow rate of the load orifice, represented in Figure 19.

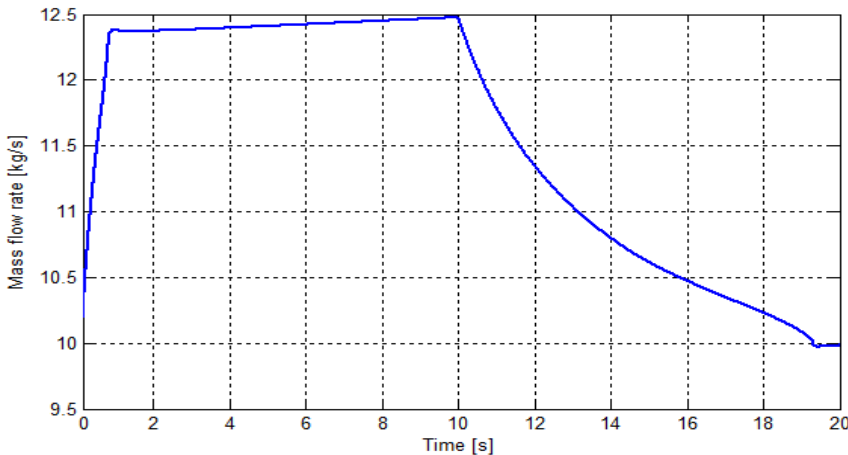


Figure 19. Mass flow rate of the load orifice.

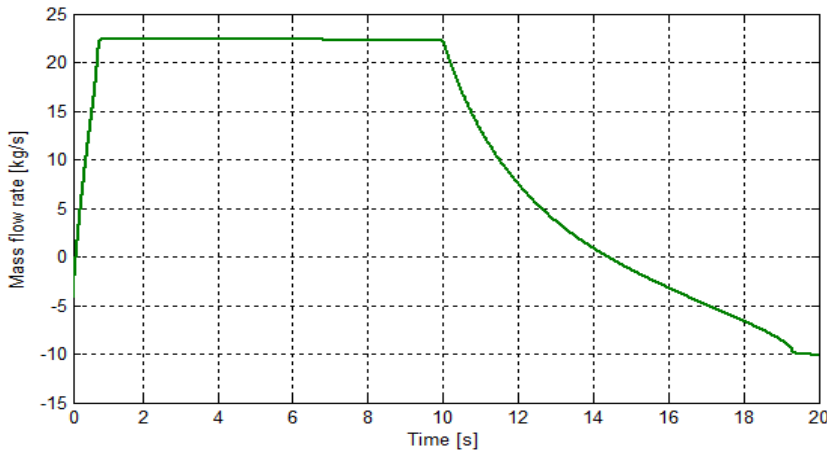


Figure 20. Mass flow rate of the hydraulic accumulator.

The pump temperature behaviour is displayed in Figure 22. Starting from a plant temperature of 65°C , since the pump efficiency is lower than 1, the work losses produce a small increment of the oil temperature. As the pump is switched off, the temperature slowly tends to its initial conditions.

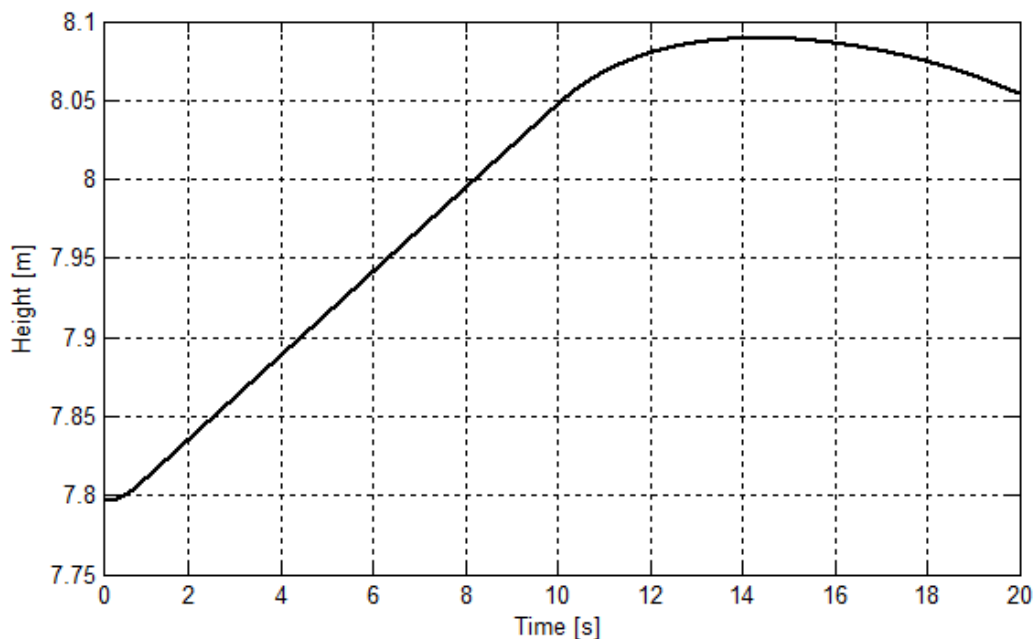


Figure 21. Oil height within the hydraulic accumulator.

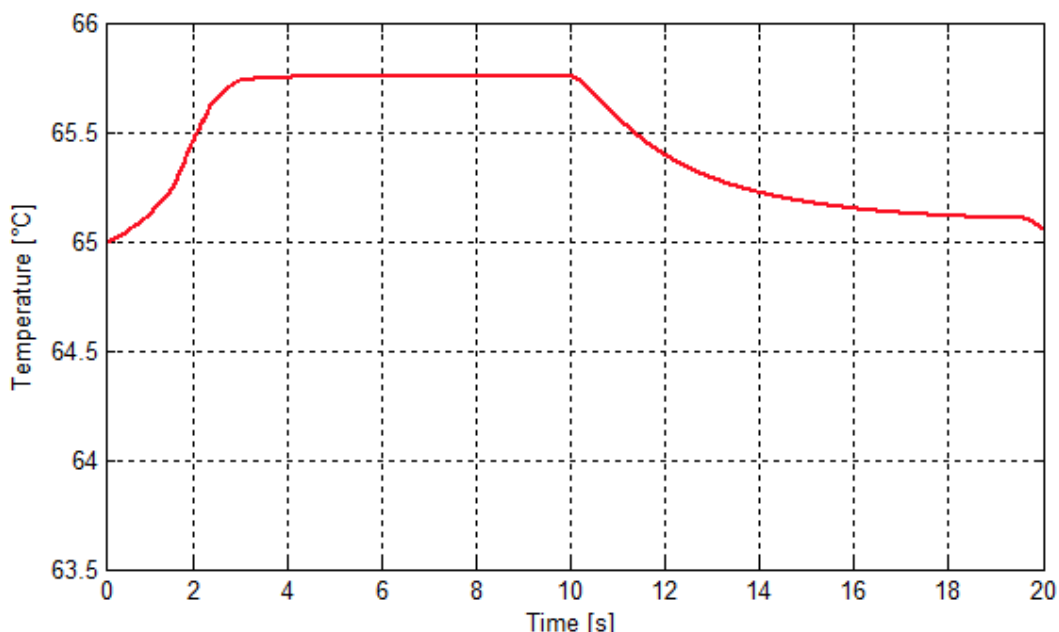


Figure 22. Hydraulic pump temperature.

The same results can be obtained compiling and uploading the simulink code in the Texas Instruments board, considering a discretized model and the matlab solver *discrete (no continuous state)*, instead of *ode14x*.

The computational resources occupied by the two boards are respectively about 50% and 5% for the TMS320F28335 and the MicroAutoBox II. The resulting turnaround time (for a task, is that time which passes between triggering and the end of its execution) is about 50 μ s for the MicroAutobox II, which is quite smaller than the integration time step; while for the TMS320F28335 board, it is about 0.5 ms.

CONCLUSION

In the present chapter some basic notions concerning the modelling, the RT implementation and simulation of fast and efficient lumped thermal-hydraulic and thermal-pneumatic systems is proposed.

The general concepts for the modelling of lumped parameters components are introduced, in particular the information exchange and the blocks coupling strategies are pointed out. Resistive and capacitive elements are treated in detail, focusing on the distributed and lumped losses modelling.

Moreover, an efficient formulation of the main physical properties for the thermal-hydraulic and thermal-pneumatic components is introduced. Such formulation has been necessary for the Real Time implementation of the developed models on commercial electronic control units whose computational resources are limited.

Some modelling application examples are introduced: pneumatic orifice, hydraulic orifice, hydraulic pump and hydraulic accumulator. These components, commonly used in many industrial fields, are implemented in Matlab-Simulink, and the examples have been properly chosen to highlight the various modelling strategies applicable for both the resistive or capacitive elements.

Finally, according to the modelling philosophy shown by the authors (R-C discretization), a simple hydraulic plant model, consisting of 9 states, has been realized and the simulation results obtained by the implementation in the Real Time platform MicroAutobox II have been presented. The results show a physically coherent behaviour; in addition, high readiness and robustness with respect to variations in the plant conditions can be noticed. The simulations are carried out considering a fixed step solver (*ode14x*) and an integration frequency of 1kHz, with a turnaround time of about 50 μ s.

ACKNOWLEDGMENTS

The Authors wish to thank the people of the Industrial Engineering Department of University of Florence and the industrial partners that have cooperated to this research activity.

ABOUT THE AUTHORS



Emanuele Galardi has his Master Degree in Electrical and Automation Engineering and is a Ph.D. researcher at the Dept. of Industrial Engineering, University of Florence. His current research interests are Control, Vehicle Dynamics and Mechatronics (including Electric, Fluidic and Mechanic Systems).



Daniele Nocciolini has his Master Degree in Mechanical Engineering and is a Ph. D Researcher at the Dept. of Industrial Engineering, University of Florence. His current research interests include Vehicle Dynamics and Mechatronics, including Mechanic and Fluidic Systems.



Luca Pugi received the degree in Mechanical Engineering in 1999 from the University of Florence, Florence, Italy, and the Doctorate degree in applied mechanics in 2003 from the

University of Bologna, Bologna, Italy. He currently works at the department of industrial engineering, University of Florence, Florence, Italy, where he is involved in design and simulation of mechatronic systems, mainly for vehicle applications collaborating with relevant industrial partners such as General Electric, Trenitalia SPA, Ansaldo Breda, Ansaldo Signal, Pramac SPA, ECM SPA, Velan ABV, Italcertifer SPA, etc. He also perform didactical activities concerning mechatronics and modelling of dynamical systems and electric traction systems. He is the author or co-author of about 170 publications. He is the winner of several international awards: In 2000, the “Cesare Bianchi” award from the Italian Association of Railway Engineers (CIFI), Rome, Italy. In 2009, he was awarded by CIFI with the Mallegori Award. In 2011 at WCRR (World Congress of Railway Research), he was awarded with a premium for the section “increasing freight capacities and services”.

REFERENCES

- Borutzky, W., Barnard, B. and Thoma, J. 2002. *An orifice flow model for laminar and turbulent conditions*. Simulation Modelling Practice and Theory 10 141–152.
- Bouamama, B. O. 2003. *Bondgraph approach as analysis tool in thermofluid model library conception*. Journal of the Franklin Institute, Volume 340, Issue 1, Pages 1–23.
- Conti, R., Lo Presti, G., Pugi, L., Quartieri, E., Rindi, A. and Rossin, S. A preliminary study of thermal hydraulic models for virtual hazard and operability analysis and model-based design of rotating machine packages, Proc IMechE Part E: J Process Mechanical Engineering 0(0) 1–17 DOI: 10.1177/0954408913499910 uk.sagepub.com/jpme
dSpace website: <http://www.dspace.com/de/gmb/home.cfm>
- Hughes, W.F. and Brighton, J.A. 1982. *Fluidodinamica*. Schaum ETAS libri. Milano.
- Karnopp, D.C. and Rosenberg, R.C. 1975. *System dynamics, a unified approach*. J. Wiley, New York, NY.
- Kulakowski, B. T., Gardner, J. F. and Shearer, J. L. 2007. *Dynamic Modelling and Control of Engineering Systems*. 3rd Edition, 2007 Cambridge University Press ISBN 9780521864350.
LMS Amesim Technical Documentation (on line help version 4.1 or later).
LMS website: <http://www.lmsintl.com/>
- Manring, N. D. 2005. *Hydraulic Control Systems*. Jonh Wiley & Sons Inc. New York ISBN 0471693111.
- Mathworks website:* <https://www.mathworks.it/>
- Merrit, H. E. 1967. *Hydraulic Control Systems*. Jonh Wiley & Sons Inc. New York ISBN 0471596175.
- Munson, B.R., Young, D.F. and Okiishi, T.H. 1998. *Fundamentals of Fluid Mechanics*, John Wiley and Sons, Inc.
- Pugi, L., Malvezzi, M., Tarasconi, A., Palazzolo, A., Coccia, G. and Violani, M. *Simulation of WSP Systems on MI-6 Test rig*. Vehicle system and dynamics (ed.Taylor and Francis) Vol. 44, Supplement 2006 pp.843-852 ISBN 978-0-415-43616-8
- Shampine, L. F. 1994. *Numerical Solution of Ordinary Differential Equations*, Chapman & Hall.
- Texas Instruments official site* with tec. Doc. <http://www.ti.com/product/tms320f28335>

Wagner W. et al. 2000. *The IAPWS Industrial Formulation 1997 for the Thermodynamic Properties of Water and Steam*, ASME J. Eng. Gas Turbines and Power, 122, 150-182,
<http://www.iapws.org/>

White, F.M. 1999. *Fluid Mechanics*, McGraw- Hill.

Yu, L. and Qi, X. 2012. *Bond-Graph Modelling in System Engineering*, International Conference on Systems and Informatics.

Chapter 4

THE LOW COST DESIGN OF A 3D PRINTED MULTI-FINGERED MYOELECTRIC PROSTHETIC HAND

***Drew van der Riet^{*1}, Riaan Stopforth^{#2}, Glen Bright^{#3}
and Olaf Diegel^{§4}***

¹Mechatronics and Robotics Research Group (MR²G)

Bio-Engineering Unit, School of Engineering,
Howard College Campus,

University of Kwa-Zulu Natal, Durban, South Africa

²Mechatronics and Robotics Research Group (MR²G)

Bio-Engineering Unit, School of Engineering,
Howard College Campus, University of Kwa-Zulu Natal,

Durban, South Africa

³Mechatronics and Robotics Research Group (MR²G),

School of Engineering, Howard College Campus,
University of Kwa-Zulu Natal, Durban, South Africa

⁴Massey University, School of Engineering and Advanced Technology,

Palmerston North, New Zealand

ABSTRACT

The design and manufacture of a low cost, modular prosthetic hand is discussed in detail in this chapter. A fully actuated hand was developed with individually actuated fingers. A wrist was designed and manufactured to allow for a single degree of freedom, which allows for the rotation of 180 degrees. An experimental upper arm was developed using a pair of air muscles mimicking the bicep and triceps. The hand was tested in terms

^{*} E-mail address: 213569879@stu.ukzn.ac.za.

[#] E-mail address: stopforth@ukzn.ac.za; phone: +27 31 260 1063.

[‡] E-mail address: brightg@ukzn.ac.za; phone: +27 31 260 1275.

[§] E-mail address: o.diegel@massey.ac.nz

of gripping strength and grip adaptability to differently shaped objects. The performance of the hand was compared to that of a human hand. The prosthetic hand was shown to meet the target grip strength of 250 g in a cylindrical grip. It was also capable of adapting its grip to a variety of differently shaped objects and showed a close comparison to the movement and speed of a human hand. The prosthetic hand was built using low cost materials and manufacturing techniques allowing the full cost of manufacturing to be under US\$1'000 for one hand and the full weight (including prosthetic socket and electronics) is 1.6 kg.

1. INTRODUCTION

Contemporary upper limb prosthetics bring a lot of benefits to the amputee community. However, there are still a number of challenges facing the field of upper limb prosthetics. These challenges include high cost and low functionality. A normal human hand has three basic functions: gripping objects, manipulating them and exploring the surrounding environment (Carrozza et al., 2003).

The loss of a limb has a significant impact on the productivity and ability of an individual including stress placed on the psychological strength of a person. In spite of several research efforts aimed at innovating artificial hands technology, surveys on user satisfaction showed 30-50% of the upper arm extremities amputees do not use their prosthetic arm regularly (Massa et al., 2002). The reasons for this lack of use are:

- Low aesthetic appeal
- The low degrees of freedom
- Extremely high cost
- Low comfort

More complex control schemes were needed hence the development and implementation of myoelectric systems, which provides more direct control of the prosthesis. A synergy between control algorithms and mechanical elements was to be achieved. It is the aim of chapter to contribute research and innovation into aesthetic appeal and dexterity whilst maintaining an affordable cost for the general public. A fully operational and effective prosthetic hand must allow for voluntary action and must provide the user with some measure of sensory feedback. The two basic components required in a complete system are; the dexterous and sensorized mechatronic hand and a user-prosthetic interface (UPI), (Cipriani et al., 2009).

One of the major drawbacks in the use of these state-of-the-art prosthetic hands is the high cost involved. State-of-the-art prosthetics start from US\$ 35'000 (van der Riet et al., 2013) just for the hand. Many people are looking for cheaper alternatives to these prostheses. An example of this is the Robohand (Van As, Owen, 2013), a purely mechanical 3-Dimensionally (3D) printed prosthetic hand that works on a cable/leverage actuated system. It was released in 2013 and costs around US\$ 150. This device is very simple and has only one grip position (the tripod grip) in comparison to the multi-grip state-of-the-art commercial prosthetic hands. Despite this, the Robohand has received a large amount of popularity due to its cheap design.

The research in this chapter looks into low cost solutions to provide a modular prosthetic hand that will be suitable for both transradial and transhumeral amputees. The design of a modular approach to prosthetics allows for mass production of the separate modules, reducing the overall cost of the prosthesis. The hand is to be controlled through electromyography (EMG) which has had the most success in upper prosthetic control (Matrone et al., 2012).

The prototype to be constructed will be based on parameters taken from the client, a man who has lost both his arms when struck by lightning. A functional prosthetic arm is manufactured for the mentioned client who then assisted in the testing of the prosthetic arm.

1.1. Objectives

The purpose of this research was to design and build of myo-electrically controlled prosthetic hand that is capable of using an adaptive grip to grasp different shaped objects. The hand needs to have individually actuated fingers and wrist capable of rotation. It should mimic the natural motion and grip of a human hand.

The hand, including all electronics, must be within the size and weight of an adult male's hand.

An adult male average of 400 g (Cipriani et al., 2011). Grip strength is favoured over grip speed in the prosthetic hand. It has been found however, that the grip strength of commercial prosthetic hands is much lower than that of an able-bodied individual (van der Niet et al., 2010). The hand should be capable of lifting at least 250 g in a cylindrical grip (to perform such actions like drinking out of a glass).

Prosthetic hands are used by amputees that are amputated anywhere from the wrist all the way up to the shoulder.

In order to cater for these varying degrees of amputation the hand needs to be designed in a modular way allowing for easy connection to the prosthetic socket of a transradial amputee or to the prosthetic arm used by a transhumeral amputee. It is important to keep the cost of the prosthetic hand as low as possible through the use of low cost manufacturing techniques and the use of low cost materials.

2. MECHANICAL DESIGN

The mechanical design process will be discussed in detail in this section. The mechanical design objectives for the prosthesis were low cost, modularity for both transradial and transhumeral (through the connection to a prosthetic arm) use, individually actuated fingers with adaptive grasping and simplicity in design, manufacturing and use. The success of these design objectives will be outlined in the course of this chapter.

2.1. Design

The final mechanical design of the prosthetic arm was decided on based on several concepts. There has been several multi-grasp prosthetic hands developed in recent years

(Dalley et al., 2010). These hands range between one and six actuators working independently which control a varying number of fingers from just the index and thumb in a “claw” style to each finger individually. The hand contains six motor and worm gear pairs for the fingers (1 DOF each) and thumb (2 DOF). The wrist (1 DOF) houses the servo motor for wrist rotation and has a connection that can be attached to the socket of transradial amputees. A hypothetical prosthetic arm was designed and used to demonstrate the full range of motion of the prosthetic arm. The telescopic forearm is adjustable to allow for different arm lengths. The elbow (1 DOF) is actuated by the air muscles located around the transhumeral socket connection and coupled with a pulley rigidly connected to the elbow joint. Close ups of the hand and wrist are shown in Figure 1 and Figure 2.

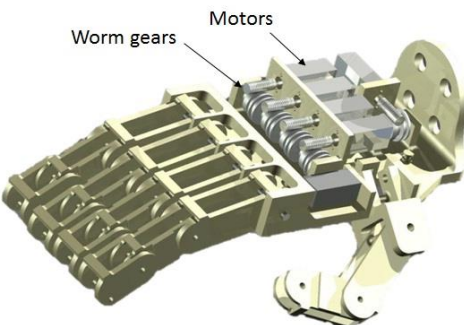


Figure 1. Final design of the hand.

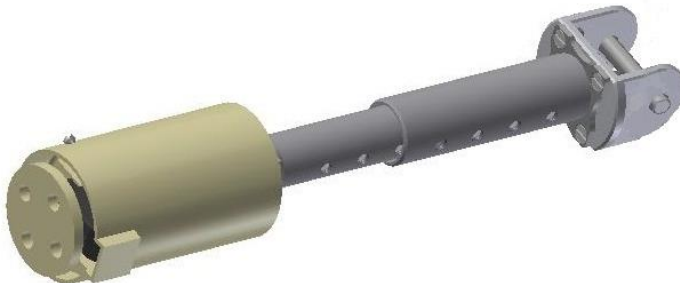


Figure 2. Final design of the wrist and conceptual forearm for transhumeral applications.

Figure 3 shows the final design of the prosthetic hand and wrist connected with the prosthetic socket which is to be manufactured and tested. Figure 4 shows the conceptual design for the elbow actuation and upper limb.

The mechanical design will contribute an inexpensive modular upper limb prosthetic arm. The hand and wrist are 3D printed with acrylonitrile butadiene styrene (ABS) plastic allowing a quick and inexpensive manufacturing process.

As the name states, this material comprises of 50% styrene and the balance is divided between butadiene and acrylonitrile (Celanese, 2013). It can be processed by any of the standard thermoplastic processing methods. Its disadvantage, that could be more fatal to prosthetic use, is that it is flammable in the range of 110 °C to 125 °C with high smoke generation (Rutkowski, Levin, 1986).

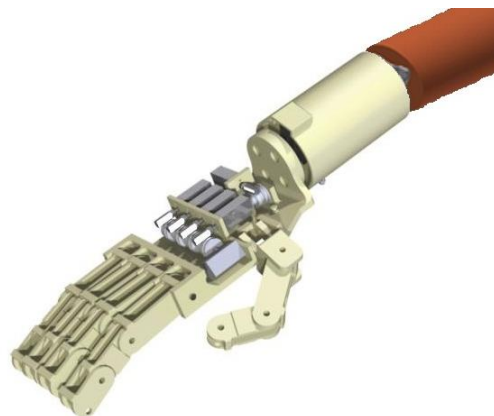


Figure 3. Final design of the transradial prosthetic hand.

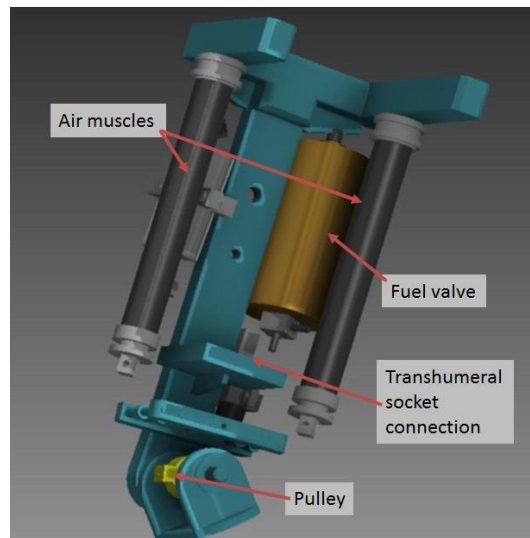


Figure 4. Conceptual design of the upper limb actuation.

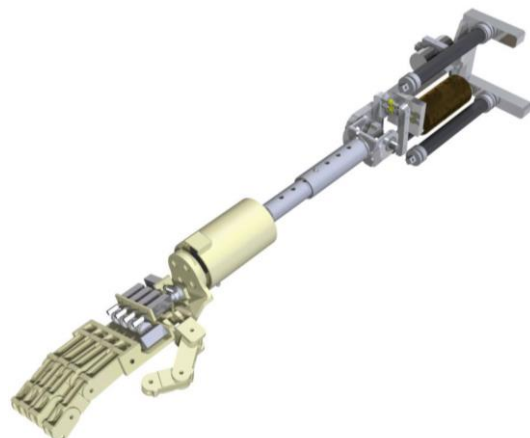


Figure 5. Conceptual final design of transhumeral prosthetic arm.

The prosthetic wearer must be alert of open flames as the material may catch on fire. It is thus recommended that ABS plastic is not used for commercial use. The full conceptual transhumeral arm design is shown in Figure 5.

2.2. Stress Analysis

Finite Element Analysis (FEA) was used to perform stress analysis on the prosthetic hand and arm to test the design for possible weak spots. The deflection analysis was not performed as small deflections in the hand and arm will not affect the performance of the prosthesis in any way. The simulation was run assuming the hand was using a power/column grip to lift a 3 kg weight. As can be seen in Figure 6, the hand experiences a maximum stress of 35.98 MPa at the hinge connection with the wrist. This stress is within the yield stress of ABS plastic which is 42.5 MPa.

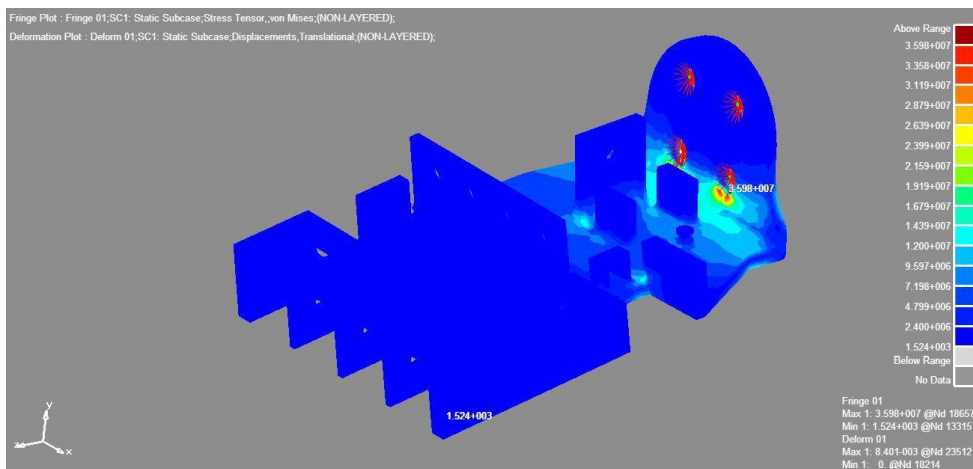


Figure 6. Stress analysis of hand.

2.3. Kinematic Models

The range of motion of the prosthetic arm can be described through kinematics. This section covers the kinematic equations used to plot the range of motion graphs. The Denavit–Hartenberg (D-H) convention is used to generate the kinematic equations. The base equation is shown in equation 1, describing motion from joint 0 to joint 1.

$$A_{01} = \begin{bmatrix} c_\theta & -s_\theta c_\alpha & s_\theta s_\alpha & ac_\theta \\ s_\theta & c_\theta c_\alpha & -c_\theta s_\alpha & as_\theta \\ 0 & s_\alpha & c_\alpha & d \\ 0 & 0 & 0 & 1 \end{bmatrix} \quad (1)$$

The arm can be divided into two parts in order to analyse its range of motion as shown in Figure 7. The hand is the effective end effector of the prosthetic arm. However, beyond merely gripping objects, the prosthetic hand is designed to mimic the natural motion of the

human hand. The hand has been given six DOF (four fingers and two DOF in the thumb). Each digit on the hand can be treated as a robotic arm in order to apply kinematic modelling to predict the fingers' range of motion. The prosthetic arm is considered as a standard robotic arm with two DOF, with the hand as a standard end effector to predict the full range of motion of the prosthetic arm.

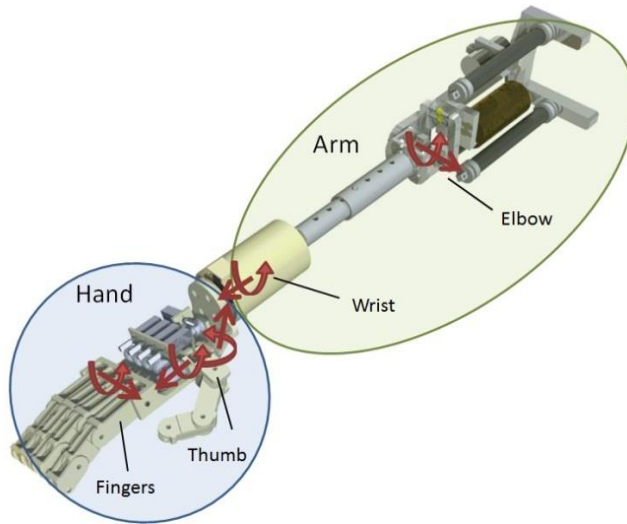


Figure 7. Overview of the final design prosthetic arm system.

2.3.1. Hand

Each finger is identical in the hand, and so only one equation is necessary to describe all of them. All three joints in the finger are in the same frame of reference and are all actuated by the same motor. All the fingers are parallel to one another, allowing them to move freely without risk of collision. The thumb is slightly different as it has two motors actuating it. The first controls the rotation of the thumb between the opposed and non-opposed positions. The second closes the thumbs two additional joints in the same way as the fingers. The hand is simplified to joints and links as seen in Figure 8.

The kinematic models derived from the hand for the finger are shown in equation 2, equation 3 and equation 4. Using these D-H equations, a plot of the range of motion of the finger is given in Figure 9, which includes the 120 mm long hand.

$$A_{01} = \begin{bmatrix} c_1 & -s_1 & 0 & a_1 c_1 \\ s_1 & c_1 & 0 & a_1 s_1 \\ 0 & 0 & 1 & 0 \\ 0 & 0 & 0 & 1 \end{bmatrix} \quad (2)$$

$$A_{12} = \begin{bmatrix} c_2 & -s_2 & 0 & a_2 c_2 \\ s_2 & c_2 & 0 & a_2 s_2 \\ 0 & 0 & 1 & 0 \\ 0 & 0 & 0 & 1 \end{bmatrix} \quad (3)$$

$$A_{23} = \begin{bmatrix} c_3 & -s_3 & 0 & a_3 c_3 \\ s_3 & c_3 & 0 & a_3 s_3 \\ 0 & 0 & 1 & 0 \\ 0 & 0 & 0 & 1 \end{bmatrix} \quad (4)$$

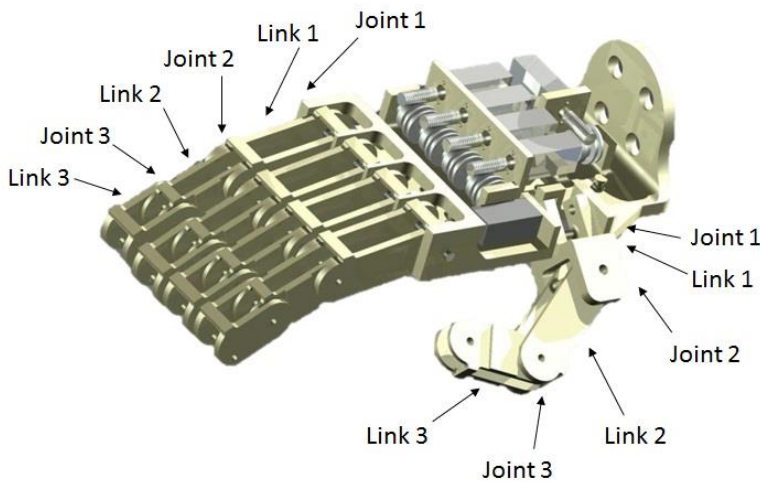


Figure 8. Joint and link diagram of the hand.

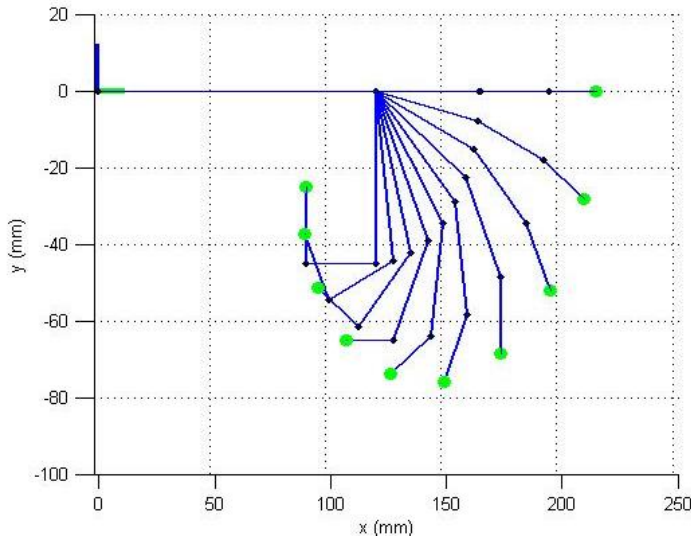


Figure 9. Kinematic model of the finger.

The kinematic models derived from the hand for the thumb are shown in equation 5, equation 6 and equation 7. Using these D-H equations, a plot of the range of motion of the thumb is given in Figure 10. In Figure 11, all the fingers and thumb are then combined for a full plot of the hand.

$$A_{01} = \begin{bmatrix} c_1 & 0 & -s_1 & a_1 c_1 \\ s_1 & 0 & c_1 & a_1 s_1 \\ 0 & -1 & 0 & 0 \\ 0 & 0 & 0 & 1 \end{bmatrix} \quad (5)$$

$$A_{12} = \begin{bmatrix} c_2 & -s_2 & 0 & a_2 c_2 \\ s_2 & c_2 & 0 & a_2 s_2 \\ 0 & 0 & 1 & 0 \\ 0 & 0 & 0 & 1 \end{bmatrix} \quad (6)$$

$$A_{23} = \begin{bmatrix} c_3 & -s_3 & 0 & a_3 c_3 \\ s_3 & c_3 & 0 & a_3 s_3 \\ 0 & 0 & 1 & 0 \\ 0 & 0 & 0 & 1 \end{bmatrix} \quad (7)$$

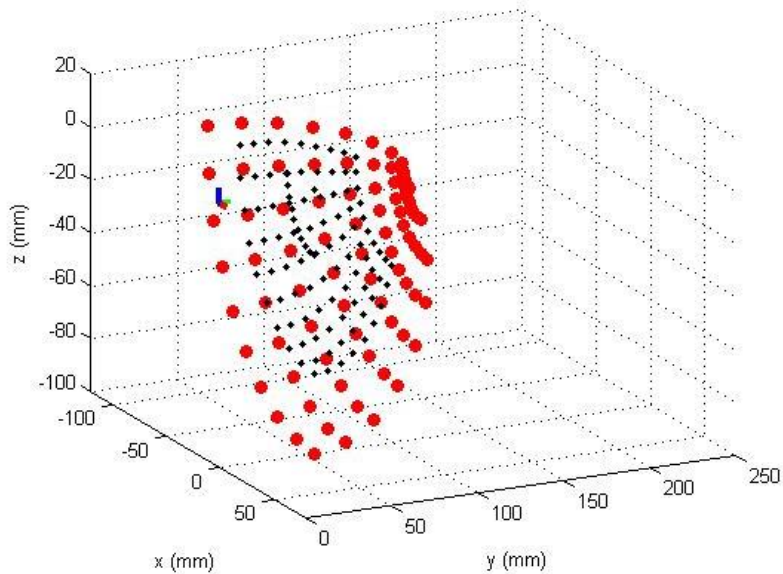


Figure 10. Kinematic model of the thumb.

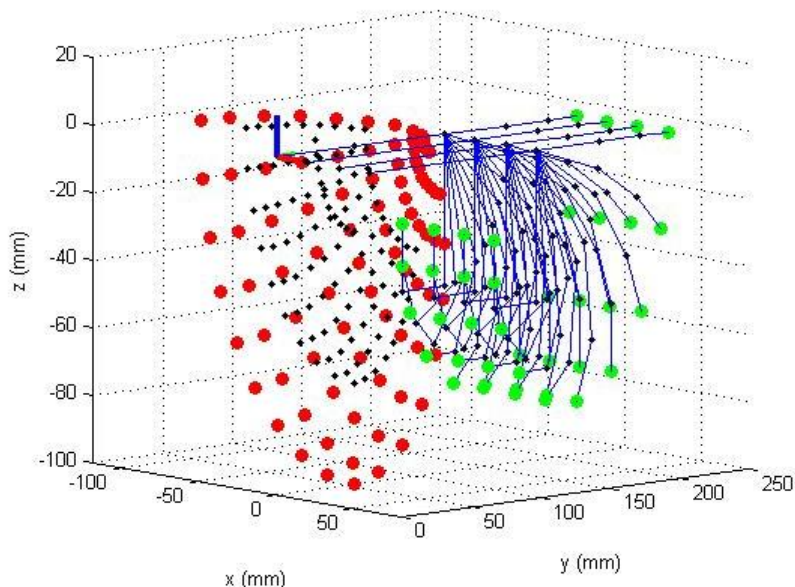


Figure 11. Kinematic model of the hand.

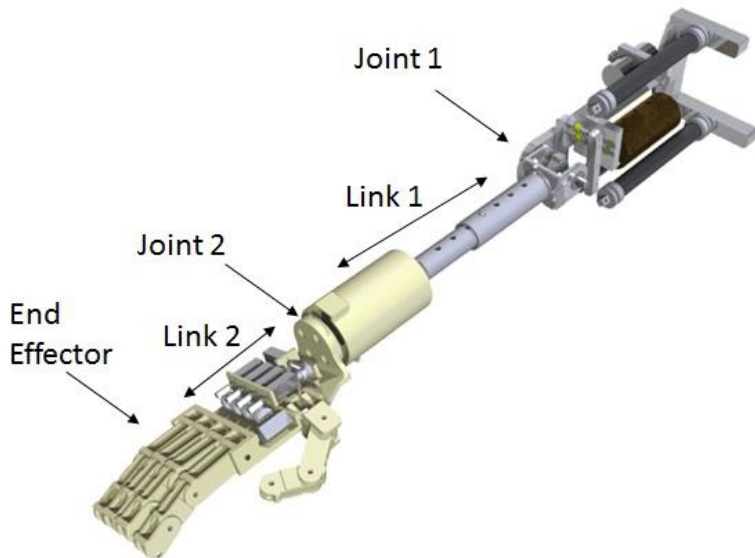


Figure 12. Joint and link diagram of the arm.

2.3.2. Arm

The full prosthetic arm with the transhumeral socket connection is then considered as the robot arm. The arm uses two air muscles to flex and extend the elbow. A servo motor capable of 180 degrees of rotation is used to rotate the wrist. The prosthetic arm is simplified into joints and links as shown in Figure 12.

The kinematic models derived from the arm are shown in equation 8 and equation 9. Using these D-H equations, a plot of the range of motion of the arm is given in Figure 13.

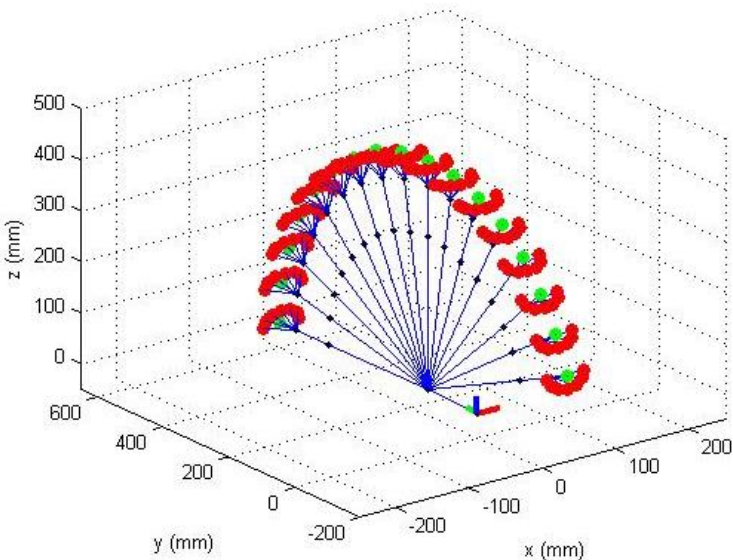


Figure 13. Kinematic model of the arm.

The outer dots located on the end effector in Figure 13 represent the thumb as it rotates around the index finger (inner dot).

$$A_{01} = \begin{bmatrix} c_1 & 0 & -s_1 & a_1 c_1 \\ s_1 & 0 & c_1 & a_1 s_1 \\ 0 & -1 & 0 & 0 \\ 0 & 0 & 0 & 1 \end{bmatrix} \quad (8)$$

$$A_{12} = \begin{bmatrix} c_2 & -s_2 & 0 & 0 \\ s_2 & c_2 & 0 & 0 \\ 0 & 0 & 1 & d_2 \\ 0 & 0 & 0 & 1 \end{bmatrix} \quad (9)$$

3. MANUFACTURING

The manufacturing process and the final prosthetic hand and arm prototype will be shown in this section and its strengths and weaknesses will be discussed. Current commercial prosthetic hands involve sophisticated and expensive actuators, electronics and materials. It has been shown that a functional grasping end effector can be achieved using suitable materials, off-the-shelf electronic components and open-source coding architecture. The advent of advanced 3D printing as a manufacturing medium allowed for complex design features whilst accommodating the short time frame in which to manufacture and assemble the complete hand. The design of the hand incorporates only the basic degrees of freedom that enable functional operation and grasping abilities whilst allowing ease of control for the amputee.

3.1. Hand Manufacturing Process

A final design concept was chosen after reviewing various concept designs. The conceptual components chosen are compared with their respective manufactured versions. After comparisons are made, the various amendments that either improved performance, functionality or made assembly simpler are stated.

Many challenges were encountered during the design and manufacture processes, this section will explain the solutions posed and illustrate the processes in which these solutions were formulated. Figure 14 shows an overview of the overall process from concept to final prototype. Only the right hand prosthetic arm was designed and manufactured. A left hand prosthesis would simply be the mirror image of the right hand prosthesis.

3.2. The Working Area

The hand design had to meet certain core specifications. In implementing the final concept into a working prototype, a ‘work-area’ needed to be established. This working area is the space available in which an anthropomorphic and functional end effector can be

implemented. The working area (illustrated by the white box shown in Figure 15) is a function of the level of amputation. As the client is double amputated, it is not clear exactly how long the prosthesis should be, as he has no human arm length to compare it too.

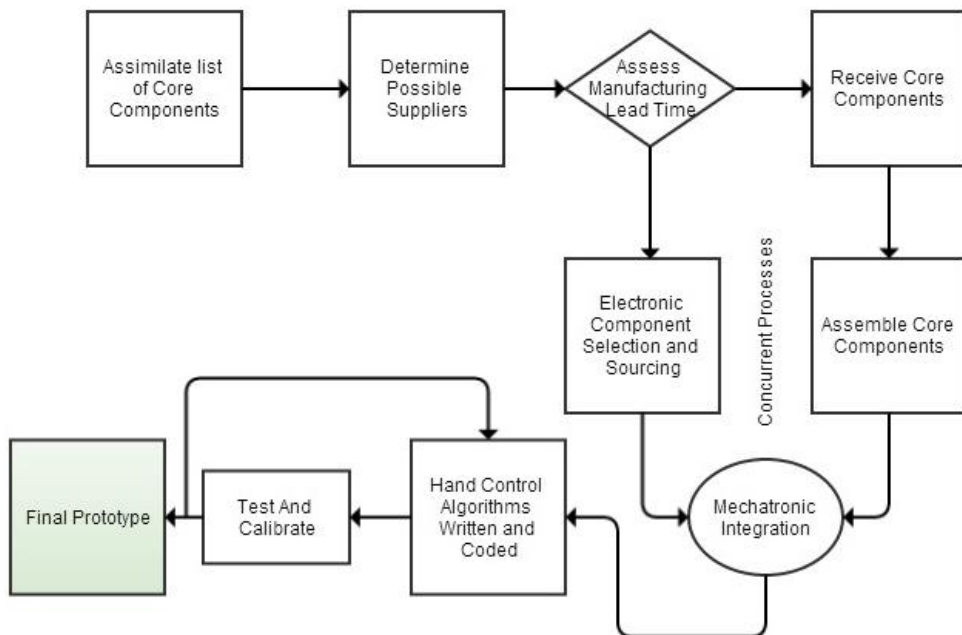


Figure 14. Prosthetic hand development process overview.



Figure 15. Working area illustrated by white box.

The working area must start at the point of amputation and terminate at the point where a human arm of typical length would end. This gives a good idea of the dimension and size of components needed. A length of 350 mm was agreed upon as the desired length of the prosthesis. This working area indicated that all actuators and electronic components were to be housed inside the hand itself. The small work area posed many practical challenges ranging from sourcing inexpensive components of the required dimension to assembling the hand itself. The final concept chosen was one that met these specifications within an allowable tolerance at a length of 410 mm, 17 % longer than desired. This compromise was acceptable as this design is only a proof-of-concept prototype. Future streamlining of the electrical and mechanical components would result in a smaller hand design.

3.3. Manufacture of Fingers and Thumb

This section presents the construction processes undertaken to take the hand from concept to prototype. It also highlights the challenges in constructing the mechanical components, assembly and how these challenges were overcome. The finger is divided into three segments (phalanges). Each of the four fingers are identical which results in simpler manufacturing and assembly. A computer simulated kinematic analysis was carried out to attain dimensions that matched the motion of the human finger as close as possible.

All core structural components were 3D printed at the Massey University. Three dimensional printing allowed for an accelerated manufacturing process without limitations being imposed on the complexity of the design. The three printed phalanges along with their respective 3D printed versions are shown in Figure 16.

It can be seen that the CAD model of each component was accurately realized by the 3D printer. Holes for joint pins were added as features to be printed. The accuracy of the printing process seemed to be a disadvantage when it came to inserting pins into the holes. The stainless steel pins were 3 mm in diameter. The dimensional accuracy of the pins were at a lower degree than that of the printed holes thus causing inconsistencies in the fit.

A solution to this was to enlarge the diameter by drilling through the pre-existing holes with a 3.1 mm drill bit. A fine fit was achieved allowing for minimal friction between the mating surfaces.

Assembly of the fingers began by sliding the ends of the distal and proximal phalanges onto the corresponding ends of the middle phalanx. The middle phalanx acts as the core pivot frame for the entire finger. The stainless steel pins are inserted into each phalanx, creating revolute joints between each segment of the finger. Figure 17 shows a complete assembled finger. Each of the four assemble fingers are identical.

The thumb consists of the middle and proximal phalange only. This simplification made manufacture of all the fingers simple and time effective. The fingers are actuated using a cable which would only actuate flexion of the fingers. It was decided that an elastic element would be utilized to actuate the extension of the fingers. Elastic rubber strips, shown in Figure 18, were attached across the top of the fingers to produce the necessary joint torque for extension.

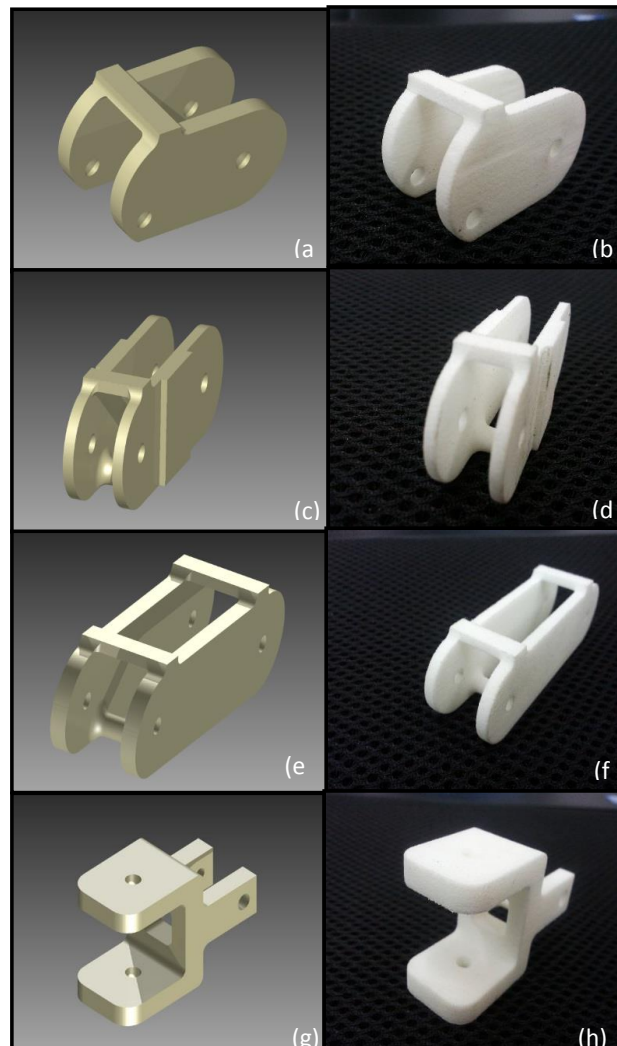


Figure 16. (a) CAD render of distal (b) 3D printed distal (c) CAD render of middle (d) 3D printed middle (e) CAD render of proximal (f) 3D printed proximal (g) CAD render of thumb base (h) 3D printed thumb base.

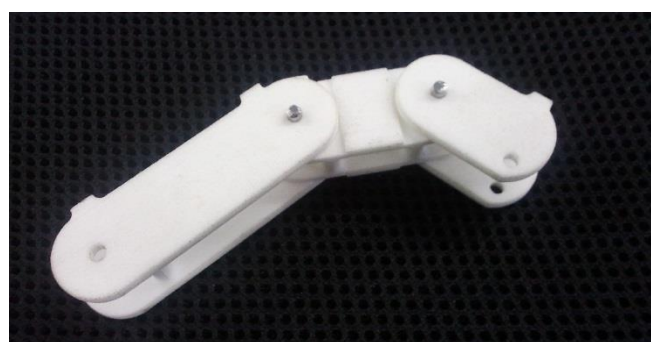


Figure 17. Assembled finger.



Figure 18. Elastic rubber strips used for extension of the fingers.

3.4. Finger and Palm Assembly

Once the fingers had been assembled they could be connected to the palm unit. The palm unit, pictured in Figure 19, was designed with the required holes and features that would facilitate a secure mechanical hand assembly in which all electromechanical and electronic components were to be mounted. The palm was 3D printed utilizing the same printing technique as the fingers. The palm has a high dimensional accuracy and is extremely light weight.

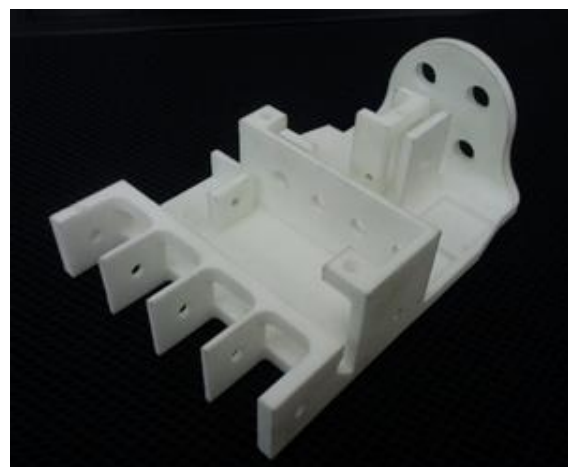


Figure 19. 3D printed palm chassis.

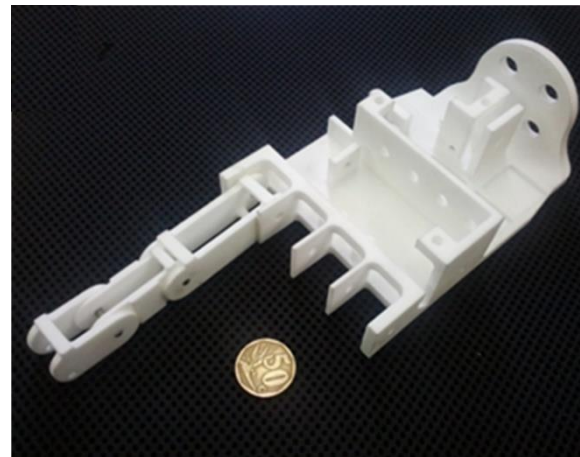


Figure 20. Example of complete finger joined to the palm.

Minimal effort was needed to ensure a clearance of 1 mm between the fingers and the palm due to this high dimensional accuracy. A single 3 mm stainless steel pin was used to create the revolute joint between the palm and proximal phalanges. Figure 20 shows an example of a complete finger connected to the palm. The assembled hand with all components attached was 220 mm in length, 120 mm in width at thumb, 90 mm in width at knuckles, 70 mm in height at palm (including electronics) and 25 mm in height at knuckles. These dimensions can be seen on the hand in Figure 21.

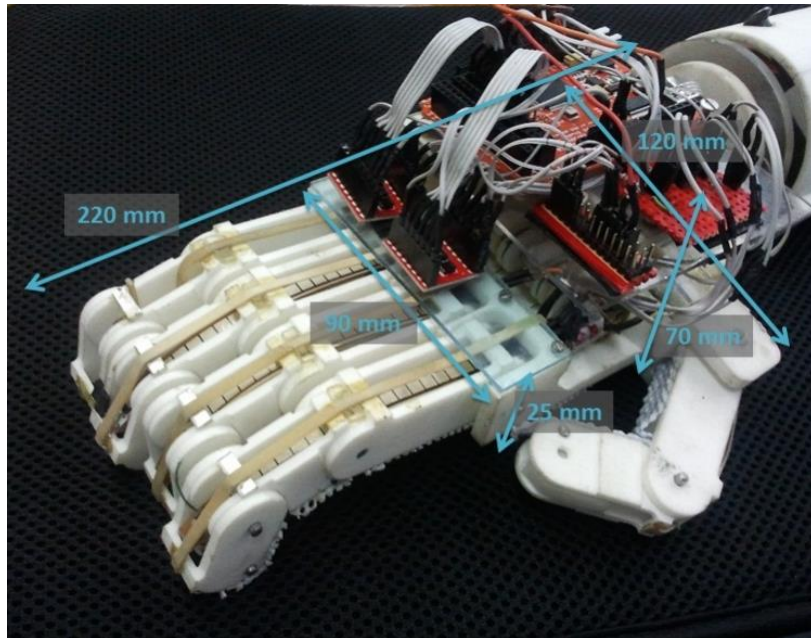


Figure 21. Complete hand with dimensions.

3.5. Assembly of Actuator and Drive System

Actuating the fingers posed a significant challenge as quantized by the working area. The space allowed for installation of the actuation system was one of the key criteria for motor selection. Suitable calculation and selection tools were utilized to choose the most effective actuator for the purposes of this research.

A 6V Pololu motor with a 50:1 gear ratio was chosen (Pololu, 2013). The motor was rectangular with rounded edges having dimensions of 12 mm x 10 mm x 24 mm. Figure 22 shows the motor that was used securely mounted to their respective positions.



Figure 22. A mounted motor used for thumb flexion and 4 finger motors.

The worm gear drive system allowed grips to be held without having to continually power the motors due to its self-locking property, thus increasing battery life. The worm wheels were secured to the palm using a single 3 mm diameter shaft. A 3D printed cable pulley was designed to feed or retract the actuating cable (tendon). Shown in Figure 23 is the complete worm wheel and pulley assembly.



Figure 23. Complete assembly of worm wheel and cable pulley.

The full drive system assembly is shown in Figure 24. Slight adjustments were made through the assembly process as it was found that tool placement and accessibility was a critical aspect of easy maintenance and repair.

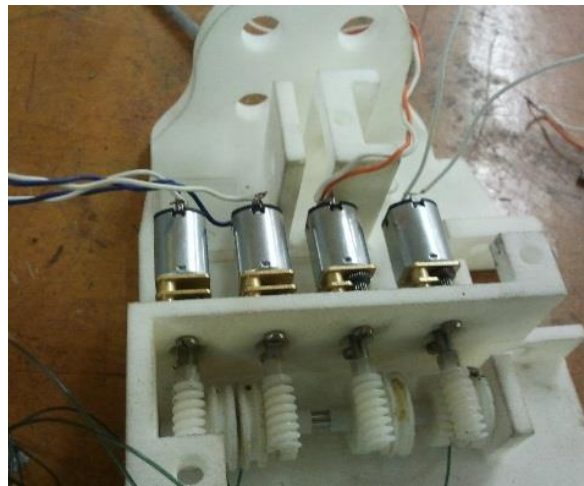


Figure 24. Complete finger actuation system.

3.6. Wrist

The wrist is a joint found between the hand and the distal end of the forearm. Its purpose is to couple the two so that they work in harmony when one is using his/her hand. The biological wrist has three degrees of freedom (DOF); that is flexion or extension, abduction or adduction and pronation or supination (American Society for Surgery of the Hand, 2013). The wrist was designed with one DOF, pronation and supination (rotation). This degree of freedom was based on one of many requirements of the client and is seen as the most critical of the wrist's three DOF.

The pronation and supination of the wrist is produced with a servo motor (MG945). This motor has a speed of 0.22 seconds per 60 degrees. It has a range of motion from 0° to 180°. As the wrist must be able to withstand and rotate a mass of 2 kg, the motor produces a torque force of 1.2 N.m at 4.8 V. The metal output shaft of the servo motor is splined to make a perfect fit with a black ABS servo horn attachment and has a mounting hole to secure it. The servo horn allows for output shaft to mechanically link to the rest of the mechanism. In this case, it was bonded to the mounting disc of the hand to transmit rotation (pronation and supination) of the hand.

The mounting disc is 64 mm in diameter, 5 mm in thickness and made from clear perspex material. It has four 8 mm holes drilled onto it using a vertical drilling machine, which are used for coupling the wrist to the hand. The centre hole of 15 mm diameter in the disc is for placing circular part of the servo horn to attach it to the servo motor metal splined shaft. The mounting disc and the servo horn were bonded together. As part of the prototype evaluation of the wrist the servo motor is mounted in a 3D printed semi-circle housing by four M4 socket cap head bolts high tensile black. The housing is made of ABS plastic material. The housing and servomotor are shown in Figure 25.

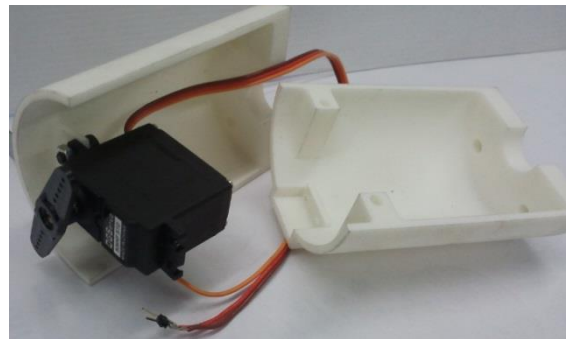


Figure 25. 3D printed wrist housing from ABS plastic.

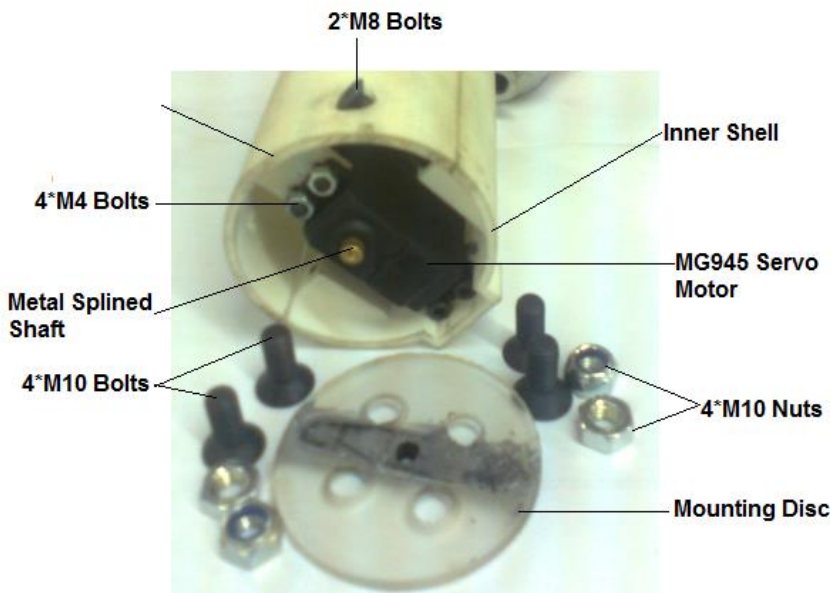


Figure 26. Components of the wrist housing.

The housing is 70 mm in diameter and 100 mm in length. At the front end where the motor fits, the inner shell was extended in a rectangular shape so that the motor shaft is centralised in the middle of the housing. The full labelled components of the wrist are shown in Figure 26.

3.7. Prosthetic Socket

The socket is the most critical element of the whole prosthesis because it forms the mechanical interface between the amputee and the prosthesis. As the socket transmits forces from the prosthetic device to the amputee's residual stump, the socket must be precisely fitted to limb. This ensures that the amputee does not get skin irritation or damage. The prosthesis can be state-of-the-art but if the prosthetic socket is uncomfortable to the wearer, he/she will

reject it. Another factor which may lead to rejection of the prosthesis is the ease of attaching and detaching the device.

In this section the fabrication of the prosthetic sockets and the suspension system will be discussed. It must be stated that the prosthetic socket was not designed but a new pair was fabricated to fit the amputee, according to his existing socket specifications, on whom the prosthetic hand was tested on.

Figure 27 shows the current prosthetic hand being used by the amputee. The cable mounting parts and end effectors (hooks) were eliminated in order to accommodate Myoelectric parts.



Figure 27. Amputee's current prosthetic hand with cable and hook end effector.

There were three main stages implemented to obtain the final prosthetic sockets; measurement and casting, rectification and fabrication. Plaster wrap was used to cover the limbs of the amputee. For easy removal of the cast, the plaster wrapped limb was coated in a separator. The plaster of paris was then used to make the plaster cast of the limb which is termed a negative mold. The negative mold was then used for creating positive mold by filling it with gypsum plaster. Figures 28 shows the stump of the amputee ready for measurements and wrap casting.

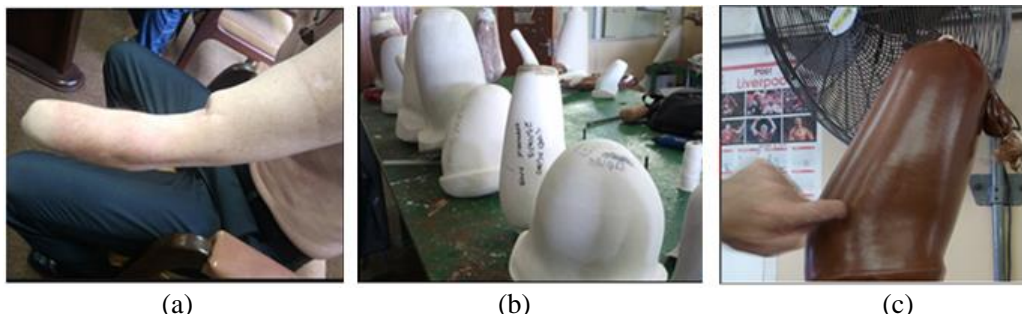


Figure 28. Fabrication stages of prosthetic socket: (a) amputee's stump before measurements and wrap casting; (b) white gypsum plaster positive molds of stumps; (c) a finished prosthetic socket.

In rectification, the measurements of the positive mold and residual limb of the amputee were compared for any indifference. All the molds were found to be in perfect length dimensions with respect to the amputee limbs. The modifications made on the mold differ for each amputee as their requirements and needs are unique. The customisation process of the socket involves adding and removing of the gypsum plaster on the mold. This is done to

ensure that the amputee will bear the load ideally according to his/her stumps pressure tolerances.

After the adjustment of socket shape was done and agreed by the amputee, the alignment marks were made to indicate how the prosthesis should hang on the arm in order to reach the amputee's mouth. The final socket was produced from the adjusted socket shape mold by laminating plastic resin with fiberglass as reinforcement material on the mold. The socket was then fitted to the amputee to check the comfort and placement of the end effector connection. The angle of the end effector was found to be 45 degrees; it was from the amputee's current prosthetic socket as shown in Figure 29.

The prosthetic socket was then bonded to a steel pyramid which connects to the wrist housing female adapter. The socket is attached to the wrist as shown in Figure 30 when the client was fitting the device. The method of keeping the socket attached to the residual limb (the method of suspension) is also important. Upper-extremity prostheses must be suspended throughout the entire range of motion and be able to tolerate loading during normal use. This is done through either suction cups or through the use of a harness, depending on the amputee's preferences. Suspension of the socket was gained using a figure of eight harness. It was made from 25 mm wide nylon webbing belt. The finished harness mounted to the socket is shown in Figure 31.



Figure 29. Fitting of the socket and end effector angle.



Figure 30. Socket and end effector.



Figure 31. Prosthetic harness.

This harness is different from that of the current used mechanically powered prosthetic harness as this was made for one arm which is myoelectrically controlled. It does not have the paddings for protecting the amputee from moving actuation cables. The fitting of the prosthetic harness is shown on Figure 32 where the amputee was wearing the transradial prosthetic arm for the first time.



Figure 32. Amputee wearing prosthesis.

3.8. Device Modulation

The client that participated in this research was a transradial amputee. It was the intention of the research, however, to design a prosthetic hand that could be used both for transradial and transhumeral amputees. By designing the prosthetic hand in a modular way the hand and wrist can be easily attached to a prosthetic arm for transhumeral amputees.

The wrist housing forms the base of this prosthetic hand. When the housing is connected to the socket, the prosthesis is transradial. Any type of transradial amputee would be able to wear it as long their sockets are fitted with the standard pyramid adapter at the distal end.

Figure 33 shows the transradial prosthetic hand. The final weight of the prosthetic hand and socket with all electronics was measured at 1.6 kg. In the case of a transhumeral amputee, the prosthetic arm would connect at the same adapter as that of where the current prosthetic socket connects.

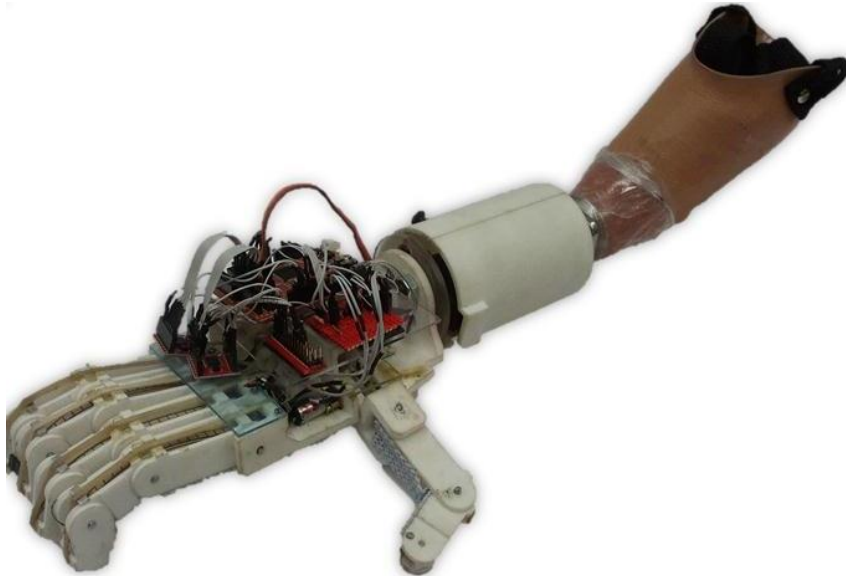


Figure 33. Transradial; model on the left and actual on the right.

4. TESTS AND RESULTS

The prosthetic hand's performance is tested and discussed in this section. The ability of a prosthetic hand to grip objects is the fundamental purpose of any prosthetic hand and therefore the most critical aspect of the prosthetic hand to test. The prosthetic hand was designed to mimic the natural movements of the human hand. The shape and speed of the prosthetic hand is compared to that of a human hand to evaluate how closely this is achieved.

4.1. Grip Strength Test

To test the gripping strength of the prosthetic hand, a water bottle was used with varying degrees of water levels. This allowed the prosthesis' grip to be tested against a controlled object weight. A 250ml bottle was marked with 9 equally spaced graduation marks as shown in Figure 34. A corresponding weight of 28 g for each level increment was measured and calibrated using water. The hand easily grasped the empty bottle. The core aim of this test was to support the application of a nylon non-slip covering on the inner surface of the palm and fingers. The grip weight attained with and without the nylon covering was compared. Figure 35 shows the hand with the nylon non-slip covering.



Figure 34. 250ml graduated water bottle.



Figure 35. Nylon non-slip covering to increase grip strength.

The grip feel and solidity was given a rating out of 10, where a rating of 10 being a completely secure grip. Each graduation mark represents a different level of grip security (how easily the object is dropped from the hand during movement of the hand). A rating of 0 represents the complete inability of the hand to lift the bottle. The test was carried out using water as the filling liquid. Figure 36 represents the results of this test.

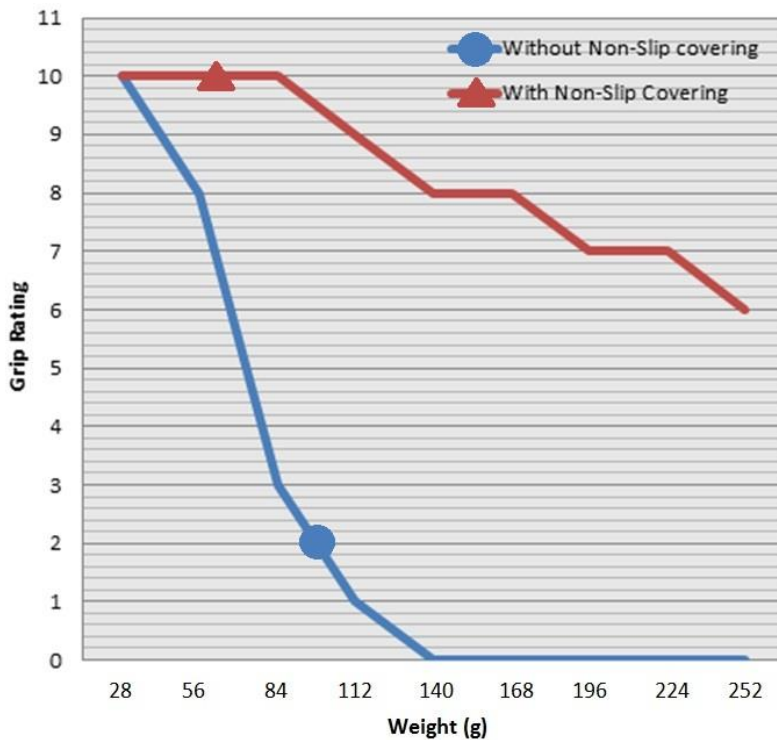


Figure 36. Graph showing how secure a grip felt as weight of water bottle increases.

It can be seen that the gradient of the circle trend line is steep. The shape of the circle line shows that the grip is weak when low loads are applied and does not offer a secure grip. The addition of the nylon non-slip cover decreases the gradient of the graph, indicating that the surety and strength of the grip performs better when applying a larger load.

4.2. Kinematic Video Analysis

A video analysis of the hand was aimed to validate the prosthetic hand's ability to mimic a human hand in its motion. The open-source video analysis tool Kinovea (Kinovea, 2014) was used to conduct this analysis. The software is capable of tracking objects in real-time. The joint paths of both the prosthetic hand and human hand were compared using this software. The results showed the kinematic behaviour of the prosthetic hand. It also allowed the maximum joint speeds to be compared.

The analysis procedure involved the setup of a white background to enhance contrast between the object being tracked and the surrounding environment.

A reference frame had to be setup on the white background to give the software a known length and scale. The program is capable of accurately calculating the absolute velocities of the joints with the aid of this reference frame. Figure 37 shows a snapshot of the kinematic video analysis at the point where the joints of the human hand are at their maximum. The hand was recorded closing all fingers in a smooth and natural manner to measure the closing speed of an average human grasp.

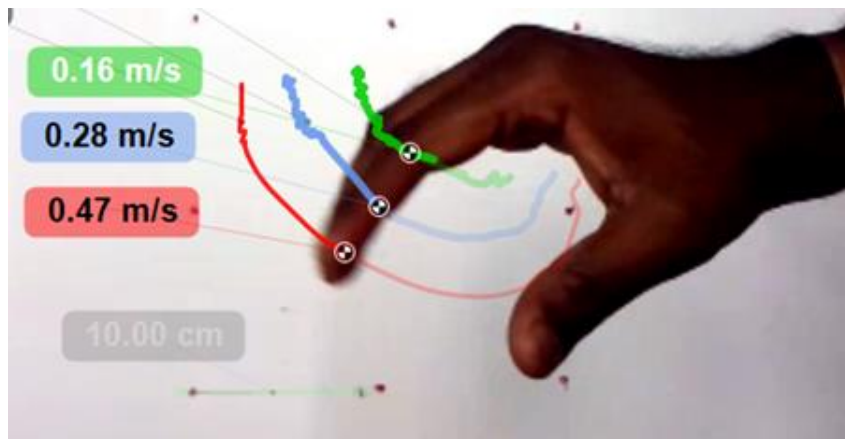


Figure 37. Joint paths tracked and velocities measured using Kinovea kinematic analysis software.

The prosthetic hand was recorded under the same reference conditions to make sure that the measurements correlated for both the human and prosthetic hand. Figure 38 shows a snapshot of the prosthetic arm at its maximum distal joint velocity.

The results showed similar joint paths to that of the human hand. Figure 39 shows the graphs of joint velocities against time. The joint velocity graph compares the differences in joint velocity and overall closing time.

It can be seen that the human hand closes faster in the natural closing grip task than that of the prosthetic hand at maximum power. The friction between joints and cables slows the speed of the prosthetic hand. The human hand was measured to close in 1.5 seconds whereas the prosthetic hand took 2 seconds. Positional and displacement data was also extracted from the kinematic video analysis. It is important to compare the motion of the prosthetic hand to a human hand. The prosthetic hand must mimic its biological counterpart as closely as possible to enable controlled grasping and aesthetic appeal.

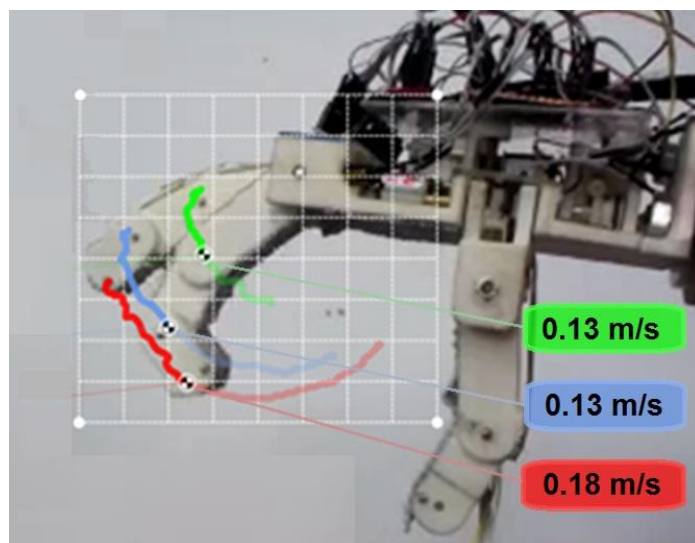


Figure 38. Joint paths and Velocities tracked of the prosthetic hand.

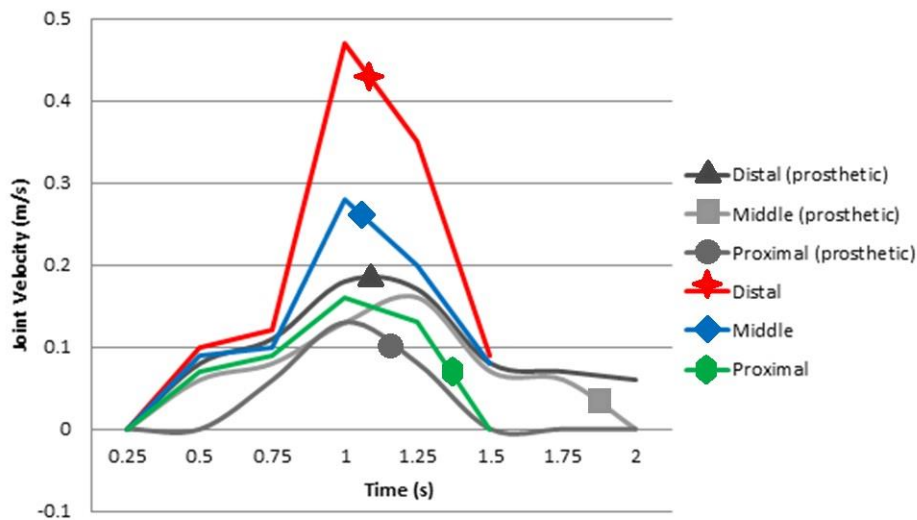
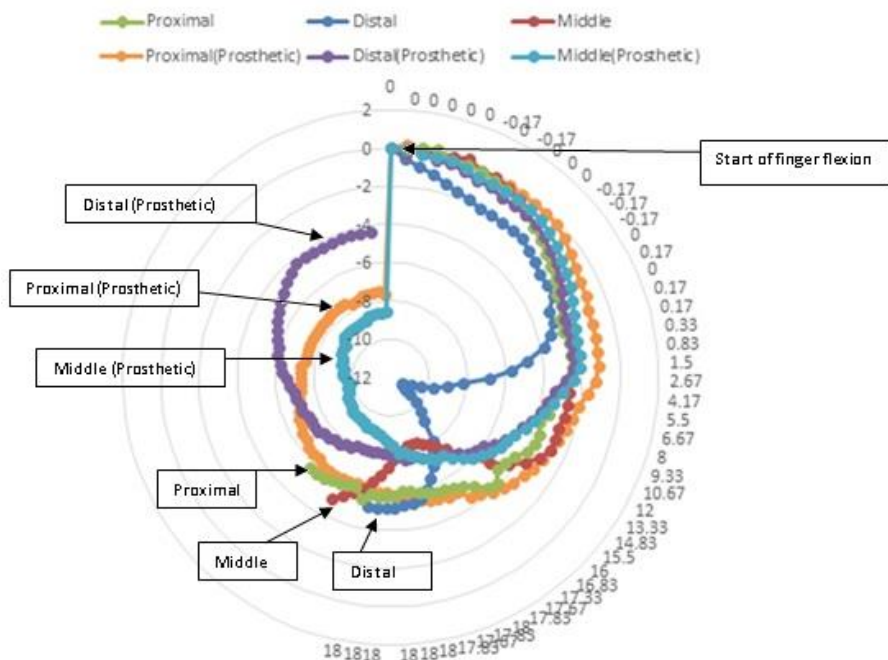


Figure 39. Graph of Joint Velocities for both Human and Prosthetic Hands.

A radar chart was used in order to compare the kinematic behaviour of the human and prosthetic hand. The radar chart was used because it is a graphical method of displaying three or more quantitative variables on the same axes starting from the same point therefore enabling the two motions to be displayed. The same reference points and recordings were used to extract displacements in Cartesian coordinates. Figure 40 shows the plot of X and Y coordinates in the radar chart.



It can be seen that the displacements of the respective middle, proximal and distal joints follow the same path (display the same displacement) for approximately the first quarter of its motion. The movements of the joints in the prosthetic hand can be seen to start off with very similar kinematic behaviour to that of a human hand. It is then seen that as the finger reaches halfway between its fully open and fully closed position the joint displacement differs from that of the human hand. The rigidity of the prosthetic finger attributes to the variation between it and the human finger during the halfway point of closure. The human proximal joint is a flexible joint with more than one degree of freedom hence allowing the finger to curl through a larger degree than that of the prosthetic finger.

The prosthetic fingers differ in kinematic behaviour compared to the human finger at the latter stages of flexion. It can be seen from the radial chart that the distal segment rotates about the distal joint earlier than that of its biological counterpart, this caused inconsistencies in the pinch grip tasks. The fundamental dimensions of the prosthesis' distal segment and the nature of its actuation cause the inconsistency in the pinch grip. The overall behaviour of the prosthetic fingers is as close to human finger motion. The hand moves in a natural way in which the user can feel comfortable with utilizing.

4.3. Gripping Objects

The hand's gripping capabilities had to be demonstrated to fully test the effectiveness of the end effector as a functional prosthetic. A simple procedure of gripping objects of different shapes and dimensions was undertaken. The hand was tested with rigid objects as soft objects are easier to grip. The hands ability to adaptively grasp objects is tested and proven by a range of grip tests. Figure 41 illustrates example of square objects being grasped.

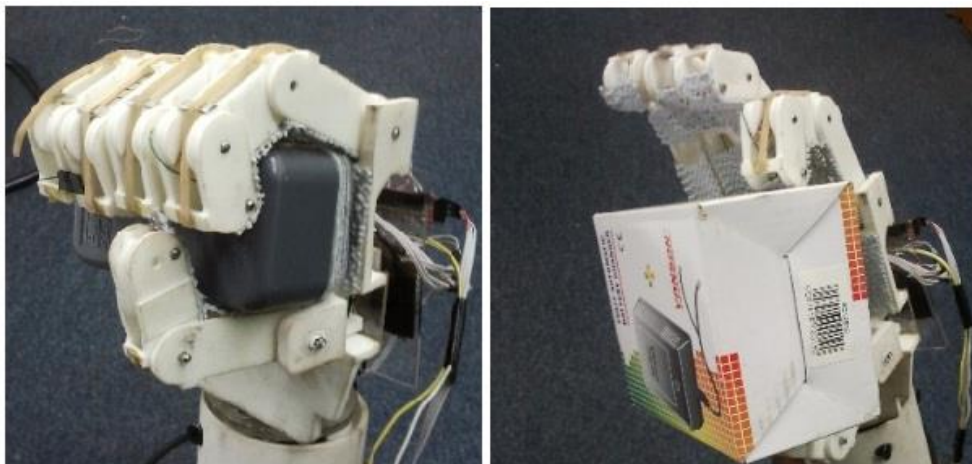


Figure 41. Hand gripping square objects.

Grasping square objects posed no challenges as the fingers adaptively grasped the corners with ease. Figure 42 shows the hand grasping different types of plastic bottles.

The hand also handles round or spherical objects. Figure 43 shows the hand grasping a cricket ball.

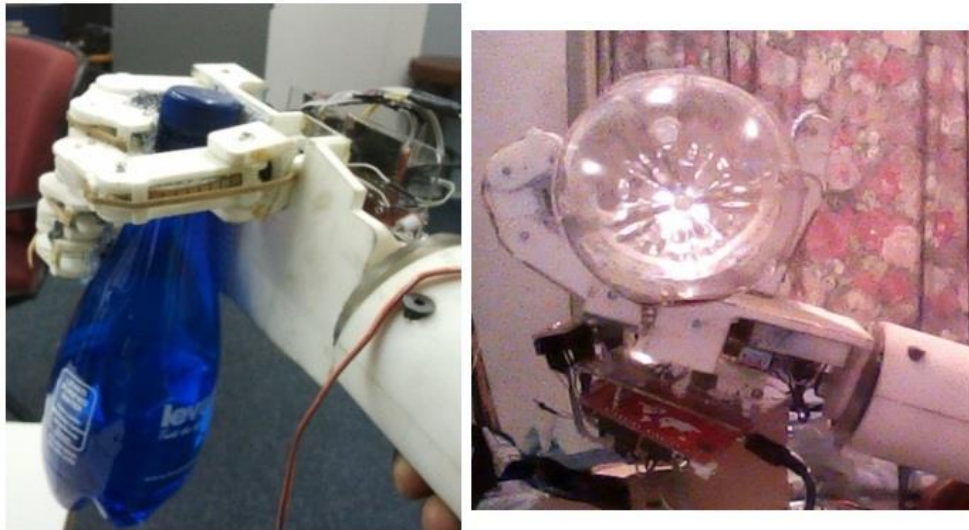


Figure 42. Hand gripping unusually shaped bottle and a 2 litre bottle.



Figure 43. Hand Gripping a spherical object.

CONCLUSION

As shown from the kinematics, the hand and fingers have a good range of motion, which cover the basic degrees of freedom (DOF) of a human hand. A more complex model allowing full DOF would be actuator heavy, thus increasing the weight, size and cost of the prosthetic hand. For this reason the hand is optimized for weight, cost and function. The size of the hand is slightly larger than a human hand and its size should be reduced in future versions.

The wrist was designed with only a single DOF (rotation). However the flexion and extension movements are very important in daily life and inclusion of this second DOF would improve the overall function of the prosthetic hand. An additional DOF would bring added

complexity, weight and cost to the hand. A modular approach could be taken here, allowing for the second DOF to be an attachable part to the prosthetic hand, allowing it to be used as necessary.

The connecting adapters were all made from stainless steel which increased the weight of the prosthesis. With the new technology of 3D printing they can be reproduced and be made from a much lighter material such as titanium. The overall system was built within a small budget of US\$ 1'000. The low cost design and manufacturing of the prosthetic hand achieves the low cost goal of the research.

5.1. Discussion of Results

The prosthetic hand performed satisfactorily according to the amputee, and is capable of gripping a variety of differently shaped objects. The prosthetic hand also mimics the movement of the human hand to a satisfactory degree. The hand is capable of lifting 250 g with the cylindrical grip. The grip strength can be further improved.

Increasing the motor power would improve grip strength. However, a more powerful motor will be larger and heavier than the motors currently selected. Therefore a balance between size, weight and grip strength needs to be decided upon. Using more powerful motors will also increase the overall cost of the prosthetic hand.

It is noted that the prosthetic hand closes slower than the human hand by 0.5 seconds. The motor's gear ratio controls the balance of torque to speed. Grip strength was indicated as being more important than hand closing speed by the amputee at the beginning of the research. The decision was made to favour grip strength over speed.

The results from the grip strength test showed significant improvement with the use of the non-slip covering. The hand is capable of lifting suitable weights for eating and drinking purposes and is able to carry loads up to 500 g as per the initial specifications.

5.2. Future Work

For future recommendations, it is acknowledged that a more efficient system for actuation can be developed. The grip force in prosthetic hands needs to be increased in future versions of the hand. The grip force can be increased by implementing a larger, higher power motor into the hand.

The monocoque design offered structural rigidity but there was little room for tools to reach inside, making the assembly very time consuming. The design should be modified to allow for the easy installation of the mechanical and electrical components. Further consideration could be given to allowing the hand to have modular mechanical and electrical components. This would allow for a high degree of customizability and would allow the amputee to choose only the components he/she wants to be in his/her prosthetic hand.

ACKNOWLEDGMENT

The financial assistance of the National Research Foundation (NRF) towards this research is hereby acknowledged. Opinions expressed and conclusions arrived at, are those of the author and are not necessarily to be attributed to the NRF.

REFERENCES

- American Society for Surgery of the Hand, [Online]. Available: www.assh.org, date viewed: 28 February 2013.
- Carrozza, M, Vecchi, F, Sebastiani, F, Cappiello, G, Roccella, S, Zecca, M, Lazzarini, R, Dario, P, *Experimental analysis of an innovative prosthetic hand with proprioceptive sensors*, IEEE International Conference on Robotics & Automation Taipei, Taiwan, September 2003.
- Celanese, [Online]. Available: www.plastics.ides.com, date viewed: 20 June 2013.
- Cipriani, C, Controzzi, M, Carrozza, M, *Progress towards the development of the SmartHand transradial prosthesis*, IEEE International Conference on Rehabilitation Robotics Kyoto International Conference Center, Japan, June 2009.
- Cipriani, C, Controzzi, M, Carrozza, M, *The SmartHand transradial prosthesis*, *Journal of Neuroengineering and Rehabilitation*, 2011.
- Dalley, S, Wiste, T, Varol, H, Goldfarb, M, *A multigrasp hand prosthesis for transradial amputees*, International Conference of the IEEE EMBS Buenos Aires, Argentina, 2010.
- Kinovea, [Online]. Available: www.kinovea.org, date viewed: 12 February 2014.
- Massa, B, Roccella, S, Carrozza, M, Dario, P, *Design and development of an underactuated prosthetic hand*, IEEE International Conference on Robotics and Automation, Vol. 4, 2002.
- Matrone, G, Cipriani, C, Carrozza, M, Magenes, G, *Real-time myoelectric control of a multi-fingered hand prosthesis using principle components analysis*, *Journal of NeuroEngineering and Rehabilitation*, 2012.
- Pololu, [Online]. Available: www.pololu.com, date viewed: 16 September 2013.
- Rutkowski, J, Levin, B, *Acrylonitrile–butadiene–styrene copolymers (ABS): Pyrolysis and combustion products and their toxicity—a review of the literature*, *Fire and Materials*, Vol. 4, pp. 93–105, September 1986.
- Van As, R, Owen, I, *Coming up short handed (the Robohand blog)*, [Online]. Available: www.comingupshorthanded.com, date viewed: 13 February 2013.
- van der Niet, O, Reinders-Messelink, H, Bongers, R, Bouwsema, H, van der Sluis, C, *The i-limb hand and the DMC plus hand compared: a case report*, *Prosthetics and Orthotics International*, Vol. 34, pp. 216–220, June 2010.
- van der Riet, D, Stopforth, R, Bright, G, Diegel, O, *An overview and comparison of upper limb prosthetics*, IEEE AFRICON Conference, Mauritius, September 2013.

ABOUT THE AUTHORS



Drew van der Riet was born in Port Elizabeth, South Africa. He graduated Bio-Mechatronics Engineering (M.Sc. Eng), at the University of KwaZulu-Natal.



Riaan Stopforth graduated with a B.Sc. Eng (Electronics), M.Sc. (Computer Science) and Ph.D. Eng (Mechanical) from the University of KwaZulu-Natal, who has specialized in the field of Mechatronics Engineering. His research interest is in the area of search and rescue robotics and bio-engineering systems. He is currently appointed as an Associated Professor at the University of KwaZulu-Natal.



Glen Bright graduated with a B.Sc. Eng (Mechanical), M.Sc. Eng (Mechanical), Ph.D. Eng (Mechanical) and MBA from the University of KwaZulu-Natal, who has specialized in the

field of Mechatronics Engineering. His research interest is in the area of advanced manufacturing systems. He is currently appointed as a Professor at the University of KwaZulu-Natal.



Olaf Diegel is professor of product development at Lund University in Sweden. He is heavily involved in all aspects of product development and is widely published in the areas of additive manufacturing and rapid product development and mechatronics. In his consulting practice he develops a wide range of products for companies around the world. Over the past 10 years he has developed over 60 commercialized new products and, for this work, has received numerous product development awards.

Chapter 5

MECHATRONIC INTEGRATION FOR SEARCH AND RESCUE APPLICATIONS: UAV VISION SYSTEM FOR MINING AND MANUFACTURING ENVIRONMENTS

Sibonelo Motepe^{*} and Riaan Stopforth[†]

Mechatronics and Robotics Research Group (MR²G) –
Search and Rescue Division

School of Engineering, University of KwaZulu-Natal, Durban, South Africa

ABSTRACT

The advancements of technology allows for development of robots for that can improve human lives and safety. One such application is search and rescue mission using unmanned ground vehicles, underwater vehicles and air vehicles. This paper present a Haar Cascade full body detection model developed for human detection in mine search and rescue applications. The model is for use on an unmanned aerial vehicle (UAV). The model development is discussed. The tests conducted on the model are presented and the results discussed. The model is compared to its preliminary stage and a generic model distributed with the open source computer vision library. The comparison results are presented and discussed.

1. INTRODUCTION

Disaster scenes present challenges to rescuers as they often have to enter areas that may have unstable structures, without assurance of the presence of victims and the state victims. This causes rescuers to expose themselves to possible hazards that can place their lives in

^{*} E-mail address: 206522329@stu.ukzn.co.za; phone: +27 78 257 5430; fax: +27 86 736 8522. Mechatronics and Robotics Research Group (MR²G) Search and Rescue Division, School of Engineering, Howard College Campus, University of Kwa-Zulu Natal, 4041, Durban, South Africa.

[†] E-mail address: stopforth@ukzn.co.za; phone: +27 31 260 1063. Mechatronics and Robotics Research Group (MR²G) Search and Rescue Division, School of Engineering, Howard College Campus, University of Kwa-Zulu Natal, 4041, Durban, South Africa.

danger (Motepe et al., 2012). In 2010 no survivors were found after a four day rescue mission for the mining accident that happened at a coal mine in West Virginia. The explosion had caused damage to the mining environment and created a lot of obstacles in the form of blown up machines or rocks. These obstacles made the rescue mission complex and timeous (Urbina, 2013). In 2011, a gold mine rescue mission led to the death of two of the three rescue workers (SAPA, 2013). South Africa is one of the main mining countries in the world. This fact makes addressing mine safety and mine search and rescue mission a priority to be taken highly in South Africa (Reuters, 2013). The University of Kwa-Zulu Natal (UKZN) has a research team that conducts research towards using robots for search and rescue missions. This chapter presents research, conducted within this team, on the development of an Unmanned Aerial Vehicle (UAV) for use in mining search and rescue applications and a vision system for on the UAV for human detection in these environments. The vision system is also used to present the rescuers with visuals of the search and rescue environment. A visual of the victim's location will assist rescuers with knowing the condition of the victims and the condition of the area that they are to be rescued from.

2. SYSTEM OVERVIEW

2.1. Unmanned Arial Vehicles

Unmanned Aerial Vehicles are aircrafts that don't have on-board pilots and are controlled from remote locations. UAVs can carry sensors and cameras which can be used to get an analysis of the rescue environment. UAVs can also be used to carry other payloads to the victims where rescuers are experiencing challenges in gaining access. There are various sizes and shapes of UAVs (Motepe et al., 2012). The UAV in this research is a mini quad rotor copter. The size enables the UAV to have easy access to areas that rescuers may not be able to easily and quickly access to due to obstacles. The UAV is controlled over Wi-Fi as opposed to tethering to enable it to maneuver obstacles. The UAV has a symmetrical cross structure with one propeller at each of the four arm ends. The quad rotor setup is used due to the stability it presents stability. Figure 1 shows the quad rotor UAV used in this research (Motepe et al., 2012).

- Four brushless DC motors that spun the propellers.
- Four Electronic Speed Controllers (ESCs) to control the speed of the motors
- An Arduino Pilot Mega(APM) for flight control
- The Odroid-X2 as the main processor
- An Arduino Mega to interface the main processor and the APM

Odroid-X2 was used because of its compact size. The reason it was chosen over other developments boards such as the Raspberry Pi is its high speed (1.7 GHz Quad Core Processor), High RAM (2 GB) and more USB ports (6 high speed USB 2.0 host port) for peripheral connection. The system overview is shown in Figure 2.



Figure 1. UAV quad frame structure and assembled system.

The UAV system was divided into the onboard system on the actual copter and the ground station the UAV was controlled from. The onboard system had:

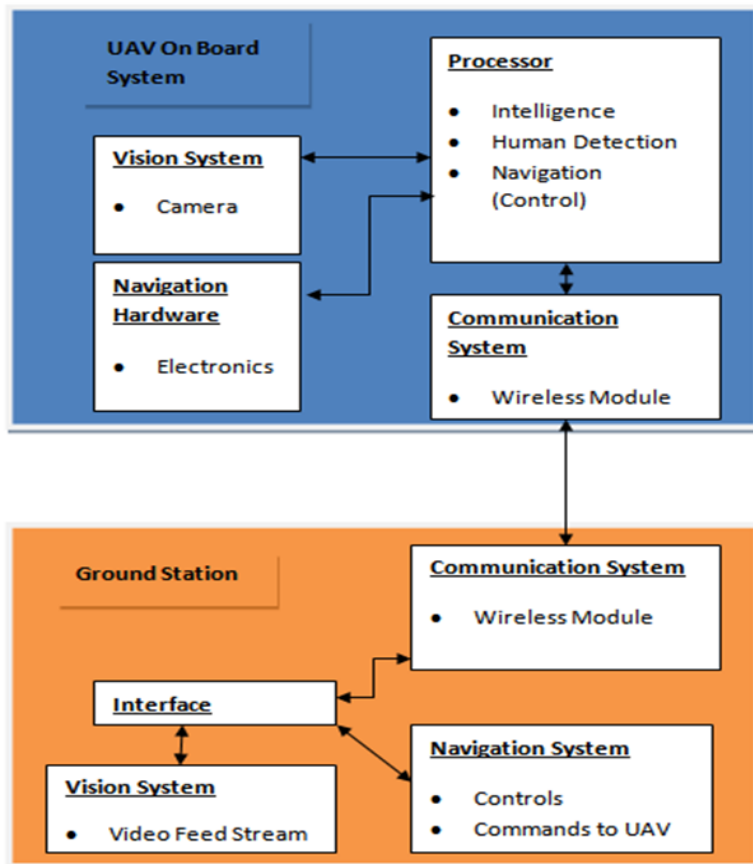


Figure 2. System Overview.

2.2. Human Detection Algorithm

The UAV was intended to have the ability to detect human beings in the rescue mission. This section discusses some of the human detection algorithms considered for this application.

2.2.1. Template Matching

Template matching is a matching algorithm that matches an image portion (Template) against an input image by sliding the template over the input image. This function uses different methods to perform the matching. In OpenCV the following methods are used; square difference matching methods, correlation matching methods, correlation coefficient matching methods and normalized methods (Bradski & Kaehler, 2008).

Template matching is illustrated in Figure 3 (Latecki, 2005). The square difference matching methods match the squared difference of the template and image as described by equation 1 (Bradski & Kaehler, 2008).

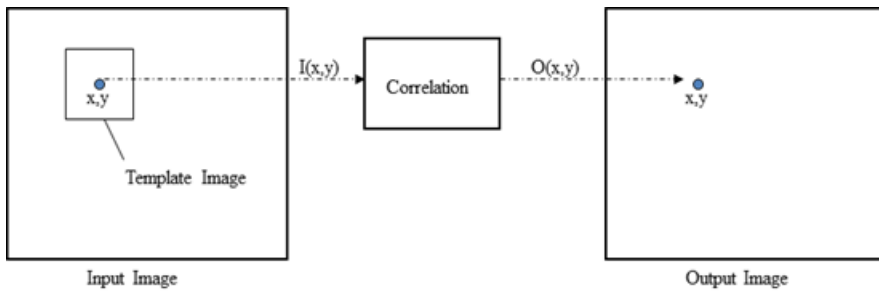


Figure 3. Template Matching.

$$R = \sum_i^x \sum_j^y |T_{ij} - I_{ij}| \quad (1)$$

where:

R is the Results

T is the template image

I is the input Image

A perfect match will give a result of zero, while a large number would not be a match. The correlation matching methods use multiplication to match the template to the image. Hence the results would be the opposite of the previous method. A zero represents a non-match and a big number represents a match. The correlation coefficient methods match a template and an image relative to their means. A perfect mismatch and match will be -1 and 1 respectively. The normalized methods help reduce the effects of lighting difference between the image and template. This method works best when the template is part of the input image that the object has to be found in. Template matching has been used to detect human beings from thermal images. The template used is an average template to capture variations in human shape (Nanda & Davis, 2002).

2.2.2. Chamfer Matching

Chamfer matching is a form of template matching that uses a binary image (I) and a binary edge template (T) to do the matching. The binary image's distance transform is found and the template matching is performed. The aim is to find a placement of the template on the distance image such that the sum of the distance transformed image (D) multiplied by the pixels values in the template image is minimized. The perfect match at a location is 0. A good match can still be found if the edges are slightly displaced. Match score is calculated using equation 2 below (Kosecka, 2006):

$$R = \sum_i^x \sum_j^n |T_{ij} \times D_{ij}| \quad (2)$$

This method has disadvantages, including when objects are slightly occluded, as the light and shading are different to the input image and template. Chamfer distance matching was used as one of their algorithms to detect humans in a moving camera. A silhouette templates database is used to perform the search in input frames. A stabilization algorithm is used to get the foreground image from three consecutive input frames. The fore ground image is thresholded to get the binary image for the matching (Hussein et al., 2006).

2.2.3. Chamfer Matching

The Haar-classifiers are used for human detection on the UAV. This method was originally developed for face detection, but can be used to detect other objects (Viola & Jones, 2001). The Haar-like cascade classifier has been used in license plate detection (Zheng et al., 2012). Haar-classifiers have also been used in object tracking (Mahalingam & Mahalkshmi, 2010) and car theft detection (Ahilan & James, 2011). The Haar-classifiers allow for fast feature evaluation by selecting a number of important features, which are used to train the model using AdaBoost. A cascade structure is used to combine more complex classifiers. The small features used are rectangular features that form an intermediate representation of an image called an integral image. Figure 4 shows the rectangular Haar like features.

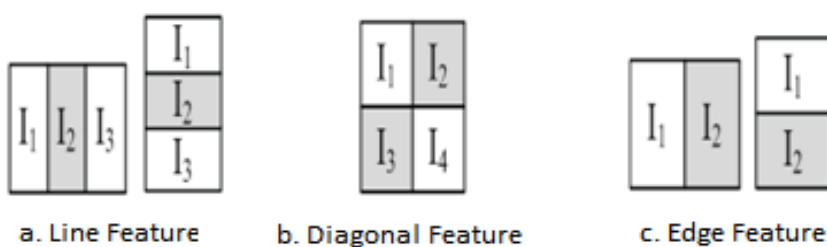


Figure 4. Integral Image Rectangular Haar like features.

The model detects the objects by applying a series of classifiers to every sub-window in the target image. The first stage eliminates non object containing sub-windows with minimal processing. The following stages require more computation to eliminate non object containing sub-windows. This process is summarized in Figure 5 (Viola & Jones, 2001).

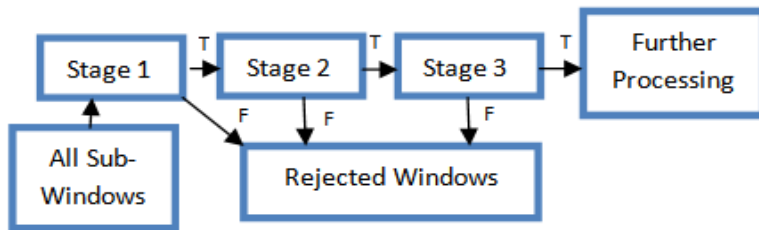


Figure 5. Illustration of cascade detection.

3. MODEL TRAINING

The algorithms mentioned in the previous section were tested for the possibility of use for the intended application. Template matching worked only when the template image was exactly the same as the input image or the template image was contained in the input image. This algorithm would not work for the application as the image of the person being rescued would need to be used to as a template image. With the person to be rescued is not known before the rescue mission, hence this model would not work in this application. The Haar cascade model distributed with OpenCV had a challenge when a human was obstructed and not facing the camera.

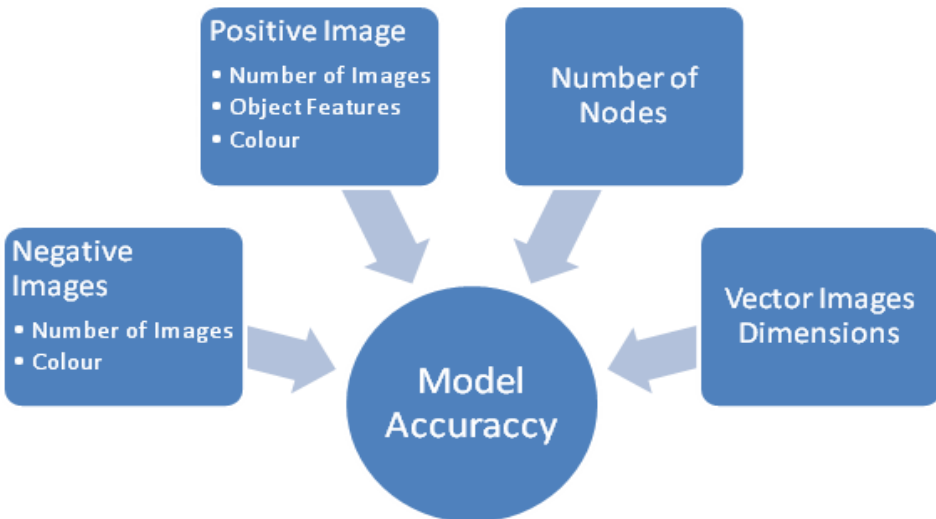


Figure 6. Factors that affect model accuracy/performance.

This algorithm was further researched. This involved developing a Haar cascade model. The Haar cascade training involves collecting negative images and positive images. The negative images are images not containing the object of interest, human beings in our case. The positive images contain human beings. The humans are marked in the positive images and a vector file is created for the training. The training started with 2024 positive sample images that contained people in different poses in the positive images. In some images people were obstructed and in some images they are distant. The model used 2030 negative images.

The 1st preliminary model to complete training had 1924 positive images after some positive images were deleted from the initial model. The images deleted were images that had people obstructed and the ones where people were at a distance. This model used 8771 negative images. There different factors that affect the model accuracy/performance are summarized in Figure 6.

These factors we manipulated until the final model with 988 positive images contain clear views with unobstructed human, and 8771 negative images. A sample of the positive images used in the final model is given in Figure 7. Figure 8 shows a sample of the negative images used in the training (Weber, 2003).



Figure 7. Sample positive images used in final model.

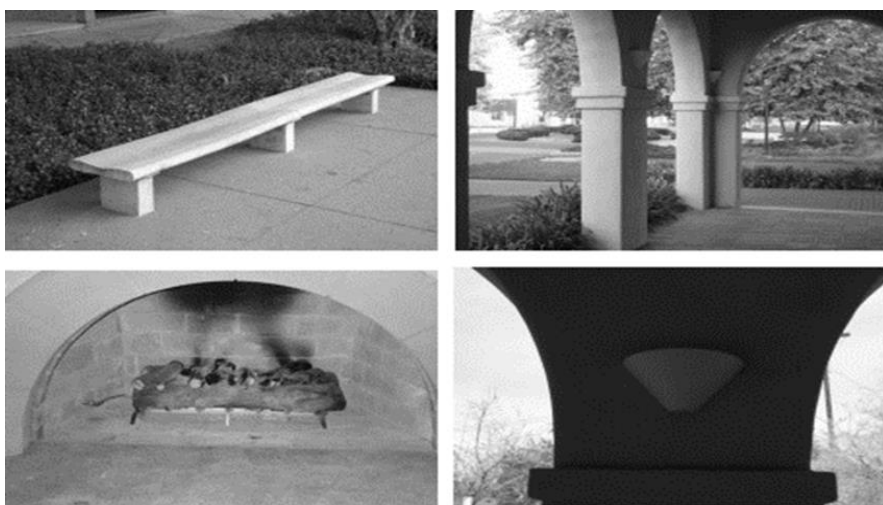


Figure 8. Negative images sample.

The 8871 grayscale negative images were found to be the optimum images in image color type (as opposed to true color images) and image number. This was achieved by testing the negative images effects on the False Alarm Rate during model training. The factors considered were the number of images and the color of the images. Figure 9 shows the effect of negative images on the false alarm rate (FAR).

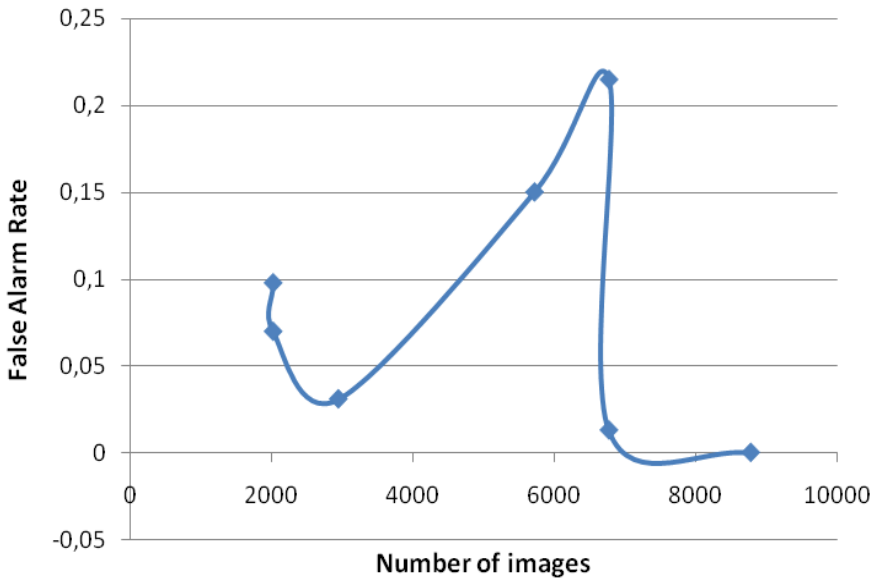


Figure 9. Effects of negative images on false alarm rate.

Here the number of negative images is increased, from 2949 (the graphs third point from the y-axis) to 5719 on the fourth point, the FAR increases from 0.031 to 0.14. The negative images introduced here to the 2949 grayscale images are true color images. Further true color images are introduced taking the total negative images to 6771 and the FAR to 0.21. When the images were all converted to grey scale and the model retrained an FAR of 0.013 was obtained.

This illustrated that the best negative images to use in this training were grayscale images. Further grey scale images were added to obtain the optimum number of negative images. Figure 10 shows the effects of the number of negative grayscale images on the FAR. The FAR decreases up to an optimum point (lowest point on graph) with an increase in the number of negative images. This point was found to be where the number of negative was equal to 8771. The FAR was found to be 2.25×10^{-4} at this point.

The false alarm rate for the initial, preliminary and final model are summarized in Table 1. An increase in the number of stages/nodes leads to a decrease in the true positive and false positive detections. The effect of this will be shown in Section III, where one model will exhibit high false positive and a high true positive detection.

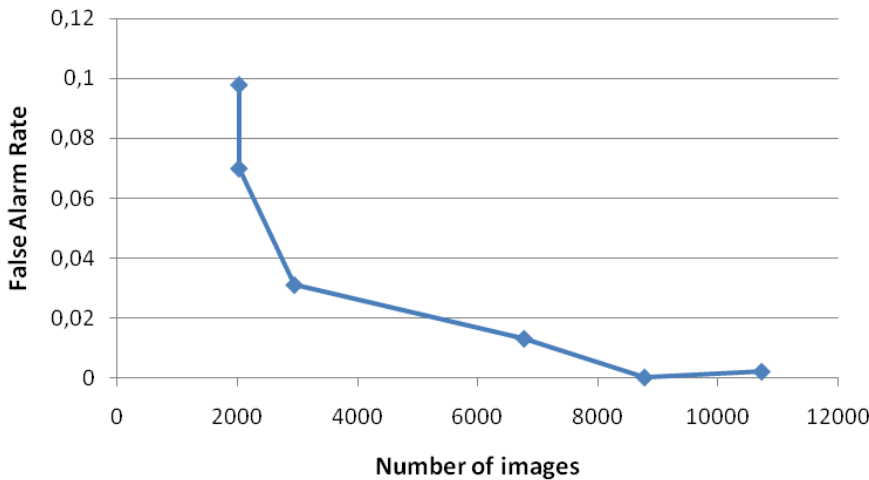


Figure 10. Effects of the number of negative grayscale images on FAR.

Table 1. Model training factors and false alarm rate

Model	No. Positive Images	Number Negative Images	False Alarm Rate	Number of Nodes attained
Initial	2024	2030	9.77×10^{-2}	5
Preliminary	1924	8771	2.25×10^{-4}	20
Final	988	8771	5×10^{-5}	23

4. EXPERIMENTS

This section presents the experiments carried on the final mode to determine its behavior and accuracy. A comparison of the final model, preliminary model and the OpenCV distributed full human body detection model is also presented. The comparison also provides the justification for using the final model as opposed to the distributed model and why the preliminary model had to be improved.

4.1. Final Model Testing

The final model was trained successfully and its application in real life situation was tested. The tests were to determine how well the model detects people in different poses. This was also to check how well the model can detect people when parts of their bodies were obstructed. The model was implemented on the ODROID-X2 Board. The model was loaded and the tests performed with a person approaching the UAV. A live video stream from the camera was used. The experiment was done in a light indoor surrounding. The distance between the person and UAV was kept between zero and five meters. The person rotated to all four sides (front, back, left and right) at every meter while approaching the UAV. The person remained in the same side for approximately 3 seconds. The detections were tabulated for four experiments. The average detection for each side was determined. Figure 11 shows

the average detection over the distance. For the front view the model was able to detect the person each time and gave an average of 100 percent.

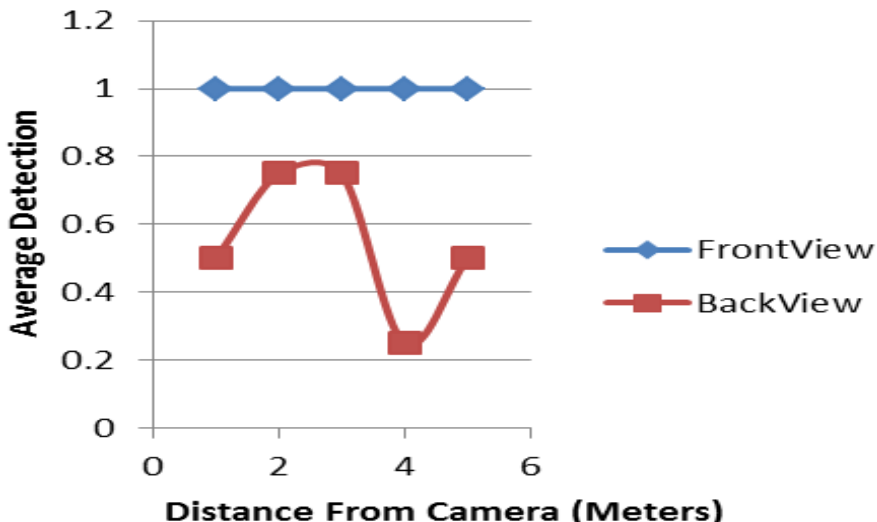


Figure 11. Average detection against Distance.



Figure 12. Back and Frontal detections.

The front view used mainly the face for the detection apart from using the hands and legs. The back view model used the arm posture (upper body) and hands more to detect the person. In Figure 12 the model uses the hand and the head to detect a person from the back. The model detects the upper body and face in the frontal model. The model was able to detect frontal view better than the back view. The side view detections were better when the camera was closer to the object. The software was configured to mark the detected objects using red squares. The detection drops from 100% when the object's distance from the camera becomes greater than four meters (as shown in Figure 13). The average detection rate drops to 75% and

25% for the left and right side respectively. Hence the detection rate will increase as the UAV approaches a victim in a rescue mission.

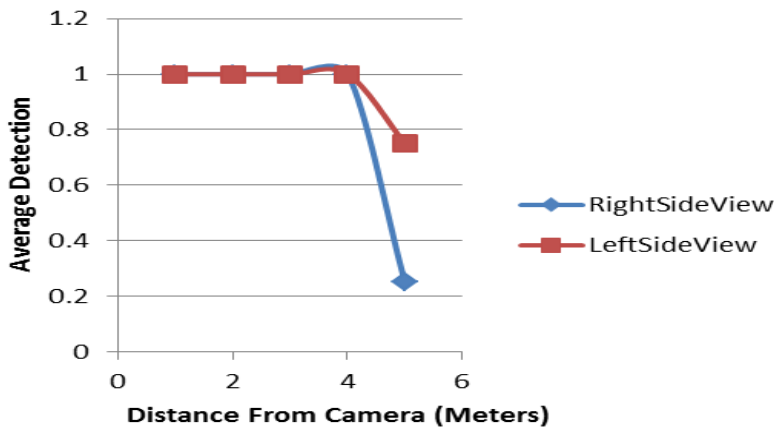


Figure 13. Average detection against distance.

Figure 14 shows the detections when the person is 1 meter away from the camera and when the person is 4 meters away from both sides. The model can therefore be used in real life detection and has an acceptable combined detection rate.

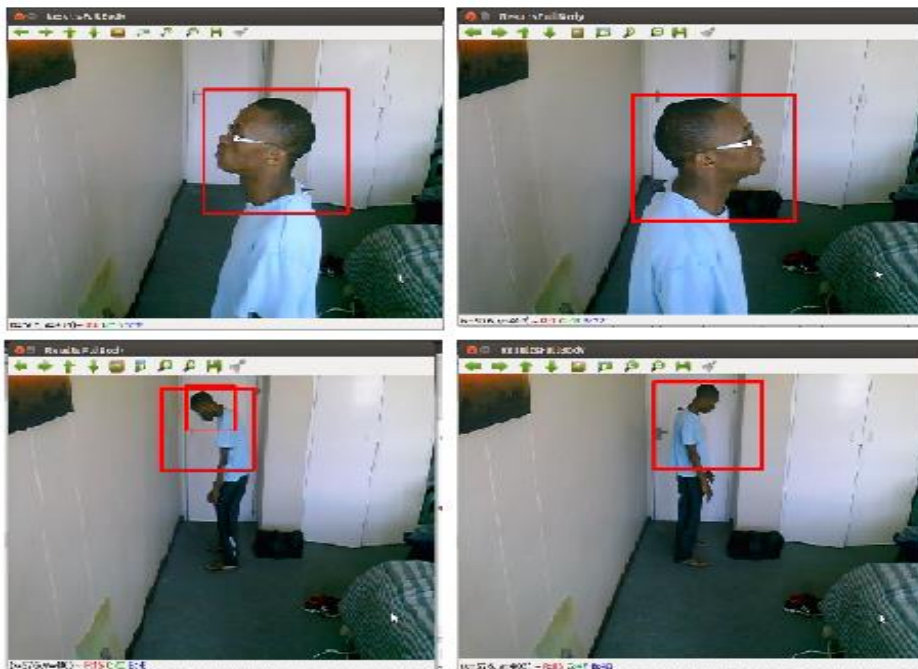


Figure 14. Side detections at 1 meter (top) and 4 meters (bottom) from the camera.

Figure 15 shows the model detecting a human hand. The results below are from consecutive frames that were captured one second apart during the experiment. The sequence of the video frames left to right, top to bottom.

The full body model was found to also be able to detect an obstructed person. The experiment was conducted with the human approximately three meters away from the camera as shown in Figure 16. The model was able to detect the foot and hand.

This represented a case where a human would be trapped under a rock with a limb showing. The frames follow each from left to right, top to bottom.



Figure 15. Final full body model detecting human hand.

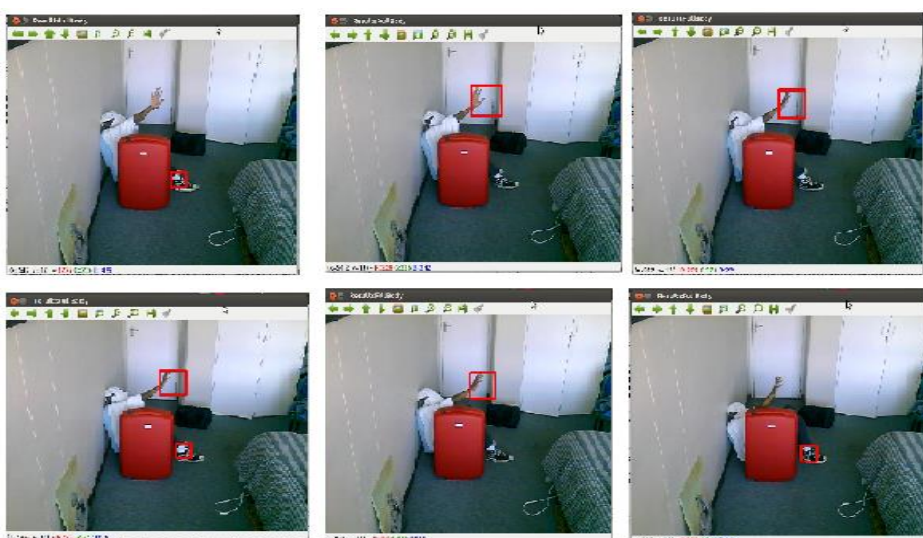


Figure 16. Final full body model detecting human hand and foot.

4.2. Model Comparison

OpenCV has a full body human detection Haar Cascade model that is distributed with it. This model was initially tested before the development of the final model tested above and was found to have challenges in side view and back detections. A new model was developed and tested throughout the different stages of development. This section presents a comparison between the OpenCV distributed model (Generic model), the developed model in its preliminary stages that was briefly discussed in Section 3 and final model. The experiment was carried out with one video with the human rotating to each of the human body side (left, front, right, rear), at every meter ranging from 1 meter to 5 meters from the UAV. These steps towards the UAV were repeated ten times to create 10 samples for each of the four sides. The same video was used so that the models were tested on the same data, making the comparison to have one same reference and the results comparable. The lighting conditions were not the same as those in the experiments presented in section 2.2.1. a). The lighting conditions were not uniform (darker toward the camera and lighter further from the camera). The latter part represented a case where there could be a light source that makes the rescue environment lighting non uniform. The video was then processed in Ubuntu and the true positive and false positive detections recorded. The average true positive and false detection percentage, at the different distances, was then calculated and plotted. The video contained one person. A true positive detection was recorded as one (hundred percent). A false positive detection was counted as one, where a false positive detection counted as a 100% false detection. The aim is to get the lowest false detection and the highest positive detection, which is a one (100%) in this case. The results for the average detection and average false detection are presented in Table 2 and Table 3 respectively.

The results in Table 2 and Table 3 were plotted. From the results it was observed that the average false detection was highest for the preliminary model, followed by the generic model and the final model, which had the lowest average false detection. The generic model's average detection was the lowest of the three models. The preliminary model had a better average positive detection in comparison to the final model at two meters for all the sides except the right side. For the right side the average positive detections are equal at all distances for both models (preliminary and final model). At five meters the rear side average positive detection of the preliminary model is higher than that of the final model. From the results we can thus see that the low average detection and high false detection of the generic model does not make it practical for real world applications, as it will give false impressions to the rescuers.

The final model has a low average false detection with a minimum average true positive detection of 80 percent at two meters on the rear and front side. The final models average true positive detection is high enough for practical use. The rear view average true positive detection and average false detection results for the different models discussed is given in Figure 17.

Figure 18 shows the front view results for the average true positive detection and average false detection for the three models discussed. The average detection and average false detection results of the left side are presented on Figure 19. Figure 2020 presents the image processing results of the three models on the right side view.

Table 2. Average Detection

Average Detection												
	Rear			Front			Left			Right		
Distance	Generic	Prelim	Final									
1	0.1	0.9	1	0.2	1	1	0	1	1	0.3	1	1
2	0.6	1	0.8	0.4	1	0.8	0.7	1	0.9	0.5	1	1
3	0.4	1	1	0.8	1	1	0.5	1	1	0.7	1	1
4	0.9	1	1	1	1	1	0.9	1	1	0.9	1	1
5	0.8	1	0.9	0.9	1	1	0.2	1	1	0.5	1	1

Table 3. Average False Detection

Average False Detection												
	Rear			Front			Left			Right		
Distance	Generic	Prelim	Final									
1	0.4	2.5	0	0.6	2.7	0.1	0.6	2.7	0	0.9	3.6	0
2	0.7	4.2	0.1	0.8	5.6	0	0.7	4.7	0	0.6	5.6	0.1
3	1.1	5.4	0.1	0.9	8.1	0	0.7	3.9	0	0.8	7.3	0
4	0.9	5.5	0	1	6	0	1.2	5.9	0	1.2	5.7	0
5	0.8	4.9	0.1	1.1	5	0	1.2	4.7	0	0.8	5.5	0

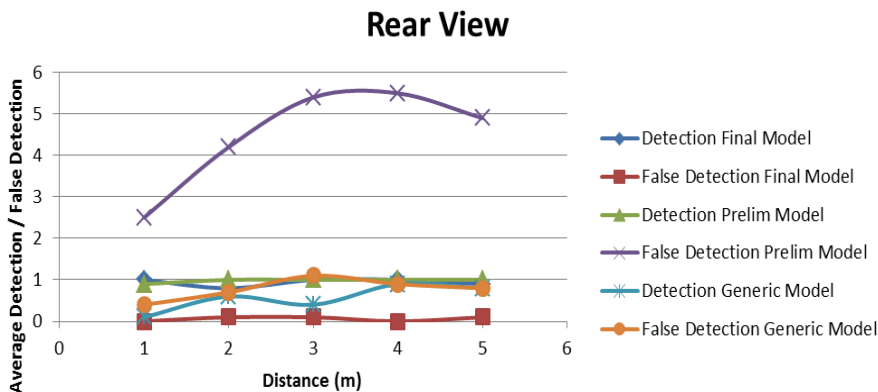


Figure 17. Rear View Models Results.

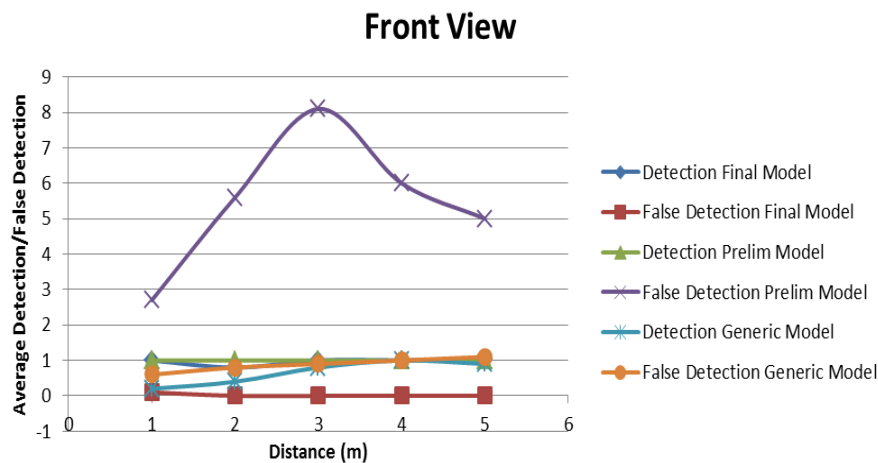


Figure 18. Front View Models Results.

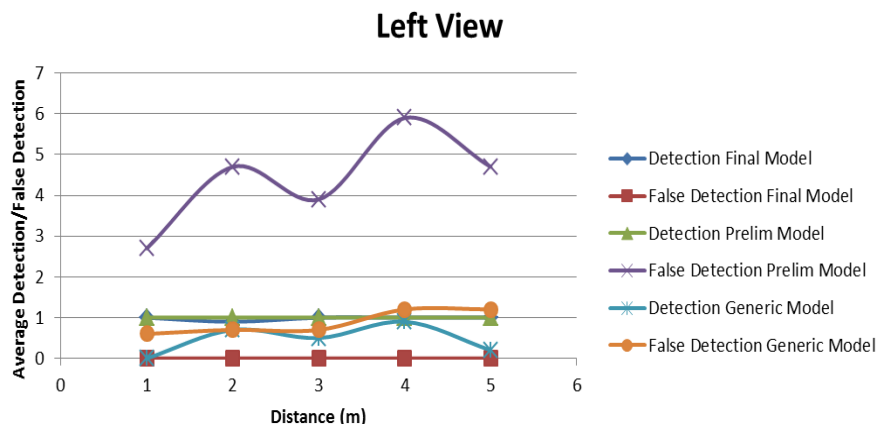


Figure 19. Left View Models Results.

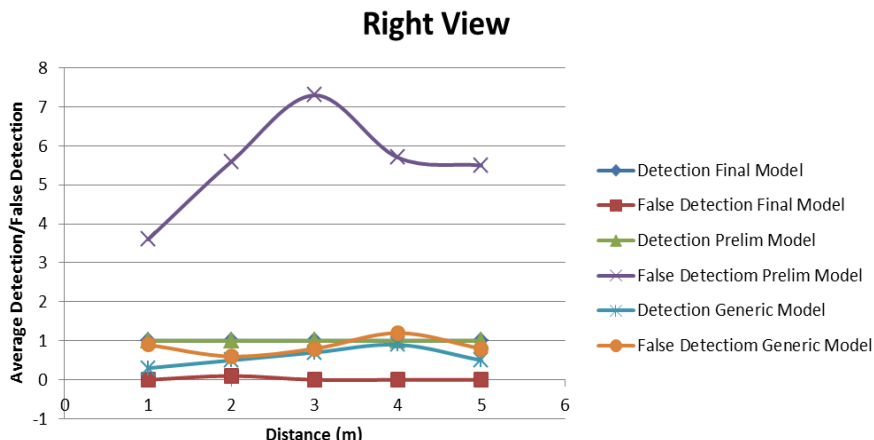


Figure 20. Right View Models Results.

Figure 21 shows the results from the first experiment on the left side view, with the object four meters away from the UAV camera. The top left image shows the generic model's positive detection and a false detection. The top right image in Figure 21 shows a true positive detection results from the final model. The bottom image shows the preliminary model results. The preliminary model had six false detections and a positive detection. Multiple detections are seen on the object due to the model evaluating different human features in the image.

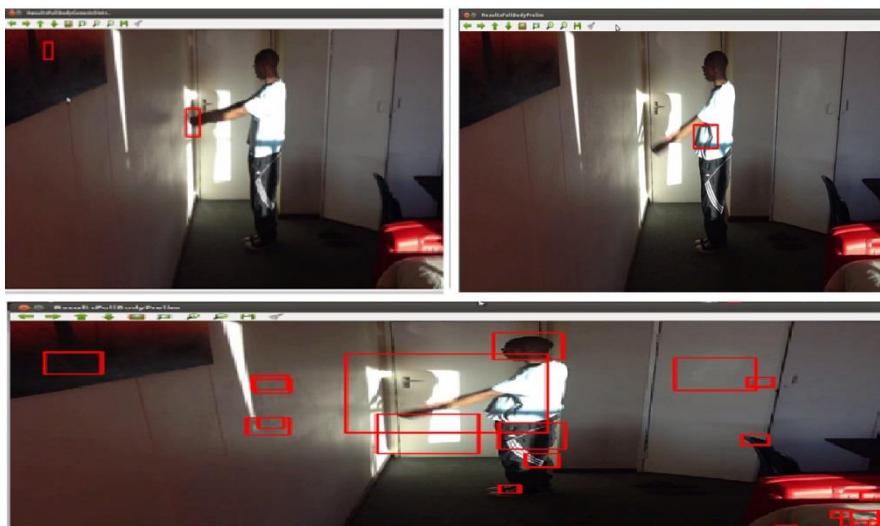


Figure 21. Left side detection of different models, clockwise from top left; generic model, final model and preliminary model.

Sample positive images were used to verify the three different models. Figure 22 shows the generic model results, while Figure 23 and Figure 24 show the results of the preliminary and final model respectively.

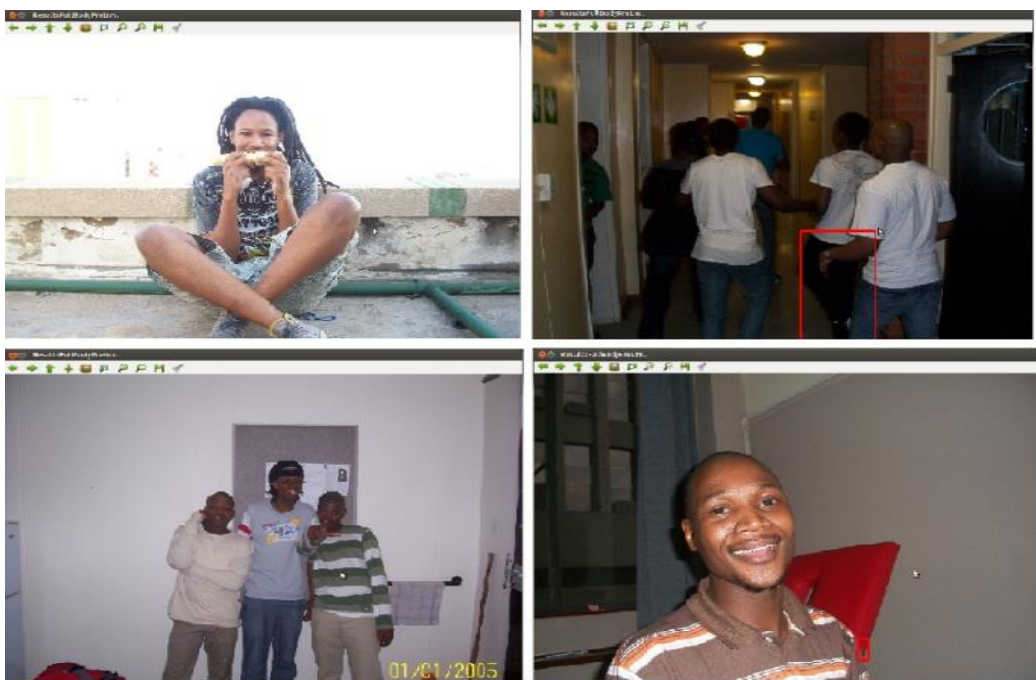


Figure 22. The results of the generic model on the positive sample images.

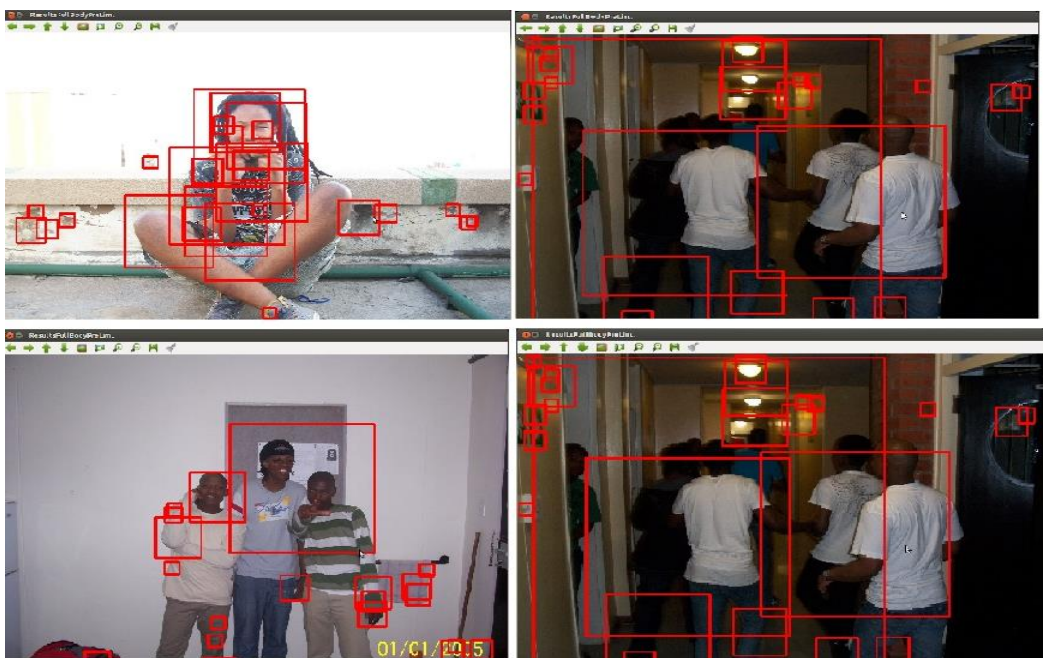


Figure 23. The results of the preliminary model on the positive sample images.



Figure 24. The results of the final model on the positive sample images.

CONCLUSION

The vision system for the UAV was presented and the development of the system was also discussed. The need for the development of a model was shown by comparing the generic model and final model. The need to improve the preliminary model was shown by testing the model. The generic model had an average false detection that was higher than its average detection. This high average false detection makes the model impractical in search and rescue missions, as it will generate a large number of false alarms to rescuers. Similar results were observed with the preliminary model, with this model (preliminary model) having the highest average false detection as compared to the other two models. This high average false detection the preliminary model was observed as a tradeoff for the high average true positive detection. The final model had a low false average detection and a high average positive detection. The average detection is greater or equal to ninety percent in all experiments except the two cases on the right and left side view, where the human was at two meters away from the UAV.

The final model had a maximum false average detection of ten percent (10%) as opposed to the eight hundred and ten percent (810%) and one hundred and twenty percent (120%) maximum values of the preliminary and generic model respectively. Thus the final model was the best model to use for the application.

This final model can also be used for unmanned ground vehicles (UGV) vision systems in human search and rescue missions. Future work can look at applying the human detection model in game reserves where a signal can be sent to game rangers if there is a person that is in an area without authorization. This application can help reduce rhino horn poaching. Future work also includes development of mobile expandable wire-less communications for use in underground mining environments during rescue missions.

ACKNOWLEDGMENTS

Sibonelo Motepe thanks a lot his wife, for the continuous support through the long research hours. He thanks his MSc. Eng research supervisor, Prof. Stopforth, for his insight and guidance. He also thanks the Council of Scientific and Industrial Research (CSIR) for funding his research.

ABOUT THE AUTHORS



Sibonelo Motepe was born in South Africa, in 1988. He graduated in 2010 for a BSc. Electrical Engineering and an MSc. in Mechanical Engineering (Mechatronics) from the University of Kwaz-Zulu Natal. He is currently working as a power system network optimization engineer at Eskom.



Riaan Stopforth graduated with a B.Sc. Eng (Electronics), M.Sc. (Computer Science) and Ph.D. Eng (Mechanical) from the University of KwaZulu-Natal, who has specialized in the field of Mechatronics Engineering. His research interest is in the area of search and rescue robotics and bio-engineering systems. He is currently appointed as an Associated Professor at the University of KwaZulu-Natal.

REFERENCES

- Ahilan, A. and James, E., "Design and Implementation of Real time Car Theft Detection in FPGA", 3rd International Conference on Advanced Computing (ICoAC), Pages 353 – 358, 2011
- Bradski, G. and Kaehler, A., "Chapter7: Histograms and Matching", Learning OpenCV, O'Reilly Media, USA, 2008
- Bradski, G. and Kaehler, A., "Learning OpenCV", September 2008
- Hussein, M., Abd-Almageed, W., Ran, Y. and Davis, L., "Real Time Human detection in Uncontrolled Camera Motion Environments", IEEE International Conference on Computer Vision Systems, 2006
- Kosecka, J., "Shape based matching", Lecture notes, March 2006
- Latecki, L.J., "Template Matching", Temple University, Lecture Slides, March 2005
- Mahalingam, T. and Mahalkshmi, M., "Vision Based Moving Object Tracking through Enhanced Color Image Segmentation using Haar Classifiers", Trendz in Information Sciences & Computing (TISC), Pages 253-260, 2010
- Motepe, S., Chikwanha, A., Stopforth, R., "Survey and Requirements for Search and Rescue Ground and Air Vehicles for Mining Applications", M2VIP, New Zealand, 2012
- Nanda, H. and Davis, L., "Probabilistic template based pedestrian detection in infrared videos", Intelligent Vehicle Symposium, 2002. IEEE, vol. 1, pp. 15 -20, June 2002
- Reuters, "Mine rescue mission continues", <http://www.theage.com.au/news/world/mine-rescue-mission-continues/2007/10/04/1191091228892.html>, 4 Oct 2007, last accessed 24 Feb 2013
- SAPA, "Rescuers killed searching for miner", <http://www.news24.com/South Africa/News/Rescuers-killed-searching-for-miner-20110927>, 27 Sept 2011, last accessed 24 Feb 2013
- Urbina, I., No Survivors Found After West Virginia Mine Disaster, <http://www.nytimes.com/2010/04/10/us/10westvirginia.html> , 9 Apr 2010, last accessed 24 Feb 2013
- Viola, P. and Jones, M., "Rapid Object Detection using a Boosted Cascade of Simple Features", Conference on Computer Vision and pattern Recognition, 2001
- Weber, M., Background image dataset, California Institute of Technology, <http://www.vision.caltech.edu/html-files/archive.html>, 2003
- Zheng, K., Zhao, Y., Gu, J. and Hu, Q., "License Plate Detection Using Haar-like Features and Histogram of Oriented Gradients", 2012 IEEE International Symposium on Industrial Electronics (ISIE), 1502-1505, 2012

Chapter 6

A LOW COST, EXTENDABLE PROSTHETIC LEG FOR TRANS-FERMORAL AMPUTEES

Drew van der Riet¹ and Riaan Stopforth^{#2}

¹Mechatronics and Robotics Research Group (MR2G)

Bio-Engineering Unit, School of Engineering,
Howard College Campus, University of Kwa-Zulu Natal,

Durban, South Africa

²Mechatronics and Robotics Research Group (MR2G)

Bio-Engineering Unit, School of Engineering,
Howard College Campus, University of Kwa-Zulu Natal,
Durban, South Africa

ABSTRACT

People who have lost a leg have a diminished capacity to complete daily tasks. While prosthetic limbs are not a new field, adjustability of such limbs is proposed to increase the life span of the prosthesis. The increased life span of a prosthetic limb will greatly decrease the cost an amputee has to spend over the years on prosthetics; the need for a replacement will be less.

The main objective for the research was to design a low cost, adjustable upper-limb prosthetic leg. The adjustability of the leg allows the user to keep the same prosthesis for a longer period of time as the prosthetic leg is able to adjust to match the growth of the body. The design of the leg allowed for an electric knee, should the user wish to upgrade to one. The leg was designed to focus on strength, natural gait mimicry and promote adjustability of both leg and foot length. The design of the foot and ankle was aimed at simplicity and affordability.

* E-mail address: 213569879@stu.ukzn.ac.za

E-mail address: stopforth@ukzn.ac.za; phone: +27 31 260 1063.

1. INTRODUCTION

Prosthetic legs provide an amputee with the opportunity to have a fully functioning limb. The use of prosthetic legs prevents the need for a wheel chair. These artificial limbs assist handicapped people in leading a more regular life. People (especially children) who need prosthetic legs have to replace them in periodic times as the person develops and grows. This research requires the design and development of prosthetic legs that will consist of modular integration to allow the people to add links or sections to their prosthetic legs, depending on their development. The aim of this research is to design and build adjustable prosthetic legs. An adjustable prosthetic leg will allow the user to keep the same prosthesis for a longer period of time, despite the user's growth.

There are two types of prosthetic legs: above the knee prosthetics and below the knee prosthetics. Below the knee prosthetics are known as trans-tibial prosthetics, where the patient only requires the lower limb to be replaced. These prosthetics consist of a socket, shank (shin) and a foot. The socket needs to protect the residual limb, as well as providing the means for the amputee to effectively transfer their weight to the ground via the actual prosthesis. A means of suspension is also required to ensure that the socket remains secured to the residual limb (Kelly, 2012).

Above the knee prosthetics are known as trans-femoral prosthetics. These are more complicated as a knee system needs to be incorporated. A trans-femoral prosthesis is made up of a socket, a knee system, a shank, an ankle joint and a foot. Modern day trans-femoral prostheses disregards the use of an upper shank (connected between the socket and knee), but rather the knee is connected directly to the socket and the prostheses only consists of the lower shank, which is connected from the knee down to the ankle. Trans-femoral prostheses require swing phase control to control the gait cycle of the prosthetic leg (Micheal, 2012).

Before designs and ideas can be produced the way in which humans walk needs to be studied. This method of walking is called the gait cycle. The term gait describes a particular manner or style of walking while the term normal gait is a general walking pattern applicable across sex, age and other variables. Developments in feet and ankle prosthetics have allowed for more freedom when moving. Innovations have led to more stability in the heel and better absorption of shock when moving (Zahedi et al., 2004). Amputees could want to swim, cycle or snow ski. They could want to run, dance or play golf. All of these different lifestyles include different requirements of the ankle. With developments in prosthetics; the amputees now have these options available to them (Osborne, 2012) so that they can partake in such activities.

The normal gait cycle is divided into two major phases, the stance phase and the swing phase. The stance phase describes the time that the foot is on the ground. It is during this phase that the leg is loaded with the weight of the user. The swing phase refers to the time when the foot is in the air, swinging forward. The stance phase takes up 62% of the gait cycle and the swing phase takes up 38% (Schaffer, 2012).

The quadriceps and hamstrings provide the control needed for the knee joint to extend and flex correctly during the gait cycle. They both move the knee and lock it so that it does not bend incorrectly. The ligaments and bony structure of the knee joint provide a strong foundation for both static and dynamic function. The hip and ankle joint also increase the level of control and stability during walking but the knee is the most critical.

A percentage scale is used to describe the events of the gait cycle as everyone walks at with different cadences. By definition the initial foot strike occurs and 0 % and the second foot strike happens at 100 % (Lim, 2008).

A more in depth approach to the gait cycle shows that within the two phases of swing and stance, there are eight different branches. The stance phase is broken into the initial contact (IC), loading response (LR), mid-stance (MSt), terminal stance (TSt) and pre-swing (PSw). The swing phase consists of the initial swing (ISw), mid-swing (MSw) and terminal swing (TSw). (Lim, 2008). The percentage of time that these phases take up of the gait cycle can be seen in Table I.

Table 1. Phases of the Gait Cycle

Phase	IC	LR	MSt	TSt	PSw	ISw	MSw	TSw
Percentage (%)	0	0 – 12	12 – 30	30 – 50	50 – 62	62 – 75	75 – 85	85 - 100

1.1. Objectives

The leg needed to be able to withstand the static and dynamic loads produced by a person during walking. The components that have been designed are: a socket which is fitted around the quadriceps and residual limb of the user; shanks, commonly referred to as pylons; a knee system and an ankle/foot system.

While the research is not focused on redesigning the prosthetic legs, it looks at overcoming the budgetary constraints to provide lower income citizens with the opportunity to invest in a long lasting prosthesis. The main focus of the research is the criteria of low cost and adjustability.

The inter-changeability of parts will accommodate for both trans-tibial and trans-femoral prosthetics. In other words, because of the modular structure, the prosthesis will be able to function as either a below the knee or above the knee prosthesis. To change between the two, one will simply change where the socket connects, either to the lower shank or the higher one. This will determine if a knee joint is included in the prosthesis or not. The prosthetic leg has the following design objectives:

- The design needs to be adjustable
- The legs need to be modular in structure to allow for inter-changeability of parts
- The structure needs to be lightweight so as to not hinder the user who may have diminishing muscles in the residual limb
- The prosthetic needs to be strong enough to support a weight of 100 kg.
- The prosthetic needs to be applicable to situations faced by young and old people

2. DESIGN

The complexity of the leg depends on the design of the knee joint as the knee decides the walking speed. The knee joint also supports the user and allows the leg to bend when sitting

and walking. Artificial knee joints are generally classified as single axis or polycentric (multi-axis). Naturally single axis knees only have one degree of freedom while polycentric knees have multiple axes of rotation (Dupes, 2012).

The major difference between the different kinds of prosthetic knee joints is the method they use to control the swing phase of the gait. The different swing phase control techniques include hydraulics, pneumatics, springs, constant friction, varying friction and robotics.

A purely mechanical knee that doesn't offer swing phase control is the manual lock knee. Manual lock knees are used by those who lack stability as well as individuals who often walk on uneven terrain (Dupes, 2012). The manual lock knee is usually locked completely straight when the user is walking. With this knee mechanism the user provides no voluntary stance control as the prosthesis does it all. However a stiff knee may be dangerous in the event of a stumble as the knee cannot be bent to allow the user to stabilize them self. A person using a manual lock knee has to pull a release lever to unlock the knee when sitting down. This procedure is often awkward and can be frustrating for the user. However, manual lock knees are better suited to running as people with prosthetic legs usually run with a straight leg that swings in an arc, similar to the swing phase created when using a manual lock knee. Manual lock knees are also very light which makes them advantageous for children.

Another mechanical knee joint is the friction controlled knee joint which uses friction to control the swing phase of the gait. These consist mainly of a mechanical hinge and are the most durable as well as economic knee joints. Friction knees often use constant friction to control the knee extension and are more specifically known as the single axis constant friction knee. It consists of a basic mechanical knee that bends freely. Friction in the knee and hence the ease of bending, can be adjusted by tightening a bolt in the knee (Artisan Orthotic and Prosthetic Technologies, 2012). As previously stated this knee joint is cheap, durable and it also requires the least maintenance. However, it has various disadvantages. This type of knee requires the amputee to rely on their own muscle control for stability. For this reason it is generally used by children, who have a lower centre of gravity, and by patients with good musculature control.

Another disadvantage is that the user is only able to walk at one speed and cannot walk faster at will as the friction is not able to vary itself. This is where variable friction comes in as a means to control the extension of the knee. Variable friction allows the user to walk at different speeds. However, variable friction knees require lots of adjustment and repair to moving parts. Variable friction knees are considered less advanced than fluid control knee systems despite the need for regular maintenance of the variable friction knee (Dupes, 2008).

2.1. Knee Design

The knee joint is where the lower leg and the upper leg meet. The knee joint is only required to have a single degree of freedom (DOF) allowing the knee to bend. The lower leg part of the knee joint is referred to as the support, which connects the knee joint mechanism to the lower leg. A rectangular design was created to provide a maximum weld length. Figure 1 shows how the horizontal cross piece fits around each vertical frame piece and holds the frame together. The bolting, in addition to welding, would offer extra support and would also allow the knee joint to be disassembled if a component broke. The maximum shear stress of the welds was found to be 18.74 MPa.

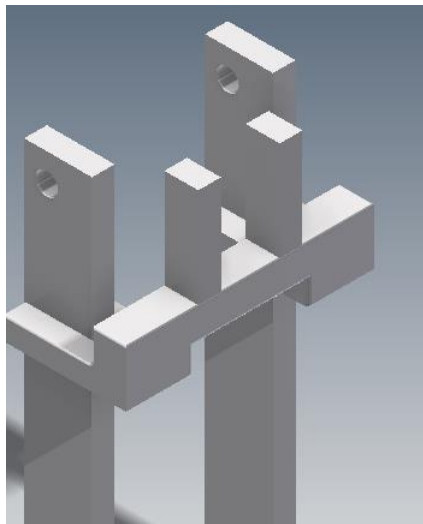


Figure 1. Final support design.

The shaft of the knee joint needs to hold the weight of the person during the stance phase of the gait cycle. If the shaft fails it will fail in shear as the force acting on it is perpendicular to its axis. Using the general stress equation, Equation 1, the stress in a 10 mm shaft was calculated to be 28.10 MPa where a safety factor of 1.5 was used. The force used in this equation was the maximum mass of the user for which the prosthetic is being designed (150 kg). The stress in the shaft with a diameter of 10 mm was well below the shear yield strength of aluminium which is 207 MPa. A reserve factor of 7.3 is obtained, which is very high. However, the diameter of the shaft cannot be reduced as the shaft diameter is determined by the bearing specifications.

$$\sigma = \frac{S_f F}{A} \quad (1)$$

The final dimensioned shaft can be seen in Figure 2. Each hinge piece sits on a bearing and the connector piece sits on the hinges as seen in Figure 3. The distance between the centre of the hinges (bearings) was determined by the distance between the holes in the connector piece which was 36 mm. Naturally, the hinges should have the same width as the bearings (14 mm). This width resulted in a distance of 22 mm between the hinges as the distance between the centres needed to be subtracted by half the thickness of each hinge/bearing, which was how the length of the stepped diameter was determined.

The swing phase control length is made up of the piston housing, the piston and the connection units that allow the swing phase control to pivot on each end. The piston in the spring design is made up of an 8 mm diameter rod that has a spring around it. A few millimetres of the bottom of the rod rest inside the piston housing when the leg is straight, which will prevent the rod from moving out of the housing. The top of the rod connects to the hinge piece through a clevis joint.

The piston in the mechatronic design consists of a threaded power screw. In this mechatronic design there is a nut that fits the power screw. The motor will turn this nut

through the use of a gear. In an attempt to make the switching between the mechanical and mechatronic design easier, the same piston is used for both.

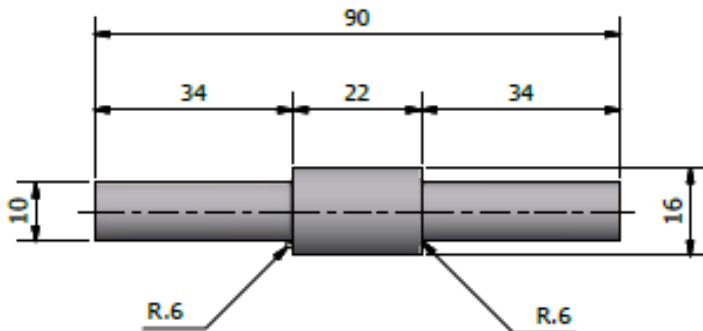


Figure 2. Shaft dimensions.

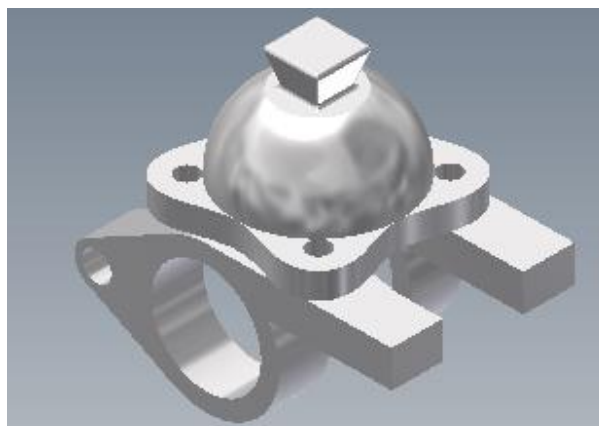


Figure 3. The connector on the hinge pieces.

The principle of operation for these designs is very different. The spring system uses momentum and resistance to control the bending of the knee. The knee joint relies on momentum of the lower leg to cause the knee to bend and the lower leg to rise when the residual limb is lifted during toe-off. The spring system then slows down this rotation of the lower leg by compressing as the knee bends. The spring then simulates the extension of the knee by extending again. This type of operation assumes that when the residual limb is lifted during toe off, the knee bends as a result of momentum.

The mechatronic system is based on a very different principle of operation. With this design the motor will lift the lower leg during flexion and extend it forward. This design assumes that there is no momentum lifting the lower limb after toe-off.

When the leg is straight and the spring is at its maximum length during the gait cycle, it is still slightly compressed. The preload force may be great enough to prevent the backlash of the leg after extension. This will be the case if the force of the backlash is less than the preload of the spring. However, if the preload is too high then the momentum of the lower leg might not be large enough to compress the spring and bend the knee. The preload of the spring can also be adjusted by adding thicker plastic bushes between the base of the spring

and the piston housing. A thicker bush will compress the spring more when the leg is straight thus creating a larger preload. The preload solution also assists the problem of variability in walking speeds as a higher preload means a higher momentum force can be absorbed and that extension of the leg will occur faster.

A smaller knee joint needed to be designed to increase the adjustability range of the leg. The joints that offered swing phase control were too large to have an adjustable pylon between the knee joint and the ankle. It was decided to design a manual lock knee as this type of knee joint has no swing phase control due to the fact that it remains straight while walking.

As with the swing phase control knee, the manual lock knee design consisted of a frame and a top section that could lock onto the frame or be free for when the user wishes to sit.

The frame of the manual lock knee needed to be a lot smaller than that of the swing phase control knee.

The frame design can be seen in Figure 4. The frame needed to be tall enough to allow the rear end of the top section to fit into the frame when the joint was bent.

As mentioned earlier in the chapter, the line of the leg needed to be 6 mm in front of the centre of rotation of the joint. Using this fact and the size of the pyramid connector (52 x 52 mm), the length of the joint in the sagittal plane could be determined.

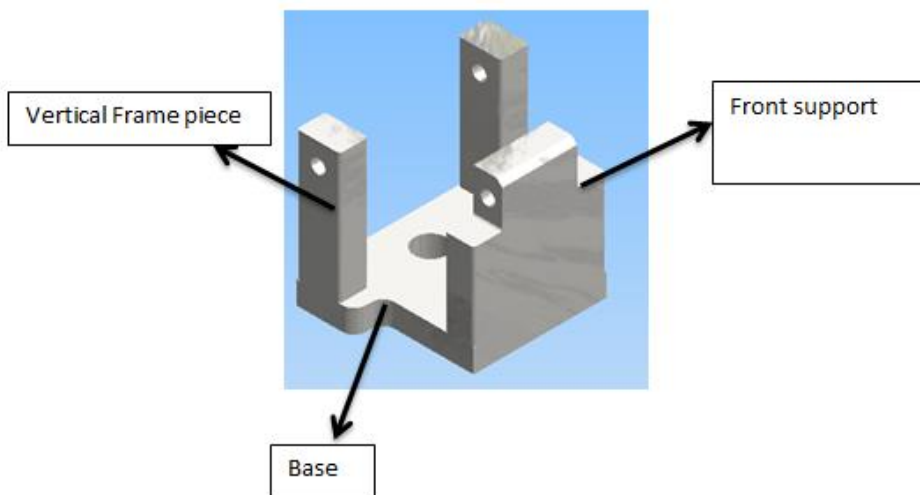


Figure 4. Manual lock knee frame design.

The support piece at the front of the joint assists in carrying the load of the user, meaning the lock pin would not need to take the full load during walking. The frame was designed to bolt together and have small welds to add to the bolt strength.

The pyramid connector bolts onto two beams that rotate relative to the frame work, causing the knee to bend. The pin locks/unlocks the joint that locks these two beams to the support piece at the front of the frame. This configuration can be seen in Figure 5.

The shaft at the joints centre of rotation does not need to have bearings as the joint would not be bending as often as the swing phase control knee. Working with the maximum user weight of 150 kg, the minimum possible shaft diameter was calculated to be 4.29 mm.



Figure 5. Manual lock knee in the lock position.

This calculation was done using the general stress equation where the subject of the formula was changed to result in Equation 2. The shear yield stress of the material is 207 MPa. A safety factor of 2 was used.

$$d = \sqrt{\frac{4 \times F \times S_f}{\pi \times \tau_Y}} \quad (2)$$

Rounding up the minimum diameter yields a shaft diameter of 5 mm which was therefore selected. The same calculation can be done for the pin of the joint which was therefore also chosen to have a diameter of 5 mm.

The two columns that hold the shaft, around which the joint rotates, could be susceptible to buckling. As with the frame analysis, the buckling was only investigated in the plane with the lowest moment of inertia. The critical load was calculated to be 104 MN according to Equation 3. The columns will not buckle as the critical load is far greater than the load induced by the user.

$$P_{cr} = \frac{\pi^2 EI}{(KL)^2} \quad (3)$$

As discussed earlier the resultant gait of a user that is using a manual lock knee is awkward. The swing phase takes place in an arc where the hip swings outward away from the body and then back in as the leg travels forward. This swinging arc results in lateral loading of the manual lock knee. The lateral loading will cause a shearing force on the bolts that attach the base to the support and the vertical frame pieces. These bolts were selected to be class 8.8 M4 bolts. It was assumed that the lateral force was the mass of the user. The resultant stress in each bolt was 175.65 MPa. A safety factor of 1.5 was used and a reserve factor of 2.2 was obtained.

A two piece bracket was designed to mount the motor to the cylinder that makes up the piston housing. One piece is used to fit onto the piston housing. It is a rectangular block with a hole in the middle, where the cylinder fits. This block is kept in place through the use of grub screws. The other piece bolts onto the first part and extend to the motor where it will bolt into the motor. The motor has four tapped holes on the top of it which makes it easy to bolt to a plate. An additional keeper plate was designed to hold the gear in place so that the power screw will move and not the gear (nut). This keeper plate attached to the motor mount and the full mounting system can be seen in Figure 6.

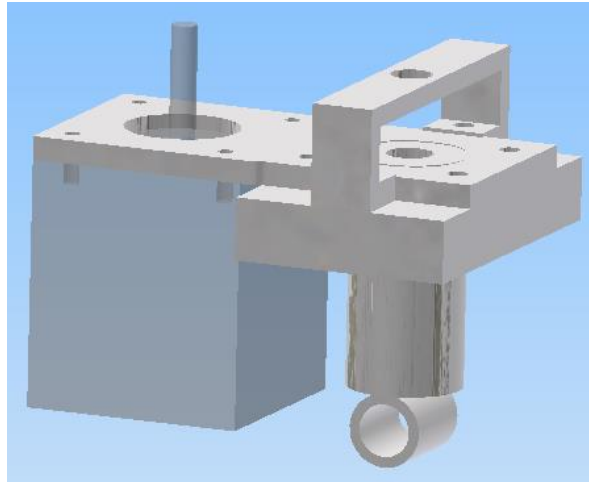


Figure 6. Motor mount.

This motor mount design is easily removable as it can be taken off the cylinder once the grub screws have been taken out. This design also allows the gear ratio to be changed if desired. If the gear ratio is altered, then all that needs to be done is the top plate needs to be remade, either longer or shorter, depending on the new gear ratio.

The motor connects to a threaded rod which acts as power screw. The torque required to lift a load (W) by turning a power screw is given by Equation 4. (Juvinal, 2006).

$$T = \frac{Wd_m}{2} \times \frac{f\pi d_m + L \cos \alpha}{\pi d_m \cos \alpha - fL} + \frac{Wf_c d_c}{2} \quad (4)$$

The power screw in this design has a nominal diameter of 8 mm. The root diameter is 6.47 mm and the pitch is 1.25 mm (Juvinal, 2006). The lead (L) is the linear distance travelled by the power screw for one revolution and is equal to the pitch. This lead value is important when calculating the required speed from the stroke. The mean diameter is an average between the nominal and root diameter. The mean diameter for this power screw is 7.235 mm. A friction coefficient was assumed to be 0.7 (worst case scenario). The friction of the collar (f_c) was taken to be 0.2 (Juvinal, 2006). The angle alpha for metric threads is 30°. As these values remain constant Equation 4 can be simplified into Equation 5.

$$T = W \times 0.0044682 \quad (5)$$

As the line of force is continually moving when the hip and knee bend, the torque required to lift the lower shank was found at different angles of the knee and hip joint. The angles used were taken from a walking trial that was done at Waterloo Kinesiology Department (Winter, 2009).

The torque required to lift the lower shank was calculated at only three points of the swing phase. The first point being at toe-off, the second point was at half way through the flexion movement and the final point was at the end of the flexion.

The force that was used for the motor torque was the weight of the pylons, the weight of the foot, the weight of the knee and the weight of the motor. The moment of the foot about the knee joint also had to be calculated and an opposing force had to be applied at the power screw location. This opposing force is the force that the motor experiences. The results can be seen in Table II.

Table 2. Knee and thigh angles and motor torque at those points

	Beginning	Midway	End
Knee angle	0	33	67.3
Thigh angle	82.7	90	104
Torque required (Nm)	0.3	0.35	0.37

Once the motor has lifted the pylon to 67.3 °, it will lower the pylon to extend the leg. The torque required to lower the leg will be lower as the friction term is subtracted from the load term in Equation 4, instead of being added to it.

As stated above, it is vital for the motor to be as light and small as possible so that the weight of the joint is not compromised. It has been noted that speed will have to be a compromise. The main aim of this mechatronic application is not to try better the designs that are currently on the market, but to rather try and make the prosthetics more affordable. Keeping this in mind, a low cost solution was sought after. A stepper motor was used to control the linear actuation of the power screw as the positional control of a stepper motor is highly accurate (OMEGA Engineering Technical Reference, 2012).

Stepper motors also do not require feedback control which reduces the complexity of the system and hence reduces the cost. Stepper motors have good repeatability and precise positioning as they have an accuracy of 3 to 5% of a step and this error is non-cumulative from step to step (OMEGA Engineering Technical Reference, 2012).

After analysing the required torque of the motor, the 0.48 N.m stepper motor was selected. The characteristics for this motor can be seen in Table III (Netram technologies, 2012).

Table 3. Stepper motor specifications

Step angle (degrees)	0.9
Steps per revolution	400
Rated voltage (V)	3
Holding Torque (N.m)	0.48

2.1.1. Stress Analysis

The material assigned for the knee was an isotropic material with the properties of aluminium. A fixed constraint was applied to the base of the frame to prevent any rotation or translation. The load was then applied in the form of a pressure load over the area in contact with the hinge transferring the force. For this design the pressure load on each vertical support was 9.81 MPa (using a user weight of 150 kg). This simulation was run for the worst possible scenario where the force through each support was the user's full weight. It was assumed that the load was not shared by the two vertical columns. Figure 7 shows that the maximum stress occurred in the regions of high stress concentrations due to 900 bends in the material. The maximum stress was 130.1 MPa.

In addition to the stress tensor results being obtained for this simulation, the deformation plot was also viewed. Figure 7 also shows the deformation plot of the rectangular support structure. Although the image shows a highly deformed structure, this is a relative plot so that the user can see clearly where the deformation is. The maximum deformation of the structure is 0.27 mm which is negligible.

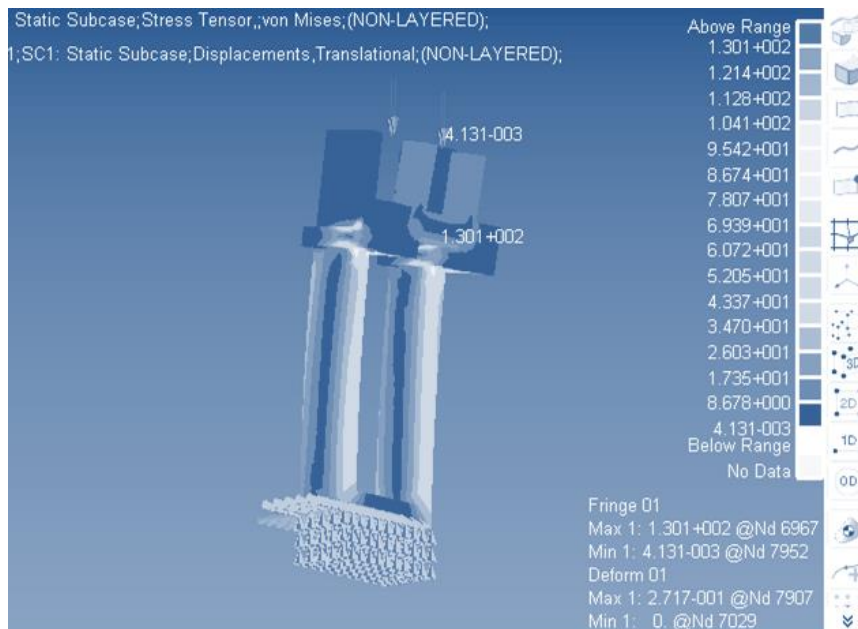


Figure 7. Fringe and deformation plot of the final support design.

2.2. Leg Pylon Design

The crutch-thread pylon consists of three aluminium rods connected to each other to form the pylon framework. These three rods were purchased in standard form and then further fabricated to meet the desired requirements. The Ø 25.40 mm rod, as can be seen in Figure 8, forms the first of two crutch system parts. An 8 mm hole was drilled 12.5 mm from the bottom of the rod. This hole will allow the push button to extrude out from the rod. The push button was attached to a spring steel wire which lies on the inside of the rod. The flexible

nature of this wire enables the button to be pushed in and out of the rod for incremental adjustments.



Figure 8. Upper Rod with Brass Push Button.

The middle rod, in Figure 9, forms the connection of the whole pylon system. It is a Ø 31.75 mm rod which allows the large and fine adjustment.



Figure 9. Middle Rod.



Figure 10. Lower Rod with Thread.

The larger adjustments occur by means of 14 7 mm holes drilled equal increments away from each other, starting from the top of the rod. These holes allow the push button from the upper rod to connect through. The holes were also drilled in a winding shape so as to make the rod less susceptible to failure when put under the stress of the weight of the person. Furthermore, the inside bottom end of the rod is threaded with a pitch of 1.5 mm. This connects to the lower rod by means of mutual threads.

The last component of the pylon system is the lower rod which has a diameter of 25.40 mm. This rod, as seen in Figure 10, possesses a corresponding thread so as to connect to the middle rod. The thread is situated on the outer upper part of the rod. A thread of 20 mm enables fine height adjustment if necessary. An additional 15 mm of this rod is reserved for a connector fitting.



Figure 11. Complete Pylon Assembly.

Figure 11 shows the complete pylon system, whereby each of the three rods is connected to each other. The push button joined the upper rod to the middle rod, whereas the lower rod screwed onto the middle rod via a thread.

2.2.1. Stress Analysis

Stress analysis simulates the pylon under its different loading conditions and depicts where the maximum stress acts. In the first loading condition, the user is predicted to be at standing or heel strike phase, thus experiencing an estimated 105 kg according to Pylon Specifications. An axial force of 1030.05 N acts at the top of the upper rod, causing the predicted buckling of the rod, as exhibited in Figure 12. Furthermore, a maximum stress of 28.94 MPa occurs at the push button. This maximum stress cannot be viewed to the restricted screenshot. The simulation yields favourable results, therefore further deeming the pylon safe to use under loading condition 1.

A similar simulation as the one above was also performed for loading condition 2. However, in this instance, the loading being applied is the maximum weight specification of 150 kg. This weight is due to the toe off phase, whereby all the weight of the person is acting on the one leg rather than two. The force acting on the pylon system is 2060.1 N. The stress analysis yielded favourable results yet again, as can be seen in Figure 13. A stress of 57.87 MPa is experienced on the push button.

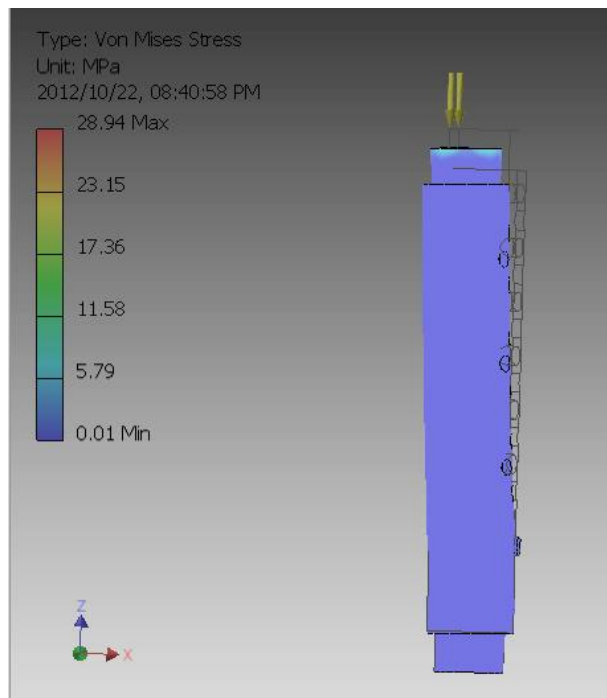


Figure 12. Pylon Stress Analysis under Loading Condition 1.

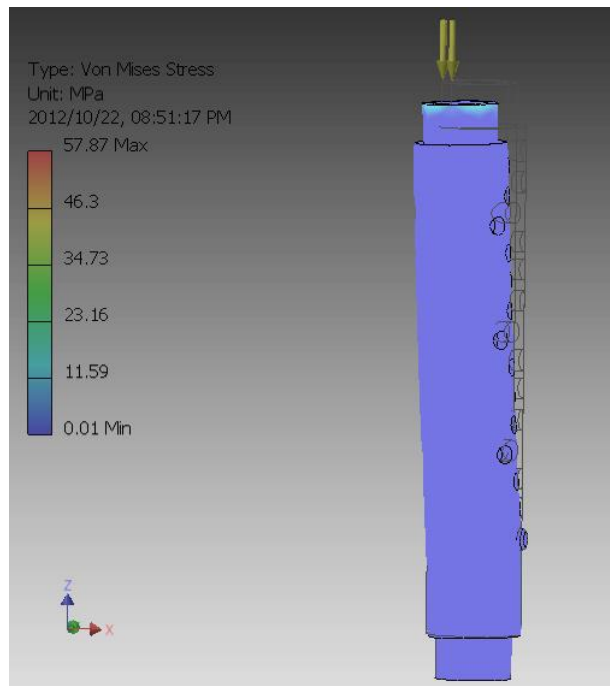


Figure 13. Pylon Stress Analysis under Loading Condition 2.

2.3. Ankle and Foot Design

The upper and lower ankle designs can be seen in Figure 14. A mount for a spring which would simulate the Achilles tendon was also added to the rear of the lower ankle component. The ankle mechanism is a multi-axis system constructed of two serially connected revolute joints. The three components that make up the ankle joint are linked by means of two shafts about which they rotate. The two joints act at 90 degrees to each other and give the foot its two degrees of freedom. The arrangement of the mechanism is described with the aid of the diagram labelled Figure 15.

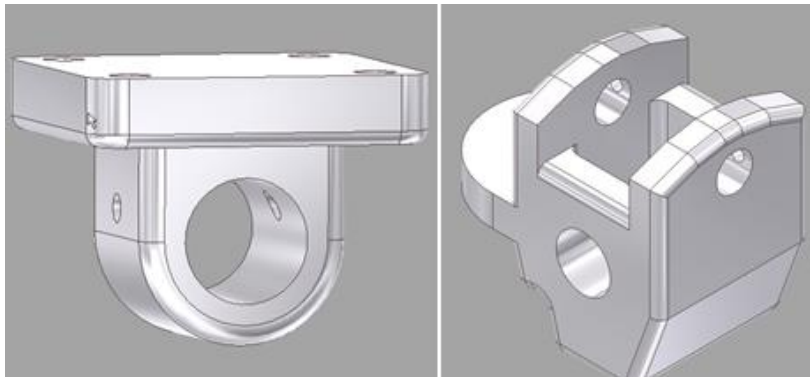


Figure 14. Final Upper and Lower Ankle Joint Design.

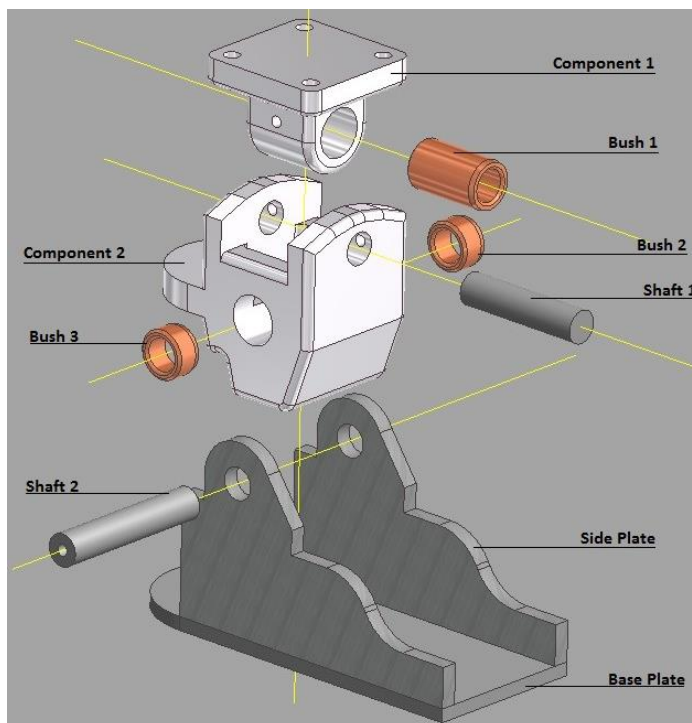


Figure 15. Mechanisms Configuration.

Bush 1 is press fitted with a slight interference fit into component 1, restricting its movement with respect to component 1. Bushes 2 and 3 are press fitted in the same manner into component 2 restricting their movement with respect to it.

The final component is the hind foot subassembly and is made up of two side plates and a base plate. These three individual plates are welded together to form the final hind foot assembly. With the base plate acting as the sole of the foot, the side plates are welded on at 90 degrees to the base plate to create the side wall of the foot to which the rest of the ankle mechanism will attach. The hind foot also included two mechanical stops not seen here, whose location can be seen in Figure 16 in the construction section. These stops act to mechanically limit the maximum range of motion of the joints to within the range attained by the human foot during the gait cycle. This restriction ensures that in the event of a system failure or overloading the ankle will not over rotate. A relatively stable platform remains and the likely hood of injury is reduced.

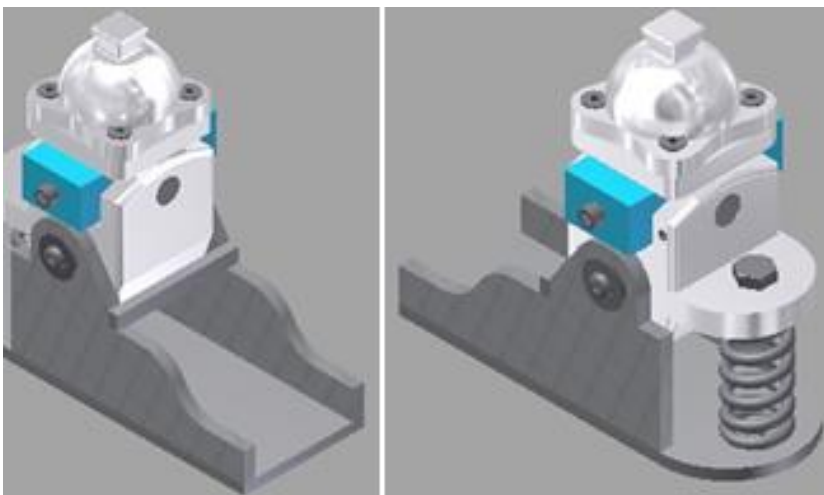


Figure 16. Final Ankle/Heel Model.

Safe and controlled movement of the joints is achieved with the implementation of a range of customisable springs and bumpers. The upper ankle joint is controlled by means of a pair of polyurethane bumpers positioning in the space between components 1 and 2. The lower ankle joint is controlled by means of a spring positioned between the base of the hind foot and mounting platform present on component 2. It is positioned at the rear of the foot and replicated the function of the Achilles tendon. The exact locations of the bumpers and the springs can be seen with complete ankle/hind foot design in Figure 16.

The sole of the foot (shown in Figure 17) has to be made from a flexible material to relieve shear stresses and absorb shock created from the motion of walking while having high strength properties to manage the weight of the prosthesis and the amputee. A polyurethane rubber has the characteristics to meet the specifications to prevent slippage and is the most suitable material for the application. Polyurethane is a unique material that offers the elasticity of rubber combined with the toughness and durability of metal. Urethanes have better abrasion and tear resistance than rubbers, while offering higher load bearing capacity.

More importantly it has an extremely high flex-life and is water-proof; two properties which are imperative for this application (San Diego plastics, 2012).

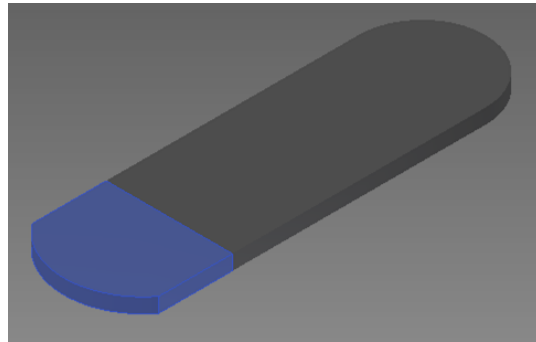


Figure 17. Sole design.

The minimum length (with no extension) of the sole is 200 mm with a thickness of 8mm. The sole splits at the toe and the length may expand to 300 mm, allowing the foot to cover a range of sizes. There are two sliding rods which provide the foot with its unique ability to adjust to a range of different sizes. Furthermore, the foot sliding rods are an integral part of the design and undergo more stress than any of the other components of the foot. During walking, consideration is made towards the body weight of the amputee as well the reaction force of the ground.

The final component of the adjustable foot is the slider and clamping mechanism. As the name suggests, the 16 mm diameter rods slide through this component and are locked in place depending on the foot size of the patient. Therefore the rod guide serves as a support to the rods as well as being a locking device. The large holes for the rods are shown in Figure 18 and are 8 mm in radius with a tolerance 0.15 mm. The tolerance allows for ease of adjustment and prevents friction between the surfaces. A 2 mm chamfer was implemented on the side that meets the housing surface when the foot is not extended. Therefore there is a flush contact between the two components when they meet. A 2 mm fillet was used on the opposite face.

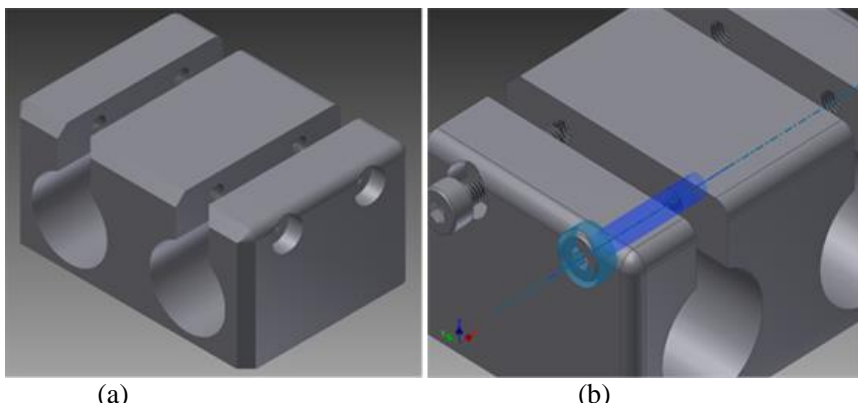


Figure 18. (a) Slider; (b) Clamping Mechanism.

To lock the rods in place, a socket head cap screw was implemented. There are two screws on either side of the slider to clamp each rod. As shown in Figure 18b, the threaded holes run across the 5 mm spacing allocated for tightening. The selected size was a standard M3 x 20 mm cap screw. This method is very simple yet it is practical for the application of a prosthesis. The intention is to make the functionality of the foot as easy as possible considering the user is disabled. The model of the complete foot can be seen in Figure 19.

2.3.1. Stress Analysis

The Finite Element Analysis (FEA) analysis, shown in Figure 20, was performed with a pressure load of 0.378 MPa acting across the entire surface of the base of the foot and with the foot constrained at the point where the ankle connects to the shaft of the leg. The analytical calculations performed yielded a maximum shear stress of 39.04 MPa acting on the shafts of the joints.

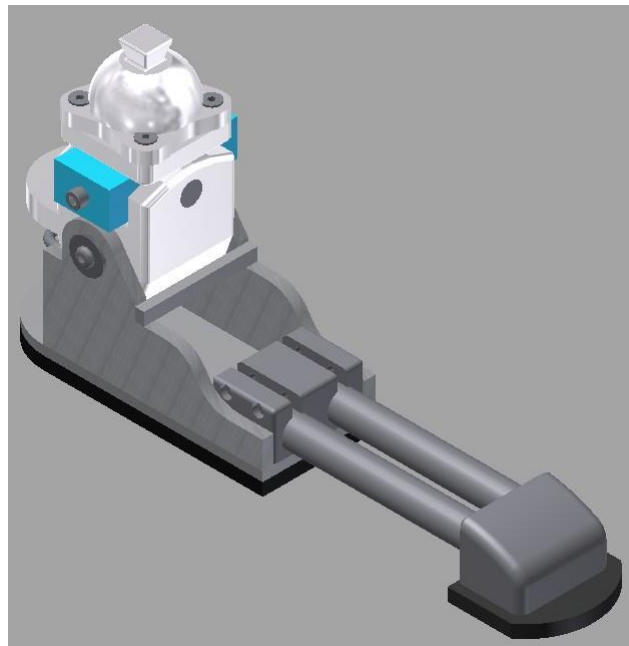


Figure 19. Complete Foot Assembly Model.

The simulation reflected a significantly higher result of 86.9 MPa on the shaft as seen in Figure 20. A slightly higher stress concentration of 89.2 MPa can be seen on one of the corners of the side plate, but this is limited to a very small area and is well below the Ultimate Tensile Strength (UTS) of the specified material and so it was not considered an area of concern.

The exact forces produced during running are very difficult to determine and can vary from person to person. For this reason the FEA analysis, shown in Figure 21, considered the worst case scenario of a force twice that of the maximum user's body weight concentrated at the toe section of the foot. With a maximum stress in the shaft of 168 MPa and a stress concentration of 208.2 MPa on the lower ankle component, the simulation exhibits significantly higher stresses than those in the FEA analysis shown in Figure 20. However, the

stresses for the ankle and hind foot are still well below the UTS of the specified material, proving that even under extreme operating conditions there will be no failure.

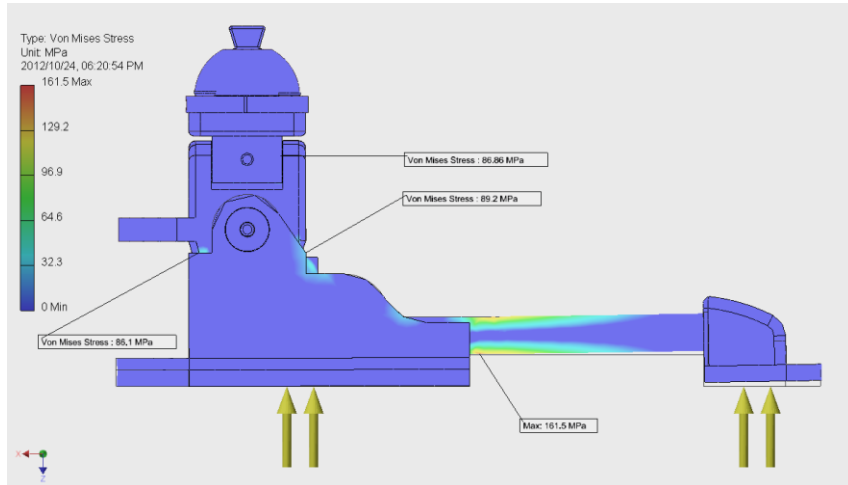


Figure 20. FEA Analysis of flat foot.

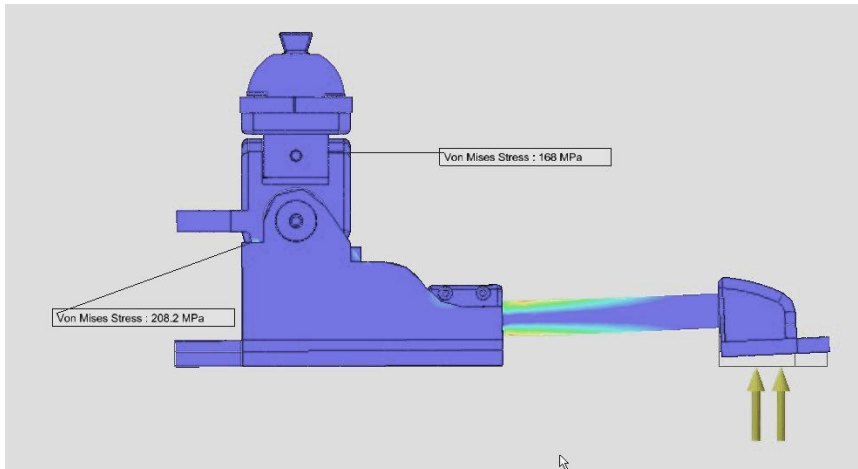


Figure 21. FEA Analysis of running foot.

All results were well within the operating characteristics of the chosen materials. The fatigue stress of Aluminium 7075 T6 is marked as 159 MPa, with a life of 5×10^8 cycles. This corresponds to an approximate life span of 270 years at 10000 steps per day. The force that would be needed to be generated to achieve this level of stress would be equivalent to a person with a mass of 115 kg running. Although the worst case stresses exceed the fatigue stress and would decrease the life span significantly, it is unlikely that the mechanism would be subjected to this sort of stress on a regular basis and failure due to fatigue would be highly unlikely. A maximum theoretical stress of 208.2 MPa results in an overall safety factor of approximately 2.7 which is more than sufficient.

3. TESTS AND RESULTS

Once the construction of the different components was completed, tests could be performed. Various factors regarding the operation of the knee joint were to be determined from testing such as the best spring option and the optimum level of micro-stepping.

3.1. Knee Range of Motion Test

The objective of the test was to determine the range of motion of the two knee joints and then compare the limits of motion to that of other prosthetic legs. The range of motion of the knee joints should not be too large but the knee should be able to bend at least 90 ° to allow the user to sit. The knee could be allowed to rotate more than 90 ° but it does not benefit the user in any way. A negative bend in the knee would result in hyperextension of the knee joint which is highly undesired.

The swing phase control knee joint was bent to its maximum limit in the sagittal plane to simulate extension/flexion of the joint. The angle of the joint was tabulated and compared to existing designs. The same procedure was carried out for the manual lock knee.

Figure 22 and Figure 23 depict the maximum levels of rotation in the sagittal plane. In both knee joints, the rotation only simulated the flexion moment of the knee joint. In simulating the extension of the joints the angle was zero as no hyperextension of the knee is desired.

The results of this test are presented in Table IV, where the results are compared to existing knee joints in the possession of the authors. The lateral rotational limits of the knee joints were not tested as both joints are single axis knee joints. All angles were measured from the horizontal in an anti-clockwise direction. The minimal angle for all knee joints was zero, corresponding to a straight leg.

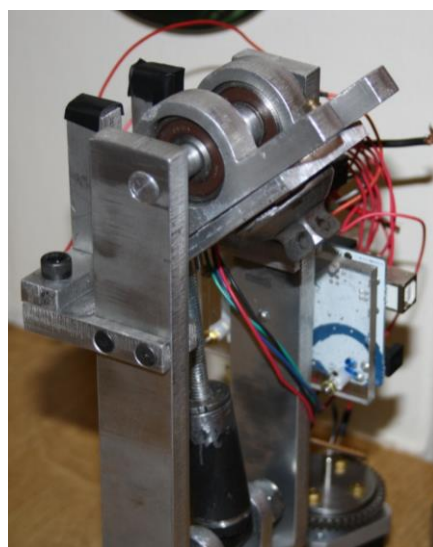


Figure 22. Maximum rotation of the swing phase control knee.



Figure 23. Maximum rotation on the manual lock knee.

While the knee system does not need to rotate more than 90 °, the swing phase control knee exceeds this by a fair amount. The manual lock knee is limited by the base of the connector that clashes with the frame work at 90 °.

Table 4. Range of motion results

Knee Joint	Maximum angle (°)
Manual Lock Knee	90
Swing Phase Control Knee	145
Pneumatic Knee (Carbon fibre frame)	110
Spring Loaded Hydraulic Knee	143
Ossurs Mauch Knee	115

The danger of rotating the swing phase control knee more than 90 ° is that it is fairly unnatural and quite difficult to get back into the normal working range again.

Once the joint goes past 90 °, the spring in place, extends and instead of straightening the knee joint, bends it further as the joint has moved out of the regular working range. The knee stops at 145 ° because the back of the hinges collides with the mechanical stop. The range of the swing phase control knee can be limited by introducing mechanical stops within the frame system. However, another method to limit the range is to extend the length of the piston. By extending the piston, the base of the piston collides with the bottom of the housing when the joint is at 90 °. The results show that other prosthetic knees typically bend to about 110 °. There is no need for them to bend to a greater angle than 90 ° other than comfort when sitting down. As the knee joint does not need to bend more than 90 ° for any particular reason the piston has been extended so that when the joint is bent to 90 °, the piston makes solid contact with the base of the housing. While the human knee joint does have a small amount of hyperextension (negative bend), all the above prosthetic joints do not have any negative bend in them at all. The lack of hyperextension prevents the knee from buckling and sending the

user falling forward during stance phase. Hyperextension is introduced into the joint by placing the line of the leg in front of the centre of rotation of the joint. However, this hyperextension is not as a result of the knee bending backwards but rather it is a result of the misalignment of the line of the leg.

The range of the knee joint has been discovered as well as the fact that the joint does not need to bend more than 90 °. For this reason an adjustment has been made to the design that prevents the joint from bending more than 90 °. With one of the springs in place in the swing phase control knee, the over rotation of the joint can be a nuisance for the user to have to correct after sitting down.

3.2. Knee Micro-Stepping Test

Stepper motors have the ability to divide the step resolution into smaller steps. This is known as micro-stepping. Although micro-stepping makes the motor operation smoother, it decreases the maximum torque the motor is capable of producing as well as decreases the speed. The objective of the test was to find the level of micro-stepping that still created a smooth operation but did not limit the speed or torque. The main concern here was the smoothness of the motor and whether or not the motor would cause unwanted vibrations when micro-stepping was disabled.

The motor was run on the different levels of micro-stepping. To change between the micro-stepping levels, the pins MS1, MS2 and MS3 on the motor driver have to be connected to either ground (low) or voltage (high) according to Table V (Allegro, 2012).

Table 5. Different logic truths for different micro-stepping resolutions

Micro-step Resolution	MS1	MS2	MS3
Full Step	0	0	0
Half Step	1	0	0
Quarter Step	0	1	0
Eighth Step	1	1	0
Sixteenth Step	1	1	1

The motor driver (big easy driver), was powered using a 12 V DC power supply. The motor was run at various speeds for a minute in which time the motor would run for several revolutions in one direction then in the opposite direction.

All of the micro-stepping levels presented a fairly smooth level of operation. When micro-stepping was disabled (full step resolution), the vibration was quite noticeable but not excessive. It was noted that the speed had to be lowered at the lower resolutions (half step and full step). It was decided to use a half-step resolution as the difference in speed between half step and full step was negligible. The half step resolution also provided a smoother operation than the full step resolution, which was desired. Despite the difference in speed not being noticeable, the maximum speed achievable was slow when compared to the speed desired to bend the joint. It took just over 2 seconds to bend the joint which is well over the time desired. However, this problem was expected.

The half-step resolution provided the best combination of speed and smoothness. The full step was not significantly faster than the half step resolution but had a more noticeable vibration. The half step resolution was selected as the most suitable resolution for the motor's operation.

3.3. Ankle Workspace Test

The objective of this test is to evaluate the range of motion of the joints of the prosthetic ankle by measuring the angles achieved and compare them to that of a normal ankle during the gait cycle. The operational range of motion is not desired to replicate the full extent of the human ankle range of motion, as it is not fully utilised during the gait cycle. Suitably constrained joints offer a sufficient range of motion and can protect the user from injury in the event of a system failure. The test will also assess whether the foot achieved the minimum dimensional requirements as laid out in the specifications.



Figure 24. Ankle Maximum (a) dorsiflexion and (b) plantarflexion.

The prosthetic ankle was driven to its joint limits for each ankle movement. This was done for dorsiflexion and plantarflexion as well as for inversion and eversion. The angles achieved were documented and tabulated. The results that were documented and were compared against values associated with normal human motion of the ankle. The ankle joints are shown driven to their limits in Figure 24 and Figure 25.

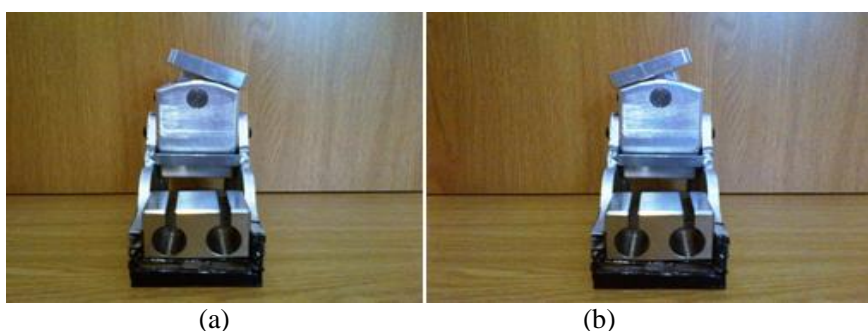


Figure 25. Ankle Maximum (a) inversion and (b) eversion.

Table 6. Comparative table of ankle ranges of motion

	Human (normal)	Designed Prosthetic Ankle	The Gait cycle
Plantar Flexion	50 degrees	20 degrees	0 – 20 degrees
Dorsi Flexion	20 degrees	15 degrees	0 – 10 degrees
Inversion	20 degrees	20 degrees	None (if otherwise not on an uneven terrain)
Eversion	5 degrees	20 degrees	None (if otherwise not on an uneven terrain)

The workspace limits are displayed in Table VI. There is a comparison between the normal human range of motion (Williams, 2012), the designed prosthetic ankle and the range of motion through the gait cycle (Study Stack, 2012).

Another part of testing in this section was to determine whether the prosthetic would fit into the minimum dimensional volume which it was designed for and would be required to fit in. This means that it was tested with a shoe; the smallest type of shoe that could be expected under normal circumstances in line with the requirements of the design itself (200 mm). Depicted in Figure 26 is the prosthetic in a shoe.

The prosthetic device was never intended to perform to the full range of motion of the normal human ankle. The main requirement was to achieve the range of motion used during the normal gait cycle thereby providing a natural gait. The limitation of the range of motion was necessary in order to restrict the possibility of unnatural movements during the gait cycle and improve user safety. In the case of inversion and eversion; the prosthetic will be able to deal with walking on uneven terrain.



Figure 26. Workspace testing.

In terms of the gait cycle; the prosthetic falls well within the required degrees for both plantar and dorsi flexion. It is important to note that whilst the designed prosthetic falls under the normal range for plantar flexion, it will not adversely affect the Gait cycle. In other words; whilst human range is 50 degrees for plantar flexion and the designed prosthetic is only able to achieve 20 degrees, the 20 degrees are all that are required of it during the motion of walking.

In terms of the fitting of the prosthetic in a shoe, it was clear that it fit well. It was secure. It fit comfortably even in a small shoe size (200 mm). The shoe would obviously be designed and catered specifically for the patient, their needs and the prosthetic but in this case, it is clear that a normal shoe would suffice.

CONCLUSION

The prosthetic leg was divided into the socket, pylons, the knee system, the ankle system and the fore foot adjustability.

The designs were converted into final products through the construction processes described. The various objectives of the prosthetic leg included modularity, adjustability, safety and the ability of the leg to accurately mimic the natural gait.

The leg also had to be low cost to allow lower income citizens to be able to purchase one if the need arises. While the structural objectives and a low cost solution were met, the ability of the leg to mimic the exact natural gait cycle was compromised.

Structurally, the leg met all the objectives in terms of its height adjustability. Through the design of two knee joints, the leg can be used for users as young as ten years old.

The adjustable pylons then allow the user to grow while using the same prosthesis. The strength of the leg was tested through FEA analysis. Crude strength testing was done on the knee joints and they withstood the loads applied. The system is not ideal but offered a low cost solution to the problem at hand.

The mechatronic system had problems with the speed of actuation. A low speed for the prototype was expected to prove the concept but the actual speed of the motor caused the knee to bend in two seconds. The most ideal scenario to test a prosthetic leg would have been to have a trans-femoral amputee walk with the leg and give feedback on its performance. However, this was not a viable option.

When prosthesis users walk with a new leg they have to attend physiotherapy sessions to ensure no muscle damage occurs. The recommended number of sessions is five to ten (Centre for Prosthetics, 2012). In addition, when a person uses a new prosthesis for the first few times, the gait is awkward and uncomfortable which would have meant that no valuable feedback could have been gained from this testing until a few session had passed. Strict ethical clearance and procedures need to be approved for these tests to be performed.

The use of standard connectors and adapters meant that if the user wished to purchase a separate joint/link that is not part of the system, it can still be integrated into the design. This characteristic means that the objective of modularity has been maximised.

ACKNOWLEDGMENTS

The financial assistance of the National Research Foundation (NRF) towards this research is hereby acknowledged. Opinions expressed and conclusions arrived at, are those of the author and are not necessarily to be attributed to the NRF.

REFERENCES

- Allegro, *DMOS Microstepping Driver with Translator*, [Online]. Available: www.allegromicro.com, date viewed: 3 September 2012.
- Artisan Orthotic and Prosthetic Technologies, “*Prosthetic Knees*,” [Online]. Available: www.aoptinc.com, date viewed: 23 February 2012.
- Centre for Prosthetics, Inc, [Online]. Available: www.cpo.biz, date viewed: 14 April 2012.
- Dupes, B, *Military in step, prosthetic knee systems*, Amputee Coalition of America, USA, 2008.
- Dupes, B, *Selecting the right mechanical knee*, [Online]. Available: www.calumetoandp.com, date viewed: 7 February 2012.
- Juvinal, R, *Fundamentals of machine component design*, Fourth ed. Hoboken: John Wiley and Sons, 2006.
- Kelly, B, *Lower limb prosthetics*, [Online]. Available: www.medscape.com, date viewed: 21 February 2012.
- Lim, J, *The mechanical design and analysis of an active prosthetic knee*, University of Waterloo, Ontario, Canada, 2008.
- Micheal, J, *Prosthetic primer: prosthetic knees, in motion*, [Online]. Available: www.amputee-coalition.org, date viewed: 18 February 2012.
- Netram technologies, [Online]. Available: www.netram.co.za, date viewed: 16 July 2012.
- OMEGA Engineering Technical Reference, [Online]. Available: www.omega.com, date viewed: 22 September 2012.
- Osborne, H, *Prosthetic feet*, [Online]. Available: www.amputee-coalition.org, date viewed: 21 February 2012.
- San Diego plastics, [Online]. Available: www.sdplastics.com, date viewed: 4 May 2012.
- Schaffer, E, *The prosthetic knee, in motion*, [Online]. Available: www.astepaheadonline.com, date viewed: 13 February 2012.
- Study Stack, *The gait cycle*, [Online]. Available: www.studystack.com, 23 September 2012.
- Williams, B, *Normal human range of motion*, [Online]. Available: www.livestrong.com, date viewed: 24 September 2012.
- Winter, D, *Biomechanics and motor control of human movement*, Fourth ed. Waterloo: John Wiley and Sons, 2009.
- Zahedi, S, Harris G, Smart, C, Evans, A, *Holy grail of prosthetic foot design*, Elite Foot Innovation Centre, Chas. A Blatchford & Sons Ltd, Basingstoke, UK, 2004.

ABOUT THE AUTHORS



Drew van der Riet was born in Port Elizabeth, South Africa. He graduated Bio-Mechatronics Engineering (M.Sc. Eng), at the University of KwaZulu-Natal.



Riaan Stopforth graduated with a B.Sc. Eng (Electronics), M.Sc. (Computer Science) and Ph.D. Eng (Mechanical) from the University of KwaZulu-Natal, who has specialized in the field of Mechatronics Engineering. His research interest is in the area of search and rescue robotics and bio-engineering systems. He is currently appointed as an Associated Professor at the University of KwaZulu-Natal.

Chapter 7

INTEGRATION OF SENSORS AND ACTUATORS TO SUPPRESS VIBRATIONS ON CARBON FIBER STRUCTURES

Gabriele Cazzulani, Simone Cinquemani and Francesco Braghin*

Dept. of Mechanical Engineering, Politecnico di Milano, Milano, Italy

ABSTRACT

Composite materials, such as carbon fiber, offer several advantages with respect to traditional alloys, i.e., reduced mass, high stiffness and low thermal expansion. However, when realizing mechanical structures using these materials, some problems must be considered. In particular their small damping can cause high dynamic amplification of vibrations, especially when the structure is forced near its natural frequencies. These vibration phenomena can be very dangerous, causing unwanted system behaviour and structural failures. Active control techniques have been widely developed to suppress vibrations and great progresses have been achieved. In this field researches on sensors and actuators and on their integration into the structure have a great importance.

In the last years a class of materials, called smart, has been widely developed. These transducing materials, which are able to convert mechanical energy into another form (electrical, magnetic, thermal, etc.) and vice versa, are suitable for the realization of both sensors and actuators. The paper discusses the opportunity to use piezoelectric actuators (PZT) and Fiber Bragg Grating sensors (FBGs) to realize a smart structure embedding both the sensing and the actuating devices. Fiber optic strain sensors, have a great potential in the use in smart structures thanks to their small transversal size and the possibility to make an array of many sensors. They can be embedded in carbon fiber structures and their effect on the structure is nearly negligible. Such a structure is able to measure its state of excitation and to reduce the amplitude of vibration using the embedded actuators. Control forces are designed to increase the damping of the structures, thus suppressing undesired vibration. Different control strategies can be synthesized to achieve the best performance exploiting potential of distributed sensors and actuators.

* Corresponding author: E-mail address: francesco.braghin@polimi.it; phone +39 02 2399 8306; fax +39 02 2399 8492. Address: Via La Masa 1, 20156, Milan, Italy.

1. INTRODUCTION

In mechanical and aerospace fields, the last decades were characterized by a wide development of large and light structures, due to the need of reducing weights and to the large use of lightweight materials such as carbon fiber. These structures are typically characterized by high flexibility, due to the low stiffness of the structure, and low damping ratio caused by the low energy dissipation associated to these materials. These characteristics cause a high sensitivity to external disturbance forces and consequently to vibration problems, especially when the system is forced close to its natural frequencies. This condition can be very critical, causing a degradation of system performance (consider, for example, the precise positioning required to a robot manipulator) and structure health.

For these reasons, many solutions have been developed during the years to reduce vibrations of flexible structures. The first and simplest one, was represented by passive devices, such as the Dynamic Vibration Absorber (DVA) [Igusa, 1994] which consists in a mass-spring-damper system mounted on the structure. The parameters of this added system can be tuned in order to dissipate energy at a given natural frequency of the structure. This solution have been applied with success in many fields, typically on large systems such as cables [Cai, 2006], buildings [Pinkaew, 2003] or bridges [Xiang, 1992]. The main disadvantage of this methodology is that it becomes ineffective far from the frequency it was designed for and consequently when the system dynamic characteristics change over time.

In recent years, the performance increase and cost reduction of electronic devices and processors led to the development of semi-active and active vibration control techniques. The first ones are based on the same approach of passive devices, but some parameters can be actively modified [Abdel, 2006, Lin, 2005]. This solution, with respect to a simple passive system, is able to adapt itself to different operating conditions or to the variation of the structure properties over time.

Active control, on the contrary, provides forces typically proportional to measured vibrations and/or to the system dynamic properties. In fact, all the feedback control logics for vibration suppression are based on three main steps:

- measurement or identification of the system vibratory state;
- formulation of the control law, defining the mathematical relationship between the input measurements and the output control forces and evaluating possible undesired effects associated to the implementation of the logic on a real system;
- actuation of the control forces through suitable actuators in terms of requested force and displacement, bandwidth and dimensions.

With regards to the actuators, many solutions are available for vibration control applications depending on the required forces, displacements and bandwidth. Traditional actuators, such as hydraulic or pneumatic actuators and electrical motors are typically suitable for large structures and robotic applications [Resta, 2010], where high strokes and high control forces are required.

In recent years a class of actuators regarded as smart have been developed [Pons, 2011]. These actuators are based on transducing materials, which are able to convert mechanical energy into another form (electrical, magnetic, thermal, etc) and vice-versa. Among them the

most known are probably piezoelectric actuators, which provide a force on the structure by transforming electrical power to mechanical power thanks to the so-called piezoelectric effect. These actuators are suitable for a large range of applications thanks to their large bandwidth (from zero to 10/20 kHz) and to their reduced dimensions, which allow them to be easily embedded inside the structure [Correa, 2011]. Different piezoelectric actuators have been developed during the last years, such as piezoelectric patches [Correa, 2011], suitable for low-power applications, and piezoelectric stacks [Simoes, 2007], which provide higher control forces and are also suitable for precision applications such as micro-positioning.

Among the control logics, modal-space approaches represent an attractive solution for the vibration suppression of linear flexible structures. Indeed, in most practical applications only few modes (typically the low-frequency ones) have a significant contribution on the system motion, since the ones associated with higher eigen-frequencies are typically highly damped and difficult to be excited. For this reason, the dynamic model of the system can be designed to include only these modes, strongly reducing the number of degrees of freedom and the complexity of the control definition. Control gains can be tuned using many different approaches, such as pole placement or optimal control [Friedland, 1986, Preumont, 2011]. To modify the behaviour of a single mode independently from the other, the so-called Independent Modal Space Control (IMSC) [Meirovitch, 1990, Kulief 2001] has been introduced. This control logic has been designed to independently impose the natural frequency and damping of each controlled mode. The main limit of this control logic is the spillover effect [Chait, 1989], due to the interaction between the modeled and unmodeled modes and the control action. In particular, control spillover is the effect of the control force on the unmodeled modes, while observation spillover is the effect of the unmodeled modes on the estimation of the modeled modal coordinates. The combination between the two effects worsens the control performance and in some cases leads the system to instability.

To overcome this problem many solutions have been proposed in the years, such as a nonlinear variation of the control law [Preumont, 1988], the so called Modified IMSC [Fang, 2003] or the resonant controllers like Positive Position Feedback (PPF) [Shan, 2005]. Anyway, the spillover effect can only be reduced and not completely removed by all these approaches. Modal sensors could be used to cancel out this problem, being able to separate the effect of different structural modes [Lee, 1990]. Anyway, although this approach is theoretically able to solve the problem, some limitations occur in practical applications [Clark, 1996]. Recently an approximated modal measurement (called quasi-modal sensors), in which distributed modal sensors are replaced by a finite number of lumped piezoelectric elements, has been proposed [Pagani, 2009, Sun, 2001]. Anyway the size, cost and load effect of piezoelectric patches limits the number of sensors that can be applied on the structure.

For this reason, the present work investigates the use of Fiber Bragg Grating (FBG) sensors for distributed vibration control. FBG sensors are optical strain gauges, measuring a deformation through the measurement of the wavelength of the light reflected by the sensor. The great advantage of this technology is the possibility to insert a large number of sensors on a single optical fiber wire [Grattan, 2000, Othonos, 1997]. Besides, the negligible load effect (small cross-section and reduced weight) and the electromagnetic immunity of the optical fiber make it suitable for a large number of applications and allows it to be easily embedded into the structure [Luyckx, 2010].

In literature the most common applications of FBG sensors are structural health monitoring, fault detection [Huston, 1991] or strain measurement in harsh environments

[Comolli, 2010], while only a limited number of cases deal with active control [Chau, 2004, Ambrosino, 2010]. Anyway all these applications analyze only some particular cases, since only co-located sensors and actuators are considered, while the control action is based on a simple direct velocity feedback [Balas, 1979]. None of these works really takes advantage of the full potential of the FBG technology and its possibility to have a large number of measurements using a non-invasive measurement setup.

For this reason, this research activity aims at exploiting this opportunity, considering a chain of FBG sensors for the active vibration control of a beam. Thanks to the large number of measurement points, different control solutions can be introduced and analyzed depending on the number of sensors and actuators involved in the control algorithm. In particular, considering those control logics based on the modal approach, the distributed measurement provided by FBG sensors allows to strongly improve the estimation of the contribution of the different modes on structure vibrations, reducing the spillover effect.

The paper is organized as follows. Section 2 introduces the theory about the use of distributed sensors for active vibration control and in particular for the sensor averaging technique. Section 3 recalls the main features of FBG sensors and focuses on the analysis of the sensor properties for control. Section 4 describes the experimental layout, while section 5 shows and discusses the main results obtained with the proposed approach. At last, the conclusions are drawn in section 6.

2. ACTIVE CONTROL WITH DISTRIBUTED SENSORS

Consider the dynamic equation of a mechanical system with n degrees of freedom (dof)

$$\mathbf{M}_x \ddot{\mathbf{x}} + \mathbf{C}_x \dot{\mathbf{x}} + \mathbf{K}_x \mathbf{x} = \boldsymbol{\Lambda}_c \mathbf{F}_c + \boldsymbol{\Lambda}_d \mathbf{F}_d \quad (1)$$

where \mathbf{M}_x , \mathbf{C}_x and \mathbf{K}_x are the $n \times n$ inertia, damping and stiffness matrices, \mathbf{x} is the vector containing the displacement of the degrees of freedom, \mathbf{F}_c and \mathbf{F}_d are the control and disturbance forces and $\boldsymbol{\Lambda}_c$ and $\boldsymbol{\Lambda}_d$ are their Jacobian matrices.

A typical method to reduce the vibrations of a structure consists of increasing its damping and consequently its capability to dissipate energy. This result can be achieved providing feedback forces proportional to velocity. In order to guarantee the stability of the controlled system, a series of co-located control loops can be introduced: the information coming from each sensor placed on the structure is used to drive the corresponding co-located actuator. In this way, having n_c sensor-actuator pairs, the control force vector \mathbf{F}_c for damping increase becomes

$$\mathbf{F}_c = \begin{bmatrix} r_1 \dot{\varepsilon}(\xi_1) \\ \vdots \\ r_{n_c} \dot{\varepsilon}(\xi_{n_c}) \end{bmatrix} \quad (2)$$

where $\varepsilon(\xi_i)$ represents the displacement of the sensor placed in ξ_i , while r_i is the control gain of the i -th loop. This control strategy, called Direct Velocity Feedback (DVF) has many advantages, since it is simple, modular (all the control loops are identical) and, with co-located sensors and actuators, it guarantees the closed loop stability for any value of the control gains. Anyway, care must be taken in the position of the sensor-actuator pairs and in the definition of the control gains to obtain a significant performance in terms of damping increase. For this reason, different approaches, such as modal-space ones, can be used to enhance the control performance.

Remembering the coordinate change from physical to modal space

$$\mathbf{x} = \Phi \mathbf{q} \quad (3)$$

where \mathbf{q} contains the modal coordinates and Φ is the eigenvector matrix of $\mathbf{M}_x^{-1} \mathbf{K}_x$, the eq. (1) can be re-written as

$$\mathbf{M}\ddot{\mathbf{q}} + \mathbf{C}\dot{\mathbf{q}} + \mathbf{K}\mathbf{q} = \Phi^T(\xi_c)\mathbf{F}_c + \Phi^T(\xi_d)\mathbf{F}_d \quad (4)$$

where \mathbf{M} , \mathbf{C} and \mathbf{K} are the diagonal modal inertia, damping and stiffness matrices, while $\Phi(\xi_c)$ and $\Phi(\xi_d)$ are the system eigenvector matrix evaluated respectively in the application points of the control and disturbance forces. If the control aim is the damping increase, the control action can be designed as

$$\mathbf{F}_c = (\Phi^T(\xi_c))^{-1} \mathbf{G} \dot{\mathbf{q}} \quad (5)$$

where \mathbf{G} is the gain matrix. The modal coordinates \mathbf{q} , required for the computation of the control forces, cannot be directly measured and need to be estimated. Suppose to have m sensors available, the following cases can be considered:

- If $m = n$ the problem is determined and the information coming from measurements are enough to calculate modal quantities of the reduced model. In this case, modal velocities can be obtained through the equation

$$\dot{\mathbf{q}} = (\Phi(\xi_M))^{-1} \dot{\mathbf{e}} \quad (6)$$

Since matrix Φ has to be invertible, it has to be:

$$\det(\Phi(\xi_M)) \neq 0 \quad (7)$$

This condition can be traced back to system observability, i.e., if a set of sensors can provide measurements containing information of every mode of the system.

- If $m < n$ the problem is under-determined and the information from measurements is not sufficient to calculate modal quantities. A way to overcome this difficulty is to design a state observer to estimate missing information.
- If $m > n$ the problem is over-determined. Modal quantities can be obtained exploiting the information of available sensors in different ways. The simplest is to adopt pseudo-inverse matrix instead of the inverse matrix of $\Phi(\xi_M)$. The pseudo-inverse matrix allows us to filter out measurement noise since it provides the least-squares solution of a system of linear equations minimizing the Euclidean norm $\|\Phi(\xi_M)\dot{\mathbf{q}} - \dot{\mathbf{\varepsilon}}\|_2$. Having more measurements, errors on estimation of modal quantities can be effectively minimized.

However, when a huge number of sensors is available ($m \gg n$), more efficient techniques can be used. Sensor-averaging technique [Simoes, 2007] consists of properly weighting the outputs of a distributed array of sensors to obtain a spatial filter able to separate the contribution of one mode from the others. In this way, a control force can be designed to work on a single mode or on a number of selected modes. A graphical representation of this technique is shown in Figure 1. This method allows to exploit the characteristics of a centralized control avoiding the unwanted observation spillover effect typical of these controllers.

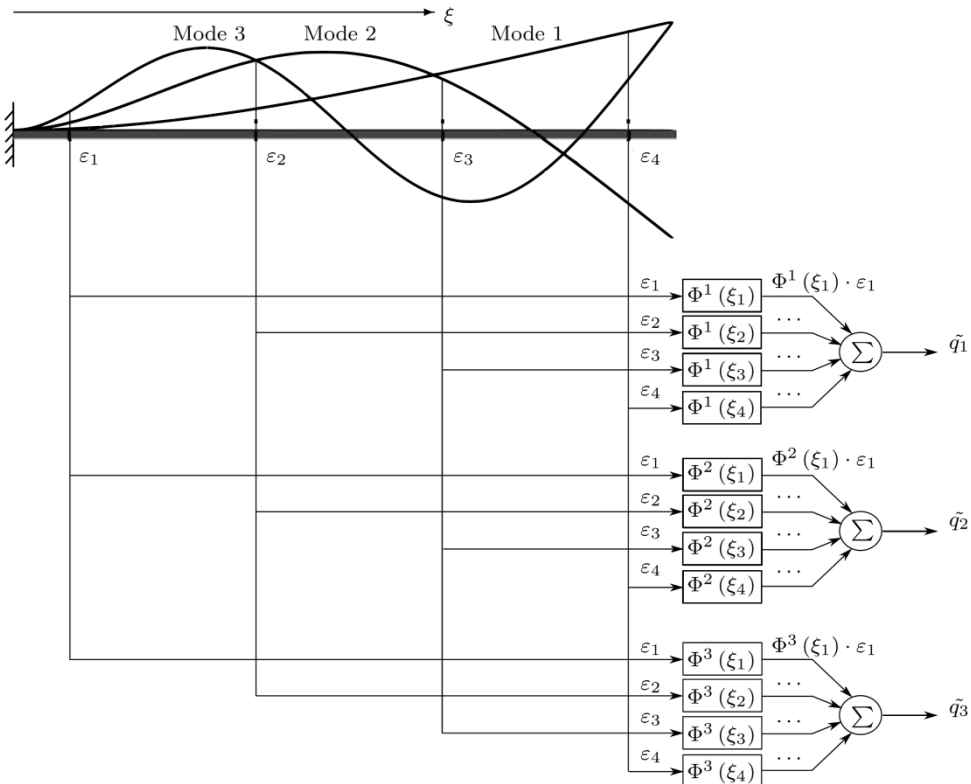


Figure 1. Graphical representation of sensor averaging control technique.

Supposing that the aim is to design the controller to suppress vibration of the i -th mode and that one wishes to control the i -th mode using only one actuator and m sensors, the control force can be obtained as

$$F_{ci} = -r_i \dot{q}_i \quad (8)$$

where \dot{q}_i is the linear average of measurements provided by sensors, related to the i -th mode. The averaged feedback signal is

$$\dot{q}_i = \Phi^i(\xi_{M1})\dot{\varepsilon}_1 + \Phi^i(\xi_{M2})\dot{\varepsilon}_2 + \dots + \Phi^i(\xi_{Mm})\dot{\varepsilon}_m = \Phi^i(\xi_M) \times \dot{\varepsilon} \quad (9)$$

being the operator \times the scalar product,

$$\Phi^i(\xi_M) = \begin{bmatrix} \Phi^i(\xi_{M1}) \\ \Phi^i(\xi_{M2}) \\ \vdots \\ \Phi^i(\xi_{Mm}) \end{bmatrix} \quad (10)$$

the vector of the Jacobian matrix corresponding to the position of the m sensors and

$$\dot{\varepsilon} = \begin{bmatrix} \dot{\varepsilon}_1 \\ \dot{\varepsilon}_2 \\ \vdots \\ \dot{\varepsilon}_m \end{bmatrix} \quad (11)$$

the vector of the corresponding physical velocities measured. This operation provides a linear averaging of measurements, thus increasing the signal to noise ratio and improving the quality of the feedback used to calculate the control force. Estimated modal velocity is then:

$$\dot{q}_i = \Phi^i(\xi_M) \times \Phi(\xi_M) \dot{\mathbf{q}} \quad (12)$$

Thanks to the property of orthogonality of modes, one gets

$$\Phi^i(\xi_M) \times \Phi(\xi_M) = \begin{bmatrix} 0 & \dots & \Phi^i(\xi_M) \times \Phi^i(\xi_M) & \dots & 0 \end{bmatrix} \quad (13)$$

and then

$$\dot{q}_i = \begin{bmatrix} 0 & \dots & \Phi^i(\xi_M) \times \Phi^i(\xi_M) & \dots & 0 \end{bmatrix} \dot{\mathbf{q}} \quad (14)$$

The control force can be obtained as

$$F_{ci} = -r_i \begin{bmatrix} 0 & \dots & \Phi^i(\xi_M) \times \Phi^i(\xi_M) & \dots & 0 \end{bmatrix} \dot{\mathbf{q}} \quad (15)$$

The modal damping matrix due to the added control can be obtained by substituting equation (15) in equation (4) and gathering $\dot{\mathbf{q}}$ as

$$\mathbf{R}_c = r_i \begin{bmatrix} 0 & \dots & \Phi^i(\xi_M) \times \Phi^i(\xi_M) & \dots & 0 \end{bmatrix} \quad (16)$$

As it can be seen, the control effectively acts only on the desired mode. However, since the matrix is not diagonal, nor symmetric, modes become coupled and the system has a stability limit. Similar considerations can be done to control k modes.

3. FIBER BRAGG GRATING SENSORS

This section presents a brief overview of FBG sensors, describing their working principle, their main characteristics and their advantages and drawbacks with respect to the classical measurement techniques for vibration control.

3.1. Working Principle of FBG Sensors

As previously introduced, Fiber Bragg Grating sensors are a class of optical strain gauges. The sensor is made by an optical fiber, whose core has been inscribed with UV light to obtain a periodic variation of its refraction index. Each FBG sensor included in the fiber reflects light in a limited wavelength band, according to its current grating step (which is different among the sensors of the same fiber) that can be modified either by mechanical strain or by temperature. The peak wavelength obtained from the spectrum of the reflected light (Figure 2) provides the information about the current deformation of the measuring point.

A FBG sensor with an inscribed grating with a spacing Λ reflects light with a wavelength λ_0 (Figure 2). This value can be found thanks to the Bragg condition, given by

$$\lambda_0 = 2n\Lambda \quad (17)$$

where n is the index of refraction of the fiber core (typically 1.5). Any strain ε applied to the optical fiber modifies the grating period Λ and changes the wavelength λ of the reflected peak. The variation in the reflected wavelength (Figure 2) is related to the applied strain by

$$\frac{\Delta\lambda}{\lambda_0} = G_f \varepsilon \quad (18)$$

where G_f is the gage factor, typically equal to 0.78. This value is due both to the mechanical strain and to the change of the refraction index due to the applied strain (photoelastic effect).

FBG sensors, as the electrical strain gauges, are also sensitive to temperature. This sensitivity can alter the strain measurement and may require a compensation. Anyway, temperature dynamics is slower than the dynamics associated to structure vibrations and, for this reason, the two effects can be easily separated and no temperature compensation is needed.

The light signal reflected by the sensor is read by means of an optical interrogator. Many different technologies are available, such as optical spectrum analyzers (OSA), linear filters or swept laser. In this work the swept laser technology has been selected, mainly thanks to its capability to manage a large number of sensors, allowing to realize a quasi-distributed vibration measurement and to place sensors in any significant point of the structure. In this way the result obtained in this work can be easily extended to a large number of practical applications and possible sensor configurations. In detail, the adopted interrogator, the MicronOptics SM130-500, has a peak resolution of 1 pm (corresponding to about 1 $\mu\text{m}/\text{m}$ for a typical FBG sensor) and a sampling frequency of 1 kHz. It is able to manage up to four optical channels, each one with several tens of sensors. The output is provided through the TCP/IP protocol, whose non-determinism can introduce time delay in the measurement signal.

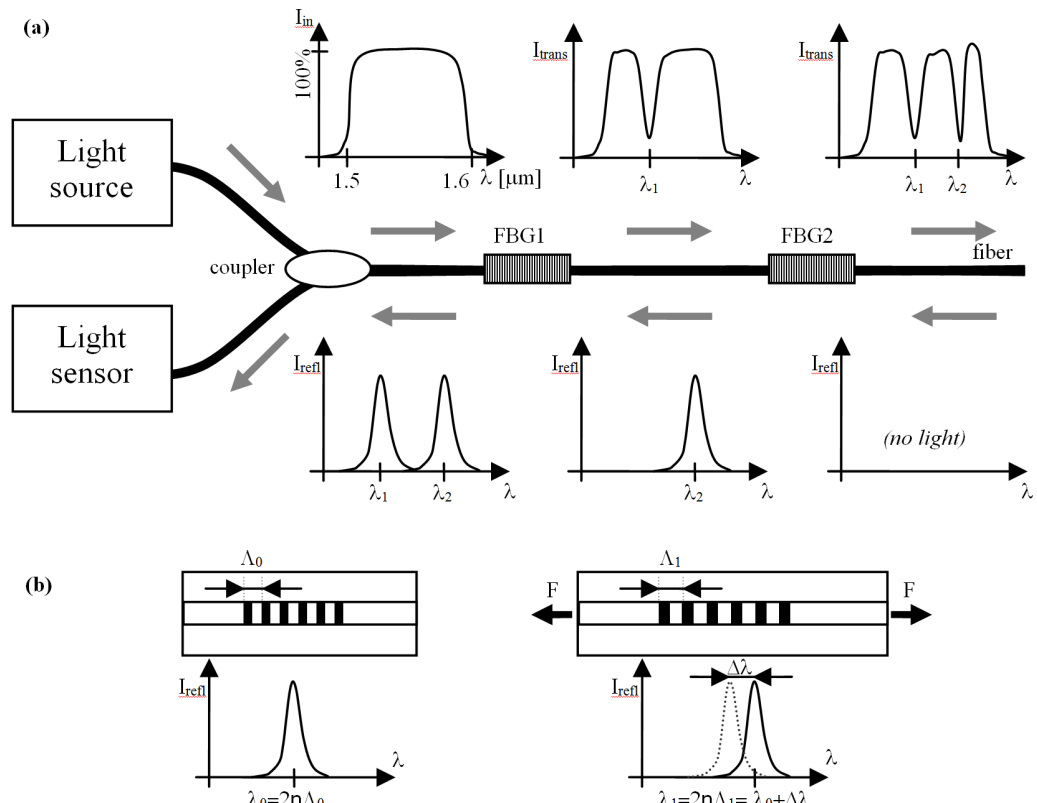


Figure 2. FBG sensors behave like reflectors for a specific wavelength and transmit all the other light. So many FBG can be chained as in (a) with only two of them, and the light reflected back will show a peak for each FBG. The wavelength of each peak depends on the grating spacing that is modified (b) when a strain is applied (but also with temperature).

3.2. FBG Sensors for Distributed Vibration Control

Optical sensors have many advantages that make them interesting for vibration control. The most significant one is that a high number of sensors can be inserted in a single optical fiber, widely reducing the number of cables on the structure and the wiring complexity. This means that a large amount of information on how the system is vibrating can be collected along the structure. Besides, their small cross-section and weight make optical fibers easy to be embedded into hybrid or composite structures, reducing the load effect of the sensor. Other advantages from a control point of view are the electromagnetical immunity and electrical insulation, which allow this technology to avoid disturbances coming from the actuators (electrical motors, piezoelectric or magnetostrictive actuators) are sensed.

On the other hand, when using FBG sensors some critical points must be evaluated. In particular when the sensor is not parallel to the carbon fibers (or if woven carbon fiber is used), it senses a 3-dimensional strain field, which produces unwanted effects on the measurement, such as double peaks, worsening the quality of the measurement. This problem can be solved by inserting the optical fiber between two layers of unidirectional carbon fiber and placing the fiber parallel to the carbon fibers.

Moreover, depending on which optical interrogator is used, particular issues must be considered. As previously introduced, the main problem of the selected swept laser interrogator is the time delay associated to the peak detection and to the data transmission. As known, all control applications are very sensitive to control delays between the system vibrations and the corresponding control action, since delays modify the relative phase between vibration and control. The delays can reduce control performance and, if they are particularly relevant, can lead the controlled system to instability. To quantify this effect, a comparison between the FBG acquisition system and another known one is needed.

To identify the time delay of the acquisition system, an FBG sensor and an electrical strain gauge have been applied in parallel on the same section of a cantilever beam, so that the two sensors measure the same strain. The beam is excited through a magnetostrictive shaker using a harmonic input. The optical fiber signal is acquired by the optical interrogator and sent to the PC through a TCP/IP connection while the electrical strain gauge is acquired in parallel through a DAC board.

The cross-correlation between the two signals (Figure 3) shows a delay of (1.7 ± 0.6) ms. The measured delay represents the total delay due to the use of this digital interrogator and the uncertainty on its value is due to the non determinism of the Ethernet transmission. From this time delay estimation, considering a maximum acceptable phase delay of 0.5 rad, the maximum controllable frequency can be computed as

$$f_{\max} = \frac{1}{0.0017} \cdot \frac{0.5}{2\pi} \approx 45 \text{ Hz} \quad (19)$$

This result sets a limitation in the use of this measurement layout for vibration control. For example, it cannot be used for high frequency applications, such as noise control. Anyway, there are many mechanical systems whose dynamics is associated to frequencies lower than this limit and, for this reason, the proposed approach is interesting for a large number of applications.

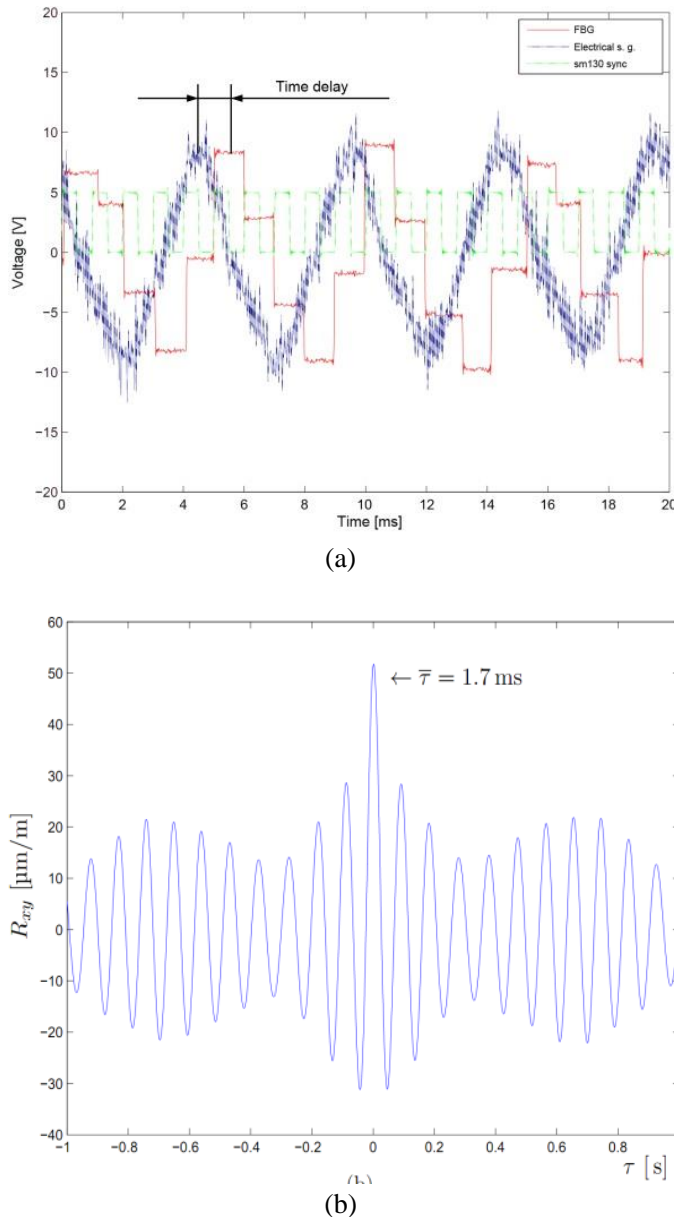


Figure 3. (a) Comparison of the measured signals from a sinusoidal vibration: the FBG signal shows a small but measurable time delay respect to the electrical strain gauge. (b) A cross correlation analysis of a band limited random noise input shows the average time delay of 1.7 ms.

4. EXPERIMENTAL SETUP

The approach proposed in the previous sections has been tested on a laboratory test rig. The control effect obtained with the distributed sensor layout has been compared with decentralized control to assess its benefit with respect to traditional solutions. The experimental layout is shown in Figure 4: structure vibrations are measured by the FBG

sensor chain and acquired by the optical interrogator MicronOptics SM130-500. The signals are high-pass filtered to separate the quasi-static effect of temperature variation from the dynamic signals due to vibrations. The output commands for the actuators are sent out by the control board and low-pass filtered to cancel out the quantization effect of the sampling time. Then the signals are amplified and sent to the piezoelectric patch actuators.

This control layout has been applied to two different structures. Both of them are made by carbon fiber composite material. As already introduced, vibrations are sensed through embedded FBG sensors, while the control and disturbance forces are provided to the system through piezoelectric patch actuators bonded to the structure. In detail, Midè QP20W actuators are considered.

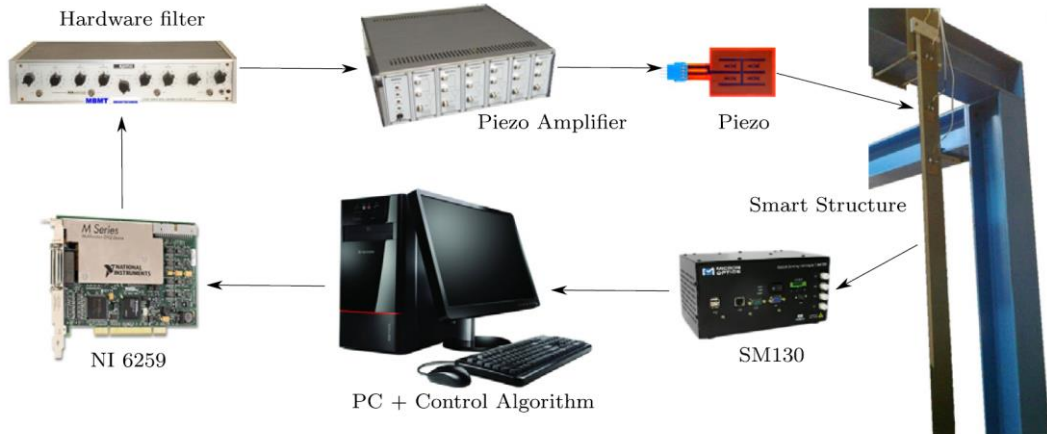


Figure 4. The experimental layout: block scheme of the control loop.

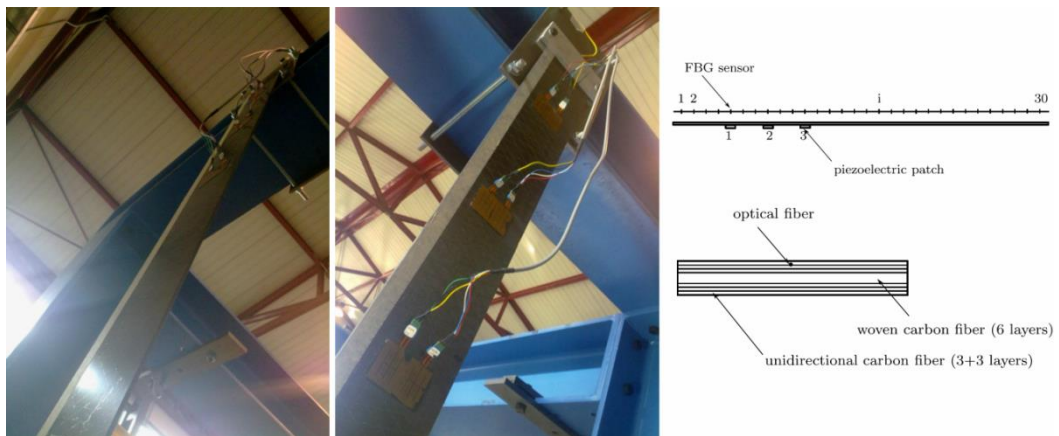


Figure 5. The first considered test rig: the 1-D structure and the layout of the sensors and actuators position.

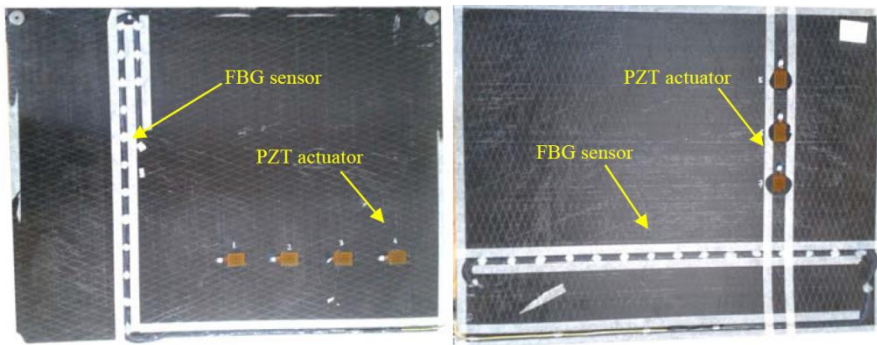


Figure 6. The second considered test rig: the 2-D structure (two sides).

The first analyzed structure is a 1-D beam (Figure 5), equipped with a 30-sensor chain of FBG sensors uniformly positioned along the beam. Three piezoelectric patches, co-located with three of the sensors, are used to apply control and disturbance forces. The second structure is a 2-D plate, equipped with two chains of 15 sensors placed orthogonal one to the other (Figure 6). This structure is useful for the paper purpose, since its modal density is very high. Indeed, unlike the 1-D structures, the natural frequencies are very close and the modal shapes are more difficult to separate. For this reason, the distributed measurement provided by FBG sensors is particularly interesting to overcome this problem, improving the modal estimation and allowing a profitable use of the modal control theory.

5. RESULTS AND DISCUSSION

This section presents the results obtained on the two structures introduced in the previous one. Considering at first the beam, the first piezoelectric actuator (PZT1) is used to provide a disturbance input, while the first sensor (FBG1) is considered to evaluate the control performance. The results are shown in terms of frequency response function (FRF) between the input voltage of the disturbance actuator PZT1 and the strain output measured by FBG1.

Figure 7 compares this FRF for the system without control and with co-located control. In this case, the control layout consists of three independent loops, where the control input of each actuator (PZT1, PZT2 and PZT3) is computed from the measurement of the corresponding FBG sensor (FBG5, FBG8 and FBG 11 respectively). As expected, co-located control increases the structure damping and correspondingly reduces its vibrations around the resonances. Anyway the maximum damping achieved on the modes is not very high and in some cases a higher damping may be required. Figure 8 shows the FRF when sensor averaging technique is applied. Different numbers of involved sensors are considered, showing a significant reduction of structure vibrations when a large number of sensors is considered: if the number of sensor is low, the performance is similar to that of co-located control, while if all the available FBG measurements are used the structure vibrations are almost cancelled out.

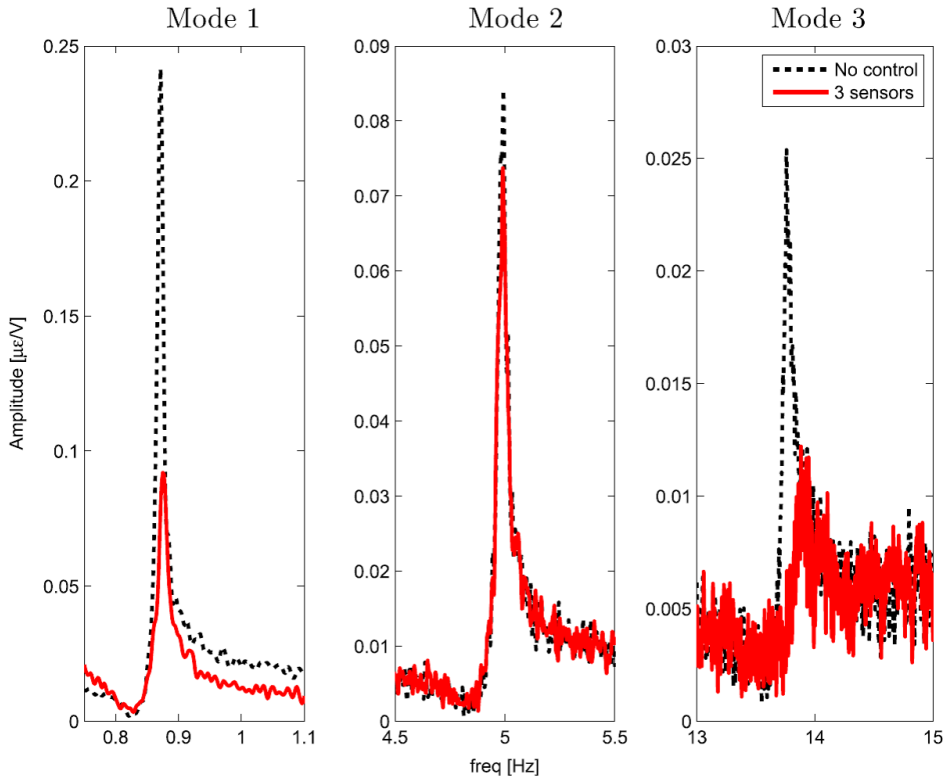


Figure 7. FRF of the beam without control and with co-located control. Result on the first mode (on the left), second mode (in the centre) and third mode (on the right).

Beam-like structures are very simple to model and control but, thanks to the distributed measurement system, similar results can be achieved also on more complex structures. This statement has been demonstrated by applying the same control layout (control loop and instrumentation) on the plate structure. Figure 9 shows the comparison of controlled and uncontrolled system referred to this structure. As for the previous case, co-located control and distributed control have been considered. As expected, increasing the complexity of the structure, a simple velocity feedback is difficult to use, since vibration phenomena interest more modes close one to the other and the contribution of each one is difficult to detect. Therefore, it is difficult to place the sensor-actuator pairs and to define the weights for the feedback forces. On the contrary, through the distributed measurement, a great increase of the damping ratio of the controlled modes and, as a consequence, a great reduction of system's vibrations can be achieved even for these complex structures. Thanks to the high number of sensors, the spillover problem does not arise and the control performances are strongly improved.

CONCLUSION

The opportunity to build lightweight structures that can actively change their mechanical properties, such as the damping, is of great interest. This work demonstrates the possibility of

realizing composite structures with embedded arrays of FBG sensors for distributed vibration control. The advantages of this solution are significant. The implementation is made easy thanks to the large number of measurements provided by these sensors. Moreover, there is no need of physically arranging for their installation, wiring and signals management.

The most significant results are achieved by implementing a spatial filter technique called sensor averaging. In fact, thanks to the large number of available FBG sensors, this technique is very effective since it allows a distributed measurement of the system deformation, providing a modal coordinates estimation and avoiding the raise of unwanted spillover effects.

Experimental tests have been carried out to evaluate control performances considering different number of FBG sensors and actuators. Two structure typologies have been considered, 1-D structures and 2-D structures, which represent a more general case from a vibration control point of view. All the experimental tests confirm the potential of this measurement technology to obtain a quasi-distributed vibration measurement and to design very efficient control logics.

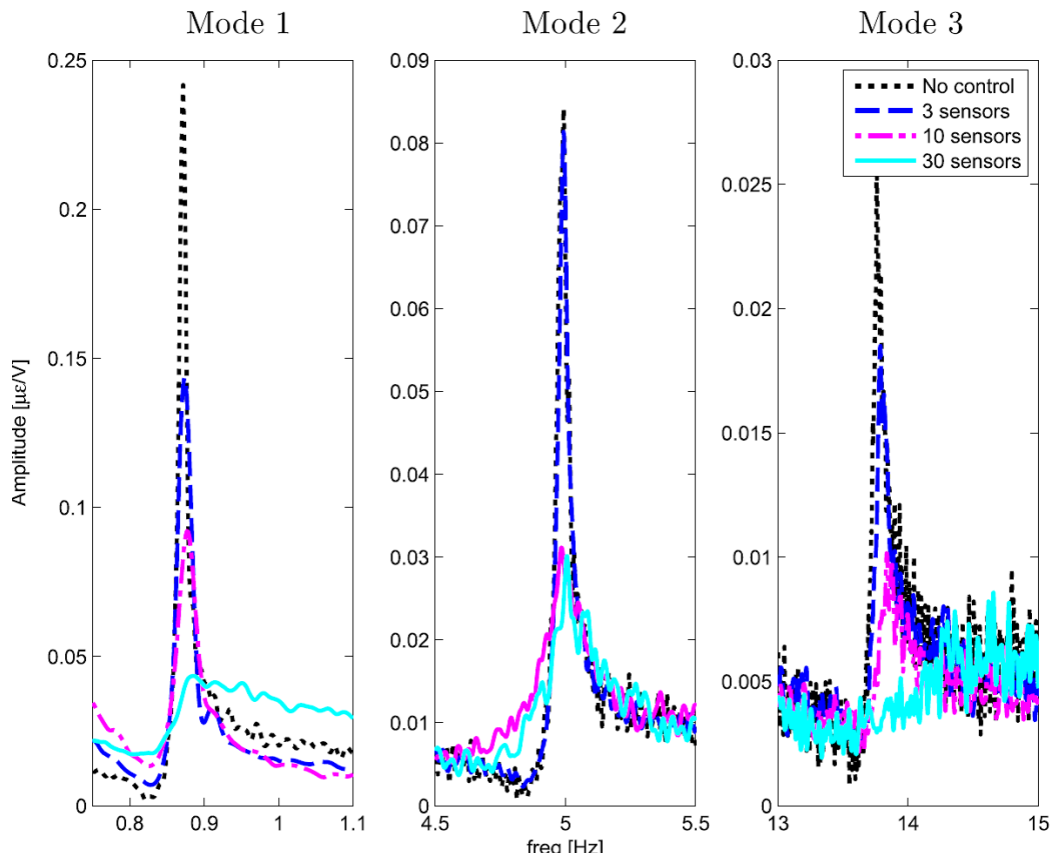


Figure 8. Effect of sensor averaging control on the FRF of the beam considering different number of sensors. Result on the first mode (on the left), second mode (in the centre) and third mode (on the right).

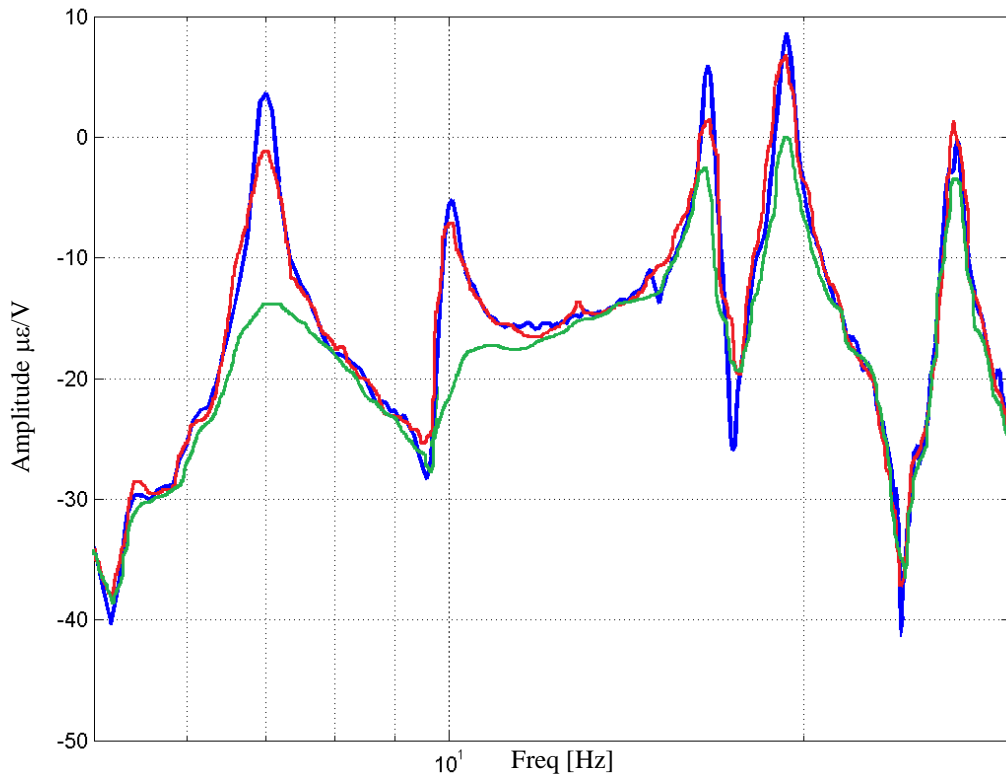


Figure 9. Comparison between decentralized and distributed control on a plate structure: uncontrolled system (blue), decentralized control (red) and distributed control (green).

REFERENCES

- [1] Igusa, T; Xu, K. Vibration control using multiple tuned mass dampers”, *J Sound & Vibr.*, 175(4), 491-503, 1994
- [2] Cai, CS; Wu, WJ; Shi, XM. Cable vibration reduction with a hung-on tmd system. part I: Theoretical study”, *J Vib Control*, 12(7), 801-814, 2006
- [3] Pinkaew, T; Lukkunaprasit, P; Chatupote, P. Seismic effectiveness of tuned mass dampers for damage reduction of structures”, *Eng Struct*, 25(1), 39-46, 2003
- [4] Xiang, H; Gu, M. Optimization of TMD for suppressing buffeting response of long-span bridges”, *J Wind Eng Ind Aerodyn*, 42(1-3), 1383-1392, 1992
- [5] Abdel-Rohman, M; John, MJ. Control of wind-induced nonlinear oscillations in suspension bridges using multiple semi-active tuned mass damper”, *J Vib Control*, 12(9), 1011-1046, 2006
- [6] Lin, PY; Chung, LL; Loh, CH. Semiactive control of building structures with semiactive tuned mass damper”, *Comput-Aided Civil Infrastruct Eng*, 20(1), 35-51, 2005
- [7] Resta, F; Ripamonti, F; Cazzulani, G; Ferrari, M. Independent modal control for nonlinear flexible structures: an experimental test rig”, *J Sound & Vibr.*, 329(8), 961-972, 2010

- [8] Pons, JL. *Emerging actuator technologies: a micromechatronic approach*. new York, J. Wiley & Sons, 2005
- [9] Correa, De Godoy T; Areias Trindade, M. Modeling and analysis of laminate composite plates with embedded active-passive piezoelectric networks”, *J Sound & Vibr*, 330(2), 194-216, 2011
- [10] Simoes, RC; Steffen, V; Der Hagopian, J; Mahfoud, J. Modal active vibration control of a rotor using piezoelectric stack actuators”, *J Vibr Control*, 13(1), 45-64, 2007
- [11] Friedland, B. *Control System Design*, New York, Mc Graw Hill, 1986
- [12] Preumont, A. *Vibration control of active structures*, third edition. Berlin, Springer, 2011
- [13] Meirovitch, L. *Dynamics and Control of Structures*, New York, J. Wiley & Sons, 1990
- [14] Khulief, YA. Vibration suppression in rotating beams using active modal control”, *J Sound & Vibr*, 242(4), 681-699, 2001
- [15] Chait, Y; Radcliffe, CJ. Control of flexible structures with spillover using an augmented observer”, *J. Guid. Control Dyn.*, 12(2), 155-161, 1989
- [16] Preumont, A. Spillover alleviation for nonlinear active control of vibration”, *J. Guid. Control Dyn.*, 11(2), . 124-130, 1988
- [17] Fang, JQ; Li, QS; Jeary, AP. Modified independent modal space control of m.d.o.f. systems”, *J Sound & Vibr*, 261(3), 421-441, 2003
- [18] Shan, J; Liu, HT; Sun, D. Slewing and vibration control of a single link flexible manipulator by positive position feedback (ppf)”, *Mechatronics*, 15(4), 487-503, 2005
- [19] Lee, CK; Moon, FC. Modal sensors/actuators”, *J Appl Mech-T ASME*, 57(2), 434-441, 1990
- [20] Clark, RL; Burke, SE. Practical limitations in achieving shaped modal sensors with induced strain materials”, *J Vib Acoust*, 118(4), 668-675, 1996
- [21] Pagani, CC; Trindade, MA. Optimization of modal filters based on arrays of piezoelectric sensors”, *Smart Mater Struct*, 18(9), 2009
- [22] Sun, D; Tong, L; Wang, D. Vibration control of plates using discretely distributed piezoelectric quasi-modal actuators/sensors”, *AIAA J*, 39(9), 1766-1772, 2001
- [23] Grattan, KTV; Sun, T. Fiber optic sensor technology: an overview”, *Sensors Actuat A: Phys*, 82(1-3), 40-61, 2000
- [24] Othonos, A. Fiber bragg gratings”, Review of scientific instruments, 68(12), 4309-4341, 1997.
- [25] Luyckx, G; Voet, E; De Waele, W; Degrieck, J; Multi-axial strain transfer from laminated cfrp composites to embedded bragg sensor: I. parametric study”, *Smart Mater Struct*, 19(10), 2010
- [26] Huston, DR; Fuhr, PL; Beliveau, JG; Spillman, WB. Structural member vibration measurements using a fiber optic sensor”, *J Sound & Vib*, 149(2), 348-353, 1991
- [27] Comolli, L; Bucca, G; Bocciolone, M; Collina, A. First results from in line strain measurements with FBG sensors on the pantograph collector of underground trains”, Proc. SPIE 2010, Vol. 7726, 772605, "Proceedings of photonics Europe", Bruxelles, Belgium, 2010
- [28] Chau, K; Mosleh, B; Song, G; Seth, V. Experimental demonstration of fiber bragg grating strain sensors for structural vibration control”, Proc. SPIE 2004, Vol, 5391, 753-764, 2004

- [29] Ambrosino, C; Diodati, G; Laudati, A; Gianvito, A; Concilio, A; Sorrentino, A; Breglio, G; Cutolo, A; Cusano, A. Fiber bragg grating sensors and piezoelectric actuators in Co-located configuration for active vibration control applications”, *Lecture Notes in Electrical Engineering*, 20, 167-181, 2008
- [30] Balas, M. Direct velocity feedback control of large flexible structures”. *J. Guid. Control Dyn.*, 3(2), 252-253, 1979

Chapter 8

EMERGING ROLE OF THE MECHATRONIC DESIGN OF INDUSTRIAL SYSTEMS FOR THE MATERIAL PROCESSING TECHNOLOGY

Eugenio Brusa*

Dept. Mechanical and Aerospace Engineering
Politecnico di Torino, Torino, Italy

ABSTRACT

Design and construction of complex systems are probably one of the most challenging issues of the current industrial technology. Complexity is very often a crucial issue of design of products like trains, motor vehicles, aircrafts, spacecrafts, microsystems and nanodevices. Nevertheless, nowadays even the industrial equipments used for manufacturing those products might exhibit a higher level of complexity, as it happens in case of the material processing technology. Need of supervision control in those plants often requires a strong interaction among the different subsystems which perform the whole process. In addition the number of subsystems is significantly growing up, because of the amount of functions to be exploited. Moreover, in material processing several coupling effects are applied to operate such systems. They make rather difficult the design activity and the process control. Electromagnetic behaviour, fluid dynamics, structural mechanics and thermodynamics are typically involved and an energy conversion among those fields is performed. More and more the actions related to those fields need to be controlled by some automatic system, with a relevant contribution of the electronic engineering and the computer science. Resorting to the so-called ‘multiphysics approach’ in the numerical prediction of the system behaviour has been almost compulsory in those cases since long time. Only recently a real mechatronic approach was implemented. It requires that design activity plays a particular attention to all the phenomena of energy conversion, to precisely predict the influence it has on the design parameters of system and to suitably set up their values. This approach allows to exploit the energy conversion to activate several functions, which might improve the system operation, as in electromechanical sensing and actuation, or in energy saving.

* C.so Duca degli Abruzzi, 24 – 10129 Torino, Italy, Email: eugenio.brusa@polito.it; phone ++39 011 090 69 00;
fax: ++39 011 090 69 99

Steelmaking plant is a very interesting example of the material processing because of the number of subsystems currently used to support the whole process. This technology is currently growing up fairly fast thanks to a wider use of the mechatronic approach, since the early concept and design of the product development. This chapter provides an overview of some examples of integration among different physical models through some numerical tools being currently performed in the industrial systems engineering as it is applied to the steelmaking process and some challenging issues of the application of mechatronics.

Keywords: steelmaking systems, multi–body dynamics and control, finite element analysis, couple–field analysis, structural mechatronics, multi–physics simulation

1. INTRODUCTION

Suitable approaches and tools for the design and construction of heavy duty machines are a current requirement of the industrial world. Practice and experiments seem no longer sufficient to build up several industrial systems, where the level of complexity is continuously growing up. This is due to many motivations. It is usually required that system provides a large number of functions. Those systems must fit several stringent requirements for a safe operation, but it is highly recommended a drastic reduction of costs, especially when the system includes a fairly high number of subsystems, components and parts. Moreover the number of interactions among those components can be fairly large. A continuous control and monitoring action is widely demanded in modern systems and very often active controls are used to increase the smartness of such systems and improve their effectiveness in service.

Those issues are effectively covered by some new approaches like the ‘Systems Engineering’ which provides a systematic development of the whole life cycle of the product and allows an early prediction of the relevant issues concerning the complexity, from the beginning of the conceptual step of the design activity. This approach looks very helpful to reduce the cost of the design, to prevent severe and expensive actions of re–engineering, when the production process is already started. Moreover a clear overview of all the actors involved in the product life cycle (the so–called stakeholders), the functions, the requirements and needs to be satisfied is assured, thanks to the availability of detailed procedures to figure the product as a ‘system’, with all the interacting components. Functional models are usually developed according to the ‘Systems Engineering’ to allow a bright prediction of the functions, the use cases, the sequences in operation and a suitable definition of the architecture of the system. Nevertheless, a physical modelling of the system, and each subsystem, component and part is even required to perform all the analyses related to the completion of the design and production procedures as well as the maintenance and assistance. This task needs itself an effective approach as far as coupling effects are exploited inside the system.

Many applications exploit the energy conversion in devices like sensors, actuators or even energy harvesters to perform an active vibration control of structures, rotors, smart structures or even to operate the system, as in MEMS (Microelectromechanical systems). In the material processing technology coupling effects are often used as a main tool for operating the whole plant. The large need of power is usually coped with an electric supply,

with related creation of electric and magnetic fields which apply some electromechanical actions to the machines. Those effects interact with fluids, solids, gasses, and under variable environmental and process conditions, mainly related to the dynamic behaviour of both the system and the materials and to the temperature variations. Automatic control systems are used to improve the response of the system to the variable operating conditions.

An effective prediction of the evolution of such complex systems and even of the materials processed is the key issue of the design activity. Nowadays the so-called ‘multiphysics approach’ allows including many kinds of interactions and energy conversion when the system physical behaviour is modelled. Moreover, integration among different tools within the same design environment may provide several answers to some critical questions for the design, being in the past poorly available.

A preliminary experience performed by the author is proposed as a collection of test cases which allow exploring some of the challenging issues of the mechatronic approach to design. They belong to the steelmaking technology, looking as a very interesting example of material processing technology where complexity is growing up as well as the performances of the new products.

2. THE STEELMAKING PROCESS

Production of steel is currently performed through several steps by resorting to several machines which compose a modular and complex system. In modern plants either the solid metallic iron obtained by a direct reduction or the scrap coming from the shredder hammers is fed into the electric arc furnace. It provides the molten steel, which is first refined then transferred to the continuous casting. The steelmaking production includes slabs, blooms and billets. Rolling mills are then applied to transform those products into plates, pipes, sheets, bars and rods. This activity is performed by means of several working units, distributed all along the production line as in Figure 1.

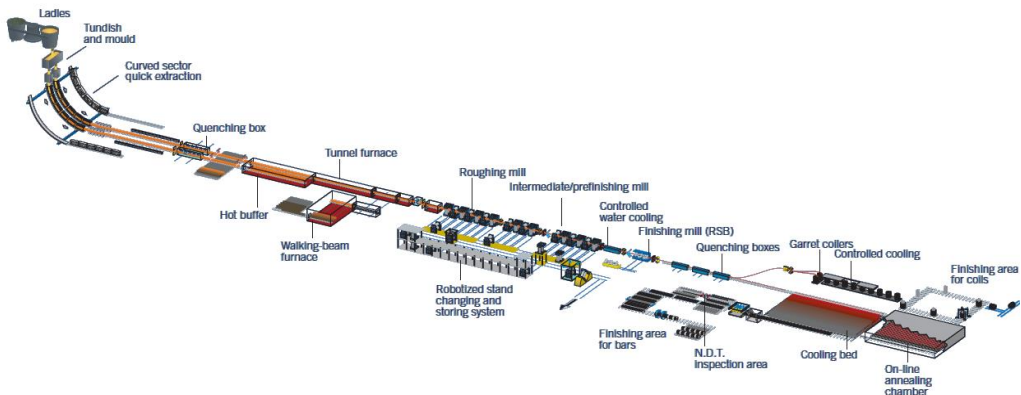


Figure 1. Example of modular system for the material processing of steel.

Peculiarities of the different machines composing the above process motivate a number of needs which are currently evidenced by the design and testing activity. In this chapter a preliminary overview of the typical coupled behaviours occurring inside some of the

machines of the steelmaking plant is proposed to describe how a mechatronic integrated approach can be developed by resorting to a tight cooperation among different design tools. Some issues will be analysed in details as the integration between functional and structural design, respectively, through a suitable cooperation between two numerical approaches like the Finite Element Method and the Multibody dynamics of rigid and flexible structures. Coupling effects due to the strong interaction between the electric field and the mechanical behaviour or between the thermal field and the structural behaviour will be even described. Moreover the tight cooperation between the system dynamics and the active process control will be analysed as an example of intelligent manufacturing based on the mechatronic approach.

3. THE SHREDDING MILL AND THE SCRAP COMMINUTION CONTROL

Use of the metallic scrap coming from the dismissed components of motor vehicles to feed the electric arc furnace for the melting process is nowadays widely preferred. Nevertheless, a reduction of size of the ferrous scrap is preliminarily required. Shredder hammers are therefore applied to cope with this need. They include a large rotor equipped with several discs. Each one bears a hammer, whose impact against the scrap reduces the dimensions of the metallic parts. Controlling the dynamic behavior of the shredding machine is difficult without an effective modeling of the whole system. System dynamics depends on the instantaneous clearance between the hammer and the pin of the disc, on the gap between the hammer and the anvil and on the friction among the materials (Figure 2). Those effects induce a severe wear of the hammer as well as some crack upon its surface. Worn configuration changes dramatically the dynamic behavior of the hammer during the shredding operation and makes harder an effective control of the angular speed and of the torque applied to the motors of the main rotor shaft.

In this case three needs were identified in daily practice. It is rather difficult measuring the magnitude of actions exerted by each hammer upon the scrap, because of the projections of material all around the operation area. Dynamic behaviour of the system depends on the two gaps above mentioned as well as on the quality of the scrap. Shredding efficiency depends on the angular speed of the rotor. Moreover the distribution of scrap along the drop is never uniform and the speed of the hammer should be regulated to induce the maximum efficiency of the shredding operation with the lowest power consumption. Some key features of the system regulation are the prevention of an excessive rotation of the hammer about the pin axis, just after the first impact, of a severe wear of the hammer material and of cracks at the pin and on the inner surface of the hammer hole (Figure 3).

To cope with those needs and provide the designer with some effective tools an integrated modelling environment was recently built up and tested by resorting to some numerical methods like the Multibody dynamics and the Finite Element Method. Regulation and control of the process could be then tested by simulating some control strategies inside the Multibody dynamics code and in co-simulation with another tool, suitable to implement the control law. Moreover an additional monitoring of the scrap drop could be associated to that regulation, if an automatic system is interoperated with the other tools, as it is in several recent plants where some inductive measuring system, or a x-rays inspection or even

automatic visual detection device is used to identify the flow of scrap approaching and to correct the angular speed of the main rotor.

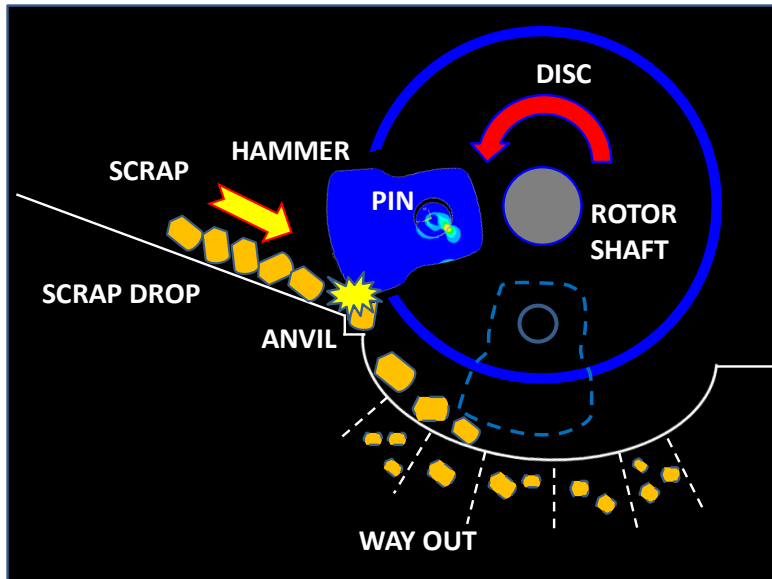


Figure 2. Functional sketch of the shredder machine operation.



Figure 3. Typical damages of the shredder hammer (cracks, ovalization, wear of the cutting edge).

Loading conditions applied to the hammer and the kinematic and dynamic behaviours of the whole rotor could be suitably predicted by modelling within the Multibody dynamics

environment the shredder machine. In this case the profile of the hammer figured as a rigid body is applied through the pin to the disc, and then the model allows writing the dynamic equilibrium equations, being then solved in the time domain.

Friction among materials, gaps, angular speed, and torque law applied by the motors upon the rotor could be set as key parameters to perform a sensitivity analysis. Multibody dynamics code allows predicting the path followed by the hammer, the impact conditions and the forces applied among the parts, although a detailed analysis of stress and strain in materials is never provided.

To complete the investigation an integrated approach based on the Multibody dynamics and the Finite Element Method is implemented to associate to each loading condition induced by the hammer while it is moving the corresponding distribution of stress and strain occurring inside the material. This analysis is helpful in preventing the damages and the failures of the shredder machine. Plastic region around the pin-to-hole connection could be easily detected and a figure of performance of the materials can be drawn, if the characteristic curve stress-vs-strain of material is known as well as inputted inside the numerical code. The mechatronic approach in this case is implemented when the stress analysis, the dynamic analysis and the control simulation are integrated within a unique tool to predict the system behaviour as well as in operation the shredder machine dynamics is suitably monitored and controlled, even in relation with to the scrap fed down.

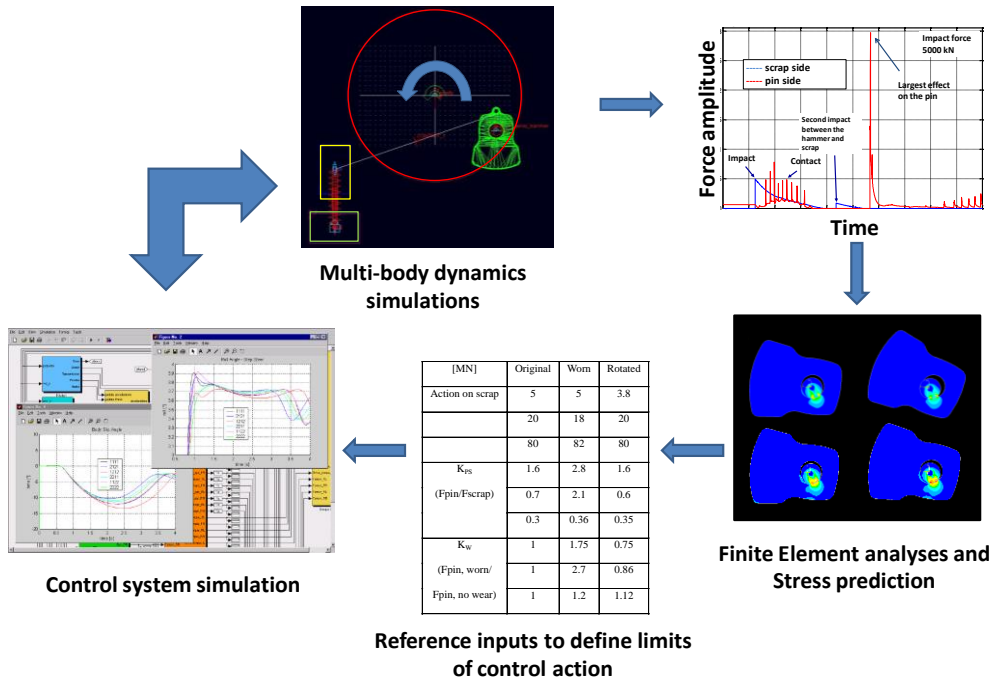


Figure 4. Integrated design tool for the shredder hammer.

A comprehensive overview of the tool assembled to predict the system behaviour is proposed in Figure 4. Actually the dynamic response of the hammer during the rotation of the main rotor and in case of impact against the scrap can be approximated in the frontal plane by a two dimensions model representing the scrap as a compliant mass-spring system, which

translates along the horizontal direction of the window and is characterized by some values of stiffness and damping. Kinematic analysis is performed to get the evolution in time domain of the hammer motion as well as of the forces applied to the scrap and to the hammer. Those actions are then inputted into the FEM model for the prediction of stress concentrations and to draw some figures of merit for the maximum impact force at a given angular speed of the rotor. The latter is saved as a look-up table of values being then used as inputs for the implementation of the rotation of the shredder, in terms of motor torque and disc spin speed.

More recently some monitoring systems have been proposed and applied to detect the amount of scrap fed to the shredder and its quality. In some cases the material is tentatively identified by means of inductive sensors, X-rays or even optical devices and a reconstruction of the acquired images allows a preliminary classification of the scrap parts in service. Although those techniques need to be assessed and calibrated for the case of the shredder machine, in principle they could improve the efficiency of the above described approach.

This issue motivated the addition of a preliminary screening of the scrap in terms of geometry and material and the related identification of the actions foreseen at the impact, by either an analytical (if geometry is standard) or numerical modeling of the collapse phenomenon, as in Figure 5.

An extension of the above mentioned model includes the modeling activity of the whole shredder machine, through a complete analysis of the rotor equipped with all the discs and the connected hammers, for a comprehensive prediction of the system dynamics.

This approach looks effective in validating the design operation and simultaneously defining the main parameters, such as the rotor spin speed at the regime condition, the mass of the hammer, the dimensions of gaps and clearances among the mechanical parts and components of this machine and the strategy of the process control to be applied for a low power consumption operation which could be associated to an effective comminution of the scrap.

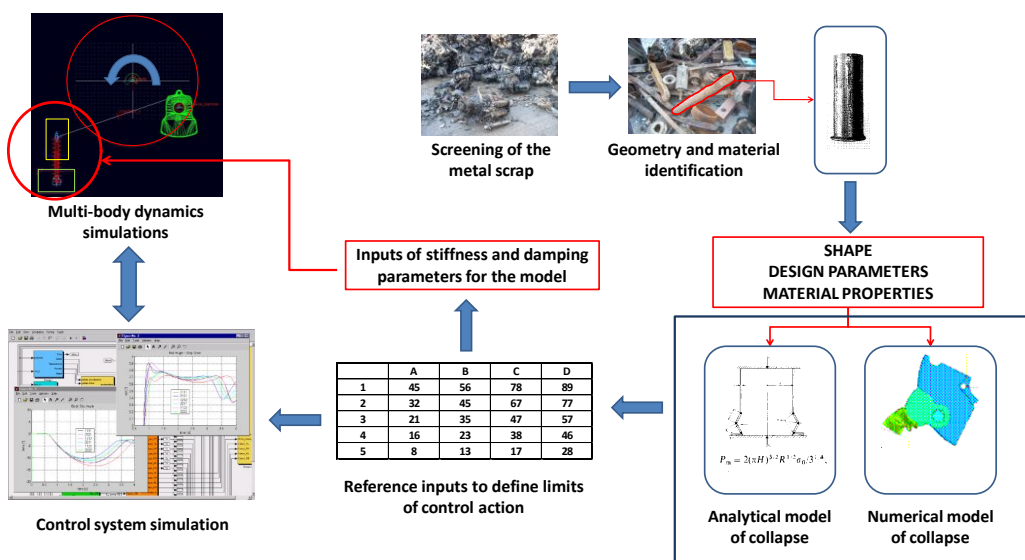


Figure 5. Introduction of a fit-to-purpose control for an identified scrap fed to the shredder.

4. THE ELECTRIC ARC FURNACE CONTROL AND OPERATION

Even more advanced in terms of application of the mechatronic approach to design is the case of the electric arc furnace (in the following briefly EAF). There two kinds of furnace, being one fed with DC current with a single electrode and a second layout in which three electrodes are connected to a AC three-phase circuit, where each phase corresponds to a mechanical structure supporting an electrode. It consists of a vertical mast column, a horizontal arm and an electrode, clamped at the end of arm. The mast column is supported by a sliding system, allowing the vertical motion and is connected to a hydraulic actuator at the bottom. A preloaded and multiple bolted flange connects the mast and the arm. The electric current flows from the cables connected to the arm back-end down to the electrode tip. Each electrode is composed by several elements, connected by nipples. Consumable electrodes are usually made of graphite to ensure a good conduction rate, even at 2000–3000°C. Arms are composed by an external double cover layer made of copper and steel and a supporting internal steel structure. Cooling water flows inside the arm to keep temperature under control (Figure 6).

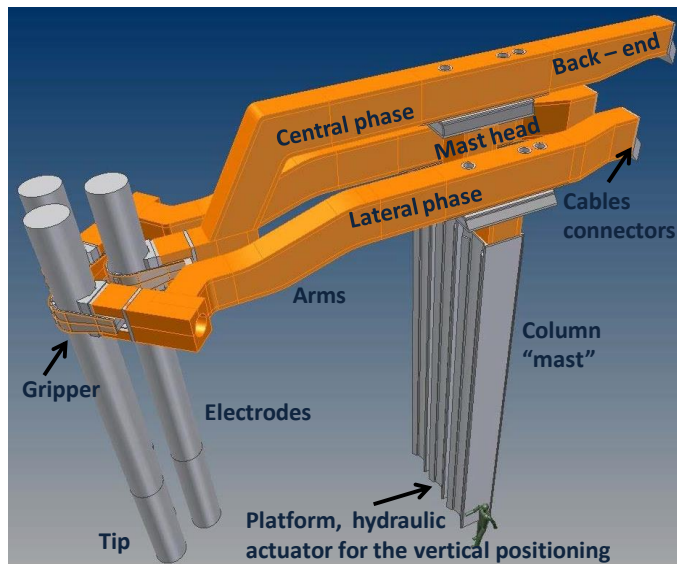


Figure 6. Sketch of the AC-EAF structure.

The electrode is lowered to create a contact with the scrap and to excite a short circuit. The electric arc is then created, thus increasing the temperature to lead to the scrap melting. The electrode is hanged by the arm, which is connected to the mast column, being constrained to the platform through a hydraulic actuator. It allows a control of the vertical position of the electrode. Each phase of the EAF system, being composed of mast, arm and electrode, corresponds to a coil.

When the current flows through the arm and the electrode, respectively, an appreciable magnetic field is generated. Each phase applies an electromechanical force upon the other two. It can be easily predicted by the Lorentz's law as is described in Figure 7. Direction of

this action rotates according to the phase of each current flowing down through the electrodes. Moreover, the electric arcs look under effect of a sort of wind due to the magnetic induction. This phenomenon turns out into an irregular behaviour of the arc voltage, being its length and direction variable over time. The scrap falling inside the furnace, the temperature growth and the melting of material change continuously the electromechanical equilibrium of the whole system.

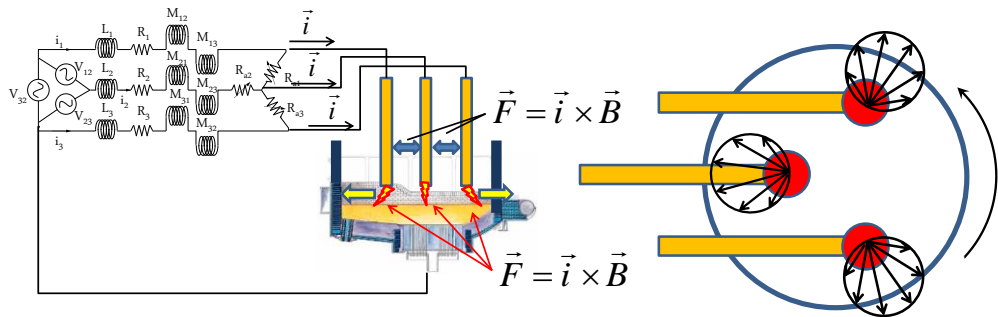


Figure 7. Description of the three-phase AC EAF with electromechanical coupling among the electrodes and the arcs (left) and sketch of the electromechanical actions applied among the electrodes during the EAF operation (top view, right).

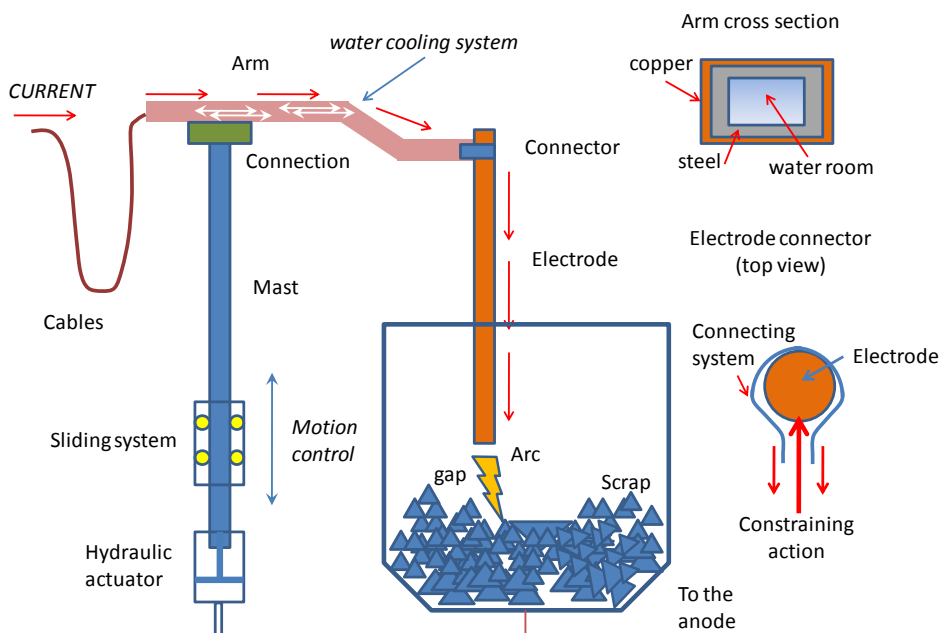


Figure 8. Sketch of a single phase of the AC-EAF structure.

A significant vibration of structures is monitored, particularly during the so-called boring operation and current of each phase remarkably fluctuates. To stabilize the arc voltage and current, respectively, a suitable action is applied to the electrode by the vertical position control. This action is aimed at keeping constant the electrical impedance of each phase and is applied by a hydraulic actuator (Figure 8). Vibration makes rather difficult this regulation,

because it strongly affects values of mutual inductance and electromechanical forces. An integrated design approach can be effectively applied in this case by resorting to a mechatronic modeling of the system, as it is depicted in Figure 9. To perform the EAF design the dynamic response of its structures has to be analyzed. Therefore, a preliminary modal analysis of the structures is carried out by means of the Finite Element Method (FEM). It might include a prediction of the thermomechanical effects occurring at different steps of the melting process, being due to the temperature changes. This model allows identifying a suitable discretization of the flexible structures to be imported into a Multi Body Dynamics code (MBD), to predict the combined rigid and flexible body motions. Dynamic equilibrium equations are there integrated in the time domain, by including the effects of the active control, the electromechanical coupling, the contact of sliding system and the electric arc dynamics. The electric circuit of the EAF is even included to compute the actions due to the mutual induction among the currents of the three electrical phases and to predict the electromechanical forces applied to their structures. Cooling water motion inside the arm is neglected, although its inertia is considered as a weight distribution along the arms. Validation of those models is quite critical; therefore a comparison among different layouts of the EAF is even included, by resorting to the experience of the manufacturer.

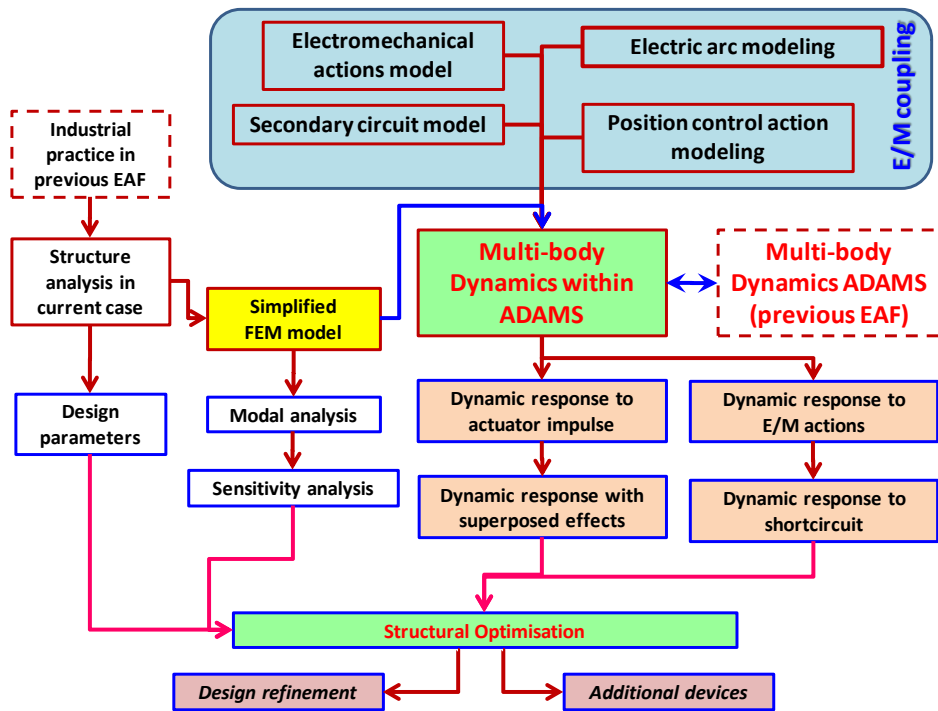


Figure 9. Architecture of the integrated model of the EAF structures.

As it is described in Figure 10 the EAF performance during the melting process is strictly related to the electric arc behaviour which dramatically depends on the dynamic behaviour of structures, on the Lorentz's forces exerted among the three-phases of the electric circuit connected to the electrodes as well as by the flicker phenomenon of the power line and by local thermomechanical coupling due to the high temperature. Only a position control of

electrodes with respect of the scrap or the liquid metal inside the vessel can assure a regular operation. This superposition of several phenomena makes highly required a numerical tool suitable to predict effects of all those interactions as well as the dynamic behaviour of structures, both in rigid and flexible body motions. This goal is achieved by means of the mechatronic analysis and modelling of the whole system. The Finite Element Method (FEM) allows predicting the dynamic behaviour in the frequency domain of the EAF structures and a suitable discretization of the flexible bodies inside the Multi-body Dynamics (MBD) code. A simplified model of the secondary electric circuit is used to compute step by step the currents flowing through the conductors. It is directly implemented inside the MBD code, although it mainly interacts with the models of the electromechanical coupling and of the arc, respectively.

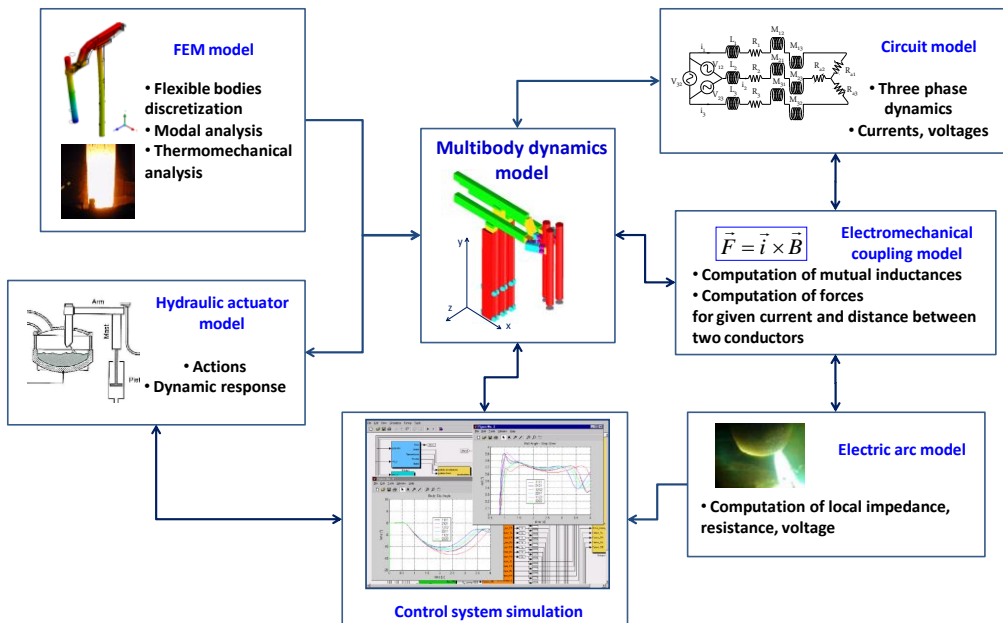


Figure 10. Layout of the interoperated numerical models for the EAF design.

The first model is aimed at updating the values of the mutual inductance of the three phases, as the distance between the elements of each couple of structures varies. Then the forces exerted by each phase upon the other ones are computed and applied. The model of the arc explicitly updates the values of current and of voltage and allows the active control system to perform a monitoring of the performance of the EAF. Control uses the reference of impedance at the arc to define a suitable command for the hydraulic actuator, which regulates the position of the mast column and of the electrode along the vertical direction, thus changing the distance between the scrap and the electrode tip. This action is aimed at making stable the arc and the power consumption. Usually the control system is even applied to perform a monitoring activity; therefore several outputs are collected in operation as well as during the simulation. A model of the hydraulic actuator is even introduced, to predict effectively its dynamic response and the effects upon the EAF structures. In some case the simplified electric circuit implemented into the related model is substituted with a complete model of the power line, being able to simulate the actual dynamic behaviour of the electric

transformers usually positioned before the EAF and the effects of the power line of the industrial plant for a more realistic prediction of the fluctuation either of current or of voltage.

In this case the integration among different models and several fields allows a comprehensive design activity of the whole system. Actually only this integration made possible an innovation of the layout of the EAF system, while in the past a detailed analysis of the performances of each part of the system was developed by resorting only to the uncoupled behaviour, without a prediction of the effects related to the coupling effects. The FEM model could be either co-simulated or used as an input for modelling the system inside the MBD code. In the first case computational effort can be fairly large and somehow unsuitable for an effective simulation during the design activity. Another possibility consists of predicting in the frequency domain the behaviour of the flexible structures eventually under the effect of a given thermal distribution, then to include those properties in terms of discretization and properties within the MBD code, as a flexible structure undergoing the application of all the actions present in such environment. In both those cases the real behaviour of the structure is foreseen fairly well, although a critical issue of design is the identification of the damping effects inside the materials as well as in the mechanical joints eventually used to assembly the whole system. This task is rather difficult to be achieved, especially if it is performed on the operating EAF system. Nevertheless, some practical approaches are currently proposed and tested in the specialised literature.

5. THE ROLLING MILL MONITORING AND CONTROL

Among the processes included within the steelmaking the cold and hot rolling operations are probably the most important and require three main control activities. Vibration of the mill frame has to be uncoupled as much as possible with the working roll operation which performs the rolling. Rolls position and pressure have to be both monitored and kept stable during the mill operation against the arising of the chatter phenomenon. Temperatures, forces, pressures and strip stretching are all to be carefully measured and controlled as well as the quality of the rolled product. All those activities need for a complete and comprehensive design of the whole rolling mill. Some differences occur between the case of cold and hot rolling, respectively. Basically in the first case speed is very high and product is fairly thin, while in the second one a relevant effect is due to the thermal transmission among the product, the rolls and somehow with the frame. Therefore even in these cases a mechatronic approach may help to reach the highest quality in the material process.

In the so-called ‘cluster’ mill, where several additional rolls are supporting the working roll, the main goal of the design concerns a suitable prediction of the roll dynamics and of the dynamic stability for given tension upon the strip, speed and friction conditions. As in previous analyses a suitable modelling activity for this system includes a multi-body model connected and interoperated together with some other models, being aimed at investigating the effects of some relevant phenomena and of the control system (Figure 11).

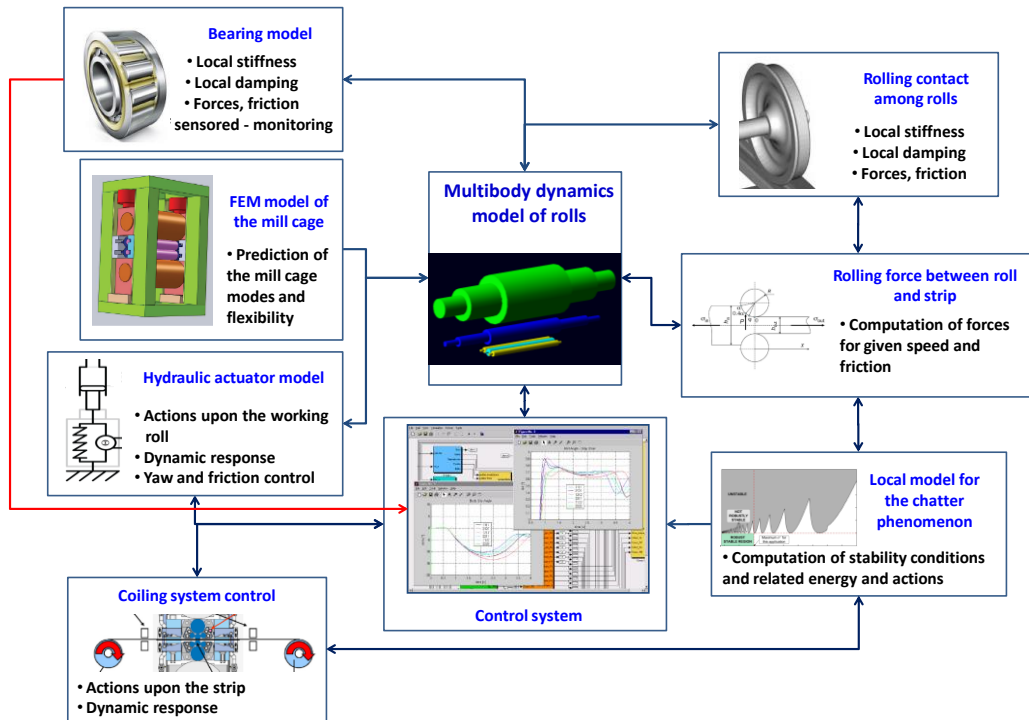


Figure 11. Layout of the interoperated numerical models for the cold rolling mill design.

In particular, in the case of the ‘cluster’ mill to include all the relevant effects of the dynamic behavior of the system, it is required that the main model of the cluster of rolls is connected to a local model of the rolling contact among the rolls, as well as to that of the rolling force, which is focused upon the interaction between the working roll and the rolled product, and with a prediction of the conditions for the occurrence of the chatter phenomenon. All those models are running in connection with the model of the control system which regulates the action of the hydraulic actuators applied to the working roll to prevent the effects of vibration and of yaw motion and with the model of the tension control system, being used to regulate the coiling and de-coiling operation, respectively, and to apply a suitable tensile loading condition to the strip. In addition a preliminary FEM modal analysis could allow taking into account the resonance of the mill cage, while a detailed model of the bearings can help in determining the actual response of the whole system. In case they are equipped with sensors, acceleration and speed are measured and directly used by the monitoring system to prevent some damage. In hot rolling mill an additional task concerns the prediction of the temperature profile inside the rolls, to update the material properties inside the other models for an effective description of the contact conditions. This could be done by analyzing preliminarily the thermal boundary conditions and the whole process through a mixed thermo-mechanical FEM model of the rolled product coupled with the working roll, this action allows preparing a reference for the above described integrated model to include the temperature changes within the whole system evolution over time and in the real plant a suitable control of the water jets being providing the cooling system (Figure 12).

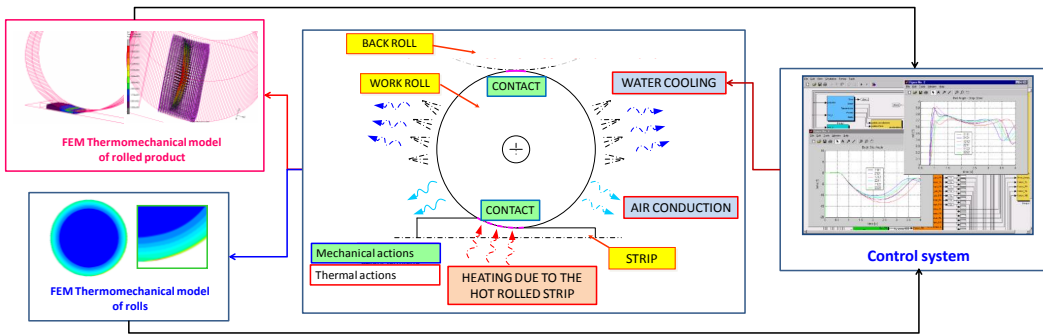


Figure 12. Overall analysis of the temperature effect in the hot rolling mill.

6. THE CUTTING OF THE STEEL RODS

A crucial activity at the end of the steelmaking process is the cutting of bars, rods, sheets and plates (Figure 13). This task has to be performed by assuring a fast operation and a precise result in such way that the rolled product can be stored and delivered. Moreover all those products have to be checked to allow rejecting the parts including some defect or damage. This task is accomplished by regulating the angular speed of the cutting device in accordance to the speed of the rolled product and to the acceleration imposed by the cutting operation upon it as soon as the two blades of the cutter rolls meet each other. Cutting of the rolled products may be optimised in terms of synchronisation of the tools with the plant behaviour. Moreover a fit-to-purpose design of the storage and delivery systems is a crucial issue of this improvement. In some case mechanical coilers for sheets are supported by magnetic bearings to increase the automation of the whole system. In case of the rod cutting to make easier the running out of the steel products a moveable deviator is used to guide alternately the cut rods towards one of the two ways out foreseen for the storage. Unfortunately the cutting operation excites the rolled product vibration, according to its modes. In case of a rod, for instance, a suitable distance between the reference plane for cutting and the deviator has to be found to assure that vibration does not induce a contact between the deviator surface and the rod, thus increasing the risk of damage and higher wear of the system components (Figure 14).

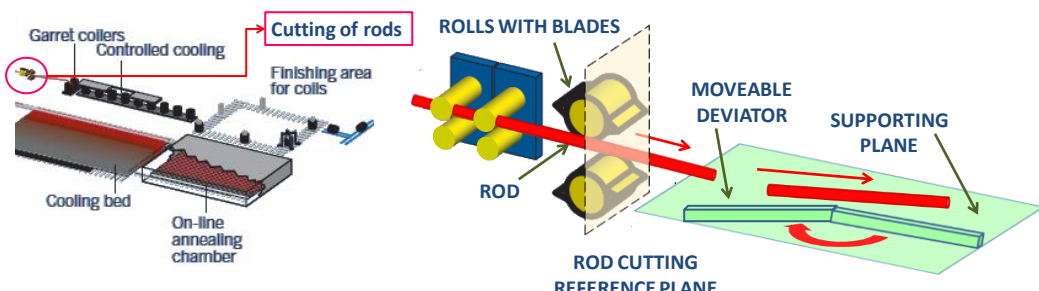


Figure 13. Sketch of the cutting operation at the end of the steelmaking plant.

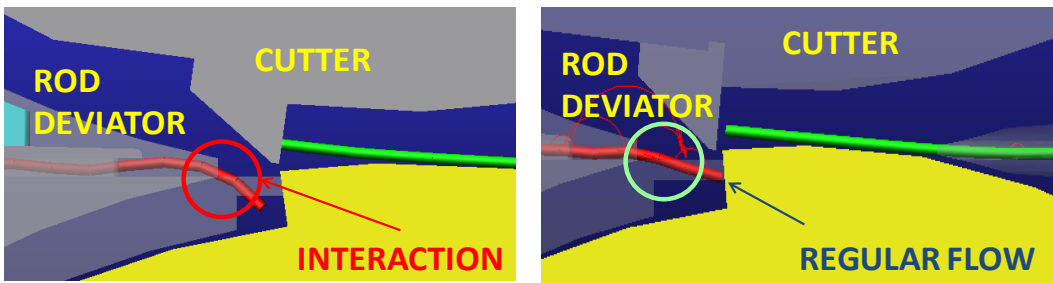


Figure 14. Numerical simulation of the cutting operation and comparison between the case of excessive vibration and strong contact with the deviator and the regular flow of the steel rod.

As Figure 15 shows even in this case a comprehensive design approach has to include several phenomena inside the integrated model of the above described system. A main model is used to predict the overall dynamics, although a detailed modeling of the contact among bodies, of the cutting edge operation and of the flexible behavior of the rod is performed. Control system simultaneously acts on the blades, by regulating the angular speed and the torque actually applied and the deviator motion. Nevertheless, a preliminary calibration of the model upon the real plant is performed by means of a high speed camera through a video monitoring, which could be eventually used in service either for the monitoring or the inspection of the plant. This activity might be used even for providing a firm of the cutting process.

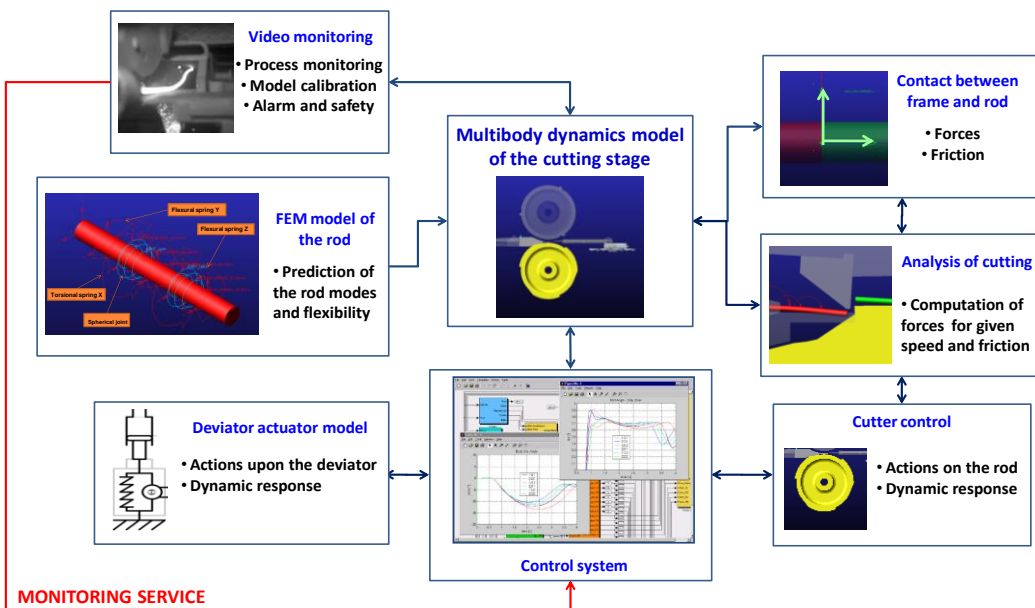


Figure 15. Integrated model of the cutting stage of the steelmaking plant.

7. OTHER EXAMPLES OF MECHATRONIC SYSTEMS FOR THE MATERIAL PROCESS TECHNOLOGY

Many other examples of mechatronic systems currently applied to the material processing technology are available in the literature. In particular, machining and tooling of material are even supported by a continuously growing up of the mechatronics, being aimed at developing some intelligent manufacturing system. A wide use of the mechatronics is currently performed in the field of the material machining. It is worthy noticing that even in that case improvements are coming from a more detailed modelling of the phenomena related to the machining operation, with particular care of the bodies flexibility, the thermal effects, the electromechanical couplings, and to an increased effectiveness of the control actions applied upon the systems. A very preliminary sketch of the current trends in mechatronics of machining and tooling systems is proposed in Figure 16. According to some recent researches within the manufacturing technologies nowadays three emerging tasks are foreseen for an improvement of the machining and tooling practice. A deeper analysis of the dynamic behavior of the tool through the FEM or other approach allows performing a better program of the part machining and an inherent optimization. Moreover, it might even affect the selection of the tool or at least of its properties and class. A direct control of the material processing, as for instance of the dynamics of the tool in turning and milling even against some critical phenomenon like the chatter, is a second goal. Application of sensors for an adaptive control may even provide a monitoring activity about the system response in service. Quality assurance and measurements performed upon the product may allow improving the effectiveness of the CAD/CAE operations, which include several options, like the discretization of the product geometry, being suitably refined if they could be correlated to the quality of the final product.

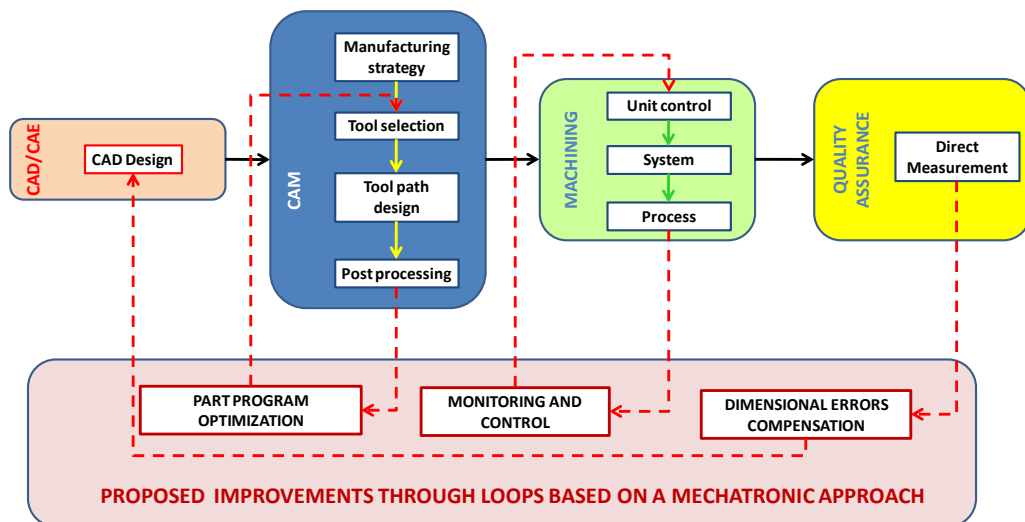


Figure 16. Sketch of the proposed actions to improve the machining and tooling systems towards the intelligent manufacturing.

8. CHALLENGING ISSUES OF THE MECHATRONIC APPROACH APPLIED TO THE MATERIAL PROCESS TECHNOLOGY

The above described examples show how the mechatronic approach is currently introduced within the industrial materials processing technology. Some typical properties among the different cases previously shown can be appreciated.

- Smartness or intelligence of the system is gradually improved by introducing some effective control and/or monitoring function. To suitably design those systems a more detailed modelling activity is required than it was in the past. Models are both functional and physical. The first ones just describe the functions and the sequence of the interactions occurring among the different actors, according to the so-called ‘Systems Engineering’ approach, being compatible and complementary to mechatronics. Physical models quantitatively describe the behaviour of the system, by resorting to some mathematical description, being usually based on equations or geometrical models.
- As soon as the mechatronic approach is applied a simulation of the real system behaviour is performed by resorting to some physical model which is integrated as far as it allows describing the relevant phenomena which affect the system performance. Sometimes those phenomena are typically predicted by different numerical and analytical tools which have to be made inter-operating or co-simulating. In the above examples the control strategy developed in some control toolbox is usually linked to the models developed within the Finite Element Method environment and the Multibody Dynamics.
- More and more the automation of the design is based on a platform of numerical tools which allow investigating the relevant coupling effects present inside the system, through some suitable tool, in a fully ‘multi-physical’ environment. In particular, fluid – structure interactions, or electromechanical coupling and thermomechanical behaviour have to be analysed and included in the reference model used by the control systems for their operation.
- A key issue of design seems to be the simultaneous prediction of the flexible body behaviour of some structural element, by including a complete analysis of stress and strain, and of the rigid body motion, being very often associated to the nonlinearity induced by some contact or gap, or even by the material behaviour.
- The complexity of several systems currently developed more and more requires an integrated approach to the design, which can fully exploit the very promising results achieved by the design tools, in conjunction with the numerical methods, the control theory and practice and by the materials, especially in the field of smart and functional matters.

All the above mentioned motivations define a clear path for the evolution of the design methodologies and for handling the increasing complexity of the newest systems. The mechatronic approach provides a holistic view upon those challenging issues and a suitable tool to face the current needs imposed by the innovation and the daily competition.

ABOUT THE AUTHOR



Eugenio Brusa was born in Turin, Italy, on 1969. Currently he is full professor of Mechanical and Machine Design at the Politecnico di Torino, Italy, being instructor of *Machine Design* and *Fundamentals of Strength of Materials*, for the B.Sc. Mechanical and Automotive Eng., as well as of *Design of industrial equipments and systems through the 'Systems Engineering' approach* for the Ph.D. in Mechanical Eng. He received the M.Sc. in Aeronautical Engineering (1993) and the Ph.D. in Machine Design (1997) from the Politecnico di Torino. He was awarded as a young scientist by the Italian Society for Stress Analysis on 1999.

He worked, from 1998 to 2001, as an Assistant Professor at Dept. Mechanics, being Head of the Spinning Test Laboratory, at the Politecnico di Torino. From 2002 to 2008 he joined the University of Udine, Italy, as an Associate Professor, being instructor of *Machine Design* and *Mechanics of Materials*, and technical director of the M.Sc. in *Project Management and Systems Engineering* (2005–2007). On 2008 he was newly enrolled by the Politecnico di Torino, at Dept. Mechanical and Aerospace Engineering, where he currently works. Appointed full professor on 2010 he was upgraded to this role on 2013, because of restrictions in the turn-over process imposed by the recent economic crisis.

Major in research activity of prof. Eugenio Brusa is *Structural Mechanics and Mechatronics*, being performed in the frame of *Laboratory of Design and Characterization of Microsystems* and of *Laboratory of Railways Systems Design*, of the Politecnico di Torino. He is leader of the Research Group on *Design of Steelmaking Equipment and System Engineering* and Scientific Coordinator of the Partnership between Danieli (Italy) and the Politecnico di Torino.

He was among the founders of the *Interdepartmental Laboratory of Mechatronics*, in Torino (1993) then of the “*Tech-UP*” *Laboratory for the Ubiquitous and Pervasive Technologies* in Udine (2005–2008), being also the technical coordinator of the *Mechatronic Section*. He is active within *Structural Mechatronics and Micromechatronics; Structural design of rotors, vehicles and steelmaking plants*. He is currently involved in some main projects concerning *Electrical and thermomechanical reliability of MEMS* and *Fracture mechanics in Piezoelectric Energy harvesters; Design of Steelmaking Equipments through the FEM–Multibody dynamics numerical approaches and Industrial ‘Systems Engineering’*.

He was instructor in Torino about the *Pressure Vessel Standards ASME VIII 1-2*, within the joint program with the University of Illinois at Chicago (1997–2004). He was invited lecturer of ‘*Structural Mechatronics*’ and ‘*Structural Micromechatronics*’ at TU Delft, The Netherlands (2000), TU Helsinki, Finland (2002), University “Blaise Pascal”, Clermont

Ferrand, France (2005), CNRS, Paris, France (2007), TU München, Germany (2009), Ecole EPF, Sceaux, France (2007, 2010) and Institute Marie Curie, Paris, France (2010). He was among the organizers and instructors of the “First European School in Mechatronics and Microsystems” (2006), at the Carolo-Wilhelmina University of Braunschweig (Germany) and of the International Course in “Microsystem Mechanical Design” (2004) at the Int. Centre for Mech. Sciences, CISM, Italy. He was even Coordinator of the “Advanced Educational Program on Design, Reliability and Safety of Structural Industrial Systems”, at CISM, Udine (2006–2008). On 2010 he was elected Vice Chair of the Board of the Italy Section of the American Society of Mechanical Engineers (ASME) for 2010–2014.

He is author of more than 160 scientific papers, either published on journals or presented to international conferences, and of some patents concerning the mechatronic stabilization of rotors. He is co-author of “*Microsystem Mechanical Design*” published by Springer (2006) and of “*MEMS: Technology, Fabrication Processes and Applications*”, published by Nova Science (2010).

REFERENCES

- Aboussouan, L, et al., Steel scrap fragmentation by shredders, *Powder Technol.*, 105, pp.288–294, 1999.
- Altintas, Y, *Manufacturing Automation: Metal Cutting Mechanics, Machine Tool Vibrations, and CNC Design*. Cambridge , Cambridge University Press, 2012.
- Avoledo, A, Bosso, N, Brusa, E, Morsut, S, Picciotto, M, Numerical modeling and dynamic behavior prediction of AC Electric Arc Furnace structures during the scrap melting process, Proc. ASMET European Steel Making Conference, EEC 2012, 25–28th September 2012, Graz, Austria.
- Bar, A, Swiatoniowski, A, Interdependence between the rolling speed and non-linear vibrations of the mill system, *J. Mat. Proc. Tech.*, 155–156, pp.2116–2121, 2004.
- Benasciutti, D, Brusa, E, Bazzaro, G, Finite elements prediction of thermal stress in work roll of hot rolling mills, *Procedia Engineering*, 2(1), pp.707–716, 2010.
- Benasciutti, D, Brusa, E, Colavitti, V, Lemma, L, Dynamics of Sendizimir cold rolling mill and correlation with bearing and roll fault, Proc. AMST '08 8th Int. Conf. on Adv. Man. Syst. Tech., CISM, Udine, 2008, pp.559–570.
- Bosso, N, Brusa, E, Morsut, S, Dynamic behavior and prevention of the damage of material of the massive hammer of the scrap shredding machine, *Meccanica*, 49(3), pp.575–586, 2014.
- Bosso, N, Brusa, E, Morsut, S, Numerical modeling of the dynamic behavior of shredder hammers and correlation with material damage, Proc. ASME Biennal Int. Conf. on Eng. Design and System Analysis, ESDA, 2012, July 2012, Nantes, France; vol.1, pp.449–458.
- Bosso, N, Brusa, E, Zampieri, N, Morsut, S, Picciotto, M, Electromechanical coupled response of the AC Electric Arc Furnace structures during the scrap melting process, Proc. ASME Biennal Int. Conf. on Eng. Design and System Analysis ESDA, 2012, July 2012, Nantes, France, vol.1, pp.459–468.
- Bowman, B, Krüger, K, *Arc furnace physics*, Düsseldorf, Stahleisen communications, 2009.

- Brusa, E, Analysis of stiffening effect and rupture in dynamics of graphite electrodes of the Electric Arc Furnace, Proc. ASME ESDA 2014, 12th Biennial Conf. on Eng. Syst. Design and Analysis, Copenhagen, 25–27th June 2014.
- Brusa, E, Franceschinis, E, Morsut, S, Compact modelling of electric arc furnace electrodes for vibration analysis, detection and suppression, *CMES–Computer Modeling in Engineering and Sciences*, 42 (2), pp. 75–106, 2009.
- Brusa, E, Lemma, L, A multi-level approach for the mechanical design of cluster mills for cold rolling of thin steel products, Proc. 8th Biennal ASME Conf. on Eng. Syst. Design and Analysis, ESDA 2006, Turin, Italy, July 4–7, 2006.
- Brusa, E, Lemma, L, Benasciutti, D, Vibration analysis of Sendzimir cold rolling mill and bearing fault detection, *Proc. ImechE – Part C: J. Mech. Eng. Science*, 224, pp.1645–1654, 2010.
- Brusa, E, Lemma, L, Numerical and experimental analysis of the dynamic effects in compact cluster mills for cold rolling, *J. Mat. Proc. Tech.*, 209, pp. 2436–2445, 2009.
- Brusa, E, Lemma, L, On the development of tools for mechanical design of cold rolling cluster mills, in *AMST '05 Advanced Manufacturing Systems Technology*, Wien, Springer Verlag, 2005, pp.403–412.
- Brusa, E, Morsut, S, Mechatronic modeling and optimization of the structural layout of the electric arc furnace, Proc. ASME ESDA 2014, 12th Biennial Conf. on Eng. Syst. Design and Analysis, Copenhagen, 25–27th June 2014.
- Byrne, G, Dornfeld, D, Inasaki, I, Ketteler, G, Konig, K, Teti, R., Tool condition monitoring (TCM) – The status of research and industrial application, *CIRP Annals Manufacturing Technology*, 44(2), pp.541–567, 1995.
- Chang, DF, Thermal stresses in work rolls during the rolling of metal strip, *J Mater Process Tech*, 94, pp.45–51, 1999.
- Craig, RR, Bamberton, M, Coupling of substructures for dynamic analysis, *AIAA Journal*, 6(7), pp.1313–1319, 1968.
- Dohner, J, et al., Mitigation of chatter instabilities in milling by active structural control. *J. Sound and Vibration*, 269(1–2), pp.197–211, 2004.
- El-Saady, G, Adaptive static VAR controller for simultaneous elimination of voltage flickers and phase current imbalances due to arc furnaces loads, *Electric Power Systems Research*, 58, pp.133–140, 2001.
- Gholamian, MR, Fatemi Ghomi, S, Meta-knowledge of intelligent manufacturing: An overview of state-of-the-art, *Applied Soft Computing*, 7(1), pp.1–16, 2007.
- Ginzburg, VB, Ballas, R, *Flat rolling fundamentals*, New York, Dekker, 2000.
- Hu, P, Ehmann KF, A dynamic model of the rolling process. Part II: Inhomogeneous model, *Int. J. Mach. Tool & Man.*, 40, pp.21–31, 2000.
- Hu, P, Ehmann, KF, A dynamic model of the rolling process. Part I: Homogeneous model, *Int. J. Mach. Tool & Man.*, 40, pp.1–19, 2000.
- Jawahir, IS, Balaji, AK, Rouch, KE, Baker JR, Towards integration of hybrid models for optimized machining performance in intelligent manufacturing systems, *J. Mat. Proc. Tech.*, 139(1–3), pp.488–498, 2003.
- Jones, J, Bowman, B, Lefrank, PA, Electric Furnace Steelmaking, in *Steelmaking and Refining*, Volume of The AISE Steel Foundation, 1998.
- Jones, N, *Structural impact*, Cambridge, Cambridge University Press, 1997.

- Junkins, JL, Kim, Y, *Introduction to dynamics and control of flexible structures*, Washington, AIAA publications, 1993.
- Kosse, V, Mathew, J, Design of hammer mills for optimum performance, *Proc. Inst. Mech. Eng., Part C, J. Mech. Eng. Sci.*, 215, pp.87–94, 2000.
- Li, CS, Yu, HL, Deng, GY, Liu, XH, Wang, GD, Numerical simulation of temperature field and thermal stress field of work roll during hot strip rolling, *J Iron Steel Res. Int.*, 14(5), pp.18–21, 2007.
- Li, ZZ, Zheng, M, Zheng, L, Wu, Z, Liu, D, A solid model based milling process simulation and optimization system integrated with CAD/CAM, *J. Mat. Proc. Tech.*, 138(13), pp.513–517, 2003.
- Lin, YJ, et al., On the characteristics and mechanism of rolling instability and chatter, *Trans. ASME J. Manuf. Sc. and Eng.*, 125, pp.778–786, 2003.
- Lo, CC, Hsiao, CY, A method of tool path compensation for repeated machining process, *Int. J. Mach. Tools and Man.*, 38(3), pp.205–213, 1998.
- Meirovitch, L, *Dynamics and control of structures*, New York, John Wiley and Sons, 1999.
- Ozel, T, Davim, JP, *Intelligent Machining*, ISTE Wiley, 2009.
- Patula, EJ, Steady-state temperature distribution in a rotating roll subject to surface heat fluxes and convective cooling, *J. Heat Transf.*, 103, pp.36–41, 1981.
- Pawelski, H, Friction inhomogeneities in cold rolling, *J. Mat. Proc. Tech.*, 125–126, pp.392–397, 2002.
- Quintana, G, Ciurana, J, Chatter in machining processes: a review, *Int. J. Mach. Tools and Man.*, 51(5), pp. 363–376, 2011.
- Roberts, WL, *Cold rolling of Steel*, New York, Marcel Dekker Inc., 1978.
- Russo, P, et al., Mechanical and metallurgical study of the fragmentation of end-of-life goods in a scrap shredder, *Int. J. Miner. Process.*, 74S, pp.S395–S403, 2004.
- Sato, S, Ishida, R, Imamura, Y, Miyata, I, Kimura, T, Theory and experiments of thermal stress fracture of graphite electrodes for steelmaking arc furnaces, *Carbon*, 35(3), pp.353–363, 1997.
- Shabana, A, *Dynamics of multi-body systems*, Cambridge, Cambridge Press, 2000.
- Soliman, E, Ismail, F, Chatter suppression by adaptive speed modulation, *Int. J. Mach. Tools and Man.*, 37(3), pp.355–69, 1997.
- Sortino, M, Belfio, S, Motyl, B, Totis, G, Compensation of geometrical errors of CAM/CNC machined parts by means of 3D workpiece model adaptation, *Computer Aided Design*, 48, pp.28–38, 2014.
- Sun, CG, Yun CS, Chung JS, Hwang SM, Investigation of thermomechanical behavior of a work roll and roll life in hot strip rolling, *Metall. Mater. Trans. A*, 29A, pp.2407–2424, 1998.
- Taylor, C, *Electric furnace steelmaking*, AIME–Iron and Steel Society, UK, 1975.
- Tseng, AA, Lin, FH, Gunderia, AS, Ni, DS, Roll cooling and its relationship to roll life, *Metall. Trans. A*, 20A, pp.2305–2320, 1989.
- Tseng, K, Wang, Y, Vilathgamuwa, DM, An experimentally verified hybrid Cassie-Mayr electric arc model for power electronic simulations, *IEEE Trans. on Power Electronics*, 12(3), pp.429–436, 1997.
- Varadan, S, Makram, EB, Gergis, AA, A new time domain voltage source model for an arc furnace using EMTP, *IEEE Trans on Power Delivery*, 11(3), pp.1685–1691, 1996.

VDE, Verein Deutscher Eisenhüttenleute, *The Steel Manual*, translation of “Stahlfibel”, Dusseldorf, Verlag Stahleisen, 1992.

Yun, IS, Wilson WRD, Ehmann KF, Review of chatter studies in cold rolling, *Int. J. Mach. Tool & Man.*, 38, pp.1499–1530, 1998.

Yun, IS, Wilson, WRD, Ehmann, KF, Chatter in the strip rolling process, Part 1: Dynamic model of rolling, *Trans. ASME, J. Man.Sc. and Eng.*, 120, pp.330–336, 1998.

Chapter 9

PREDICTION AND CONTROL OF VIBRATIONS AND CHATTER IN MACHINING

*Marco Sortino *and Giovanni Totis †*

Department of Electrical, Managerial and Mechanical Engineering
of the University of Udine, Italy

Abstract

Nowadays, high levels of automation, integration and flexibility are required to increase the competitiveness of manufacturing industries. In this perspective, an increasing interest in unmanned, intelligent machining systems has emerged. Ideally, future production systems will be designed to automatically perform complex tasks, such as planning and optimization of tool trajectories and cutting parameters, tool collision detection and tool condition monitoring, effective suppression of vibrations and chatter. Self-excited chatter vibrations may arise during machining for specific combinations of cutting parameters. This detrimental phenomenon may cause abnormal tool wear or tool breakage, damage of tooling structure and spindle bearings, poor surface roughness and dimensional accuracy of the workpiece. In the last few decades, several methodologies and systems for chatter prevention, detection and suppression were proposed in technical literature and some of them have been already successfully implemented in innovative machine tools and tooling systems. The aim of this chapter is to introduce the problem and the modern methodologies for its solution.

Keywords: machining, turning, milling, vibrations, chatter, prediction, control

1. Introduction

Nowadays, the competitive level of manufacturing industries is dependent on their capacity to increase productivity and reduce production costs by assuring, concurrently, high product quality. Moreover, the production plants are forced to direct their efforts towards the

*E-mail address: marco.sortino@uniud.it

†E-mail address: giovanni.totis@uniud.it

production of advanced products with high added value. This is particularly true for plants located in the industrialized countries where the labour cost is high. For this purpose, last generation production technologies and innovative methodologies for production planning and control are required.

In this perspective, there is a strong need of virtual engineering systems where product design, process engineering, production planning and control are integrated in a common framework.

Increasing the levels of automation, intelligence and reconfigurability of modern production systems is another key factor for enhancing their efficiency. Ideally, future production systems will be able to automatically perform complex tasks, such as planning and optimization of tool trajectories and cutting parameters, tool collision detection, tool condition monitoring, compensation of quasi-static errors affecting the machining system and suppression of undesired vibrations and chatter.

Although vibrations are always present when machining, self-excited chatter vibrations may arise only for specific combinations of cutting parameters. This physical phenomenon has to be avoided since it may greatly reduce workpiece quality and damage the tool or the machine tool.

The aim of this chapter is to introduce the problem of vibrations in machining operations and the modern methodologies for its solution.

The chapter is organized as follows. In section 2. very common machining operations such as turning and milling are introduced. In section 3. some principles for modelling the quasi-static deformations of the machining system are given. Afterwards, in section 4. the dynamic behaviour of the machining system is addressed. Machining vibrations and chatter are described in section 5.. In the same section, the main physical mechanisms responsible for chatter onset are explained, some general principles for chatter modelling and prediction in turning and milling are given. In section 6. the main sensors and methodologies for chatter detection are outlined. Eventually, the most important and effective techniques for chatter prevention and suppression are briefly illustrated in section 7..

2. Machining Fundamentals

2.1. Turning

Turning is a conventional machining operation where the material removal is obtained by the combination of workpiece rotation and translational movement of the cutting tool. Workpiece rotational speed corresponds to the spindle rotational speed n [rpm]. Alternatively, the spindle revolution frequency f_T [Hz] can be used, where

$$f_T = \frac{n}{60} \quad (1)$$

Thus, the workpiece revolution period T [s] is given by

$$T = \frac{1}{f_T} \quad (2)$$

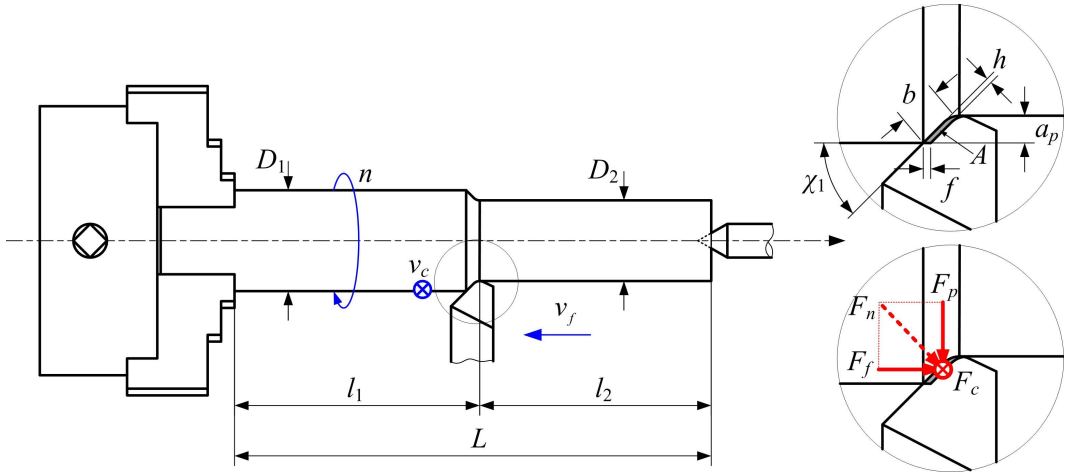


Figure 1. Kinematics and mechanics of longitudinal external turning.

At the same time, the cutting tool translates along a predefined trajectory with feed speed v_f [mm/min], which is related to feed per workpiece revolution f [mm] and with spindle speed n by the formula

$$v_f = f \cdot n \quad (3)$$

Stock material thickness measured in radial direction is the depth of cut a_p [mm]. Tool-workpiece instantaneous engagement is represented by the uncut chip section area A [mm^2] highlighted in Figure 1, which can be expressed by

$$A = f \cdot a_p = h \cdot b \quad (4)$$

where h [mm] is the uncut chip thickness (measured in the direction orthogonal to the cutting edge) and b is the length of the engaged cutting edge. The material removal rate MRR [mm^3/min] is given by

$$\text{MRR} = 1000 A \cdot v_c = \pi D \cdot a_p \cdot v_f \quad (5)$$

where v_c is the cutting speed [m/min] corresponding to workpiece diameter D [mm] and spindle rotational speed n , i.e.,

$$v_c = \frac{\pi \cdot D \cdot n}{1000} \quad (6)$$

During the cutting process significant forces are applied to the cutting tool by the workpiece and viceversa. In general, the resultant cutting force \mathbf{F} can be decomposed into the main cutting force F_c [N] (acting in the direction tangential to the workpiece, parallel to the cutting speed v_c), the feed force F_f [N] (which is parallel to spindle axis in longitudinal turning) and the back force F_p [N] acting in the radial direction.

Let us further define the thrust force F_n [N] as the projection of the resultant cutting force \mathbf{F} along the perpendicular to the main cutting edge (whose orientation is determined

by the cutting edge angle χ_1). When the influence of nose radius can be neglected - as in this simple case - such force is the vector sum of the feed and back force components.

The main cutting force F_c and the normal force F_n can be roughly expressed by the following equations

$$\begin{cases} F_c \cong k_{cs}A = k_{cs} \cdot \frac{a_p}{\sin \chi_1} \cdot h \\ F_n \cong k_{ns}A = k_{ns} \cdot \frac{a_p}{\sin \chi_1} \cdot h \\ F_p \cong F_n \cdot \cos \chi_1 \\ F_f \cong F_n \cdot \sin \chi_1 \end{cases} \quad (7)$$

where k_{cs} and k_{ns} [MPa] are the specific cutting pressures in tangential and normal directions, respectively. Typically, $k_{cs} \approx 500 \div 5000$ [MPa], and $k_{ns} \approx 0.5 \cdot k_{cs}$. These coefficients do mostly depend on the mechanical properties of workpiece material. Moreover, they do slightly depend on tool geometry and on cutting parameters. However, they will be considered constant in the following for the sake of simplicity.

An example of an experimental cutting force measurement is given in Figure 2, on the left. The measured cutting force is characterized by an average static value, which can be estimated by using the cutting force model presented in Equation (7). Nevertheless, it is worth noting that even for this simple and apparently stationary cutting process, cutting conditions vary in time, thus causing significant fluctuations of cutting forces in turning. The most common reasons for such fluctuations are:

- geometric-kinematic inaccuracies affecting the whole kinematic chain composed by the workpiece, workpiece fixture, spindle, machine tool axes, tooling system and tool, such as tooling system eccentricity or teeth run-out (error in the radial positioning of each tooth with respect to the nominal position);
- effective dynamics of machine tool axes and spindle regulation;
- machining system vibrations;
- non-stationary phenomena associated to chip formation instabilities and to workpiece material microstructure.

2.2. Milling

Milling is another fundamental cutting process where the material removal is obtained by the combination of the rotational movement of the cutter with the relative translation between tool and workpiece (which can be executed by tool, workpiece or both). In milling the rotating tool is composed of several teeth or flutes with simple or very complex geometry, which are located on the periphery of the cutter body. Basically, it is possible to classify milling operations in two main categories, depending on the orientation of the machined surface with respect to spindle axis. Specifically, the machined surface is orthogonal to spindle axis in face milling operations, whereas it is parallel to spindle axis in peripheral or tangential milling operations. For the sake of simplicity, let us consider conventional face milling operations performed with inserted cutters with z_t teeth mechanically clamped on the cutter body. Although teeth angular spacing can be irregular, here the teeth are assumed equally spaced on cutter circumference for the sake of simplicity.

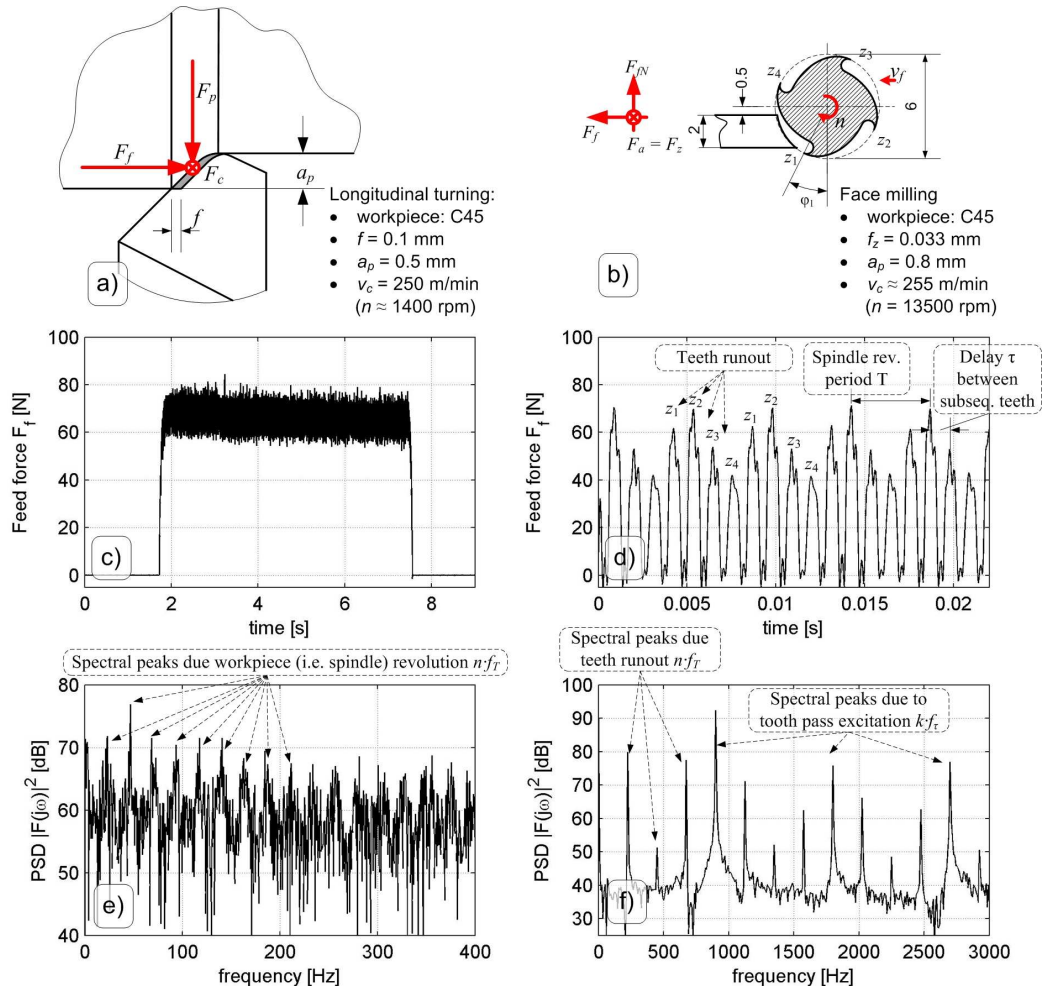


Figure 2. Experimental behaviour of cutting forces during longitudinal turning ((a), (c), (e)) and face milling ((b), (d), (f)).

As in turning, the spindle rotational speed n [rpm] and its derived quantities - the spindle revolution frequency f_T and the spindle revolution period T - are important kinematic parameters. However, the tooth pass excitation frequency f_t [Hz]

$$f_t = f_T \cdot z_t \quad (8)$$

and the corresponding fundamental time delay between subsequent teeth τ

$$\tau = \frac{1}{f_t} \quad (9)$$

play a crucial role in the context of milling vibrations. In milling the feed speed v_f [mm/min] is given by

$$v_f = f_z \cdot z_t \cdot n \quad (10)$$

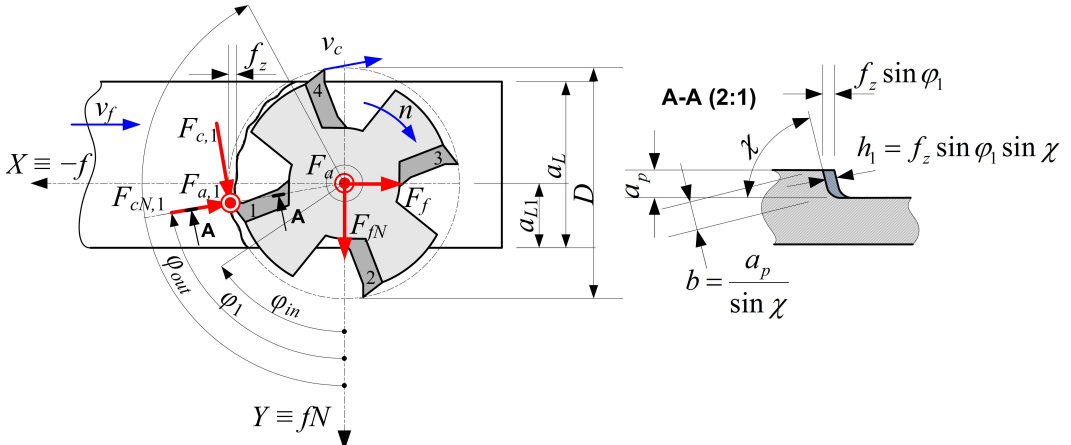


Figure 3. Kinematics and mechanics of face milling.

where f_z [mm] is the feed per tooth per cutter revolution, as shown in Figure 3. The thickness of the removed stock material measured along spindle axis is the depth of cut a_p [mm].

In milling, the material removal rate MRR [mm^3/min] is given by

$$MRR = a_L \cdot a_p \cdot v_f \quad (11)$$

where a_L is the lateral width of cut.

The uncut chip section A_j [mm^2] perceived by the j^{th} tooth is characterized by the cutting edge length b_j [mm] and by the uncut chip thickness h_j [mm]. It is worth noting that the instantaneous uncut chip thickness h_j is time-varying in milling. Specifically, it can be approximated by

$$h_j = h_j(\varphi_j) \cong f_z \cdot \sin(\varphi_j) \cdot \sin(\chi) \cdot g(\varphi_j) \quad (12)$$

where φ_j is the instantaneous feed motion angle of the j^{th} tooth and $g(\varphi_j)$ is a window function representing the effect of interrupted cutting conditions (it is equal to unity when the tooth is engaged in the workpiece, zero otherwise). Cutting mechanics are complicated by the presence of multiple teeth. During the cutting process, the force applied to the j^{th} tooth can be decomposed into the main cutting force $F_{c,j}$ [N], the cutting perpendicular force $F_{cN,j}$ [N] and the axial force $F_{a,j}$ [N], see Figure 3.

These cutting force components can be roughly expressed by the simple model

$$\begin{cases} F_{c,j} \cong k_{cs} \cdot A_j = k_{cs} \cdot a_p \cdot f_z \cdot \sin(\varphi_j) \cdot g(\varphi_j) \\ F_{cN,j} \cong k_{ns} \cdot A_j \cdot \sin(\chi) = k_{ns} \cdot a_p \cdot f_z \cdot \sin(\varphi_j) \cdot g(\varphi_j) \cdot \sin(\chi) \\ F_{a,j} \cong k_{ns} \cdot A_j \cdot \cos(\chi) = k_{ns} \cdot a_p \cdot f_z \cdot \sin(\varphi_j) \cdot g(\varphi_j) \cdot \cos(\chi) \end{cases} \quad (13)$$

The total force acting on the cutter body is the sum of forces acting on each tooth at a given instant, by taking into account their different orientation with respect to the stationary, non-rotating reference frame $OXYZ$. It can be decomposed into the feed force $F_f = -F_x$ [N], the feed perpendicular force $F_{fN} = F_y$ [N] and the total axial force F_a [N].

Each component is time varying. When considering an ideal milling process - i.e., performed by an extremely stiff and geometrically perfect machining system on an homogeneous workpiece material in stationary cutting conditions - the cutting forces are perfectly τ -periodic. In other words, their spectra are dominated by spectral peaks located at the tooth pass excitation frequency f_τ and at its integer multiples.

Nevertheless, cutting forces are more irregular in real cutting conditions, due to geometrical errors such as teeth radial run-out or spindle eccentricity. Accordingly, their behaviour in frequency domain are contaminated by harmonics located at the spindle revolution frequency f_T and at its integer multiples, as shown in Figure 2 b), d) and f).

3. Dimensional Errors due to Quasi-Static Deformations of the Machining System

As described in the previous section, cutting forces are characterized by quasi-static trends and by time-varying fluctuations, even in apparently stationary cutting conditions. Quasi-static trends cause deflections of tool and workpiece which are responsible for dimensional and form errors affecting the machined part. On the other side, time-varying fluctuations cause undesired vibrations of tool and workpiece, which may imply a bad surface quality and other severe problems, as will be illustrated in section 6..

For many practical purposes, it is important to obtain a rough, preliminary estimate of the dimensional errors due to static deflections. A good estimate can be derived by applying the Finite Element Method to the machining system by means of dedicated software.

In order to reduce the modelling and computational efforts, it is important to identify the most flexible parts of the kinematic chain - to be approximated by flexible Finite Elements - while considering the other parts as rigid. For example, when milling dies and moulds with finish endmills of small diameter, it is sufficient to model the slender overhang of the tooling system.

In order to give the flavour of this approach, let us apply it to the simple longitudinal turning operation illustrated in Figure 1. In these conditions, the tool tip compliance is negligible in comparison with workpiece compliance along the radial direction, thus the tool can be approximated as a rigid body. On the contrary, workpiece behaviour can be well described by two Euler-Bernoulli FE beams of different diameter and length, joined together at the instantaneous tool-workpiece contact point, as shown in Figure 4.

In order to estimate the dimensional errors affecting the machined cylindrical part, the following steps have to be accomplished:

- for each FE beam, the corresponding stiffness matrix has to be generated and its coefficients have to be inserted into the global stiffness matrix, by taking into account the congruence conditions among adjacent nodes (which are nodes 2 and 3 in the current example);
- the real clamping conditions have to be approximated by ideal constraints, and the corresponding degrees of freedom have to be cancelled (rotation and translation of node 1 at self-centering chuck and rotation of node 4 at the tailstock dead center); by so doing, a reduced, non-singular global stiffness matrix is obtained;

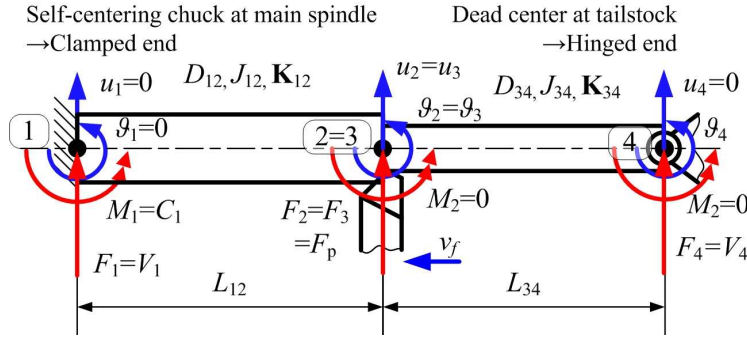


Figure 4. Modelling of a cylindrical workpiece during a basic longitudinal turning operation by means of Finite Element beams, for estimating the dimensional error caused by workpiece quasi-static deflection at the instantaneous workpiece-tool contact point.

- loading conditions have to be imposed (cutting forces at node 2 = 3 in the current example).
- the reduced global stiffness matrix can be now inverted in order to derive workpiece deflection at the central node, for a given axial position of the tool;
- the calculation has to be iterated for different tool axial positions, in order to estimate the dimensional errors affecting workpiece diameters at different axial positions;
- the whole procedure may be repeated for different clamping conditions, in order to evaluate their effect on dimensional precision, as illustrated in figure 5.

It has to be pointed out that in the current example the effective back force component (acting in the radial direction, which is responsible for workpiece deflection) is given by

$$F_2 = F_p \cong k_{ns} \cdot f \cdot (a_p - u_2) \cos \chi_1 \quad (14)$$

showing the implicit dependence of the cutting force by the deflection of the workpiece, which will be also very important when dynamic vibrations of the machining system will be investigated.

Although this implicit dependence, an exact closed form solution can be derived for this basic example, after some algebraic manipulations. The results are illustrated in Figure 5.

The numerical results presented in Figure 5 proved that only some specific clamping conditions may be adequate for achieving the desired dimensional precision, thus showing the usefulness of this kind of modelling approaches in the production planning phase, or when trying to identify and quantify the possible sources of machining inaccuracies.

Milling operations may be also affected by important dimensional or form errors due to quasi-static deflections of the tool, workpiece or both. For instance, when performing peripheral milling with slender endmills the average cutting forces acting along the engaged flutes may cause a significant tool tip deflection, thus implying overcutting or undercutting conditions, as illustrated in Figure 6.

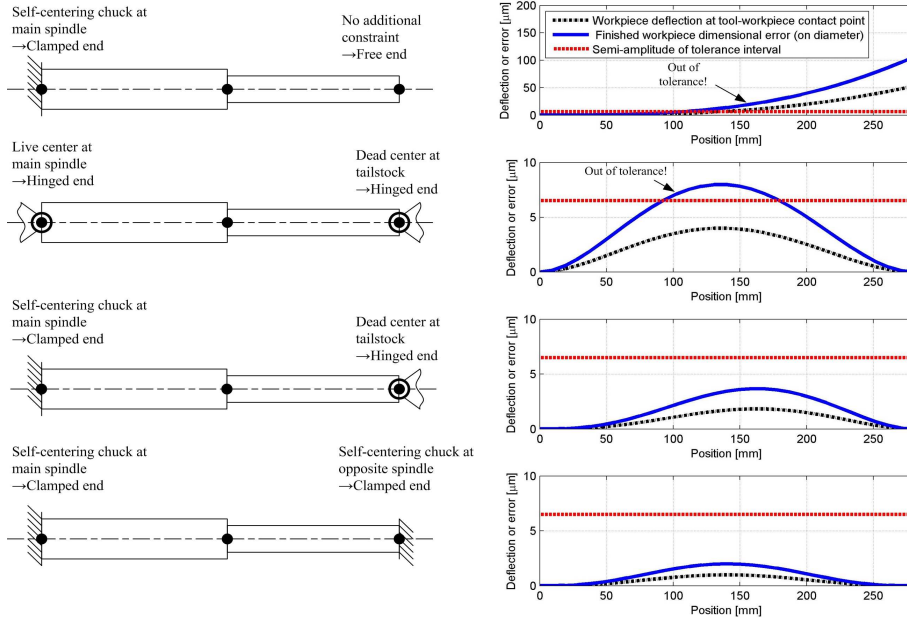


Figure 5. Effect of different clamping conditions in longitudinal turning on workpiece precision. Final diameter $D = 30$ mm with IT7 tolerance class required (admissible tolerance interval $\pm 6.5 \mu\text{m}$), total axial length $L = 280$ mm, depth of cut $a_p = 1$ mm, feed $f = 0.15$ mm/rev, cutting edge angle $\chi_1 = 60^\circ$, workpiece made of mild Ck45 carbon steel with cutting pressure in the normal direction k_{ns} of about 1100 MPa.

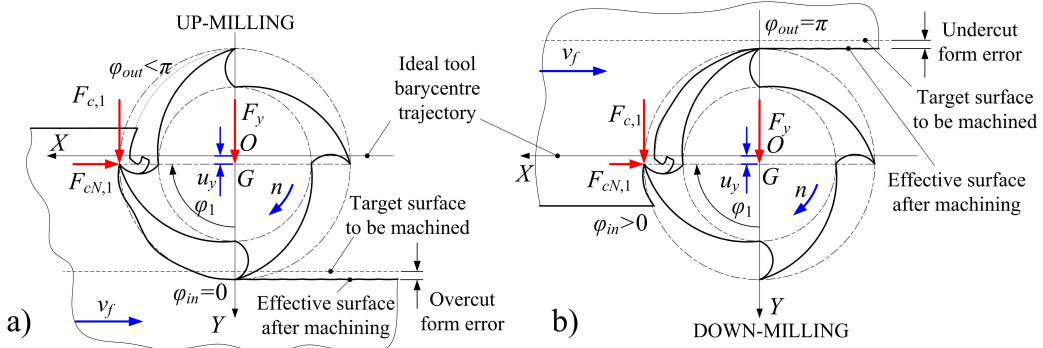


Figure 6. a) Overtcut form error in peripheral up-milling and b) undercut form error in peripheral down-milling.

Also in this case it is possible to apply FE strategies for estimating the static errors due to tool deflection, although the complexity of the required FE structural models and cutting force models is considerably higher with respect to the turning example considered before.

However, in the perspective of illustrating the general philosophy, a simplified procedure will be outlined. The tooling system is generally composed of a spindle adapter, a

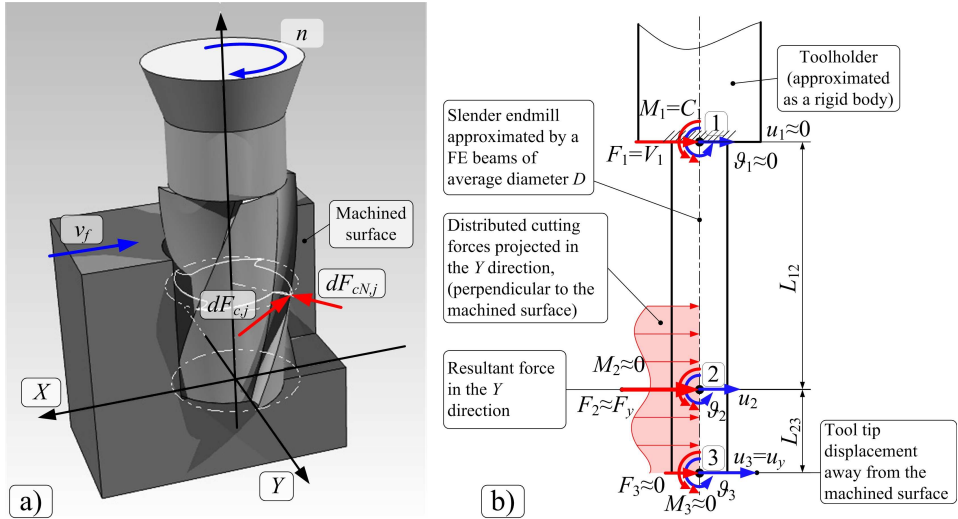


Figure 7. Static deflections in milling. a) Kinematics of a generic peripheral milling performed with a slender endmill. b) Simplified procedure for estimating the quasi-static tool tip deflection by using Euler-Bernoulli FE beams combined with basic cutting force modelling.

toolholder and other intermediate elements, a cutter body and several active teeth or flutes. The cutter body and a part of the tooling system form a slender subsystem of considerable overhang L and small cross section of average diameter D . Accordingly, such subsystem can be represented by a series of Euler-Bernoulli beams clamped at the rest of the tooling system, which can be approximated by a rigid body, as shown in Figure 7. Spindle compliance can be neglected too, since it is usually at least one order of magnitude smaller than the tooling system compliance (which is typically in the range $1 \div 0.1 \mu\text{m/N}$).

Cutting forces act along the engaged cutting edges in a non-trivial manner, especially when endmills with helical flutes are considered. Nevertheless, in order to roughly evaluate the tool tip displacement, the following procedure could be followed:

- the feed motion φ_1 representing the angular position of the first tooth should be set to zero (up-milling) or to π (down-milling);
- in this configuration, the distributed load along the beam has to be estimated by using adequate cutting force models;
- the resultant force in the Y direction (away from the machined surface) has to be estimated with acceptable accuracy; the distributed load is then substituted by such a lumped force applied at an appropriate intermediate node (node 2 in the Figure);
- the tool tip static deflection can be eventually estimated by using the following formula

$$u_y \cong \left(\frac{L_{12}^3}{3E \cdot J} + \frac{L_{12}^2 \cdot L_{23}}{2E \cdot J} \right) \cdot F_y \quad (15)$$

which can be easily derived from the Euler-Bernoulli beam stiffness matrix.

It is worth noting that node 2 can be confused with tool tip (node 3) in face milling, while it should be located at about $a_p/2$ from tool tip in peripheral milling.

For the sake of illustration, let us estimate the tool tip displacement of a down-milling operation on an aluminium alloy executed with a face shoulder cutter with $z_t = 4$ teeth, which is clamped at an extension made of a conventional steel with Young Modulus E of about 210 GPa. The total overhang of the slender part of the tooling system is $L = 150$, while the reference diameter is $D = 25$ mm. Cutting parameters are feed per tooth $f_z = 0.1$ mm, depth of cut $a_p = 1$ mm, radial immersion $a_L/D = 50\%$. The specific cutting pressure of the aluminium alloy is $k_{cs} \approx 1000$ MPa.

If we imagine a configuration similar to that described in Figure 6 (b), the following results are found: resultant cutting force in the feed perpendicular direction $F_y \approx k_{cs} \cdot f_z \cdot a_p \approx 100$ N, tool tip static compliance $h \approx 0.68 \mu\text{m}/\text{N}$, tool tip deflection of about 68 μm , which may be unacceptable if the considered operation is a finish pass and tolerances are strict.

In the light of the above arguments, it should be clear that quasi-static deformations of the machining system during the cutting process may considerably affect part precision, thus they cannot be generally neglected. Modelling approaches based on FE techniques combined with some direct experimental measurements may significantly help for the recognition and solution of such problems.

4. Machining System Dynamics

As shown in previous sections, cutting force fluctuations during machining may cause considerable vibrations between the tool and workpiece at the instantaneous point of contact, thus strongly affecting surface quality and machining system integrity. Therefore, it is fundamental to find effective models for describing the dynamic behaviour of the machining system.

For this purpose, it is essential to identify the weakest elements composing the kinematic chain, and to find their modes of vibration which may significantly interact with the chip formation mechanism.

4.1. Turning Dynamics

For instance let us consider the basic longitudinal turning operation of Figure 1 and 8. Both tool tip and workpiece may vibrate along tangential direction (parallel to cutting speed v_c), the axial direction (parallel to feed speed v_f in this case) or along the radial direction (perpendicular to the former directions, parallel to back force component F_p).

However, vibrations occurring along the tangential direction can be excluded from this treatment since they do not significantly affect cutting mechanics.

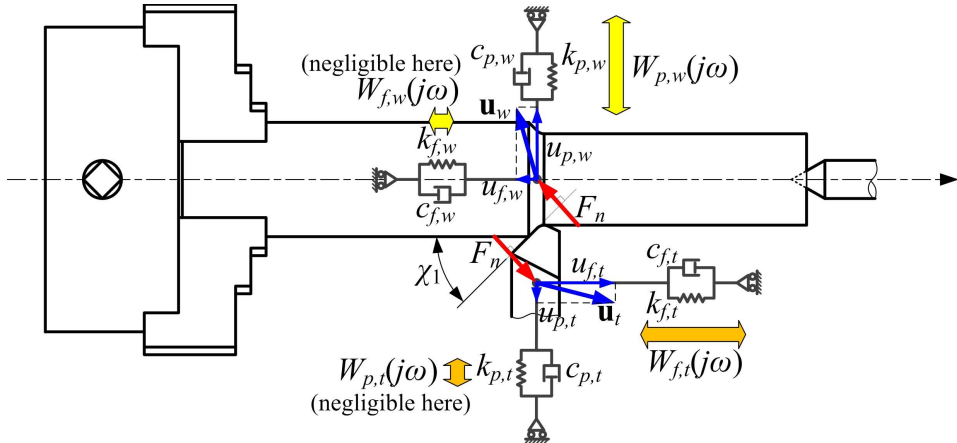


Figure 8. Dynamics modeling of a simple longitudinal turning operation

On the contrary, cutting dynamics strongly depend on tool and workpiece vibrations occurring in the axial-radial plane, and precisely on those components which tend to increase or decrease the instantaneous chip thickness $h(t)$. Accordingly, let us define $W_h(j\omega)$ as the overall frequency response of the machining system measured along such a direction, which is normal to the main cutting edge. Both tool and workpiece dynamics are included into $W_h(j\omega)$.

In longitudinal external turning axial vibrations of the workpiece can be neglected ($W_{f,w}(j\omega) \approx 0$), as well as radial vibrations of the tool ($W_{p,t}(j\omega) \approx 0$). As a consequence, $W_h(j\omega)$ does only depend on workpiece radial vibrations ($W_{p,w}(j\omega)$), on tool axial vibrations ($W_{f,t}(j\omega)$) and on main cutting edge orientation χ_1 . Specifically, it can be shown that

$$W_h(j\omega) \cong W_{f,t}(j\omega) \cdot \sin^2(\chi_1) + W_{p,w}(j\omega) \cdot \cos^2(\chi_1) \quad (16)$$

In many cases of practical interest the resulting frequency response $W_h(j\omega)$ is dominated by a single resonance peak, thus the whole frequency response can be approximated by an equivalent mass-spring-damper system, i.e.,

$$W_h(j\omega) \approx \frac{G_h}{(j\omega/\omega_n)^2 + 2\xi(j\omega/\omega_n) + 1} \quad (17)$$

where G_h is the total, static relative compliance of the machining system along the uncut chip thickness direction, ω_n is the main resonance pulsation and ξ is an equivalent damping coefficient.

When considering an internal turning operation performed with a slender boring bar - see Figure 9 - similar observations can be done.

In this case the slender tool is the most flexible part of the machining system, and it mainly vibrates along the tangential and radial directions, while it is very stiff in the axial (feed) direction. As before, its frequency response in the tangential direction does not play

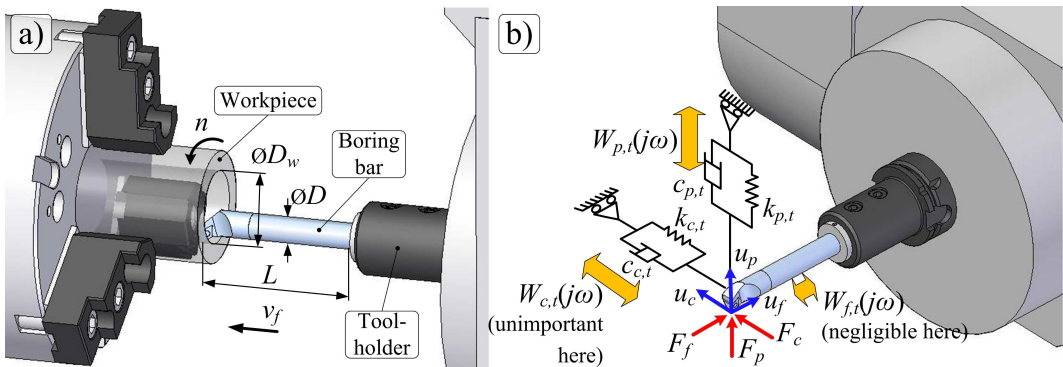


Figure 9. Dynamics modeling of a simple internal turning operation with a slender boring bar and a rigid workpiece

a significant role in the development of anomalous machining vibrations, thus it can be excluded from the analysis. On the other side, the workpiece is very stiff in comparison with the tool, thus its frequency responses can be neglected. In this case $W_h(j\omega)$ is given by

$$W_h(j\omega) \approx W_{p,t}(j\omega) \cdot \cos^2(\chi_1) \quad (18)$$

which is typically approximated by a single harmonic oscillator, Equation 17.

4.2. Milling Dynamics

Eventually, let us consider a face milling operation, as illustrated in Figure 10.

For the sake of simplicity, let us assume that the workpiece is extremely stiff in all directions, thus its dynamic behaviour can be neglected. In addition, let us neglect the axial vibrations of the tooling system, since its axial stiffness is usually very high.

On the contrary, transversal tool vibrations in the XY plane orthogonal to main spindle axis may be relatively large and they may greatly influence cutting mechanics. Accordingly, transversal tool vibrations should be adequately modelled.

For this purpose, the whole tooling system is generally approximated by a simple Jeffcott rotor which may vibrate in the transversal directions while keeping a constant rotation [1]. Accordingly, transversal tool vibrations are usually described by the dynamic model

$$\begin{cases} u_x(j\omega) \cong W_{xx,t}(j\omega) \cdot F_x(j\omega) \\ u_y(j\omega) \cong W_{yy,t}(j\omega) \cdot F_y(j\omega) \end{cases} \quad (19)$$

where $W_{xx,t}$ and $W_{yy,t}$ are the tool direct transfer functions, which are typically approximated by a single harmonic oscillator, see Equation 17.

It has to be pointed out that accurate and realistic dynamic models are required by chatter prediction algorithms in the perspective of chatter prevention. Unfortunately, large uncertainties do generally affect dynamic models of machining systems, due to unknown or unmodelled dynamics and oversimplified assumptions.

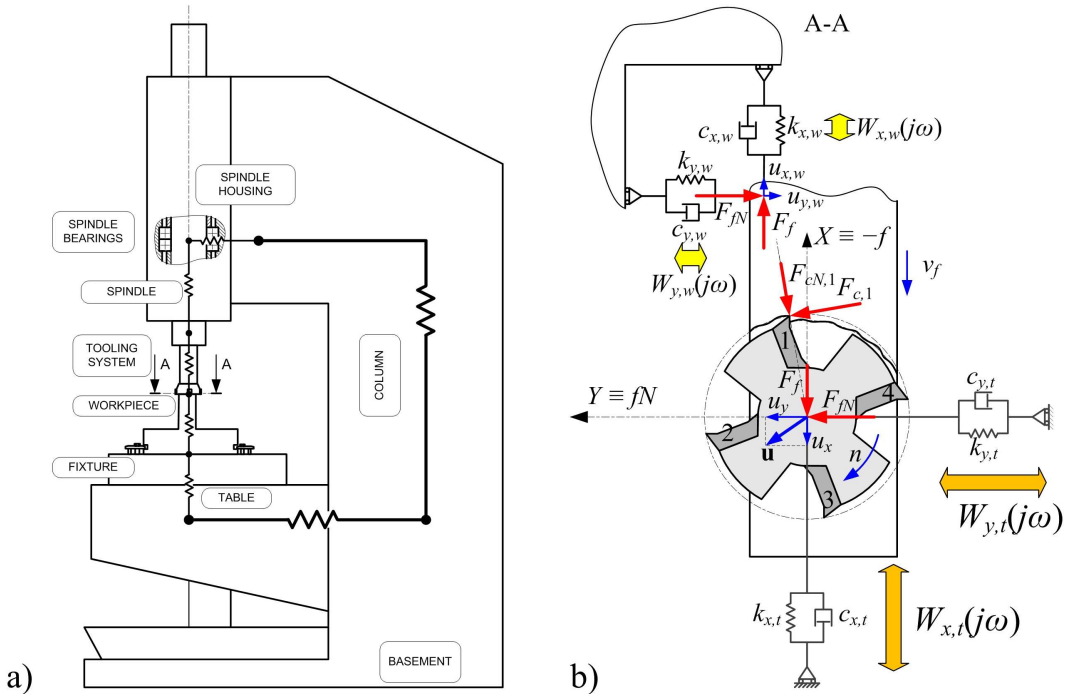


Figure 10. Dynamics modeling of a milling operation

It has to be highlighted that dynamic models derived from a pure analytic approach are usually inaccurate. However, model adequacy and accuracy can be greatly improved by performing direct experimental measurements of the dynamic behaviour of the machining system.

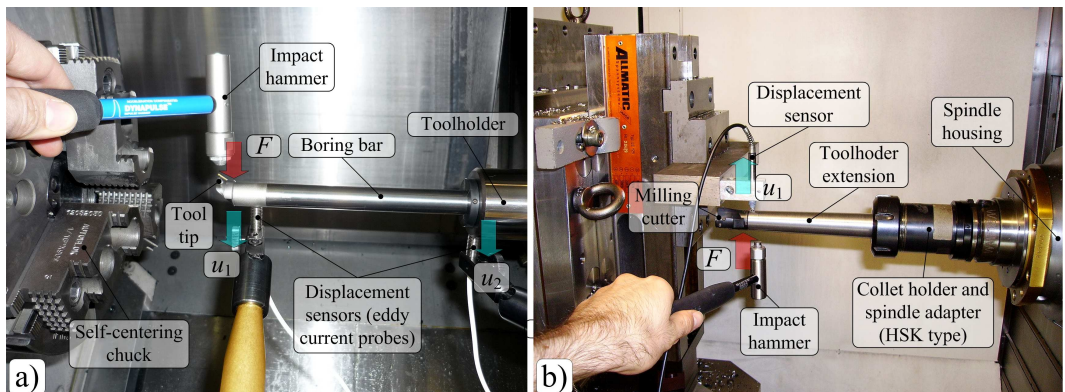


Figure 11. Experimental modal testing of machining systems for measuring their dynamic behaviour. (a) Pulse testing on a boring bar which is used for internal turning operations on a CNC lathe [2]; (b) pulse testing on a milling cutter mounted on a high speed CNC milling machine with horizontal spindle axis [4].

For this purpose, experimental modal analysis can be applied on machine tool structures. Pulse testing is a very fast and practical modal analysis technique which is based on the application of impulsive forces to the structure under examination by means of an instrumented hammer. At the same time, structural vibrations are measured by means of displacement or acceleration sensors. After signal processing in the frequency domain, the desired input-output dynamic relation can be derived. Pulse testing is commonly applied on machine tools, as illustrated in Figure 11.

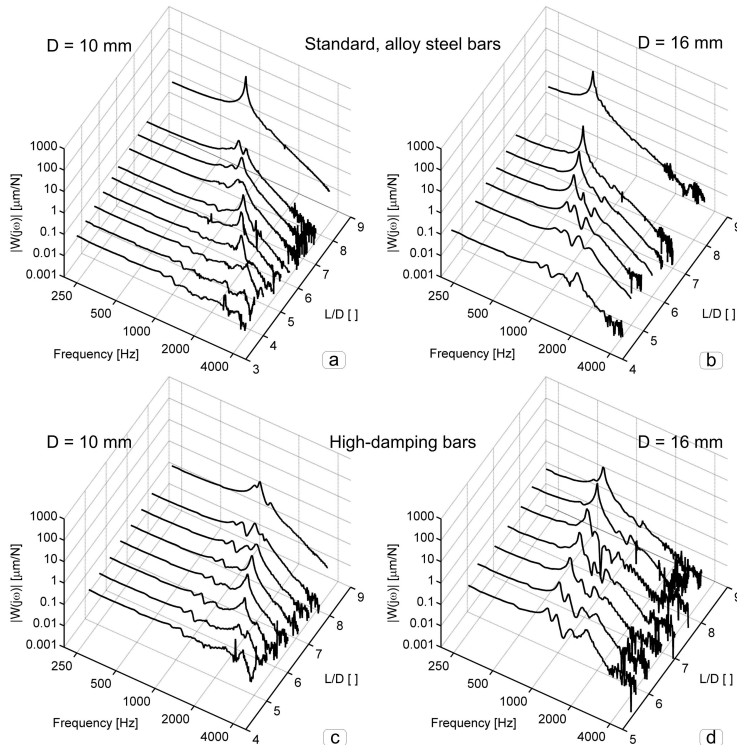


Figure 12. Examples of experimental transfer functions of boring bars measured in the radial (back force) direction [2].

In Figure 12, the dynamic response of several commercial boring bars of different diameters and materials are shown, for an increasing bar overhang to diameter ratio L/D . This data was derived from pulse test measurements performed in the experimental set-up illustrated in Figure 11(a). For a given boring bar type, its dynamic behaviour is similar to that of a single harmonic oscillator only for high L/D ratio. Even in this apparently simple case a pure analytical model based on the cantilever beam hypothesis may be affected by considerable errors, due to imperfect clamping at boring bar - toolholder interface. Dynamic behaviour becomes considerably more complicated and unpredictable for lower L/D values, or when considering high-damping boring bars, due to the dynamic interaction with toolholder dynamics.

Similar observations can be done in milling, see Figure 13. Slender tooling system configurations can be well described by a couple of single harmonic oscillators, one for

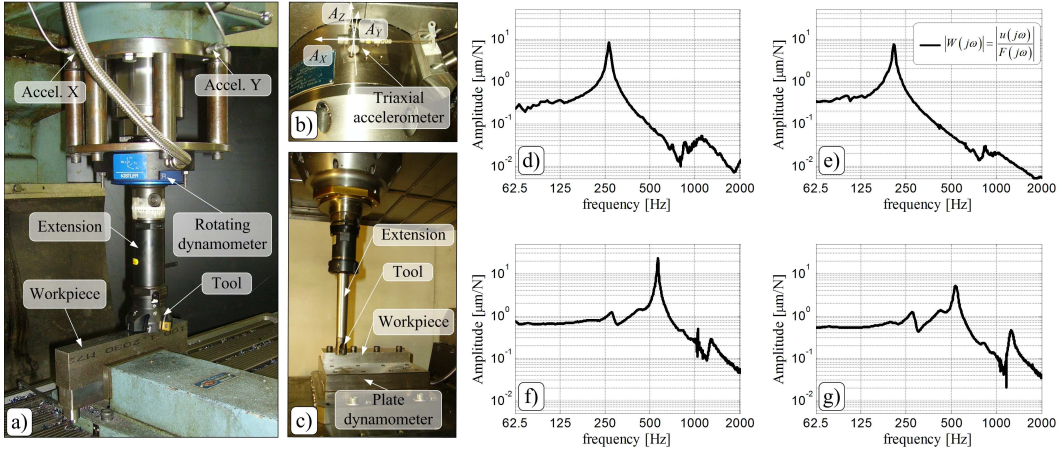


Figure 13. a) Experimental setup on a conventional milling machine where the tooling system was composed of a face shoulder cutter with $D = 80$ mm, an extension element and a rotating dynamometer for cutting force measurements; c) experimental setup on a high-speed CNC milling machine, where the tooling system was composed of a face shoulder cutter with $D = 25$ mm and a slender extension element; b) detail of triaxial accelerometer mounted on spindle housing used for detecting chatter vibrations. From d) to g), examples of transfer functions of the milling cutter measured in a transversal direction orthogonal to main spindle axis. Specifically, d) and e) were obtained with experimental setup a), with different cutters; f) and g) were obtained with experimental setup c), by adopting extension elements made of different materials (conventional alloy steel in case of f), high-damping tungsten-based alloy in case of g)) [3].

each transversal direction (see Figures 13d), e) and f)). However, when considering squat configurations or very stiff tooling systems, the resulting dynamics may exhibit multiple modes of vibrations along each transversal direction (Figure 13 g)).

It is worth noting that transfer functions of milling cutters (Equation (19)) are derived by performing pulse testing while the rotor is steady, i.e., non rotating. It is implicitly assumed that such relations are still valid and unaltered when the spindle is rotating, independently from the adopted spindle speed. This assumption is effectively true in the vast majority of cases of practical interest.

Nevertheless, it has to be remarked that spindle-tooling system dynamics can be further complicated by the dependence of tooling system dynamics on spindle speed, due to thermal effects (e.g., thermal distortions which may influence spindle bearing preload and stiffness) or centrifugal-gyroscopic effects (which may arise at high spindle speeds or for peculiar tooling system geometries).

Another technique for modal analysis is that based on the use of electromagnetic or piezoelectric shakers, which excite the structure by applying sinusoidal forces, one frequency at a time. By so doing, a wider range of frequencies can be investigated in comparison with pulse testing. On the other side, special electrical equipment and mechanical fixtures are needed, which may hinder its application in industrial environments.

5. Vibrations in Machining

As outlined in previous sections, machining vibrations during the cutting process are always present, for several reasons.

Machining vibrations may be roughly classified into three categories:

- *free vibrations*: they are due to transient cutting phenomena (e.g., when the tool is entering or leaving the workpiece in turning), or when cutting conditions are time-varying (e.g., when the lateral immersion of the milling cutter into the workpiece varies in pocket milling). These vibrations tend to extinguish exponentially because they are dissipated by mechanical damping.
- *Forced vibrations*: they represent the steady state periodic response of the machining system to periodic forces after free-vibrations have faded away.
- *Self-excited vibrations - chatter*: they are anomalous, violent vibrations which tend to exponentially increase with time.

It is worth noting that free vibrations are generally unimportant while forced vibrations are always present and cannot be completely avoided, especially when considering machining operations characterized by interrupted cutting conditions such as milling.

Nevertheless, it is very important to carefully select adequate values of spindle speed n that do not excite the mechanical resonances of the machining system. In other words, spindle speed has to be chosen such that the tooth pass excitation frequency f_τ and its integer multiples do not overlap any machining system eigenfrequency.

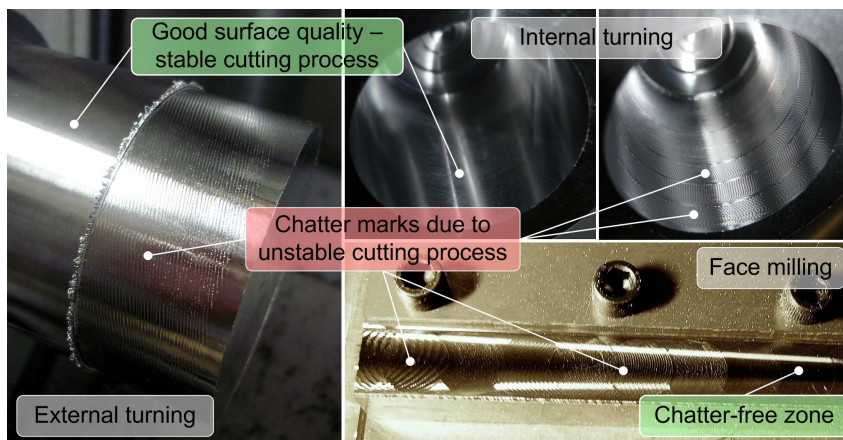


Figure 14. Effects of chatter vibrations on the machined surface.

On the contrary, chatter vibrations may arise during machining only for specific combinations of cutting parameters. Chatter vibrations are detrimental for the cutting process, since they may cause abnormal tool wear or tool breakage, damage of both tooling structure and spindle bearings, poor dimensional accuracy of the workpiece and poor surface roughness, as illustrated in Figure 14. Accordingly, chatter vibrations have to be absolutely avoided.

Chatter can be classified as primary or secondary. Primary chatter typically occurs at relatively low spindle rotational speeds, whereas secondary chatter is dominant in the medium-high spindle speed range.

Primary chatter is mainly due to physical mechanisms such as friction between the tool and the chip/workpiece on contact surfaces, stress distribution on the normal rake face, thermoplastic behaviour of the chip material, mode-coupling and others, see [4] for references.

Secondary chatter is caused by the regenerative effect, which is an unstable behaviour of the uncut chip thickness due to a combination of the instantaneous tool-workpiece relative vibrations with the waviness produced by the previous tooth passage [5]. Most machining operations are affected by the regenerative effect, therefore its comprehension and modelling is crucial.

5.1. Chatter Modelling in Turning

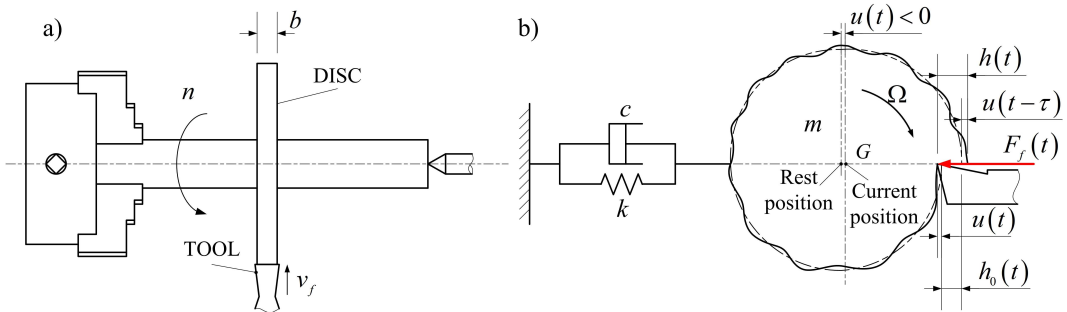


Figure 15. Concept of regenerative effect on a very simple, single degree of freedom system: a) transversal turning of a disc; b) effect of tool-workpiece relative vibrations on instantaneous chip thickness.

Regenerative effect can be understood by considering the single degree of freedom system of Figure 15. The effective instantaneous chip thickness h due to tool tip-workpiece relative vibrations is given by

$$h(t) = h_0(t) - (u(t) - u(t-\tau)) = \underbrace{h_0(t)}_{\text{static}} + \underbrace{h_\delta(t)}_{\text{dynamic perturbation}} \quad (20)$$

evidencing the dependence of uncut chip thickness on current and delayed tool vibration. Accordingly, the normal force acting parallel to feed direction can be expressed by

$$F_n(t) = k_{ns} \cdot b \cdot h(t) = k_{ns} \cdot b \cdot [h_0(t) - (u(t) - u(t-\tau))] \quad (21)$$

This force is applied to the dynamic system represented by the frequency response $W_h(j\omega)$, thus the final dynamic relation between the nominal and effective uncut chip thickness is

$$\frac{h(j\omega)}{h_0(j\omega)} = \frac{1}{1 + k_{ns} \cdot b \cdot W_h(j\omega) \cdot (1 - e^{-j\omega\tau})} \quad (22)$$

This configuration is represented by the block diagram of Figure 16, where the inner modulation due to the delayed term and the outer modulation due to current vibration are visible.

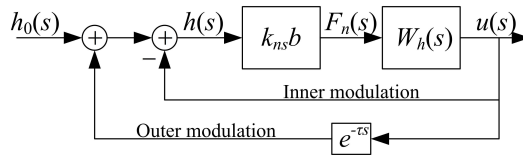


Figure 16. Block diagram of the dynamic single degree of freedom cutting process illustrated in Figure 15.

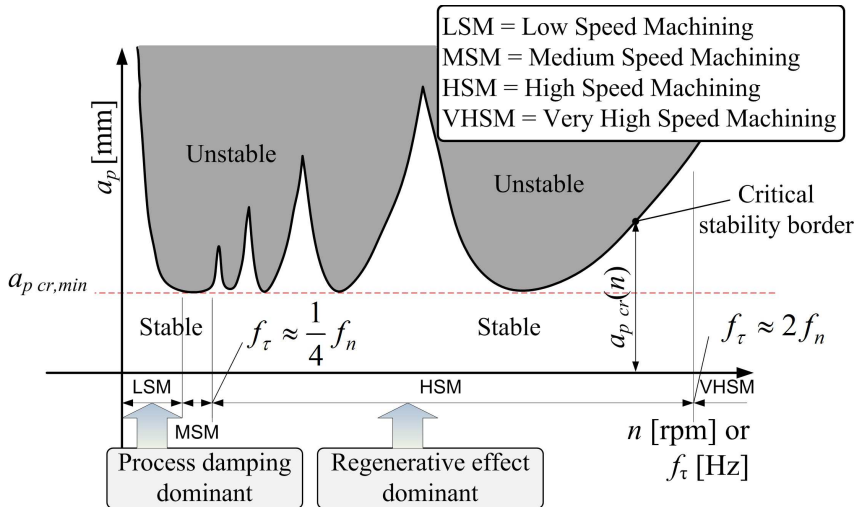


Figure 17. Example of stability lobes.

The stability of the system depends on the location of its poles. Unfortunately, the system has infinite poles because of the term $e^{-j\omega\tau}$, thus a direct evaluation of the root locus is not possible. Nevertheless, the stability analysis can be accomplished by assuming that the system is vibrating at a chatter pulsation $\omega_c \approx \omega_n$. The solution of this condition leads to the stability limit

$$b_{cr} = \left(\frac{a_p}{\sin \chi} \right)_{cr} = \frac{1}{2k_{ns} \cdot \operatorname{Re}[W_h(j\omega_c)]} \quad (23)$$

The classical result of Equation (23) is still valid for generic turning operations, when considering W_h as the frequency response of the machining system in the direction orthogonal to the main cutting edge, in accordance with Equation (17).

The same critical value can be obtained for different spindle speeds n . By changing the chatter pulsation ω_c and by repeating the calculation, the so called stability lobes can be

finally obtained. An example of typical stability charts in the (n, a_p) plane is presented in Figure 17.

The stability lobes can be split into four zones with respect to spindle speed, depending on the ratio between the fundamental excitation frequency f_τ (which is defined by Equations (1) and (8) for turning and milling, respectively) and the main natural frequency $f_n = \omega_n / (2\pi)$ of the machining system.

In the low spindle speed range the stability limit is relatively high due to the phenomenon of process damping, which is an additional damping effect caused by the action of the tool flank rubbing against the machined surface, as shown in Figure 18.

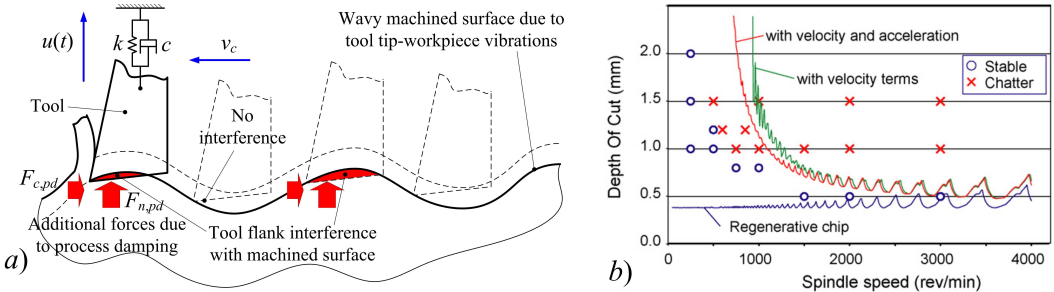


Figure 18. a) Mechanism of process damping. b) Experimental effects of process damping in turning [12].

In the medium spindle speed range the stability lobes are so densely packed that there is practically no chance of finding any stable configuration above the stability lobes minima $a_{p,cr,min}$, which can be estimated by the relation

$$a_{p,cr,min} \approx \frac{\sin \chi_1 \cdot 2\xi \cdot (1 + \xi)}{k_{ns} \cdot G_h} \quad (24)$$

Equation (24) was derived under the hypothesis that W_h is described by Equation (17). It is a simple but important result, since it does quantitatively characterize the following experimental evidence: process stability is increased when the equivalent damping ξ is increased, as well as when the static compliance G_h or the normal cutting pressure k_{ns} are decreased. On the contrary, machining system resonance f_n does only influence the lateral position of the stability lobes.

In the high spindle speed range there is a good chance of finding advantageous stable zones with $a_p > a_{p,cr,min}$ between adjacent lobes, which would allow to maximize the material removal rate.

In this perspective, a very important parameter for distinguishing the different spindle speed ranges is the lobe number defined by

$$N = \frac{f_n}{f_\tau} = f_n \cdot \frac{60}{n} \quad (25)$$

As a rule of thumb, lobe number N is about between 2 and 8 in the high spindle speed range, while it is higher in the medium and low spindle speed ranges. The transition between

the medium and low spindle speed ranges depends on process damping occurrence, which cannot be easily predicted a priori.

Eventually, some care has to be taken when choosing the cutting parameters in the very high spindle speed range ($N < 2$), since some unexpected problems may arise due to spindle dynamics. However, it should be noticed that such range is of interest only in the field of high-speed machining of light alloys.

5.2. Chatter Modelling in Milling

The evaluation of cutting process stability is considerably complicated in milling by multi-dimensional milling dynamics and by non-stationary cutting conditions.

For the sake of simplicity, let us consider a conventional face milling operation performed with constant spindle speed by using a cutter with constant angular pitch. As in turning, the relative vibrations between tool and workpiece do strongly influence the instantaneous chip thickness perceived by each tooth, which is usually approximated by the expression

$$h_j(t) \cong \underbrace{h_{j0}(t)}_{\tau\text{-periodic}} + \underbrace{h_{j,ux}(t)}_{\tau\text{-periodic}} \cdot \underbrace{[u_x(t) - u_x(t-\tau)]}_{\text{regenerative perturbation}} + \underbrace{h_{j,uy}(t)}_{\tau\text{-periodic}} \cdot \underbrace{[u_y(t) - u_y(t-\tau)]}_{\text{regenerative perturbation}} \quad (26)$$

where h_{j0} is the nominal chip thickness described by Equation (12) while $h_{j,ux}$ and $h_{j,uy}$ are τ -periodic functions depending on milling kinematics, which modulate the effect of tool vibrations on the regenerative chip thickness.

Accordingly, the force acting on the tool can be expressed in the form

$$\begin{bmatrix} F_x(t) \\ F_y(t) \end{bmatrix} \cong \underbrace{\mathbf{F}_0(t)}_{\substack{\tau\text{-periodic} \\ \text{vector}}} + \underbrace{\mathbf{F}'_1(t)}_{\substack{\tau\text{-periodic} \\ 2\times 2 \text{ matrix}}} [\mathbf{u}(t) - \mathbf{u}(t-\tau)] \quad (27)$$

Eventually by expressing the transfer function (19) in the state space form, after some algebraic manipulations the following system of linear Delay Differential Equations (DDEs) with periodic time dependent coefficients is obtained

$$\begin{cases} \dot{\mathbf{q}}(t) = \mathbf{A}(t)\mathbf{q}(t) + \mathbf{B}(t)\mathbf{q}(t-\tau) + \mathbf{B}_0(t) \\ \mathbf{u}(t) = \mathbf{C}\mathbf{q}(t) \end{cases} \quad (28)$$

where $\mathbf{q}(t)$ is a $n \times 1$ column vector representing the current machining system dynamic state, $\mathbf{q}(t-\tau)$ is the delayed state vector representing the dynamic state at the passage of the former tooth through the same angular position (at $(t-\tau)$), $\mathbf{A}(t)$ and $\mathbf{B}(t)$ are $n \times n$ matrices of time dependent, τ -periodic coefficients, $\mathbf{B}_0(t)$ is the $n \times 1$ column vector representing the τ -periodic input excitation, \mathbf{C} is the $2 \times n$ matrix transforming the state space vector $\mathbf{q}(t)$ into the 2×1 cutter barycentre vibration $\mathbf{u}(t)$.

Unfortunately, the stability analysis of the system (28) cannot be performed analytically, i.e., the critical stability border cannot be determined by a closed analytical form similar to Equation (23) obtained in turning. Numerical approximate methods have to be applied for this purpose, which are briefly described in the next paragraph.

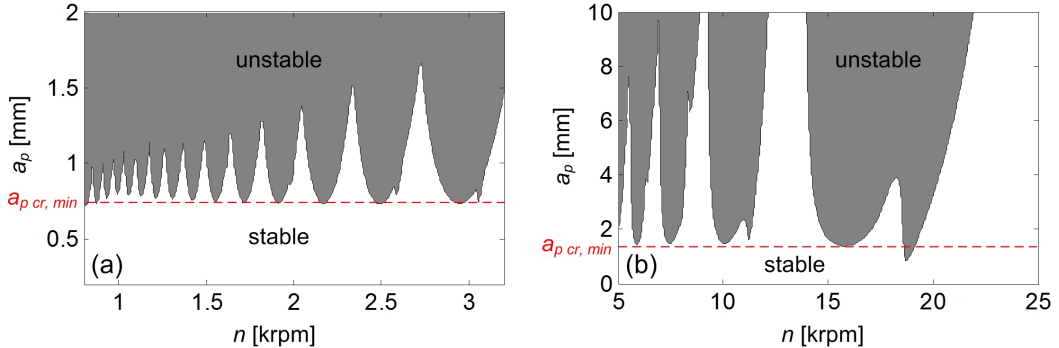


Figure 19. Examples of theoretical stability lobes in milling: a) half immersion up-milling on Ck45 steel with a face shoulder cutter ($D = 50$ mm, $z_t = 1$ tooth, $a_L/D = 50\%$, $k_{cs} \cong 1900$ MPa, $f_n \cong 270$ Hz, $\xi \cong 0.03$, $G \cong 0.28$ $\mu\text{m}/\text{N}$) [17]; b) low immersion down-milling on aluminium with an endmill cutter ($D = 10$ mm, $z_t = 2$ teeth, $a_L/D = 10\%$, $k_{cs} \cong 600$ MPa, $f_n = 922$ Hz, $\xi = 0.011$, $G = 0.75$ $\mu\text{m}/\text{N}$) [13].

Although the effective shape of the stability lobes in milling can be complex and very difficult to accurately predict a priori, some general guidelines can be drawn. As in milling, an approximate relation representing the stability lobes minima can be derived, as follows

$$a_{p cr, min} \approx 6.5 \frac{\xi}{G_h \cdot k_{cs} \cdot (a_L/D)} \text{ [mm]} \quad (29)$$

evidencing the influence of cutter geometry (teeth number z_t []), milling kinematics (lateral immersion a_L/D []), milling dynamics (equivalent damping ξ [] and static compliance G_h [m/N]) and cutter-workpiece interaction (cutting pressure k_{cs} [N/m^2]) on process stability.

As in turning, the different spindle speed ranges can be identified by computing the lobe number

$$N = \frac{f_n}{f_\tau} = f_n \cdot \frac{60}{n \cdot z_t} \quad (30)$$

and by using the same rules outlined in turning.

An example of stability lobes for different milling operations is given in Figure 19. Qualitatively the stability diagrams can be very different from those obtained in turning, especially when considering low immersion milling operations or other advanced configurations (e.g., when using variable pitch cutters). Therefore, there is a strong need of accurate and reliable algorithms for chatter prediction in milling.

5.3. Chatter Prediction in Milling

As outlined in previous paragraph, the stability analysis of the system (28) can be performed by applying approximated numerical methods only. Mainly, it can be carried out by means of time domain simulations, in the frequency domain or by applying DDE-based methods.

In the last few decades several time domain simulations of the milling process were proposed in the literature [7] [8] [9] [10]. For a given combination of cutting parameters, machining system vibrations $\mathbf{u}(t)$ are numerically simulated by discretizing the DDEs system (28) by means of Euler, Runge Kutta or Tustin's approximations. Afterwards, the stability of the system is assessed by evaluating the time behaviour of $\mathbf{u}(t)$.

Unfortunately, this approach requires huge computation times, thus its applicability in industrial conditions is limited. On the other hand, it allows a more realistic prediction of machining system dynamics, since it is capable to model complex tool geometries, the effective kinematics of milling and some important nonlinear effects which cannot be accounted for by the linear stability analysis. Therefore, the results of the time domain simulations are usually considered as a reference for the other methods.

Frequency domain methods are based on the Fourier series expansion of the periodic matrices $\mathbf{A}(t)$ and $\mathbf{B}(t)$. The most advanced and effective frequency domain algorithm is the Multi-Frequency Solution, which was developed by Merdol et al. in 2004 [11]. This method is capable of including several harmonics of $\mathbf{A}(t)$ and $\mathbf{B}(t)$ in the stability analysis. Accordingly, it showed good predictive capabilities, comparable to those of the DDE-based methods [12]. Its main drawback is the relatively slow convergence to the exact theoretical solution, and hence the considerable calculation times.

Other methods for chatter prediction are based on the Floquet theory of Delay Differential Equations [15] [16]. Basically, these approaches approximate the infinite-dimensional monodromy operator representing Equation (28) with a finite-dimensional matrix $\tilde{\mathbf{U}}$. The stability of the system depends on the modulus of the biggest matrix eigenvalue. Different DDE based methods calculate the monodromy matrix $\tilde{\mathbf{U}}$ in different ways.

In 2004, Inasperger et al. developed the Semi Discretization Method - SDM [13]. This method performs the stability analysis by discretizing time into equally-spaced time intervals. In each interval, the matrices $\mathbf{A}(t)$ and $\mathbf{B}(t)$ as well as the delayed term $\mathbf{q}(t-\tau)$ are approximated by piecewise constant terms and used for assembling the approximate monodromy matrix $\tilde{\mathbf{U}}$. The accuracy of the method is improved by increasing the number of intervals. Unfortunately, a huge number of intervals may be required for achieving a satisfactory accuracy in most cases of practical interest. As a consequence, the computation time may become too high for practical application in industry.

The Full Discretization Method (FDM) has been recently proposed [14], which is considerably faster for a given level of accuracy. As proposed by SDM, the fundamental period is split into equally spaced intervals. Nevertheless, instead of considering piecewise constant approximations of the dynamic state vectors and of the periodic system matrices, they are all approximated through interpolating Hermite polynomials.

Another very efficient alternative to SDM/FDM approaches is the Chebyshev Collocation Method [15] [16], which splits the fundamental period into uneven time intervals. Smaller time intervals are indeed taken at the beginning and at the end of the period and where discontinuities of the coefficients of $\mathbf{A}(t)$ and $\mathbf{B}(t)$ are present. In addition, such coefficients and the delayed term $\mathbf{q}(t-\tau)$ are not approximated by piecewise constant terms but by interpolating Lagrange polynomials. As in the SDM/FDM approaches, the accuracy of the method is improved by increasing the number of intervals. It is worth noting that - for a given level of accuracy - this approach is between ten and one thousand times faster than SDM in most cases [17] [22]. This method has not been directly compared to FDM

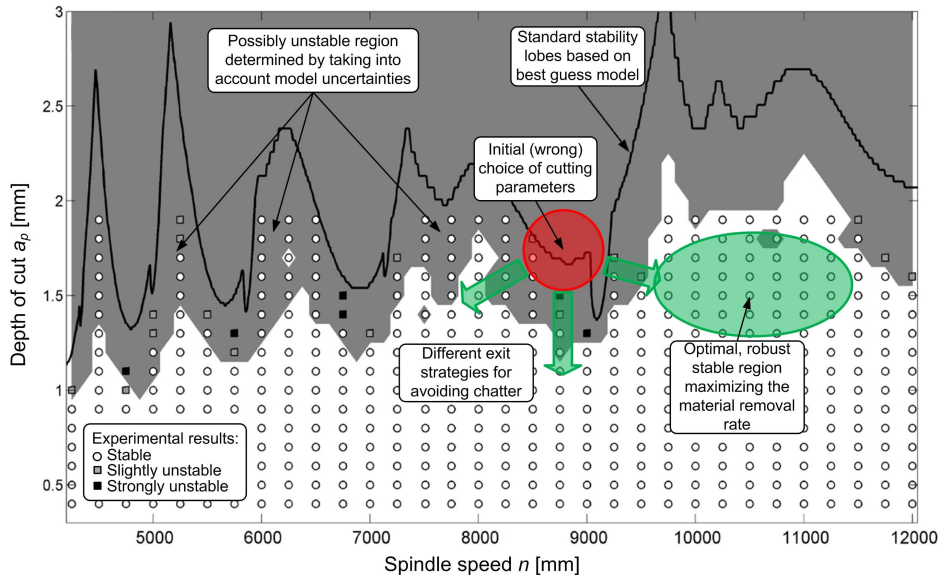


Figure 20. Comparison between standard stability lobes (black line), possibly unstable region identified by the Robust Chatter Prediction Method (grey region) and experimental results [4].

yet, nevertheless their performances are expected to be similar.

It has to be stressed out that the theoretical stability lobes predicted by the presented DDE-based algorithms are the same. They only differ in terms of the required calculation time and computer memory usage for achieving the desired level of accuracy.

However, when comparing theoretical predictions with experimental results, severe discrepancies can be found out, as illustrated in Figure 20. More reliable and robust predictions can be obtained by including the effect of model coefficients uncertainties into the stability analysis, as proposed in [4].

As a final remark, it is very difficult to apply chatter prediction methods in industry, since they require accurate estimates of the dynamic milling model coefficients, which should be preliminarily identified by direct experimental measurements (modal analysis and cutting force measurements). Therefore, in practice chatter prediction methods should be mainly considered as a powerful tool for understanding the physics of the cutting process and for developing and calibrating other (more effective) chatter suppression strategies.

6. Chatter Detection

Especially when stock material and cutting conditions are affected by large uncertainties (such as in the five-axes finishing milling of forged turbine blades), it is very important to rapidly detect chatter as soon as it appears, in order to apply adequate countermeasures for its suppression. For instance, spindle rotational speed may be automatically adjusted until a stable condition is met.

Some commercial systems for chatter detection have been already produced and installed on some modern CNC machine tools. Nevertheless, their use is still limited and their performances are not entirely satisfactory. Therefore, the development of more effective and reliable chatter detection systems is still an active field of current research.

The main characteristics required to an ideal chatter detection system are: accuracy, reliability, robustness, responsiveness, flexibility and practicality. In the perspective of industrial application, the chatter detection system should not reduce machining system stiffness, it has to be compatible to pallet changer and tool changer, it should not restrain the selection of cutting parameters. Its effectiveness should be independent from the knowledge of the actual cutting conditions and from a-priori knowledge of machining system dynamics. Eventually, it has to be insensitive to environmental noise.

For chatter identification, both the frequency bandwidth of the sensor and its location are crucial. Specifically, the frequency bandwidth of the sensor must be sufficient to detect the possible frequency range of chatter vibrations, typically from 100 Hz to 5000 Hz. The general rule for sensor location is the closer the sensor to the cutting process the more reliable its measurements will be.

Chatter detection systems are based on the integration of special sensors into the machine tool. The sensors which are mostly applied for this purpose are displacement probes, accelerometers, force sensors and microphones.

Displacement probes - for instance, eddy current sensors or lasers - are very effective but their positioning is often not compatible to the tool changer and the working space is reduced.

Accelerometers installed relatively close to the cutting process (such as on spindle housing) represent nowadays the best compromise between sensitivity and ease of application.

The applicability of force sensors for chatter detection is hampered by the need of installing them within the kinematic chain, and by their limited frequency bandwidth, which is approximately 1 kHz.

Microphones are very suitable for chatter detection, being their sensitivity to chatter onset comparable to that of other more expensive sensors. Nevertheless, microphones are affected by some limitations such as directional considerations, low-frequency response and environmental sensitivity. Particularly, the suppression of environmental noise is mandatory for a successful application of microphones.

For chatter detection different signal processing techniques were successfully applied, which can be roughly classified as time domain techniques (e.g., Once Per Revolution Sampling - OPRS), frequency domain techniques (e.g., based on the Fast Fourier Transform and the Power Spectral Density) and time-frequency domain techniques (based on Wavelets).

Basic statistics derived from the signal in time domain can be used for chatter detection.

For instance, acceleration signal variance can be used to detect chatter in the simple case of internal turning, as can be easily deduced from the analysis of Figure 21 (a).

When measuring tool tip vibrations in milling by means of non contact displacement sensors, the Once Per Revolution Sampling (OPRS) method can be applied, as illustrated in Figure 22. It is based on the analysis of signal values sampled once per spindle revolution, and the dispersion of data is used as chatter indicator.

Alternatively, in the frequency domain the machining condition may be classified as unstable when some spectral peaks exceed a predefined threshold, as illustrated in Figure

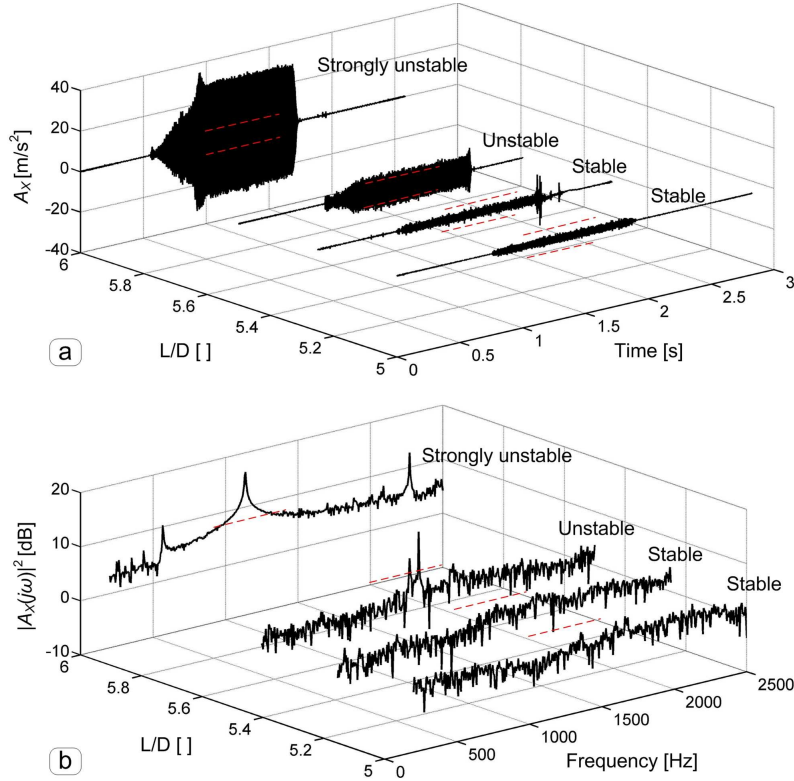


Figure 21. Machining system vibrations during internal turning operations performed with different tooling system configurations. Specifically, behaviour in time domain (a) and frequency domain (b) of machine tool head radial acceleration $A_x(t)$. Above a critical aspect ratio ($(L/D)_{cr} \cong 5.5$) the cutting process becomes unstable [19].

21 (b).

In milling chatter detection is typically based on the identification of anomalous chatter peaks emerging between the tooth pass excitation peaks in the signal spectra, as shown in Figure 23.

First generation chatter detection systems were typically based on a single sensor. In general, this configuration is not sufficiently robust to deal with process disturbances and unexpected accidents such as sensor malfunctions. Therefore, some innovative multisensor systems were recently conceived, which may overcome this drawback. For instance, a very accurate and reliable multisensor system for chatter detection in milling was developed by the authors, which was based on the application of piezoelectric accelerometers installed on spindle housing and on an additional force sensor. The system was validated experimentally, showing an outstanding accuracy of more than 90% even under the hypothesis that one sensor (among three) was malfunctioning [3].

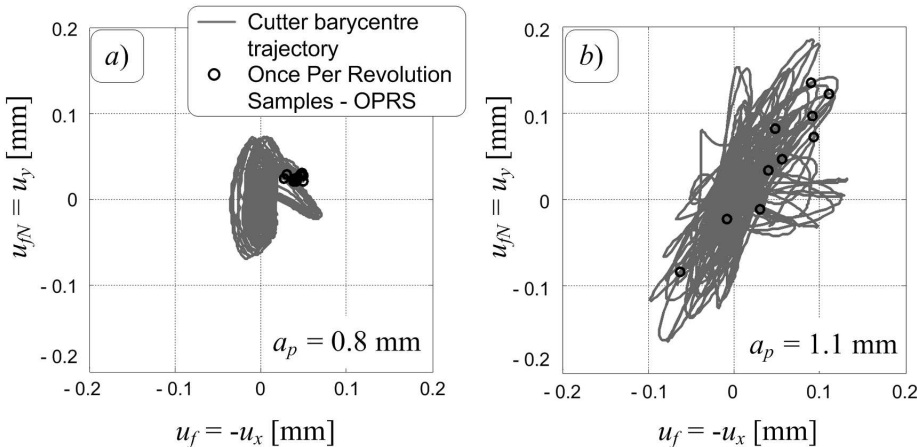


Figure 22. Cutter barycentre vibrations in the OXY plane during stable (a) and unstable (b) face milling operation [18].

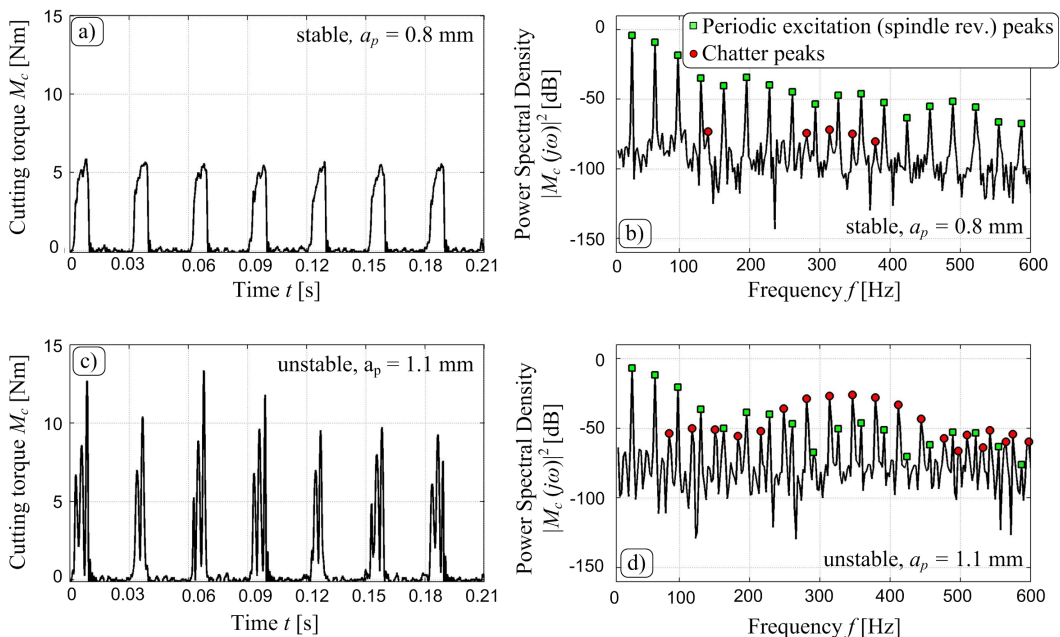


Figure 23. Behaviour of main cutting torque in a face milling operation, both in stable ((a) and (b)) and unstable ((c) and (d)) conditions [3].

7. Chatter Prevention and Suppression

Chatter prevention and suppression strategies may be roughly classified as follows:

- those based on the *a priori* selection of optimal cutting parameters which are determined by predictive algorithms.

- *Passive approaches* based on the application of passive devices, which are able to increase the stiffness and/or the equivalent damping of the machining system, or tools with special geometry.
- *Semi-active approaches*, based on the continuous in-process modulation of some geometric/kinematic/modal parameter influencing machining system dynamics, in open loop configuration.
- *Active approaches* based on real-time, closed loop feedback control systems.
- *Hybrid approaches* strategies based on chatter detection systems, empirical rules or a combination of the afore mentioned methods.

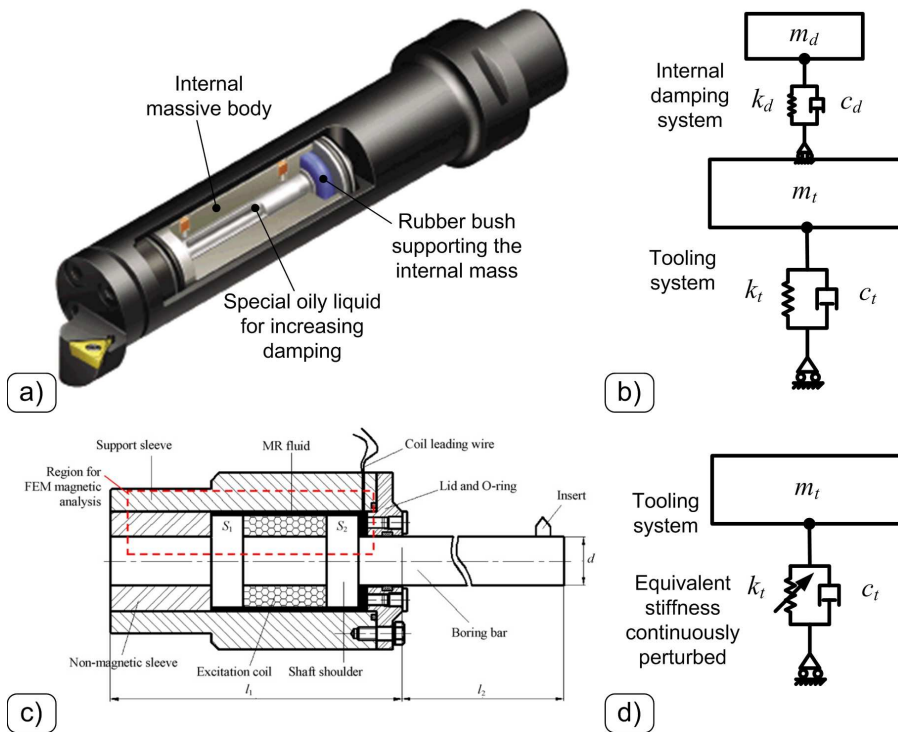


Figure 24. Application of additional damping element inside the boring bar: commercial system ((a), courtesy of Sandvik Coromant) and equivalent dynamic system (b); magnetorheological fluid-controlled boring bar for chatter suppression [24]: scheme (c) and equivalent dynamic system (d))

Predictive strategies are based on the application of chatter prediction algorithms. As already pointed out at the end of section 5., they need to be calibrated through preliminary direct measurements at the machine tool, which are rarely possible in production. However, they represent a valuable tool for developing other (more practical) methods.

Passive approaches try to avoid chatter by increasing the stiffness and by passively absorbing the vibratory energy. This can be achieved by considering tooling systems made

of special materials such as the high-density tungsten alloy studied in [2], or by considering special dampers such as the hydrostatic spindle bearings illustrated in [20]. Another example of passive device is the "silent" boring bar of Sandvik whose vibration energy is dissipated by an additional mass suspended in the core acting as a Frahm damper, see Figure 24 (a) and (b).

Tools with special geometry, such as milling cutters with variable angular pitch between subsequent teeth can be also classified as passive devices. They can be used to stabilize a given combination of cutting parameters in the perspective of maximizing the material removal rate [21].

Semi-active approaches aim at disturbing chatter onset by continuously modulating the tool geometry, machining system modal parameters or the instantaneous cutting parameters. For instance Yang et al. in [23] did continuously alter the normal tool rake during external turning, while Mei et al. [24] perturbed the stiffness of the boring bar holder by means of a magnetorheological fluid, as illustrated in Figure 24 (c) and (d).

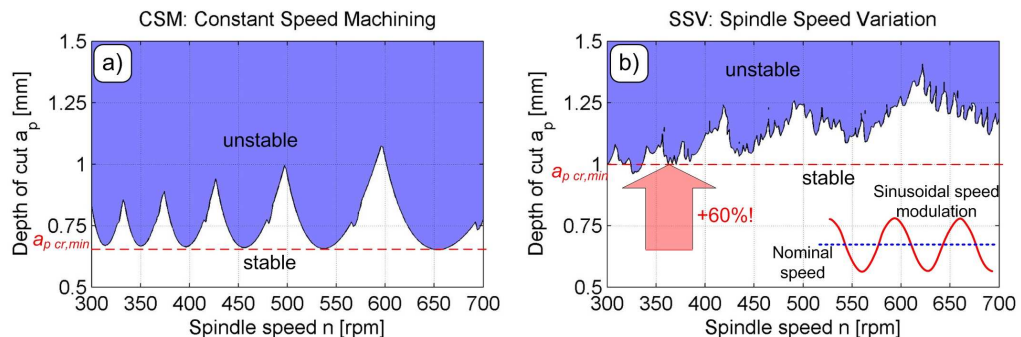


Figure 25. Application of Spindle Speed Variation (SSV) technique for chatter suppression in milling [22])

Another promising semi-active technique is the Spindle Speed Variation, consisting in a low-amplitude and low-frequency perturbation of spindle speed around the nominal value for disturbing the chatter generation mechanisms [22]. This method has a limited field of application, because it requires controllable spindle drives provided with sufficient bandwidth and power. However, it can be quite effective for increasing the material removal rate especially when the stable zones between adjacent lobes are too narrow to be safely exploited, as shown in Figure 25.

Active approaches are based on the application of vibration sensors (such as piezoelectric accelerometers or non contact displacement probes) to estimate the dynamic state of the system and actuators (typically, piezoelectric or electromagnetic) for real-time control of machining vibrations. Research prototypes have been developed both for turning and milling conditions, see Figure 26 and 27 respectively.

At present time, the applicability of such active control techniques is limited by high cost of commercial actuators and by their limited bandwidth. However, there is an increasing interest in active approaches.

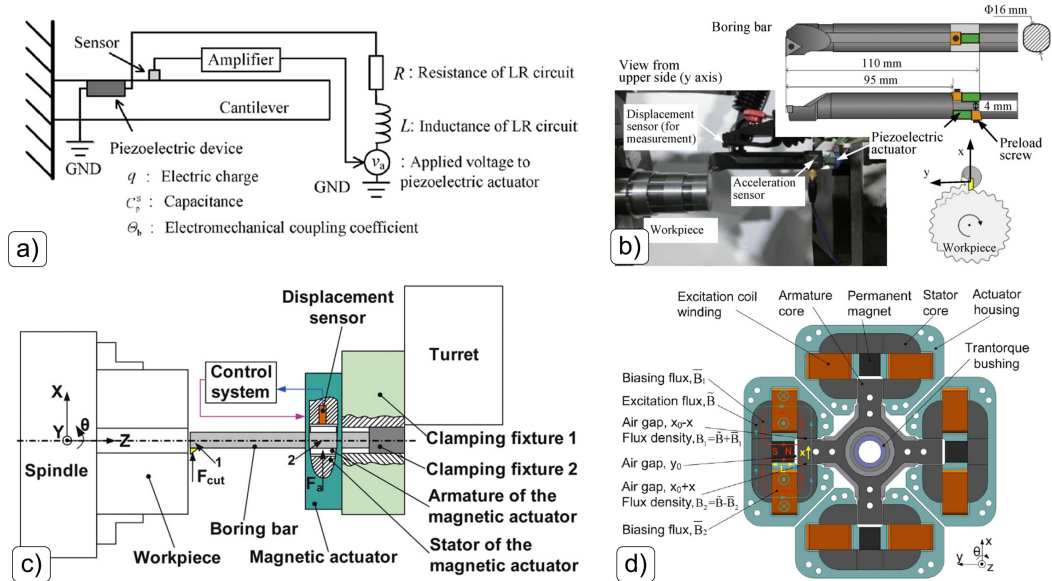


Figure 26. Active control of chatter in internal turning applications by means of piezoelectric actuators ((a) and (b), [26]) and electromagnetic actuators ((c) and (d), [27])

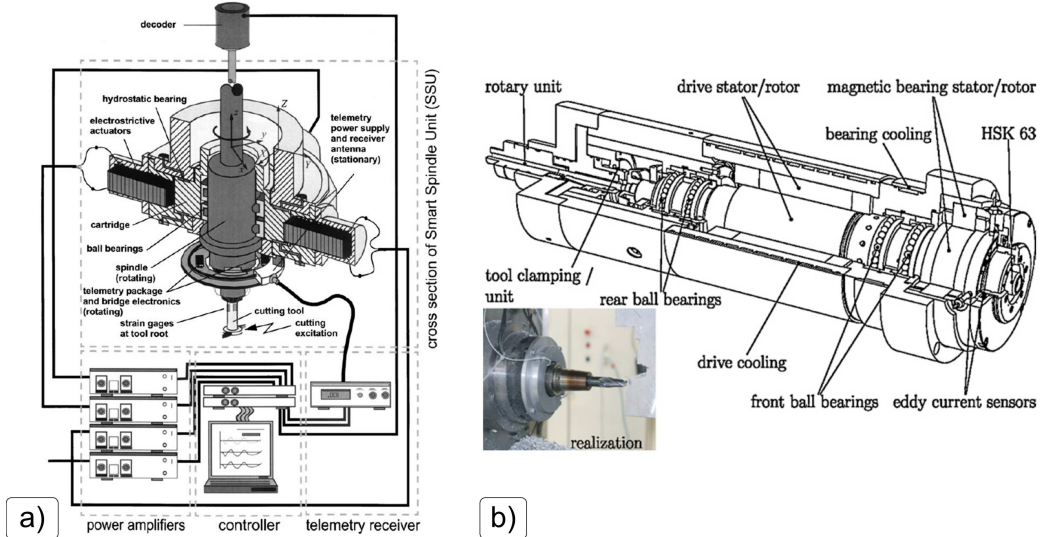


Figure 27. Active control of chatter in milling by means of piezoelectric actuators (a) [25] and electromagnetic actuators (b) [28]

Hybrid techniques are usually based on the application of chatter detection systems. As soon as the chatter is detected, the cutting parameters (typically spindle speed and/or feed) are automatically varied until a stable condition is reached [29] [30]. When the spindle rotational speed is changed from one level to another the method is known as Spindle Speed Regulation, which has not to be confused with the Spindle Speed Variation strategy.

Conclusion

During the cutting process, static deflections and relative vibrations between tool and work-piece cannot be completely avoided, because of the static and dynamic flexibility of the real machining systems.

Machining system vibrations play a crucial role in the field of precision manufacturing, since they may greatly affect the part quality and the integrity of machine tool elements.

Self-excited chatter vibrations are undesired, anomalous vibrations which may arise for specific combinations of cutting parameters. They are particularly detrimental, therefore they have to be absolutely avoided.

In the last decades several approaches for prevention and suppression of machining vibrations and chatter have been conceived, and many solutions are currently available on the market for the industrial users.

Nevertheless, vibration problems in machining cannot be considered solved, because of the new challenges deriving from advanced engineering materials, complex part geometries, increasing quality standards and production demands.

However, future solutions will probably rely on a deep interaction between physical modelling and innovative mechatronic devices.

References

- [1] G. Genta, Dynamics of Rotating Systems, (2005), Springer.
- [2] M. Sortino, G. Totis, F. Prosperi, Modeling the dynamic properties of conventional and high-damping boring bars, *Mechanical Systems and Signal Processing*, 34 (2013) 340-352.
- [3] E. Kuljanic, G. Totis, M. Sortino, Development of an intelligent multisensor chatter detection system in milling, *Mechanical Systems and Signal Processing*, 23 (2009) 1704-1718.
- [4] G. Totis, RCPM - A new method for robust chatter prediction in milling, *International Journal of Machine Tools and Manufacture*, 49 (2009) 273-284.
- [5] Y. Altintas, M. Weck, Chatter stability of metal cutting and grinding, *Annals of the CIRP*, 53/2 (2004) 619-642
- [6] Y. Altintas, M. Eynian, H. Onozuka, Identification of dynamic cutting force coefficients and chatter stability with process damping, *CIRP Annals - Manufacturing Technology*, 57 (2008) 371-374.
- [7] M.X. Zhao, B. Balachandran, Dynamics and stability of milling process, *International Journal of Solid and Structures*, 38 (2001) 2233-2248.
- [8] M.L. Campomanes, Y. Altintas, An improved time domain simulation for dynamic milling at small radial immersions, *Transactions of the ASME, Manufacturing and Engineering and Science*, 125 (2003) 29-38.

- [9] K. Ahmadi, F. Ismail, Machining chatter in flank milling, International Journal of Machine Tools and Manufacture, 50 (2010) 75-85.
- [10] J. Hoon Ko, Time domain prediction of milling stability according to cross edge radiiuses and flank edge profiles, International Journal of Machine Tools and Manufacture, 89 (2015) 74-85.
- [11] S.D. Merdol, Y. Altintas, Multi frequency solution of chatter stability for low immersion milling, Journal of Manufacturing Science and Engineering, Transactions of the ASME, 126 (2004) 459-466.
- [12] Y. Altintas, G. Stepan, D. Merdol, Z. Dombovari, Chatter stability of milling in frequency and discrete time domain, CIRP Journal of Manufacturing Science and Technology, 1 (2008) 35-44.
- [13] T. Insperger, G. Stepan, Updated semi-discretization method for periodic delay-differential equations with discrete delay, International Journal for Numerical Methods in Engineering, 61 (2004) 117-141.
- [14] Y. Liu, D. Zhang, B. Wu, An efficient full-discretization method for prediction of milling stability, International Journal of Machine Tools and Manufacture, 63(2012)44-48.
- [15] E. Bueler, E. Butcher, Stability of periodic linear delay-differential equations and the Chebyshev approximation of fundamental solutions, Technical Report 2002-2003, UAF Department of Mathematical Sciences.
- [16] E. Bueler, Chebyshev Collocation for Linear, Periodic, Ordinary and Delay Differential Equations: a Posteriori Estimates, Cornell University Library, (2004) <http://arxiv.org/math.NA/0409464S>.
- [17] E. Kuljanic, M. Sortino, G. Totis, Quick chatter prediction method - QCPM, an innovative algorithm for chatter prediction in milling, Proceedings of the Eighth AITeM Conference, Montecatini Terme, Italy, (2007).
- [18] E. Kuljanic, M. Sortino, G. Totis, Multisensor Approaches for Chatter Detection in Milling, Journal of Sound and Vibration, 312 (2008) 672-693.
- [19] M. Sortino, G. Totis, F. Prosperi, Development of a practical model for selection of stable tooling system configurations in internal turning, International Journal of Machine Tools & Manufacture, 61(2012) 58-70.
- [20] M. Weck, C. Brecher, Werkzeugmaschinen 5: Messtechnische Untersuchung und Beurteilung, dynamische Stabilität, (2006), Springer-Verlag.
- [21] E. Budak, An Analytical Design Method for Milling Cutters with Nonconstant Pitch to Increase Stability, part 2: Application, Journal of Manufacturing Science and Engineering, Trans. ASME, 125 (2003) 35-38.

-
- [22] G. Totis, P. Albertelli, M. Sortino, M. Monno, Efficient evaluation of process stability in milling with Spindle Speed Variation by using the Chebyshev Collocation Method, *Journal of Sound and Vibration*, 333 (2014) 646-668.
 - [23] F. Yang, B. Zhang, J. Yu, Chatter suppression with multiple time-varying parameters in turning, *Journal of Materials Processing Technology*, 141 (2003) 431-438
 - [24] D. Mei, T. Konga, A.J. Shihb, Z. Chen, Magnetorheological fluid-controlled boring bar for chatter suppression, *J. Mater. Process. Technol.*, 209 (2009) 1861-1870.
 - [25] J.L. Dohner, J.P. Lauffer, T.D. Hinnerichs, N. Shankar, M. Regelbrugge, C.M. Kwan, R. Xu, B. Winterb, Mitigation of Chatter Instabilities by Active Structural Control, *Journal of Sound and Vibration*, 269 (2004) 197-211
 - [26] X. Lu, F. Chen, Y. Altintas, Magnetic actuator for active damping of boring bars, *CIRP Annals - Manufacturing Technology*, 63 (2014) 369-372.
 - [27] A. Matsubara, M. Maeda, I. Yamaji, Vibration suppression of boring bar by piezoelectric actuators and LR circuit, *CIRP Annals - Manufacturing Technology*, 63 (2014) 373-376.
 - [28] S. Kern, A. Schiffler, R. Nordmann, E. Abele, Modelling and Active Damping of a Motor Spindle with Speed-Dependent Dynamics, *International Conference on Vibration in Rotating Machinery*, 1 (2008) 465-475.
 - [29] S.Y. Liao, Y.C. Young, A new On-line Spindle Speed Regulation Strategy for Chatter Control, *International Journal of Machine Tools and Manufacture*, 36/5 (1996) 651-660.
 - [30] F. Ismail , R. Ziae, Chatter Suppression in Five-axis Machining of Flexible Parts, *International Journal of Machine Tools and Manufacture*, 42 (2002) 115-122.

INDEX

#

3D printing, viii, 95, 114

A

active, viii, 164, 167, 168, 170, 182, 183, 184, 186, 188, 194, 195, 202, 204, 216, 231, 234, 235, 236, 239
control, v, vii, viii, 1, 2, 3, 4, 5, 6, 7, 8, 9, 10, 11, 13, 14, 15, 16, 17, 18, 19, 20, 21, 22, 23, 24, 26, 28, 29, 30, 31, 32, 33, 34, 38, 42, 44, 45, 47, 48, 49, 50, 51, 52, 53, 58, 65, 67, 80, 81, 82, 86, 87, 88, 95, 115, 120, 140, 142, 143, 144, 145, 148, 158, 159, 160, 164, 167, 168, 169, 170, 171, 172, 173, 174, 176, 177, 178, 179, 180, 181, 182, 183, 184, 185, 186, 188, 190, 191, 192, 193, 194, 195, 196, 197, 199, 200, 201, 204, 205, 207, 208, 209, 211, 213, 215, 217, 219, 221, 223, 225, 227, 229, 231, 233, 234, 235, 236, 237, 239
teeth, 210, 211, 212, 213, 216, 217, 228, 235

B

balance, 58, 88, 114
mass, 8, 18, 25, 54, 57, 58, 59, 63, 66, 68, 69, 70, 71, 72, 73, 75, 78, 87, 102, 143, 146, 157, 167, 168, 182, 190, 191, 218, 235
Basin of Attraction (BOA), 24, 26, 27, 35, 36, 38, 39, 42, 43
bifurcation diagram, 24, 33, 34, 38, 42, 44, 45
biped, v, 23, 24, 25, 26, 28, 30, 31, 33, 34, 35, 37, 42, 49, 51, 52

C

capacitive elements, 55, 57, 58, 80
chaos, v, vii, 23, 26, 28, 30, 33, 47, 48, 51, 52
chaotic, 23, 24, 26, 27, 28, 33, 34, 38, 42, 47, 49, 50, 52
locomotion, vii, 23, 24, 25
system, iv, v, vii, viii, 1, 2, 4, 7, 8, 9, 10, 11, 13, 14, 15, 16, 17, 18, 20, 22, 23, 24, 26, 27, 28, 29, 30, 31, 33, 34, 35, 36, 37, 38, 42, 44, 47, 49, 50, 52, 66, 67, 73, 75, 82, 83, 86, 91, 101, 102, 104, 114, 119, 120, 121, 136, 137, 140, 141, 144, 147, 148, 149, 150, 151, 153, 154, 159, 161, 163, 167, 168, 169, 170, 171, 172, 174, 176, 178, 179, 180, 181, 182, 185, 186, 187, 188, 190, 191, 192, 193, 194, 195, 196, 197, 198, 199, 200, 201, 202, 203, 205, 208, 210, 213, 214, 215, 216, 217, 218, 219, 220, 221, 222, 223, 224, 225, 226, 227, 228, 229, 231, 232, 234, 235, 237, 238
chatter, v, viii, 196, 197, 200, 204, 205, 206, 207, 208, 209, 211, 213, 215, 217, 219, 221, 222, 223, 224, 225, 227, 228, 229, 230, 231, 232, 233, 234, 235, 236, 237, 238, 239
collocation, 238, 239
chebyshev, 229, 238, 239
composite material, viii, 167, 178
computer aided, 205
design, v, vii, viii, 1, 2, 7, 10, 13, 20, 22, 23, 25, 52, 66, 68, 82, 85, 86, 87, 88, 89, 90, 91, 95, 97, 106, 114, 115, 138, 139, 140, 141, 142, 143, 144, 145, 147, 149, 153, 154, 155, 160, 162, 163, 164, 172, 173, 181, 183, 185, 186, 187, 190, 191, 192, 194, 195, 196, 197, 198, 199, 201, 202, 203, 204, 205, 208, 238
engineering, i, ii, iii, vii, viii, 1, 7, 22, 23, 50, 51, 52, 53, 80, 81, 82, 83, 85, 116, 117, 119, 137,

139, 148, 164, 165, 167, 184, 185, 186, 201, 202, 203, 204, 207, 208, 237, 238
 continuity equation, 56, 57, 58
 control, v, vii, viii, 1, 2, 3, 4, 5, 6, 7, 8, 9, 10, 11, 13, 14, 15, 16, 17, 18, 19, 20, 21, 22, 23, 24, 26, 28, 29, 30, 31, 32, 33, 34, 38, 42, 44, 45, 47, 48, 49, 50, 51, 52, 53, 58, 65, 67, 80, 81, 82, 86, 87, 88, 95, 115, 120, 140, 142, 143, 144, 145, 148, 158, 159, 160, 164, 167, 168, 169, 170, 171, 172, 173, 174, 176, 177, 178, 179, 180, 181, 182, 183, 184, 185, 186, 188, 190, 191, 192, 193, 194, 195, 196, 197, 199, 200, 201, 204, 205, 207, 208, 209, 211, 213, 215, 217, 219, 221, 223, 225, 227, 229, 231, 233, 234, 235, 236, 237, 239
 chaos, v, vii, 23, 24, 26, 27, 28, 30, 31, 33, 34, 47, 48, 49, 50, 51, 52
 distributed, 53, 55, 56, 60, 80, 119, 124, 127, 131, 167, 169, 170, 172, 175, 176, 177, 179, 180, 181, 182, 183, 187, 216
 Model Predictive Control (MPC):, 14
 predictive, 1, 2, 16, 20, 22, 229, 233, 234
 real time, 53, 54, 55, 56, 63, 65, 66, 67, 68, 80, 138
 track following, 1, 3, 5, 7, 9, 10, 11, 13, 14, 15, 16, 17, 18, 19, 21
 vibration, viii, 160, 161, 167, 168, 169, 170, 173, 174, 175, 176, 177, 180, 181, 182, 183, 184, 186, 193, 196, 197, 198, 199, 204, 217, 224, 225, 227, 235, 237, 238, 239
 co-simulation, 188
 coulomb friction, 9
 coupling effect, viii, 185, 186, 188, 196, 201
 critical, vii, 8, 54, 70, 71, 72, 102, 103, 107, 140, 146, 168, 176, 187, 194, 196, 200, 225, 227, 232
 height, 8, 25, 55, 75, 76, 78, 79, 100, 151, 163
 load, 55, 76, 78, 105, 109, 145, 146, 147, 148, 149, 154, 156, 169, 176, 216
 pressure, 25, 54, 56, 57, 58, 60, 63, 64, 65, 68, 69, 70, 71, 73, 75, 76, 77, 78, 105, 149, 156, 196, 202, 215, 217, 226, 228
 value, 13, 14, 16, 17, 22, 28, 39, 40, 42, 44, 48, 57, 61, 63, 66, 68, 69, 73, 76, 147, 171, 174, 176, 208, 210, 225, 235

D

Delay Differential Equations (DDEs), 227, 229
 Denavit–Hartenberg (D-H) convention, 90
 Direct Velocity Feedback (DVF), 170, 171
 Dynamic Vibration Absorber (DVA), 168
 dynamics, vii, viii, 2, 8, 9, 10, 11, 13, 24, 27, 28, 29, 30, 32, 33, 34, 38, 44, 47, 49, 50, 52, 66, 78, 81, 82, 175, 176, 183, 185, 186, 188, 189, 190, 191,

194, 195, 196, 199, 200, 201, 202, 203, 204, 205, 210, 217, 218, 219, 220, 221, 222, 227, 228, 229, 231, 234, 237, 239
 nonlinear, vii, 1, 2, 7, 9, 10, 11, 13, 15, 16, 20, 21, 22, 23, 24, 27, 52, 169, 182, 183, 229
 orbit, 23, 26, 27, 28, 31, 33, 35, 36, 38, 39, 40, 49, 50

E

Electromyograph (EMG), 87
 energy conversion, 185, 186, 187
 enthalpy, 54, 57, 58, 59, 60, 63, 68, 69, 70, 72, 73, 74, 75
 ergodicity, 27

F

False alarm rate (FAR), 126, 127, 146, 168, 186, 201
 Fiber Bragg Grating sensors (FBG), 167, 169, 170, 174, 175, 176, 177, 178, 179, 181, 183
 finite element, viii, 90, 156, 186, 188, 190, 194, 195, 201, 213, 214
 analysis (FEA), 90, 156
 method (FEM), 194, 195
 flow, 27, 28, 30, 31, 36, 37, 40, 53, 54, 55, 59, 60, 61, 63, 68, 69, 70, 71, 72, 73, 74, 75, 76, 78, 82, 189, 199
 coefficient, 8, 9, 54, 55, 58, 60, 64, 69, 70, 71, 72, 73, 122, 147, 218
 laminar, 60, 63, 72, 82
 mass, 8, 18, 25, 54, 57, 58, 59, 63, 66, 68, 69, 70, 71, 72, 73, 75, 78, 87, 102, 143, 146, 157, 167, 168, 182, 190, 191, 218, 235
 rate, 20, 21, 36, 54, 59, 68, 69, 70, 71, 72, 73, 74, 75, 78, 126, 127, 128, 129, 192, 209, 212, 226, 235
 resistance, 60, 61, 144, 154
 turbulent, 61, 63, 72, 82
 function, 9, 11, 13, 14, 15, 16, 24, 25, 27, 29, 33, 40, 44, 45, 48, 60, 61, 63, 64, 67, 70, 71, 72, 96, 113, 122, 140, 141, 154, 179, 201, 212, 227
 functional, 11, 87, 95, 112, 186, 188, 189, 201
 functionality, 2, 24, 86, 95, 156
 functions, 4, 8, 9, 10, 11, 31, 56, 63, 67, 86, 185, 186, 201, 219, 221, 222, 227

G

gait cycle, 140, 141, 143, 144, 154, 161, 162, 163, 164

H

Hard disc drive (HDD), vii, viii, 1, 2, 4, 5, 6, 7, 8, 9, 10, 13, 14, 15, 16, 20

Hardware In the Loop (HIL), 53, 54, 55, 65

Human Detection Algorithm (HAD), 87, 95, 99, 109, 112, 120, 121, 122, 124, 125, 127, 131, 134, 136, 148, 160, 161, 163

hydraulic, 53, 54, 55, 56, 60, 63, 64, 67, 68, 71, 72, 73, 75, 76, 77, 78, 79, 80, 82, 159, 168, 192, 193, 195, 197

actuator, viii, 5, 6, 7, 8, 9, 10, 21, 22, 101, 113, 170, 171, 173, 179, 180, 183, 192, 193, 195, 239

pump, 68, 73, 74, 75, 76, 77, 78, 79, 80

I

Independent Modal Space Control (IMSC), 169, 183
intelligent, 138, 188, 200, 204, 205, 207, 237

control, v, vii, viii, 1, 2, 3, 4, 5, 6, 7, 8, 9, 10, 11, 13, 14, 15, 16, 17, 18, 19, 20, 21, 22, 23, 24, 26, 28, 29, 30, 31, 32, 33, 34, 38, 42, 44, 45, 47, 48, 49, 50, 51, 52, 53, 58, 65, 67, 80, 81, 82, 86, 87, 88, 95, 115, 120, 140, 142, 143, 144, 145, 148, 158, 159, 160, 164, 167, 168, 169, 170, 171, 172, 173, 174, 176, 177, 178, 179, 180, 181, 182, 183, 184, 185, 186, 188, 190, 191, 192, 193, 194, 195, 196, 197, 199, 200, 201, 204, 205, 207, 208, 209, 211, 213, 215, 217, 219, 221, 223, 225, 227, 229, 231, 233, 234, 235, 236, 237, 239

machining, v, viii, 199, 200, 204, 205, 207, 208, 209, 210, 211, 213, 214, 215, 217, 218, 219, 220, 221, 223, 224, 225, 226, 227, 229, 231, 232, 233, 234, 235, 237, 238, 239

manufacturing, v, vii, viii, 51, 86, 87, 88, 95, 97, 114, 117, 119, 185, 188, 200, 203, 204, 207, 237, 238, 239

K

kinematic, 90, 91, 92, 93, 94, 97, 109, 110, 111, 112, 189, 191, 210, 211, 213, 231, 234

equation, 13, 27, 28, 29, 30, 31, 32, 44, 46, 47, 49, 56, 57, 58, 59, 61, 70, 75, 90, 91, 92, 94, 122, 123, 143, 146, 147, 148, 170, 171, 174, 210, 219, 222, 225, 226, 227, 229

model, 4, 7, 8, 9, 10, 14, 15, 17, 18, 20, 21, 22, 23, 24, 25, 26, 28, 30, 31, 33, 34, 42, 49, 50, 51, 52, 56, 60, 63, 66, 67, 68, 71, 72, 73, 76, 79, 80, 82, 93, 94, 97, 107, 113, 119, 123, 124, 125, 126, 127, 128, 129, 130, 131, 134, 135, 136, 154, 156, 169, 171, 180, 190, 191, 194, 195, 196, 197, 199, 201, 204, 205, 206, 210, 212, 213, 219, 220, 221, 229, 230, 239

124, 125, 126, 127, 128, 129, 130, 131, 134, 135, 136, 154, 156, 169, 171, 180, 190, 191, 194, 195, 196, 197, 199, 201, 204, 205, 206, 210, 212, 213, 219, 220, 221, 229, 230, 238

L

laminar motion, 60

limit cycle, 26, 27, 35, 36, 37, 42

linearization, 23, 28, 29, 31, 32, 42, 43, 44, 48

Lorentz force, 7

losses, 55, 58, 60, 70, 72, 74, 78, 80

distributed, 53, 55, 56, 60, 80, 119, 124, 127, 131, 167, 169, 170, 172, 175, 176, 177, 179, 180, 181, 182, 183, 187, 216

lumped, 53, 54, 55, 56, 57, 58, 59, 60, 80, 169, 216

lyapunov exponent, 24, 33, 34, 36, 39, 42

M

manufacturing process, 88, 95, 97

material processing, viii, 185, 186, 187, 199

method, vii, 11, 14, 23, 24, 28, 30, 31, 43, 49, 61, 66, 105, 111, 122, 123, 140, 142, 156, 159, 170, 172, 188, 190, 194, 195, 201, 205, 213, 229, 230, 231, 235, 236, 237, 238, 239

model, 4, 7, 8, 9, 10, 14, 15, 17, 18, 20, 21, 22, 23, 24, 25, 26, 28, 30, 31, 33, 34, 42, 49, 50, 51, 52, 56, 60, 63, 66, 67, 68, 71, 72, 73, 76, 79, 80, 82, 92, 93, 94, 97, 107, 113, 119, 123, 124, 125, 126, 127, 128, 129, 130, 131, 134, 135, 136, 154, 156, 169, 171, 180, 190, 191, 194, 195, 196, 197, 199, 201, 204, 205, 206, 210, 212, 213, 219, 220, 221, 229, 230, 238

distributed, 53, 55, 56, 60, 80, 119, 124, 127, 131, 167, 169, 170, 172, 175, 176, 177, 179, 180, 181, 182, 183, 187, 216

functional, 11, 87, 95, 112, 186, 188, 189, 201

lumped parameter, 55, 56, 80

Modular Prosthetic Hand (MPH), 8, 85, 87

multibody, 188, 189, 190, 201

dynamics, vii, viii, 2, 8, 9, 10, 11, 13, 24, 27, 28, 29, 30, 32, 33, 34, 38, 44, 47, 49, 50, 52, 66, 78, 81, 82, 175, 176, 183, 185, 186, 188, 189, 190, 191, 194, 195, 196, 199, 200, 201, 202, 203, 204, 205, 210, 217, 218, 219, 220, 221, 222, 227, 228, 229, 231, 234, 237, 239

multiphysics, 185, 187

N

Neural network (NN), vii, 1, 11, 13, 14, 15, 16, 17, 18, 19, 20, 21
noise, 2, 172, 173, 176, 177, 231

O

object tracking, 123
observer, 172, 183
state, 2, 7, 8, 9, 15, 27, 28, 29, 30, 31, 36, 37, 38, 47, 48, 63, 79, 86, 103, 119, 167, 168, 172, 204, 205, 223, 227, 229, 235
optical, 169, 174, 175, 176, 178, 191
device, viii, 6, 86, 103, 105, 106, 155, 162, 189, 198, 235
fibers, 176
interrogator, 175, 176, 178
sensor, 66, 169, 170, 171, 172, 174, 175, 176, 177, 179, 180, 181, 183, 231, 232
orbit, 38
Dynamics, vii, viii, 2, 8, 9, 10, 11, 13, 24, 27, 28, 29, 30, 32, 33, 34, 38, 44, 47, 49, 50, 52, 66, 78, 81, 82, 175, 176, 183, 185, 186, 188, 189, 190, 191, 194, 195, 196, 199, 200, 201, 202, 203, 204, 205, 210, 217, 218, 219, 220, 221, 222, 227, 228, 229, 231, 234, 237, 239
Unstable Periodic, 23, 27
Ott–Grebogi–Yorke method (OGY), 28, 49

P

Parallel Advanced Technology Attachment (PATA), 6
passive, 24, 33, 42, 51, 52, 168, 183, 234, 235
condition, 24, 31, 32, 33, 35, 36, 39, 40, 42, 47, 48, 49, 50, 120, 151, 152, 168, 171, 174, 190, 191, 197, 204, 207, 225, 230, 231, 236
device, viii, 6, 86, 103, 105, 106, 155, 162, 189, 198, 235
walking robot, 24, 52
piezoelectric, viii, 167, 169, 176, 178, 179, 183, 184, 202, 222, 232, 235
accelerometer, 222
actuator, viii, 5, 6, 7, 8, 9, 10, 21, 22, 101, 113, 170, 171, 173, 179, 180, 183, 192, 193, 195, 239
effect, 9, 10, 26, 52, 126, 167, 169, 170, 172, 174, 176, 177, 181, 193, 196, 198, 204, 212, 214, 215, 224, 226, 227, 230
shaker, 176

poincaré, 23, 24, 27, 28, 29, 30, 31, 32, 35, 36, 39, 40, 42, 43, 44, 46, 47, 49, 50
function, 9, 11, 13, 14, 15, 16, 24, 25, 27, 29, 33, 40, 44, 45, 48, 60, 61, 63, 64, 67, 70, 71, 72, 96, 113, 122, 140, 141, 154, 179, 201, 212, 227
map, 23, 24, 27, 28, 29, 30, 31, 32, 35, 40, 42, 43, 44, 46, 49
plane, 23, 24, 27, 35, 37, 145, 146, 158, 190, 198, 218, 219, 226, 233

Positive Position Feedback (PPF), 169, 183
pressure, 25, 54, 56, 57, 58, 60, 63, 64, 65, 68, 69, 70, 71, 73, 75, 76, 77, 78, 105, 149, 156, 196, 202, 215, 217, 226, 228

Q

quality assurance, 200

R

real-time (RT), 53, 55, 63, 65, 66, 67, 80
code, 53, 54, 66, 67, 76, 79, 188, 190, 194, 195, 196
control system, 7, 9, 20, 21, 82, 183, 187, 195, 196, 197, 201, 234
resistive element, 56, 58, 59
Robust Integral Sign of Error (RISE), 1, 3, 5, 7, 8, 9, 11, 13, 14, 15, 16, 17, 18, 19, 20, 21, 144

S

Serial Advanced Technology Attachment (SATA), 6
servo, 1, 2, 4, 6, 7, 9, 10, 13, 14, 16, 20, 22, 88, 94, 102
positioning, 2, 4, 5, 6, 17, 22, 148, 154, 168, 169, 210, 231
system, iv, v, vii, viii, 1, 2, 4, 7, 8, 9, 10, 11, 13, 14, 15, 16, 17, 18, 20, 22, 23, 24, 26, 27, 28, 29, 30, 31, 33, 34, 35, 36, 37, 38, 42, 44, 47, 49, 50, 52, 66, 67, 73, 75, 82, 83, 86, 91, 101, 102, 104, 114, 119, 120, 121, 136, 137, 140, 141, 144, 147, 148, 149, 150, 151, 153, 154, 159, 161, 163, 167, 168, 169, 170, 171, 172, 174, 176, 178, 179, 180, 181, 182, 185, 186, 187, 188, 190, 191, 192, 193, 194, 195, 196, 197, 198, 199, 200, 201, 202, 203, 205, 208, 210, 213, 214, 215, 216, 217, 218, 219, 220, 221, 222, 223, 224, 225, 226, 227, 228, 229, 231, 232, 234, 235, 237, 238
Small Computer Systems Interface (SCSI), 6
smart, viii, 164, 167, 168, 183, 186, 201

- function, 9, 11, 13, 14, 15, 16, 24, 25, 27, 29, 33, 40, 44, 45, 48, 60, 61, 63, 64, 67, 70, 71, 72, 96, 113, 122, 140, 141, 154, 179, 201, 212, 227
- material, iv, v, vii, viii, 2, 4, 61, 88, 90, 102, 105, 114, 146, 149, 154, 156, 157, 185, 186, 187, 188, 190, 191, 193, 196, 197, 199, 200, 201, 203, 208, 209, 210, 212, 213, 224, 226, 230, 235
- Structure, 21, 67, 120, 121, 123, 140, 141, 149, 167, 168, 169, 170, 175, 176, 177, 178, 179, 180, 181, 182, 192, 193, 196, 201, 207, 221, 222
- smartness, vii, viii, 186, 201
- Spatial Filter Technique, 181
- spillover, 169, 170, 172, 180, 181, 183
- stability
- system, iv, v, vii, viii, 1, 2, 4, 7, 8, 9, 10, 11, 13, 14, 15, 16, 17, 18, 20, 22, 23, 24, 26, 27, 28, 29, 30, 31, 33, 34, 35, 36, 37, 38, 42, 44, 47, 49, 50, 52, 66, 67, 73, 75, 82, 83, 86, 91, 101, 102, 104, 114, 119, 120, 121, 136, 137, 140, 141, 144, 147, 148, 149, 150, 151, 153, 154, 159, 161, 163, 167, 168, 169, 170, 171, 172, 174, 176, 178, 179, 180, 181, 182, 185, 186, 187, 188, 190, 191, 192, 193, 194, 195, 196, 197, 198, 199, 200, 201, 202, 203, 205, 208, 210, 213, 214, 215, 216, 217, 218, 219, 220, 221, 222, 223, 224, 225, 226, 227, 228, 229, 231, 232, 234, 235, 237, 238
- stability, viii, 1, 8, 11, 24, 25, 28, 51, 66, 72, 120, 140, 142, 170, 171, 174, 196, 225, 226, 227, 228, 229, 230, 237, 238
- asymptotic, 1, 11, 21, 22
- control, v, vii, viii, 1, 2, 3, 4, 5, 6, 7, 8, 9, 10, 11, 13, 14, 15, 16, 17, 18, 19, 20, 21, 22, 23, 24, 26, 28, 29, 30, 31, 32, 33, 34, 38, 42, 44, 45, 47, 48, 49, 50, 51, 52, 53, 58, 65, 67, 80, 81, 82, 86, 87, 88, 95, 115, 120, 140, 142, 143, 144, 145, 148, 158, 159, 160, 164, 167, 168, 169, 170, 171, 172, 173, 174, 176, 177, 178, 179, 180, 181, 182, 183, 184, 185, 186, 188, 190, 191, 192, 193, 194, 195, 196, 197, 199, 200, 201, 204, 205, 207, 208, 209, 211, 213, 215, 217, 219, 221, 223, 225, 227, 229, 231, 233, 234, 235, 236, 237, 239
- dynamic, vii, viii, 4, 9, 11, 14, 15, 18, 21, 23, 24, 27, 30, 33, 44, 47, 51, 52, 55, 56, 64, 66, 76, 82, 140, 141, 167, 168, 169, 170, 178, 187, 188, 189, 190, 194, 195, 196, 197, 200, 203, 204, 206, 208, 214, 217, 219, 220, 221, 224, 225, 227, 229, 230, 234, 235, 237
- limit, 26, 27, 35, 36, 37, 42, 44, 63, 154, 158, 159, 160, 169, 174, 176, 225, 226
- lobes, 225, 226, 228, 230, 235
- locomotion, vii, 23, 24, 25
- stress, 90, 149, 151, 152, 156, 202, 224
- stribeck velocity, 9
- strike transition, 28, 30, 31
- Structural Health Monitoring (SHM), viii, 169
- swept laser technology, 175
- system, iv, v, vii, viii, 1, 2, 4, 7, 8, 9, 10, 11, 13, 14, 15, 16, 17, 18, 20, 22, 23, 24, 26, 27, 28, 29, 30, 31, 33, 34, 35, 36, 37, 38, 42, 44, 47, 49, 50, 52, 66, 67, 73, 75, 82, 83, 86, 91, 101, 102, 104, 104, 114, 119, 120, 121, 136, 137, 140, 141, 144, 147, 148, 149, 150, 151, 153, 154, 159, 161, 163, 167, 168, 169, 170, 171, 172, 174, 176, 178, 179, 180, 181, 182, 185, 186, 187, 188, 190, 191, 192, 193, 194, 195, 196, 197, 198, 199, 200, 201, 202, 203, 205, 208, 210, 213, 214, 215, 216, 217, 218, 219, 220, 221, 222, 223, 224, 225, 226, 227, 228, 229, 231, 232, 234, 235, 237, 238
- chaotic, 23, 24, 26, 27, 28, 33, 34, 38, 42, 47, 49, 50, 52
- dynamics, vii, viii, 2, 8, 9, 10, 11, 13, 24, 27, 28, 29, 30, 32, 33, 34, 38, 44, 47, 49, 50, 52, 66, 78, 81, 82, 175, 176, 183, 185, 186, 188, 189, 190, 191, 194, 195, 196, 199, 200, 201, 202, 203, 204, 205, 210, 217, 218, 219, 220, 221, 222, 227, 228, 229, 231, 234, 237, 239
- engineering, i, ii, iii, vii, viii, 1, 7, 22, 23, 50, 51, 52, 53, 80, 81, 82, 83, 85, 116, 117, 119, 137, 139, 148, 164, 165, 167, 184, 185, 186, 201, 202, 203, 204, 207, 208, 237, 238
- T**
- thermoplastic processing, 88
- Track Miss–Registration (TMR), 10
- U**
- Unmanned Aerial Vehicle (UAV), v, viii, 119, 120, 121, 122, 123, 127, 129, 131, 134, 136
- unstable, 23, 27, 30, 45, 46, 48, 119, 224, 230, 231, 232, 233
- manifold, 27, 30, 46, 48
- region, vii, 26, 30, 32, 33, 35, 42, 190, 230
- structure, 21, 67, 120, 121, 123, 140, 141, 149, 167, 168, 169, 170, 175, 176, 177, 178, 179, 180, 181, 182, 192, 193, 196, 201, 207, 221, 222
- User–prosthetic interface (UPI), 86

V

vibration, viii, 176, 182, 183, 196, 204, 217, 224,
225, 227, 235, 237, 238, 239

forced, 167, 168, 207, 223
free, 7, 145, 223
self-excited, viii
Voice Coil Motor (VCM), 5, 6, 8, 9, 10, 22